

INAUGURAL-DISSERTATION

am Leibniz-Institut für Atmosphärenphysik in Kühlungsborn
zur Erlangung der Doktorwürde
der Mathematisch-Naturwissenschaftlichen Fakultät
der Universität Rostock

3-D Modeling of Noctilucent Cloud Evolution and Relationship to the Ambient Atmosphere

von
Johannes Kiliani

Abstract: Noctilucent clouds (NLC) at the polar summer mesopause are highly sensitive to atmospheric conditions. Using NLC as an indicator for atmospheric dynamics and composition requires detailed knowledge of the processes of ice formation. In this thesis, two different models of the middle atmosphere are used to study background conditions including tidal and gravity wave effects and their impact on NLC. The Leibniz-Institute Middle Atmosphere model (LIMA) features an accurate temperature climatology and thermal tides, while the Kühlungsborn Mechanistic Circulation Model (KMCM) resolves gravity waves and has a more accurate circulation. The Mesospheric Ice Microphysics And transport model (MIMAS) is a 3-D ice particle model for the middle atmosphere, it can be combined with either LIMA or KMCM. Its Lagrangian approach makes it suitable for single particle and ensemble evolution studies.

The modeled NLC resembles measured ice clouds in typical cloud altitude, brightness, and duration. The occurrence of ice clouds correlates well to ambient temperatures, and this relationship improves on large scales. Large NLC particles are studied through their life cycle. Initial growth around the mesopause is slow due to a lack of ambient water vapor. Only around 1% of ice particles grow to visible size (≈ 50 nm). Most of the radius increase takes place around 83 km, within 6 hours prior to observation. Here, upwelling keeps the altitude of NLC particles in an environment with many H₂O molecules and thereby supports ice particle growth. The particle age at 69° N is ≈ 36 h, with longer lifetimes at higher latitude. Particle shape was also taken into account: Cylindrical particles grow faster and to larger size compared to spheres, which increases the brightness of NLC. Simulating NLC on KMCM dynamics with a variable gravity wave spectrum shows that short period gravity waves reduce the brightness and particle age of the ice cloud.

Adresse:
Schlossstraße 6
18225 Ostseebad Kühlungsborn
Germany

IAP Kühlungsborn
Dezember 2014
IAP-Nr.: 44/2014
ISSN: 1615–8083

3-D Modeling of Noctilucent Cloud Evolution and Relationship to the Ambient Atmosphere

Dissertation
zur Erlangung des akademischen Grades
doctor rerum naturalium (Dr. rer. nat.)
der Mathematisch-Naturwissenschaftlichen Fakultät der Universität Rostock

vorgelegt von
Johannes Kiliani,
geboren am 24. April 1981 in Basel,
wohnhaft in Kühlungsborn

1. Gutachter: Prof. Dr. Franz-Josef Lübken,
Universität Rostock
2. Gutachter: Prof. Dr. Christian von Savigny,
Universität Greifswald

Datum des Einreichens der Arbeit: 27. Juni 2014
Datum der Verteidigung: 7. November 2014

Abstract

Noctilucent clouds (NLC) at the polar summer mesopause are highly sensitive to atmospheric conditions. Using NLC as an indicator for atmospheric dynamics and composition requires detailed knowledge of the processes of ice formation. In this thesis, two different models of the middle atmosphere are used to study background conditions including tidal and gravity wave effects and their impact on NLC. The Leibniz-Institute Middle Atmosphere model (LIMA) features an accurate temperature climatology and thermal tides, while the Kühlungsborn Mechanistic Circulation Model (KMCM) resolves gravity waves and has a more accurate circulation. The Mesospheric Ice Microphysics And tranSport model (MIMAS) is a 3-D ice particle model for the middle atmosphere, it can be combined with either LIMA or KMCM. Its Lagrangian approach makes it suitable for single particle and ensemble evolution studies.

The modeled NLC resembles measured ice clouds in typical cloud altitude, brightness, and duration. The occurrence of ice clouds correlates well to ambient temperatures, and this relationship improves on large scales. Large NLC particles are studied through their life cycle. Initial growth around the mesopause is slow due to a lack of ambient water vapor. Only around 1% of ice particles grow to visible size (≈ 50 nm). Most of the radius increase takes place around 83 km, within 6 hours prior to observation. Here, upwelling keeps the altitude of NLC particles in an environment with many H_2O molecules and thereby supports ice particle growth. The particle age at 69°N is ≈ 36 h, with longer lifetimes at higher latitude. Particle shape was also taken into account: Cylindrical particles grow faster and to larger size compared to spheres, which increases the brightness of NLC. Simulating NLC on KMCM dynamics with a variable gravity wave spectrum shows that short period gravity waves reduce the brightness and particle age of the ice cloud.

Kurzfassung

Leuchtende Nachtwolken (NLC) in der polaren Sommermesopausenregion sind sehr empfindlich gegenüber ihren Umweltbedingungen. Genaue Kenntnis des Entstehungsprozesses von Eis ist nötig, um von NLC auf die Dynamik und Zusammensetzung der Atmosphäre zu schließen. In dieser Arbeit werden zwei Modelle der Atmosphäre verwendet, um die Hintergrundbedingungen einschließlich Gezeiten und Schwerewellen sowie deren Auswirkungen auf NLC zu untersuchen. Das Leibniz-Institute Middle Atmosphere model (LIMA) weist eine akkurate Temperaturklimatologie und thermische Gezeiten auf, während das Kühlungsborn Mechanistic Circulation Model (KMCM) über aufgelöste Schwerewellen und eine genauere Zirkulation verfügt. Das Mesospheric Ice Microphysics And tranSport model (MIMAS) ist ein 3-D Eisteilchenmodell für die mittlere Atmosphäre, das sowohl mit LIMA als auch mit KMCM gekoppelt werden kann. Als Lagrangemodell ist es gut geeignet zur Untersuchung der Entwicklung von Einzelteilchen und Teilchenensembles.

Die modellierte NLC ähnelt gemessenen Eiswolken in Höhe, Helligkeit und Dauer. Das Auftreten von Eiswolken ist korreliert zur Umgebungstemperatur, dieser Zusammenhang nimmt auf größeren Skalen zu. Die Entwicklung von großen NLC-Teilchen wird über deren Lebensdauer untersucht. Das anfängliche Teilchenwachstum um die

Mesopause ist sehr langsam, da dort wenig Wasserdampf vorhanden ist. Nur etwa 1% der Eisteilchen wachsen zu sichtbarer Größe (≈ 50 nm) heran. Der Großteil des Wachstums findet um 83 km innerhalb von 6 Stunden der Beobachtung statt. Dort halten Aufwinde die NLC-Teilchen in der wasserdampfreichen Umgebung, was deren Wachstum begünstigt. Das Alter von Eisteilchen bei 69°N beträgt etwa 36 h, in höheren Breiten werden die Teilchen älter. Die Teilchenform wurde ebenfalls berücksichtigt: Zylindrische Eisteilchen wachsen schneller und werden größer als kugelförmige, was die Helligkeit von NLC erhöht. Simulationen von NLC auf KMCM-Dynamik mit variablem Schwerewellenspektrum weisen nach, dass kurzperiodische Schwerewellen die Helligkeit und das Teilchenalter der Eiswolke verringern.

Contents

1	Introduction	1
1.1	The atmosphere of the Earth	1
1.1.1	Thermal structure of the atmosphere	1
1.1.2	Gravity waves	2
1.2	Noctilucent clouds	3
1.2.1	Description and observational history	3
1.2.2	Summary of optical and microphysical properties	4
1.3	Outline of the dissertation	5
2	Dynamics of the mesosphere and lower thermosphere (MLT) region	7
2.1	Middle atmosphere dynamical modeling	7
2.1.1	The Leibniz-Institute Middle Atmosphere model (LIMA)	7
2.1.2	The Kühlungsborn mechanistic circulation model (KMCM)	8
2.2	Mean state of the summer MLT: Models and measurements	10
2.2.1	Model temperature and wind structure of the summer MLT region	10
2.2.2	Mean dynamics at 69°N: Comparison with observations	13
2.2.3	Local time dependence of winds at 69°N	15
2.3	Atmospheric waves in the summer MLT: Models and measurements	17
2.3.1	Vertical structure of dynamics in LIMA and KMCM	17
2.3.2	Zonal wave propagation in LIMA and KMCM	20
2.3.3	5-day wave: Occurrence in LIMA, KMCM and measurements	23
2.4	Conclusions	24
3	The Lagrangian Tracer Model MIMAS	25
3.1	Model structure of MIMAS	25
3.1.1	Overview	25
3.1.2	Model resolution and grid structure	26
3.2	Water vapor in the summer MLT region	26
3.2.1	Initialization and relaxation of water vapor	27
3.2.2	Water vapor advection and diffusion	28
3.2.3	Photodissociation of H ₂ O	29
3.3	Microphysical processes in MIMAS	30
3.3.1	Dust particle size distribution and relocation algorithm	30
3.3.2	Nucleation and particle growth	31
3.3.3	Particle sedimentation and diffusion	34

Contents

4	Morphology of NLC in MIMAS-LIMA	35
4.1	General NLC morphology	35
4.1.1	Snapshot of NLC in MIMAS-LIMA	35
4.1.2	NLC time series	36
4.1.3	Duration of noctilucent clouds	38
4.1.4	Morphology of NLC-related parameters	39
4.2	General trajectory shape	40
4.2.1	Sample ice trajectories	41
4.2.2	Ice trajectory statistics	41
4.3	Relationship of ambient conditions and ice clouds	44
4.3.1	Correlation between ambient conditions and NLC	45
4.3.2	Scale dependence of temperature-NLC relationship	46
4.3.3	Relationship of temperature, ice mass, and particle radius	47
4.3.4	Parametrization of NLC brightness from ambient conditions	49
5	Ice particle evolution in strong NLC	51
5.1	Description of statistical analysis procedure	51
5.1.1	NLC event selection	51
5.1.2	Particle ensemble selection	52
5.1.3	Trajectory analysis	53
5.2	Case study: Evolution of a single NLC event at 69°N	55
5.2.1	Particle transport and growth	55
5.2.2	Nucleation process	58
5.3	Statistics on NLC development at ALOMAR (69°N)	60
5.3.1	General ice particle transport and growth	60
5.3.2	Vertical motion of NLC	62
5.3.3	Nucleation process of 50 NLC events	65
5.3.4	Sublimation, visibility time and other parameters	68
5.3.5	Comparison with COMMA/IAP and measurements	69
5.4	Results from other latitudes	70
5.4.1	Spitsbergen (79°N)	70
5.4.2	Latitudes below 60°N	72
6	Sensitivity of NLC life cycle	75
6.1	Influence of aspheric particles on noctilucent clouds	75
6.1.1	Adaptations to MIMAS for non-spherical particles	75
6.1.2	Validation of particle size with 3-color lidar measurements	77
6.1.3	Influence of non-spherical particles on general NLC morphology	80
6.2	Sensitivity to dynamic wave spectrum: Ice morphology with KMCM	82
6.2.1	Introduction and analysis methods	82
6.2.2	Morphology of ice clouds in MIMAS-KMCM	83
6.2.3	Dependence of NLC life cycle on resolved gravity waves	87
7	Summary and outlook	93
7.1	Summary	93
7.2	Outlook	94

Appendix A Additional information on dynamics	97
A.1 Temperature local time dependence	97
A.2 Fourier spectrum of waves in the MLT, in models and measurements . . .	99
Appendix B Additional information on NLC	103
B.1 Light scattering on cylindrical ice particles, color ratios	103
B.2 Dust particle distribution	105
B.3 Spectrum of NLC	106
B.4 Additional ice cloud morphology of MIMAS-KMCM	107
B.5 NLC simulation with hybrid LIMA+KMCM dynamics	109
B.6 Zonal propagation of ice clouds	111
B.7 Additional nucleation-related statistics of strong NLC	112
B.8 Vertical transport over particle lifetime	114
B.9 Additional analysis of particle life cycle at different latitudes	114
Appendix C Technical details of MIMAS	119
C.1 Water vapor transport scheme	119
C.2 Diffusion scheme: Crank-Nicholson	120
C.3 UV flux parametrization, photolysis equation	120
C.4 Particle advection	121
C.5 Details of NLC tracing method	121
C.6 Improvements to dust relocation algorithm	122
C.7 Interpolation of background fields	124
Bibliography	127
List of Figures	137
List of Tables	139
List of Symbols and Acronyms	141
Acknowledgments	143

1 Introduction

1.1 The atmosphere of the Earth

The atmosphere of the Earth is defined as the gas layer surrounding the planet, it has a fundamental importance for making it a habitable environment. Only planets with an atmosphere may retain water in its liquid form and form the hydrological and carbon cycles necessary for sustaining life. Earth's atmosphere is composed of 78% nitrogen, 21% oxygen, 0.94% argon, 0.04% carbon dioxide and a large number of trace gases. The component which is most variable is water vapor, at $\approx 0.25\%$.

The atmosphere is gravitationally bound to the Earth, and as a gas becomes thinner exponentially with increasing distance from the surface. The exponent contains a variable H called the atmospheric scale height. H depends on temperature and varies between 5 and 10 km, with around 7 km typical. This means that the atmospheric pressure (and density) decrease by an order of magnitude roughly every 16 km.

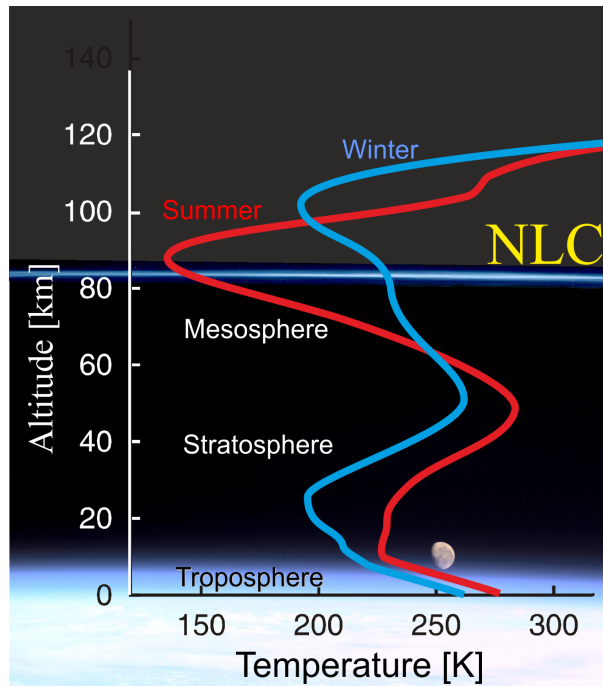


Figure 1.1 Temperature profiles of polar region atmosphere, during summer and winter and altitude of noctilucent clouds (NLC), adapted from *Baumgarten* (2001).

1.1.1 Thermal structure of the atmosphere

Since the atmosphere at the edge of space is so much thinner than at ground level, its physical state and chemical composition also change with altitude. The atmosphere is divided into several layers which are separated by temperature minima and maxima, shown schematically in Figure 1.1.

The lowest atmospheric layer is called the troposphere, reaching up to 10 – 18 kilometers. The troposphere is where most weather phenomena take place, 90% of the

Chapter 1 Introduction

atmospheric mass and more than 99% of the water vapor are located in this layer. Tropospheric processes are determined by the proximity of the boundary layer and the interaction with ground and ocean surface. Temperature decreases with altitude at a typical lapse rate of $7 \frac{\text{K}}{\text{km}}$ up to the tropopause which is typically around 220 K.

The next layer is the stratosphere, extending up to ≈ 50 km. Unlike the troposphere, it is dynamically very stable because its temperature increases with altitude, reaching around 270 K at its upper boundary, the stratopause. The main ozone layer is located within the stratosphere, and the most characteristic chemical process in this part of the atmosphere is the oxygen-ozone (or Chapman) cycle, where solar UV radiation is absorbed and converted to heat.

Above the stratopause, the mesosphere extends up to about 90 km altitude. The temperature decreases again in this layer, reaching an average minimum of 190 K at its top (the mesopause). In the mesosphere, gravity waves (see Section 1.1.2) are especially important for circulation patterns at high latitudes, causing lower temperatures in summer than in winter. In the polar summer mesopause, temperatures as low as 120 K may occur, allowing formation of noctilucent clouds which are the main topic of this thesis.

The last well-defined atmospheric layer is the thermosphere, reaching from the mesopause up to the exobase, around 500–1000 km above the surface. Above ≈ 110 km (the turbopause), air is no longer mixed by turbulence, so the constituents separate with each individual gas having its own scale height. As a result, the upper thermosphere is mainly composed of atomic oxygen and nitrogen, helium, and hydrogen. Ionization increases throughout the thermosphere (ionosphere), with electron density peaking around 250 km. The temperature increases with altitude and can reach up to 2000 K during day time. Stratosphere, mesosphere, and lower thermosphere together are also referred to as the middle atmosphere.

1.1.2 Gravity waves

A particularly important atmospheric phenomenon for the middle atmosphere is gravity waves (GW). These are generated in the troposphere, the main mechanisms are convective cells in tropospheric weather fronts and winds flowing over topographic obstacles (orographic or mountain waves) (e.g. *Fritts and Alexander, 2003; Becker, 2012*). In the troposphere the amplitude of these waves is less than 1 K, still enough to form wave patterns visible in clouds. The waves propagate upwards through the atmosphere, where the wave medium (air) gets thinner at higher altitudes. Since the wave energy is initially conserved, wave amplitudes will increase with altitude, similar to sea surface waves when approaching a shoreline. As with surface waves, this process does not continue indefinitely, and atmospheric gravity waves will eventually break once amplitudes no longer allow them to propagate further upwards. This process is very strong in the mesopause region and has several important effects on this region of the atmosphere: The energy of the breaking gravity waves cascades into smaller scales causing strong turbulent mixing around the mesopause, and eventually dissipates into heat. The momentum contained in the gravity waves is transferred to the mean flow in the altitude where the wave breaking occurs (wave drag). This drives the dynamics in the mesosphere and lower thermosphere (MLT) region (*Holton, 1983*). Thus, gravity



Figure 1.2 Occurrence of noctilucent cloud at Kühlungsborn (54°N , 12°E) on June 24, 2005, 23:35 CEST, courtesy of Gerd Baumgarten. The clouds can be recognized as silvery-blue shining structures about 2 hours after sunset.

waves are the indirect cause for the cold summer mesopause.

1.2 Noctilucent clouds

1.2.1 Description and observational history

Noctilucent clouds (NLC), also called polar mesospheric clouds (PMC), are the main objective of this thesis. They occur at altitudes of 80 – 86 kilometers within both polar regions, polewards of $\approx 55^{\circ}$ and only during summer conditions. NLC consist of ice particles with a typical size of 40 – 100 nm, far smaller than any tropospheric cloud particles (usually 10 μm and larger).

Noctilucent clouds have been observed in northern Europe since 1885, where the first documented observations were made two years after the major volcanic eruption of the Krakatoa between Java and Sumatra (*Leslie*, 1885; *Backhouse*, 1885; *Jesse*, 1885). The reason for their name is that they can be observed only during nautical twilight, while the Sun still illuminates the atmosphere in 80 km altitude but not the ground or lower atmosphere. During daytime NLC may be present but cannot be observed with the naked eye as they are obscured by Rayleigh scattering in the lower atmosphere. The typical visual appearance of NLC is shown in Figure 1.2: They are generally seen in poleward direction and resemble cirrus clouds to some extent. They can be distinguished from tropospheric ice clouds by the polarization of light scattered by the clouds and their characteristic wave structures, caused by temperature gravity waves which greatly affect the cloud development.

Today, the observation of NLC uses a much broader range of instruments. In addition to a number of cameras, noctilucent clouds are observed from the ground with lidars (LIght Detection And Ranging), where a laser is pointed into the atmosphere and the amount of scattered light indicates if mesospheric ice is present (e.g. *Fiedler et al.*, 2009). Unlike cameras, lidars can detect NLC during daylight conditions, which is a large advantage in polar summer. When observed from space, NLC are usually called Polar Mesospheric Clouds (PMC) for historical reasons. This is done with satellites like the Aeronomy of Ice in the Mesosphere (AIM) experiment. On board the AIM satellite there are two instruments devoted to NLC research: One measures scattered sunlight in the UV spectrum and is called Cloud Imaging and Particle Size experiment

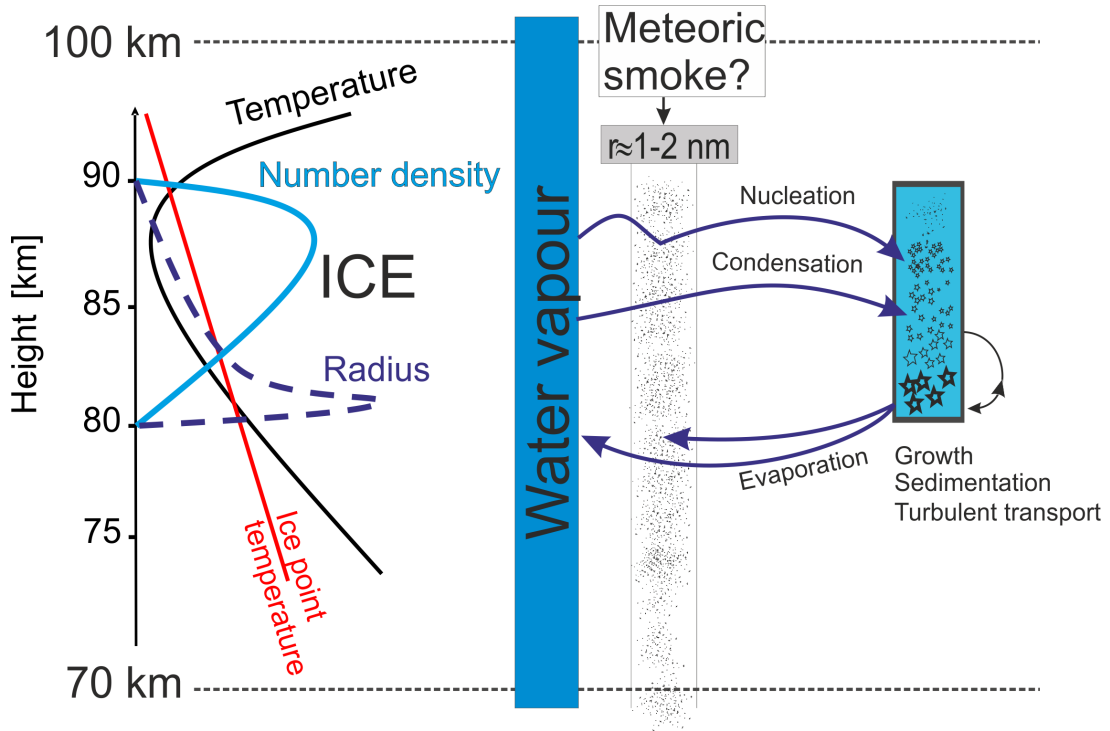


Figure 1.3 Summary of microphysical processes involved with the formation of noctilucent clouds, adapted from *Baumgarten* (2001) and *Rapp and Thomas* (2006).

(CIPS). The other one measures the extinction of sunlight by the atmosphere (Solar Occultation For Ice Experiment, SOFIE) (*McClintock et al.*, 2009; *Hervig et al.*, 2009a; *Russell et al.*, 2009).

Besides optical remote sensing, there are other instruments like radars and mass spectrometers on rockets that can detect smaller ice particles which form Polar Mesospheric Summer Echoes (PMSE). These are regularly found together with NLC (e.g. *Nussbaumer et al.*, 1996; *Gumbel and Witt*, 2001; *Rapp and Lübken*, 2004; *Li et al.*, 2010; *Kaifler et al.*, 2011).

1.2.2 Summary of optical and microphysical properties

Figure 1.3 depicts a summary of the mechanisms involved in noctilucent clouds. In a narrow region around the mesopause during polar summer, water vapor is supersaturated. This requires temperatures below 150 K in mesospheric conditions, where the amount of water vapor is very low compared to the troposphere. The water vapor condenses for example around aerosols present at this altitude, namely nanometer-sized smoke particles which form from meteors that enter the Earth’s atmosphere and commonly ablate in the mesosphere region.

These ice particles around the mesopause typically have number densities of 100 to 1000 cm^{-3} (*Hervig et al.*, 2009a; *Baumgarten et al.*, 2012). They generally stay below 10 nm in size since the amount of water vapor at this altitude is too low for larger particles. However, some of the particles end up at the lower edge of the saturated

region around 83 km as a result of sedimentation, vertical wind and turbulent mixing. Here, particles can grow to visible size (≈ 60 nm) because of the larger amount of H_2O present at this altitude. Afterwards, NLC particles sediment into the subsaturated region where they sublime quickly and release their water back into the atmosphere.

NLC particles are much smaller than the wavelengths of visible light but still large enough that their scattering cross sections have to be calculated with the Mie theory. Scattering in the Mie regime also allows the determination of particle size by optical methods (see Section 6.1.2). For particles smaller than ≈ 20 nm, the simple Rayleigh approximation $\beta \propto r^6$ suffices. Ice particles smaller than ≈ 10 nm cannot be detected by lidars or cameras because of the scatter proportionality on r^6 , only by extinction methods (SOFIE). Both small and large mesospheric ice particles also influence the radar reflectivity, as the effective radar cross section is proportional to r^2 . The large number of small particles above the NLC are detectable by radar but not by lidar. As a result, PMSE (Polar Mesospheric Summer Echoes) cover a larger altitude range than the NLC. The relationship of NLC and PMSE is more complex in reality since the radar echo also depends on both ionization and local turbulence parameters (e.g. *Kaifler et al.*, 2011). The microphysics of NLC will be explained in more detail in Chapter 3.

1.3 Outline of the dissertation

In Chapter 2, two models for the middle atmosphere are described. The dynamic structure of the summer mesosphere is discussed based on these models and a number of remote sensing techniques such as lidars and radars. Appendix A provides some additional information on mesosphere dynamics.

The Lagrangian particle model MIMAS is introduced in Chapter 3. The physics of the mesosphere region and noctilucent clouds in particular are examined, as well as their implementation in MIMAS. Some more technical aspects of MIMAS are discussed in Appendix C. In Chapter 4, the noctilucent clouds in MIMAS are characterized, including aspects like the general shape of particle trajectories and the relationship with ambient conditions.

The focus of this work is the analysis of the development of bright NLC, described in Chapter 5. This includes a case study demonstrating the mechanisms, statistics on the NLC life cycle, and the impact of latitude, i.e. distance from the pole. Finally, the sensitivity of the previous results to two key model limitations are investigated in Chapter 6. These are the assumed spherical shape of the particles and the impact of gravity waves. Appendix B includes additional details to NLC morphology, particle history, and the sensitivity studies.

2 Dynamics of the mesosphere and lower thermosphere (MLT) region

In this chapter, the dynamical processes of the middle atmosphere will be discussed. Two models used for this particular part of the atmosphere will be introduced. First is the Leibniz-Institute Middle Atmosphere model (LIMA), which adapts reanalysis data based on atmospheric measurements. The second is the Kühlungsborn mechanistic circulation model (KMCM) which focuses on first principle representations of processes like gravity waves. At the same altitude and latitude, the mean dynamic data and the general variability of both atmospheric models are then compared with each other and against actual atmospheric measurements collected over several years.

2.1 Middle atmosphere dynamical modeling

2.1.1 The Leibniz-Institute Middle Atmosphere model (LIMA)

The main atmospheric model used in this thesis is the Leibniz-Institute Middle Atmosphere model (LIMA). Its aim is to describe the thermal structure of the polar mesopause region. LIMA is a non-linear, global, 3-d Eulerian grid-point model reaching from ground level up to the lower thermosphere (*Berger, 2008*). It extends reanalysis dynamic fields into the mesosphere by taking major stratospheric and mesospheric processes into account while excluding most complicated physics of the troposphere. The LIMA fields (wind components and temperature) are constantly adjusted towards the reanalysis values with a Newtonian relaxation ("nudging", see Equation (3.1)) coefficient of $\alpha = \frac{1}{83 \text{ hours}}$ between ground level and 35 km. Up to the altitude of 45 km, the nudging coefficient linearly decreases to zero, above this boundary altitude the model is then let to run freely. In the past, the ERA-40 reanalysis supplied by the European Center for Medium-Range Weather Forecasts (ECMWF) was used exclusively for the nudging process. Recently, other data sets have been used, such as the ERA-Interim (also by ECMWF), and the "20th Century Reanalysis" from NCEP/NCAR which covers the time period since 1871 (*Lübken et al., 2013a*). The process of nudging towards reanalysis data sets is much simpler in comparison to the extremely complicated process of direct assimilation of measurements, as done by the reanalysis models themselves. The downsides of this particular model approach are the dependence on the accuracy of the reanalysis model, the possibility of sampling artifacts from poor temporal and/or spatial resolution of the reanalysis output, and some physical inconsistencies such as violation of energy and momentum conservation in the nudging

zone.

There is additional data input into LIMA, such as solar radiation data using the Ly α line at 121.6 nm, and trace gas concentrations for ozone and carbon dioxide. The main chemical and radiative processes included or parametrized in the model are the following: Photolytic absorption of Ly α by O $_2$ according to *Chabrilat and Kockarts* (1998), solar heating by oxygen and ozone absorption (*Strobel*, 1978), chemical energy storage and loss from airglow emission (*Mlynczak and Solomon*, 1993), near-IR carbon dioxide heating described by *Ogibalov and Fomichev* (2003). Cooling rates are parametrized in different altitude regions depending on the gas: Ozone from 30 to 80 km according to *Fomichev and Shved* (1988), H $_2$ O from 30 to 100 km (*Zhu*, 1994), atomic oxygen and NO $_x$ in the lower thermosphere (*Kockarts*, 1980), and carbon dioxide above 75 km (*Fomichev et al.*, 1998; *Kutepov et al.*, 2007). More details on LIMA mechanics are given in *Berger* (2008).

The horizontal structure used by LIMA is a triangular Arakawa A grid where the atmospheric variables are calculated at the vertices. These have a 1° latitude spacing from 89.5°S to 89.5°N, while the number of vertices on a given latitude band is largest around the equator and diminishes towards the pole. The vertices have an approximate horizontal spacing of 110 km resulting in a total number of 41,804 vertices per model level. The vertical resolution is approximately 1.1 km, extending from the ground up to the lower thermosphere (\approx 150 km). LIMA uses an internal time step of 150 seconds. However, model output is not usually collected as frequently, but every 6 hours for global dynamics and every hour for the polar summer mesosphere region, which is later used to simulate NLC formation.

The primary use of LIMA is to provide mesospheric dynamics and temperatures which are linked to a large number of measurements over a multi-year time period. The main strength of these dynamic fields are the seasonal and multi-year variabilities. For this reason LIMA is mainly used for trend analyses for both mesospheric temperatures and noctilucent clouds (*Lübken et al.*, 2009; *Lübken and Berger*, 2011; *Lübken et al.*, 2013b). However, LIMA has some deficiencies in its circulation patterns which will be described in the next section, and has too low variability from gravity waves on scales < 800 km. To discuss the impact of these limitations, a different model will be used to compare against the dynamics of LIMA, and later to run NLC simulations independently of LIMA in the sensitivity study described in Section 6.2.

2.1.2 The Kühlungsborn mechanistic circulation model (KMCM)

As described in Section 1.1.2, gravity waves (GW) have a very high significance for understanding the smaller scale processes in the MLT region. A specific feature of the Kühlungsborn mechanistic circulation model (KMCM) is the explicit simulation of gravity waves and their wave-mean flow interactions (GW drag and dissipation). For the MLT, the model concept has been described in *Becker* (2009). As a mechanistic model, KMCM includes those atmospheric processes which are essential for large-scale dynamic circulation. This is in contrast to LIMA where ECMWF reanalysis dynamics are adapted, giving it more of a heuristic character. While the omission of data assimilation precludes the use of KMCM for multi-year simulations, i.e., trend calculations, it is well suited to simulate gravity waves including their effects on NLC.

2.1 Middle atmosphere dynamical modeling

KMCM is a spectral model, which means that the prognostic variables are represented in spherical harmonics up to certain predefined order, not in a horizontal longitude-latitude grid. The maximum wave number, i.e. resolution, can be adapted in order to resolve smaller scale waves. The spectral dynamical core used for the simulations in this thesis resolves zonal wave numbers up to 120. Higher order waves are truncated, which translates into a minimum horizontal wavelength of 350 km. The basic version of the KMCM dynamic fields will thus be referred to as KMCM₁₂₀. Due to this spectral approach, related dynamic fields with less smaller scale waves are generated simply by truncating the higher wave numbers from the original fields. When averaged over large scales, dynamic fields derived this way are not different from the original, but locally they are very different. Three versions of KMCM output with truncated wave dynamics will be used in this thesis, with maximum zonal wave numbers 60, 30, and 15 and correspondingly referred to as KMCM₆₀, KMCM₃₀ and KMCM₁₅, respectively.

The vertical structure of KMCM is 190 hybrid levels from the surface up to ≈ 125 km, with a level spacing of ≈ 600 m up to the lower thermosphere at 105 km (*Becker, 2009; Hoffmann et al., 2010*). The KMCM spectral core has a number of advantages compared to a grid-point model: There is little numerical diffusion since energy and angular momentum are conserved except for errors in parametrizations or aliasing problems (*Becker, 2003; Becker and Burkhardt, 2007*). Additionally, the spectral method is more computationally efficient than grid-point models in resolving wave dynamics.

Diabatic heating in KMCM is realized by a number of factors: The temperature is continually relaxed towards an equilibrium state in radiative balance, with altitude-dependent relaxation time constants ranging from 16 days in the troposphere to 40 days at 100 hPa and 7 days above 5 hPa (*Dunkerton, 1991*). There is also a latent heating term in the deep tropics, with an addition of condensational heating in the middle latitudes. The temperature is also influenced by horizontal and vertical turbulent diffusion and frictional heating (dissipation) from wind shear.

The model realistically simulates gravity wave breaking in the extratropical MLT by turbulent damping of resolved GW. The typical wave parameters used are horizontal wavelengths around 500 km, time periods in the 3-6 hour range and zonal phase speeds around 40 m/s. The implementation of turbulence is based on Smagorinsky's generalized mixing-length formulation (*Becker and Burkhardt, 2007*), where both horizontal and vertical diffusion coefficients are scaled by the Richardson criterion for dynamic instability. When the Richardson number falls below 0.25, turbulent damping is strongly enhanced. The scales and periods of gravity waves resolved by the model are shown to be constrained by the spectral resolution, as test simulations with higher total wave numbers also produce GW with shorter wavelengths and periods.

For the purpose of this thesis, KMCM is run in stationary Northern hemisphere summer conditions, so the model dynamics does not include seasonal variations. It also does not include thermal tides. This limitation means that the KMCM data set used here does not describe summer MLT dynamics completely. The length of the KMCM data set is 29 consecutive days, similar enough to the 31 days of July to compare with July dynamics in LIMA and also long enough for running MIMAS with these dynamic fields (see Section 6.2). The KMCM version used here computes 128 snapshots per day which corresponds to an interval of 11.25 minutes (E. Becker, private

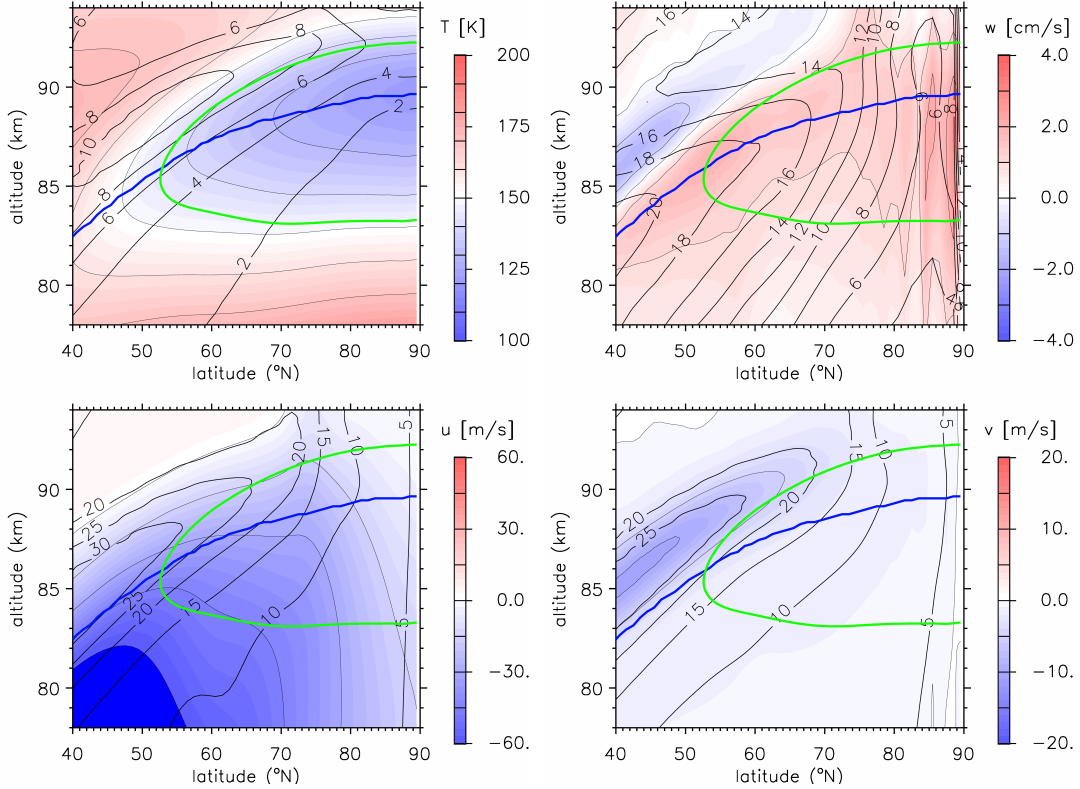


Figure 2.1 LIMA July 2009 zonal and temporal mean values of summer MLT temperature (upper left), vertical wind (upper right), zonal wind (lower left) and meridional wind (lower right) shown in colored contours. The labelled contour lines in each panel show the variance (root-mean-square deviation, RMSD) of the same parameters. Blue line: mesopause altitude, green line: boundary of supersaturated region, i.e. $S = 1$ contour (see Section 3.3.2).

communication). A more detailed description of the KMCM grid and its adaption to model ice formation is given in Section 6.2.1.

2.2 Mean state of the summer MLT: Models and measurements

2.2.1 Model temperature and wind structure of the summer MLT region

After introducing the basic structure of LIMA and KMCM, the mean state of the dynamic fields generated in both models will be investigated. The starting point for this is the LIMA version LIM3. It includes solar cycle variation but neither ozone nor CO₂ trends. In *Lübken et al. (2013b)* it is referred to as run 5. NLC modeling results in the following chapters use LIM3 with ECMWF data for July 2009 conditions. Figure 2.1 shows both the mean state and the total variability for the four main

2.2 Mean state of the summer MLT: Models and measurements

atmospheric parameters, namely temperature and the three wind components. The upper left panel shows LIMA's mean summer temperatures from 78 to 94 km. The supersaturated region extends up to a mean temperature of 148 K at its lower edge and 138 K at the upper edge. The difference is caused by a vertical gradient in water vapor, shown in Figure 3.2. The saturation region also reaches from the pole up to about 50°N. Only the mesopause temperature and the upper edge of the region depend on latitude, while its lower edge changes very little with latitude. In addition to the mean state, Figure 2.1 also shows root-mean-square deviation (RMSD) as a measure of variability. The July temperature in LIMA has a high-variability region along the upper edge of the mesopause region, mainly at latitudes south of 70°N. At higher latitudes and NLC altitudes around 83 km, the temperature variability is rather low, with an RMSD of 2 K at 70°N. At 54°N, *Gerding et al.* (2007) find mean July mesopause temperatures of 145 K at ≈ 87 km, compared to ≈ 142 K at 86 km for the LIMA mesopause. Temperatures at 69° are discussed further in Figure 2.5.

The upper right panel of Figure 2.1 shows the vertical wind. There is a mean upwelling in LIMA in the supersaturated region, but with generally small mean values peaking at around 1.5 cm/s near the mesopause and less than 1 cm/s at NLC altitudes of 83 km. There is no distinctive latitudinal gradient of mesopause mean vertical wind within the whole range of 55°N to 85°N. On the other hand, the variability of the vertical wind has a prominent latitudinal gradient with much higher amplitudes further from the pole.

The two lower panels of Figure 2.1 show the horizontal wind components. While the color scales are not ideal for LIMA, they were chosen for comparability with KMCM in Figure 2.2. The zonal wind in LIMA at 83 km and 70°N is ≈ 45 m/s westward. It switches to eastward at an altitude above the upper edge of the supersaturated region. For latitudes north of 70°N the mean meridional wind is very weak (≤ 2 m/s), it only reaches larger values at the upper edge of the NLC domain in lower latitudes. The variabilities of both horizontal wind components are low close to the pole and peak at lower latitudes above the mesopause. Horizontal winds are discussed further in Figure 2.4 for the case of 69°N, where measurements are available for comparison.

While LIMA dynamic fields are used in most of the simulations in this thesis, it is necessary to examine if the main results change when using background conditions from KMCM. Figure 2.2 shows the mean dynamics and variability for KMCM₃₀ analogous to Figure 2.1 for LIMA, so the two models can be compared directly. Figure 2.7 and Figure A.3 show that among filtered KMCM data sets, KMCM₃₀ is most similar to radar measurements. It also turns out to produce a NLC morphology comparable to LIMA (see Section 6.8).

The basic structure of mean temperature is similar compared to LIMA. The lower edge of the supersaturation region is located slightly higher in KMCM by some hundred meters, while the mean mesopause temperature and altitude roughly coincide. One notable difference is the latitudinal extent of the supersaturation region, which is further south by $\approx 7^\circ$ in LIMA compared to KMCM. Another difference is the temperature above the mesopause, it rises much more rapidly in KMCM compared to LIMA, which has a smoother gradient. However, when looking at temperature variability, the differences between the models become more pronounced: The RMSD in KMCM₃₀ is considerably higher than that of LIMA with differences most pronounced close to

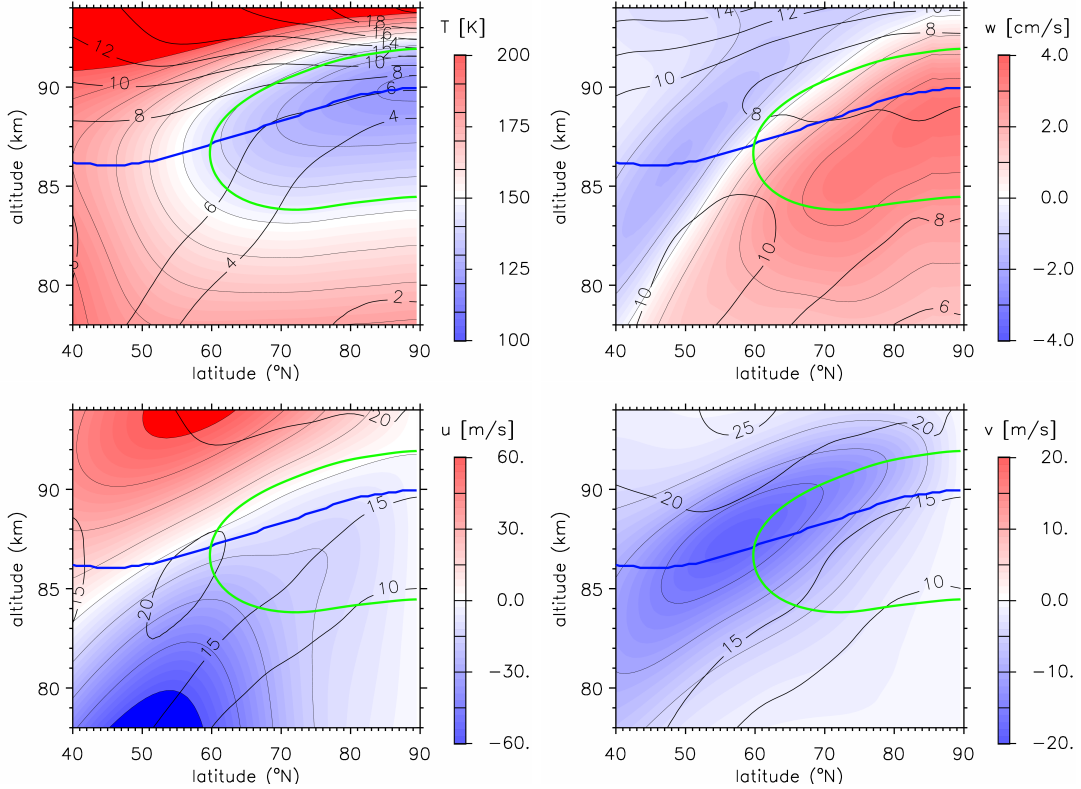


Figure 2.2 Analogous figure to Figure 2.1 for KMCM with total wave numbers up to 30 (KMCM₃₀)

the pole. At 83 km and 69°N, KMCM RMSD is ≈ 4 K compared to 2 K in LIMA. The gradient in temperature variability is mostly vertically oriented, whereas in LIMA there are significant gradients in both meridional and vertical directions.

The vertical wind structure in KMCM (upper right panel in Figure 2.2) has some distinct differences to the one in LIMA: The area of mean upwelling is somewhat smaller, with zero mean vertical wind about 3 km lower compared to LIMA. This is near the upper edge of the supersaturated region for latitudes south of $\approx 70^\circ\text{N}$. However, the upwelling in the main NLC region is larger in KMCM compared to LIMA. Below the mesopause, the upwelling usually exceeds 3 cm/s, at 83 km it still reaches 2 – 3 cm/s. The meridional dependence is also stronger compared to LIMA, with mean upwelling considerably weaker southward of 70°N. Vertical wind amplitudes are similar to the ones in LIMA for NLC altitudes at 70°N, but KMCM₃₀ shows much less latitude and height dependence. The effect of the resolution, i.e. the wave numbers extracted from KMCM, is shown in Figure 2.3.

The horizontal wind components in KMCM are also quite different from those in LIMA. The altitude of zonal wind reversal (lower left panel) is located about 4 kilometers lower in KMCM compared to LIMA. The westward wind speed at NLC latitudes is smaller in KMCM than in LIMA, the wind reversal in the lower thermosphere is much stronger. There is also a larger region with significant southward wind in KMCM

2.2 Mean state of the summer MLT: Models and measurements

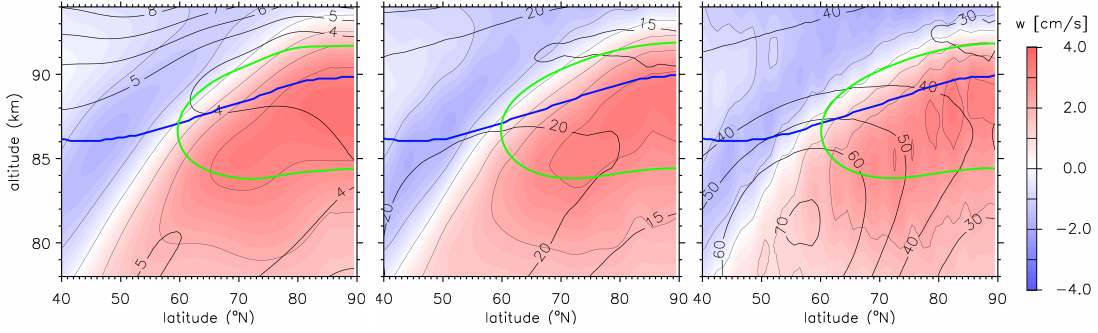


Figure 2.3 Same as the upper right panel in Figure 2.2, but for the mean vertical wind and its variance in KMCM₁₅ (left panel), KMCM₆₀ (middle) and KMCM₁₂₀ (right).

(lower right panel), with average values up to 15 m/s. The altitude of the southward wind is centered at the zonal wind reversal altitude, in contrast to LIMA where it is located below the zero zonal wind line. Concerning the RMSD of both horizontal wind components, there is a slight gradient with higher variability present further from the pole and at higher altitudes. The horizontal wind variabilities in KMCM are also quite similar to each other in structure (gradients) and amplitudes, and generally higher than variabilities in LIMA except for a region south of 60°N.

Figure 2.2 shows the mean dynamics of KMCM using only wave numbers up to 30. However, the original model simulations were conducted with waves up to a total wavenumber of 120. KMCM₁₂₀ as well as the other spectrally filtered data sets KMCM₆₀ and KMCM₁₅ have considerably different total variabilities resulting from the number of waves included. Figure 2.3 shows the effect of the truncation for vertical winds since the effects are most pronounced there. As seen by comparing the three panels and the one for KMCM₃₀ in Figure 2.2, the mean vertical winds are very similar in all four variations of the KMCM dynamics. The minor deviations are caused by the finite time window of 29 days, which cause the higher wave numbers to not cancel out completely in a zonal and temporal average. This is also the case for the other atmospheric parameters shown in Figure 2.2, meaning that the four variations of KMCM dynamics are identical in their mean state and only vary by their wave spectra. This feature will be used later on in Section 6.2 to probe the sensitivity of NLC formation to the wave spectrum.

At most latitudes and height levels, the KMCM total variability roughly doubles for every doubling of total wave number included. At latitudes close to 60°N and NLC altitudes, this factor peaks at values of 2.5 to 3. The variability in temperature and horizontal wind components also depends on the wavenumber limit: Here, the RMSD increases by about 20% per doubling of included wave number.

2.2.2 Mean dynamics at 69°N: Comparison with observations

Measurements of horizontal winds are available at 69°N from the Saura MF radar (*Singer et al.*, 2003, 2007). A four year data set allows a comparison with obser-

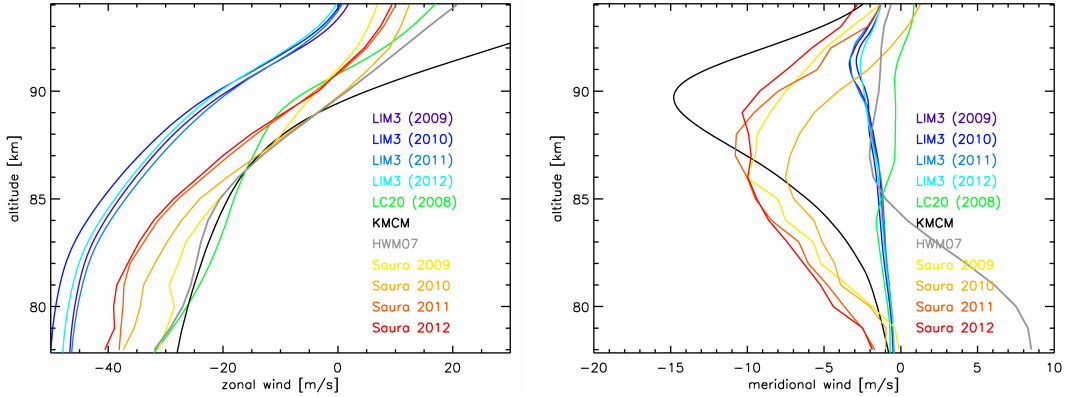


Figure 2.4 Mean zonal and meridional wind speeds at 69°N for July. Besides LIMA and KMCM, an alternative version of LIMA denoted LC20, the HWM07 model and radar measurements by the Saura radar (69°N , 16°E) are included for multiple years.

variations at this latitude (I. Strelnikova, private communication). Figure 2.4 shows mean wind profiles for July from numerous sources, including KMCM, LIMA version LIM3 for 2009-2012, LIMA version LC20 (called 20th century simulation in *Lübken et al.* (2013a)), and the Saura radar profiles, also for 2009-2012. It also includes the horizontal wind model HWM07, which was developed as an empirical model for the atmospheric circulation (*Drob et al.*, 2008). HWM07 is based on a broad range of observations, from satellites to sounding rockets, interferometers and radars at multiple locations, and interpolates these measurements to achieve global coverage.

In the zonal wind comparison, KMCM, HWM07, and the 20th century run of LIMA match the radar profile for 2009 up to an altitude of ≈ 90 km. Above this altitude, deviations from the measured profile increase for LC20, HWM07 and KMCM. LIM3 has too strong westward zonal wind at all altitudes (by ≈ 15 m/s in 2009). However, the radar profiles of the different years vary by as much as 10 m/s. In 2011 and 2012 the Saura westward winds are considerably stronger. Around 80 km, they are closer to LIM3 than to KMCM, which suggests that the overestimation of zonal wind in LIMA is closer to 10 m/s in the climatological mean.

The meridional wind measured by the Saura radar is less well replicated by most models used in this comparison. The radar data consistently show a southward wind of 5 – 10 m/s in a broad altitude region of 82 – 92 km. Among all models, KMCM comes closest with a mean southward wind ≥ 5 m/s between 84 and 93 km, slightly above the radar wind peak. Meridional wind in LIM3 peaks at 91 km and reaches only 3 m/s, while southward transport in the 20th

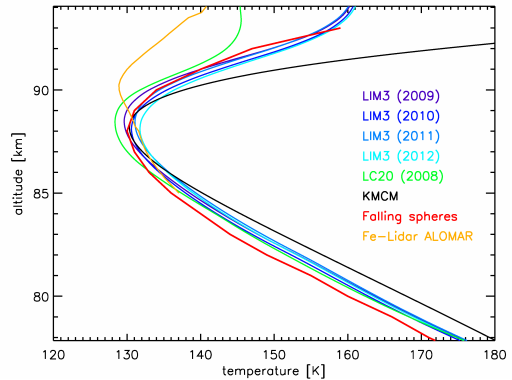


Figure 2.5 Mean July temperature at 69°N , including sounding rocket (falling sphere) and Fe-Lidar climatologies.

2.2 Mean state of the summer MLT: Models and measurements

century simulation LIMA is even less and HWM07 shows a mean northward transport for altitudes below 84 km contradicting both measurements and other models.

For temperatures at 69°N, different data sets are available for comparison: The falling sphere sounding rocket climatology (*Lübken, 1999*), and iron lidar measurements at ALOMAR in 2008 and 2009 (*J. Höffner, private communication*). LIMA, KMCM and the rocket measurements all show mesopause altitudes of 88 km and temperatures around 130 K, while the mesopause in the iron lidar measurement is slightly colder and higher, at 90 km. At NLC altitudes around 83 km, LIMA is 3 – 4 K warmer than the rocket climatology, while KMCM is ≈ 7 K warmer. The interannual temperature variations in LIMA (LIM3) are small at all NLC altitudes (< 2 K). Above the mesopause, the variations are much larger: Temperatures in LIM3 still agree well with the falling spheres, while LC20 features a much slower temperature increase in the lower thermosphere which is closer to the lidar than to the falling spheres at 93 km. On the other hand, KMCM temperature rise very quickly above ≈ 90 km, which is not supported by either set of measurements.

2.2.3 Local time dependence of winds at 69°N

Since wind measurements feature local time variations (e.g. *Hoffmann et al., 2010*), Figure 2.6 shows a 4 year composite of July data from radar and LIMA. KMCM is not included in the comparison since it does not include tides. Gaps in the radar data coverage are excluded from the averaging process. Model data values are taken at the MIMAS grid point closest to the position of the radar, at 69.5°N, 15°E (see Section 3.1.2).

In the zonal wind, both the model and the measurements show a strong local time variation, with two clearly defined maxima and minima each at most altitudes. The main zonal wind maximum occurs at 19 – 20 UT, with excellent agreement between model and measurement in timing. The Saura zonal wind also has a secondary maximum at 8 – 10 UT depending on the altitude. This feature is also present in LIMA, but only around the mesopause. The timing of the main minimum at 2 UT in the model and measurements is very similar again. In summary, the local time variation of zonal wind as measured by the Saura MF radar is matched by LIMA to a high degree. Wave amplitudes are very similar, while the phases are in best agreement between 84 and 88 km and still similar below 84 and above 88 km.

The meridional wind measured by the radar also has a distinctive local time variation, with a pronounced minimum around 23 UT. This feature is matched by LIMA. The strong maximum around 16 UT is also present in LIMA, but somewhat weaker below 88 km. The tidal phases in the radar change only slightly with height. LIMA shows a similar behavior below 89 km, but a rapid shift of the phases above. The winds measured by the radar have a secondary maximum at approximately 5 – 7 UT and a secondary minimum around 10 – 12 UT. These features are also visible in LIMA, though the secondary minimum especially is weaker in the model as compared to the radar. Similar to zonal wind, the tidal phases are most similar in an altitude range of ≈ 85 – 90 km. In general, the meridional wind diurnal variation seems well represented by LIMA, only the wave amplitudes are slightly underestimated.

It would be of particular interest to compare the temperature local time variation

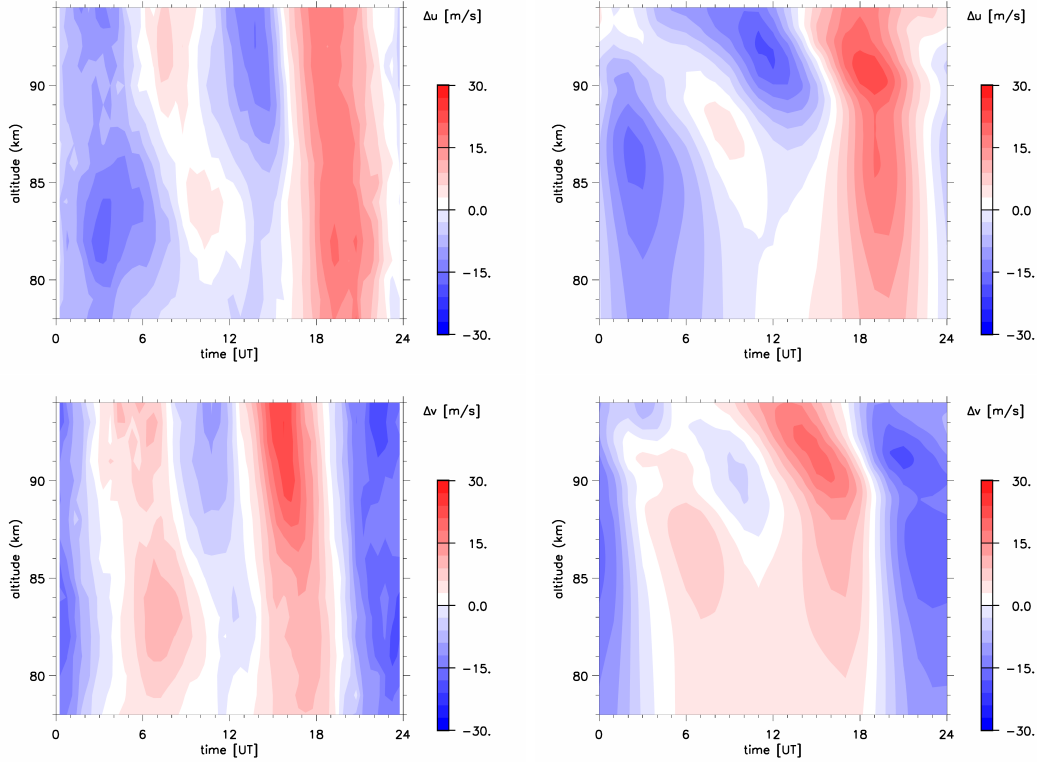


Figure 2.6 Diurnal variation of horizontal wind components at 69°N , shown as deviation from daily mean. Left side: Four year July average of Saura radar (69°N , 16°E) from 2009-2012. Right side: 2009 to 2012 July average in LIMA (LIM3 version). Upper panels show the zonal wind, lower panels the meridional wind.

in LIMA with measurements, since temperature is most important for NLC formation (see Section 4.3.1). However this is very difficult due to the scarcity of available measurements. Satellite temperature measurements are available (*Xu et al.*, 2006; *Xu et al.*, 2007; *Stevens et al.*, 2012), but Earth observation satellites are typically in sun-synchronous orbits. The local time of such measurements is fixed except for gradual orbit changes, which hinders the use of satellites for this type of comparison. In-situ data from sounding rockets provide the best accuracy, but such measurements are available only sporadically because of the high cost and effort of rocket campaigns. The only remote sensing technique suited for the purpose are resonance lidars (*Höffner and Lübken*, 2007; *Gerding et al.*, 2013; *Chang et al.*, 2012). A number of such measurements were available, the comparisons are discussed in Appendix A.1. These results are less conclusive in general than for horizontal winds.

2.3 Atmospheric waves in the summer MLT: Models and measurements

The general structure of gravity waves, inertia-GW, and planetary waves occurring in both models will now be explored and compared with measurements where data are available. The starting point are time series at a single location, e.g. ALOMAR. These are well suited for validation of models with measurements, as this simulates the view of the atmosphere that ground-based remote sensing instruments share. Later, time-longitude diagrams at a given latitude and altitude (Hovmöller diagrams) will show the main modes of horizontal wave propagation in the models. The analysis is extended in Appendix A with a comparison of Fourier spectra and concluded with a look at long-period planetary waves, especially the quasi 5-day wave.

2.3.1 Vertical structure of dynamics in LIMA and KMCM

The first parameter analyzed by fixed location time series is the meridional wind at 69°N , 16°E where Saura radar measurements are available (I. Strelnikova, private communication). In Figure 2.7, LIMA, KMCM₃₀, KMCM₁₂₀, and the Saura radar are compared over 4 days. For Saura, the time period of July 20-23, 2009 was selected because of its good radar data coverage, i.e. few measurement gaps. The NLC formation shown in the Figures is discussed in Section 4.1 and Section 6.2.2.

Figure 2.7 demonstrates that the tides in LIMA winds discussed in Section 2.2.3 are the dominant component of meridional wind variability. The vertical gradient in wave amplitudes seen in Figure 2.1 is also clearly visible here, along with the transition from mainly diurnal tide to a mix of diurnal and semidiurnal tides at higher altitudes. The phase of the waves is only slightly tilted below 88 km, and strongly tilted with clear downward propagation at higher altitudes.

In comparison, the meridional wind in KMCM₃₀ features waves with a period around 15 h which are most likely inertia-gravity waves. These waves are also prominent in KMCM₁₂₀, but here they are overlaid with shorter-scale gravity waves with typical apparent periods of 2.5 to 5 hours. The inertia-GW have a strongly tilted, downward propagating phase with a vertical wavelength around 15 km. The phase propagation of the short-period waves is also downward but less tilted. The vertical gradient of wave amplitudes is also pronounced in KMCM, but slightly less than in LIMA.

Finally, the Saura radar winds have similarities to all of the three model time series in different aspects. As in LIMA, the local time variation shown in Section 2.2.3 is clearly visible, but less dominant since it is overlaid with gravity waves up to the Saura resolution limit of ≈ 2 h. The total variability of the radar is best matched by KMCM₃₀, while the observed short-period gravity waves are included only in KMCM₁₂₀. However, the measured shorter scale GW have smaller amplitudes than waves with comparable period in KMCM₁₂₀. There is only a very slight vertical gradient in wave amplitudes, much less than in both LIMA and KMCM. Phase propagation of the waves is harder to see than in models, but appears to be generally downward with a slope similar to KMCM.

Figure 2.8 uses the same altitude-time projection as Figure 2.7, but it shows temperature instead of wind since this is the atmospheric parameter being most important for

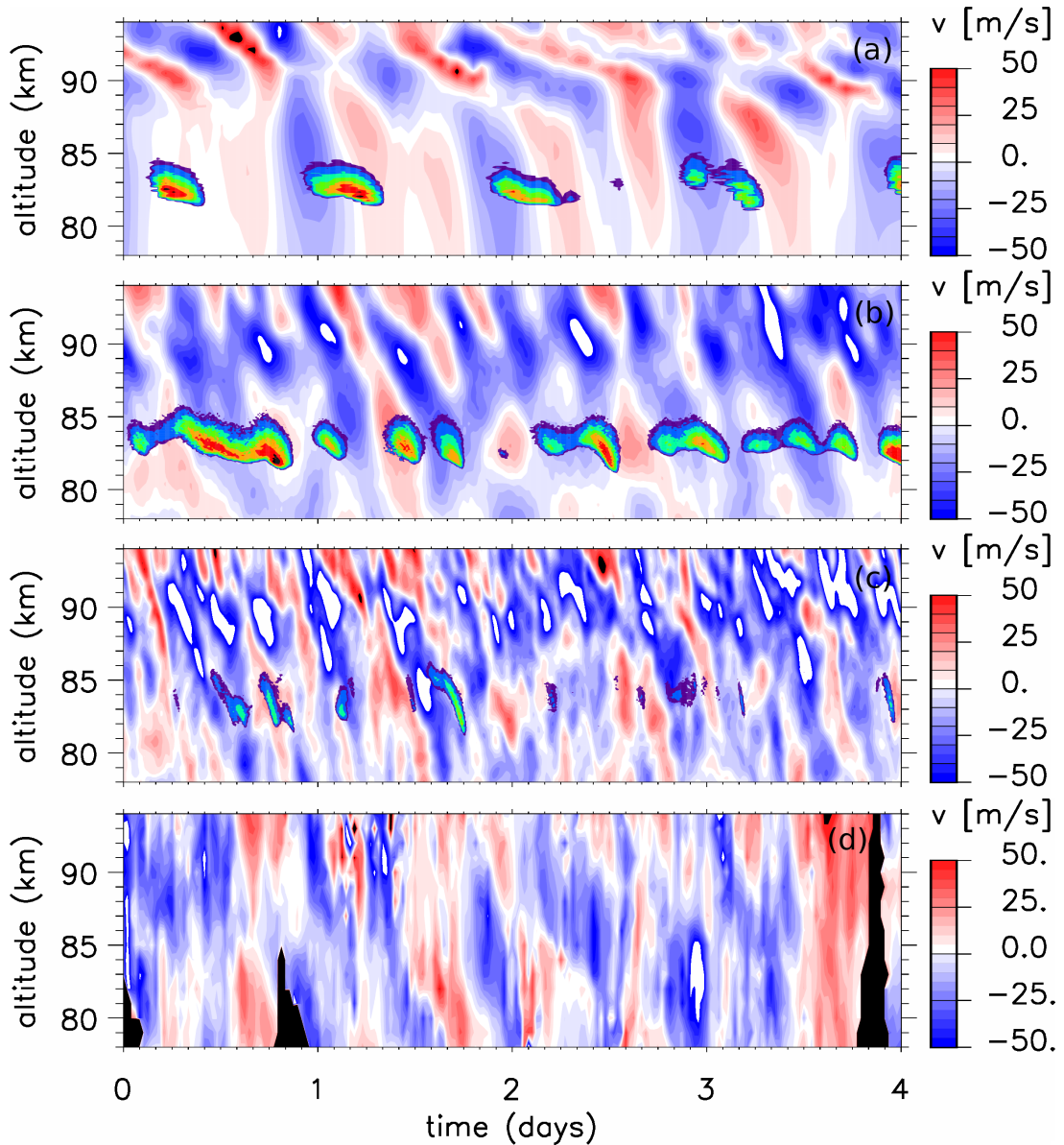


Figure 2.7 Time series of meridional wind at 69°N , 16°E . Panels show LIMA (LIM3, 2009) (a), KMCM_{30} (b), KMCM_{120} (c) and Saura MF radar (d). Black patches in the radar data are measurement gaps. All model time series include NLC formation as simulated by MIMAS, shown with colored contours.

ice formation. Ground-based temperature measurements at this altitude during summer are only possible by resonance lidar, but a time series of comparable length and signal quality was not available for ALOMAR. The lidar data used here (J. Höffner, private communication) is from a different location, namely the Antarctic Davis station (68°S , 78°E). Davis is located on a Southern latitude equivalent to ALOMAR in the Northern hemisphere. As this measurement lasts for two days, LIMA and KMCM time series were shortened accordingly.

2.3 Atmospheric waves in the summer MLT: Models and measurements

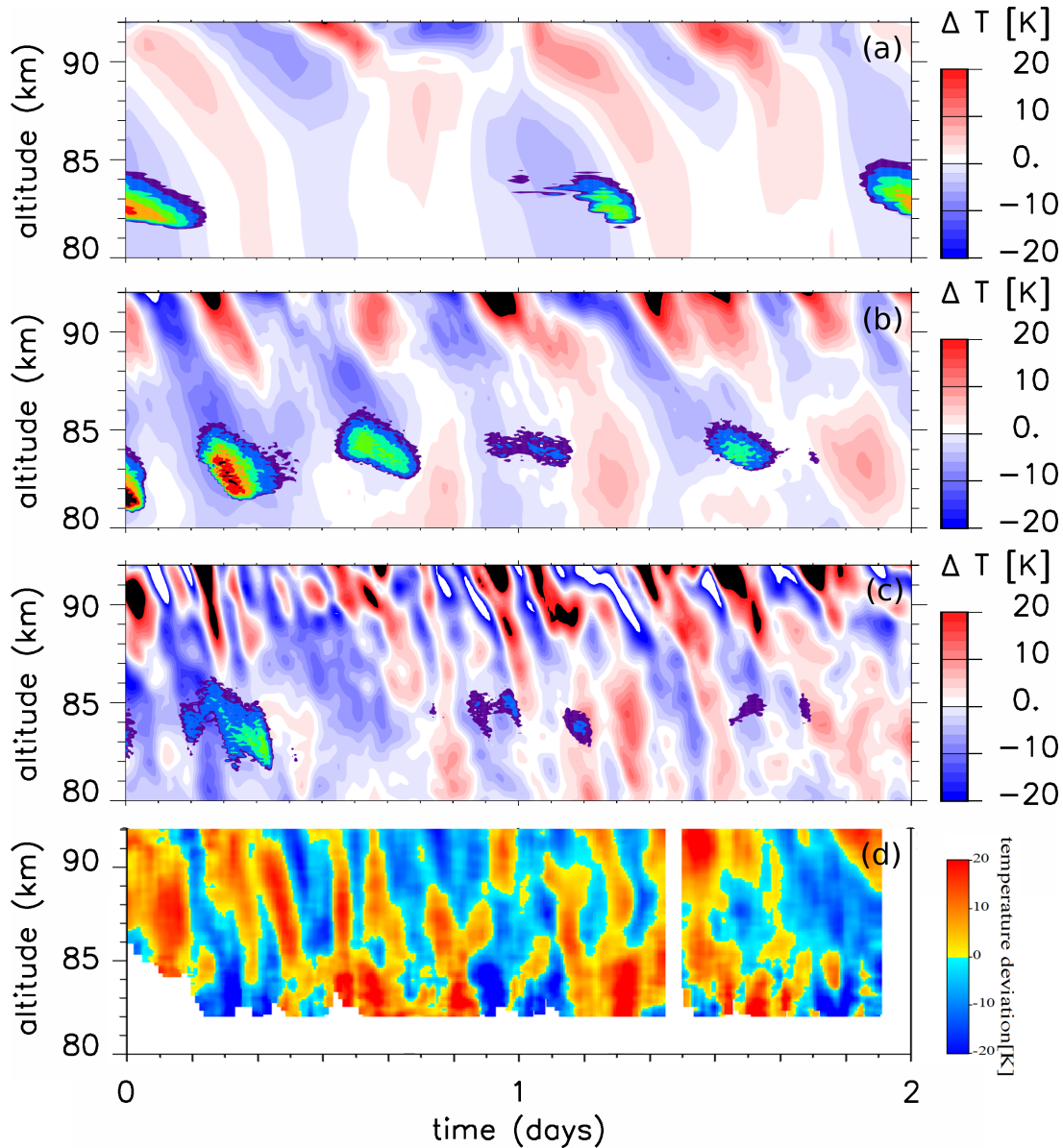


Figure 2.8 (a)-(c): 2 day ALOMAR temperature and NLC time series of LIMA (a), KMCM₃₀ (b) and KMCM₁₂₀ (c). (d): Temperature measurement by Fe-lidar during austral summer (January 17-19, 2011) at Davis.

The temperature waves in LIMA look quite similar to the ones in the meridional wind. They appear to be mostly tides with downward phase propagation, and with a semidiurnal component more obvious than in Figure 2.7. Wave amplitudes increase with altitude even more strongly than for wind. The two KMCM time series show the same wave structures as visible in meridional wind, however the downward propagation of the inertia-GW is more difficult to see. As with LIMA, wave amplitudes increase strongly with height. The variability even in KMCM₃₀ is higher than in LIMA at all

altitudes.

The Davis lidar time series features a superposition of tides and gravity waves. The phase propagation of the GW is usually downward, but the apparent phase tilt is small, similar to the wind time series measured by radar. The measured gravity waves at 85 km are rather strong, so the lidar data looks most similar to KMCM₁₂₀ among the model time series when one disregards the lack of tides in KMCM. However, at higher altitudes (90 – 95 km) GWs in KMCM are stronger than those measured by lidars: This is significant since the RMSD of lidar observations is known quite precisely, and the wave amplitudes in this data set agree with results from other locations (*Rauthe et al.*, 2006; *Höffner and Lübken*, 2007).

The preliminary conclusions from Figure 2.7 and Figure 2.8 are as follows: LIMA approximates the local time (tidal) variations of dynamic components to a reasonable degree as shown in Section 2.2.3, but it underestimates the amplitudes of short scale gravity waves. KMCM on the other hand provides a GW spectrum which agrees with measurements at least at lower altitudes (more detail in Appendix A.2), however it does not include tides in the present version. Both models seem to overestimate the increase in wave amplitudes with altitude.

2.3.2 Zonal wave propagation in LIMA and KMCM

Tides in LIMA, gravity waves and inertia-gravity waves in KMCM have been introduced in Section 2.3.1. However, the time-altitude projection used is not suitable for analyzing horizontal wave propagation. Figure 2.9 shows temperature, meridional and vertical wind of LIMA and KMCM₁₂₀ in a 4-day longitude-time projection, at the latitude of ALOMAR and an altitude typical for NLC formation (83 km). This so-called Hovmöller diagram is used to establish zonal wave number, phase speed, wave period and dissipation when applicable.

In LIMA, two types of waves can be distinguished in the left side panels of Figure 2.9. Unlike in Section 2.3.1, the diurnal tide in T and v can now be clearly recognized by its westward propagation and zonal wavenumber 1. It is most dominant in the horizontal wind components, recognizable in temperature and very faint in vertical wind. Furthermore, another type of wave is visible in temperature and vertical wind which propagates eastward with an apparent period around 4 days. The zonal wavenumbers are around 5 – 8, which is hard to determine since these waves tend to disperse within less than 1 day. The apparent wave period seen by a stationary observer is $\approx 10 - 20$ hours. Moreover, this particular type of wave constitutes most of the variability in vertical wind, while in the temperature fields these waves are combined with a (mainly diurnal) tidal signal. These waves might be associated to large scale inertia-gravity waves, however their precise nature is presently unknown. To date they cannot be validated by observations because mesospheric vertical winds are not measured routinely and available observations are not free from doubt.

Three types of waves are recognizable in KMCM₁₂₀, two of which were discussed in Section 2.3.1: The short-period waves from the lower-middle panels in Figure 2.7 and Figure 2.8 are mid-frequency gravity waves with zonal wavenumbers around 20 – 25, these propagate eastward with periods of ≈ 80 hours. These GWs are best visible in the vertical wind and least apparent in the meridional wind, with zonal wind (not

2.3 Atmospheric waves in the summer MLT: Models and measurements

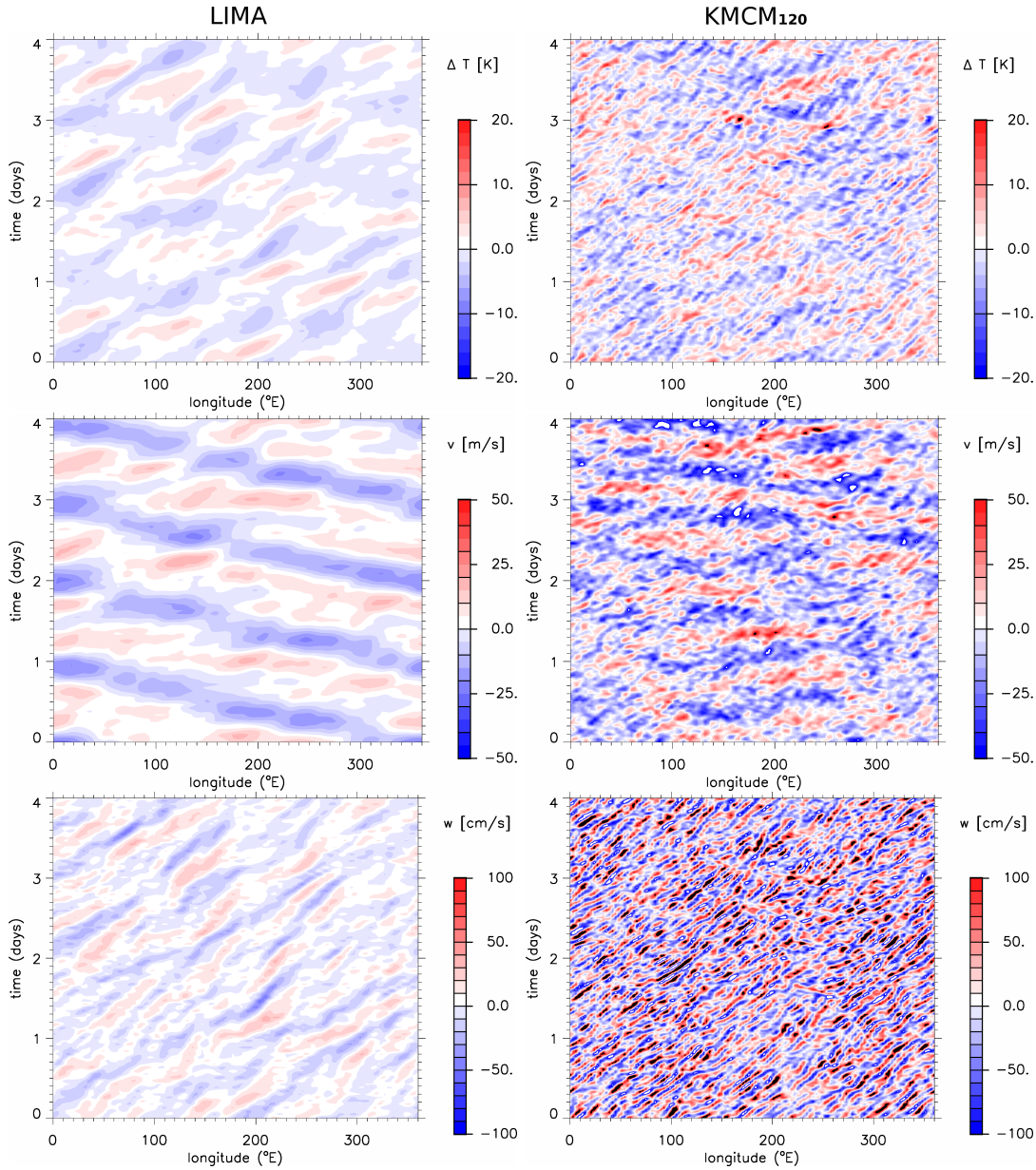


Figure 2.9 Zonal propagation of waves in LIMA (LIM3, left) and KMCM₁₂₀(right) during 4 days in July 2009, at 69°N and 83 km altitude. Filled contours show meridional wind (middle panels), vertical wind (lower panels), and deviation from zonal mean temperature (upper panels).

shown) and temperature in between. The next type of waves are inertia gravity waves present in both KMCM₁₂₀ and KMCM₃₀ in Section 2.3.1. These are most pronounced in the horizontal wind components and less clear in temperature. They are hardly detectable in the vertical wind for KMCM₁₂₀. The main propagation direction for the inertia GW is eastward: For temperature at least, no westward propagating waves were found. However, in the horizontal wind components both propagation directions occur.

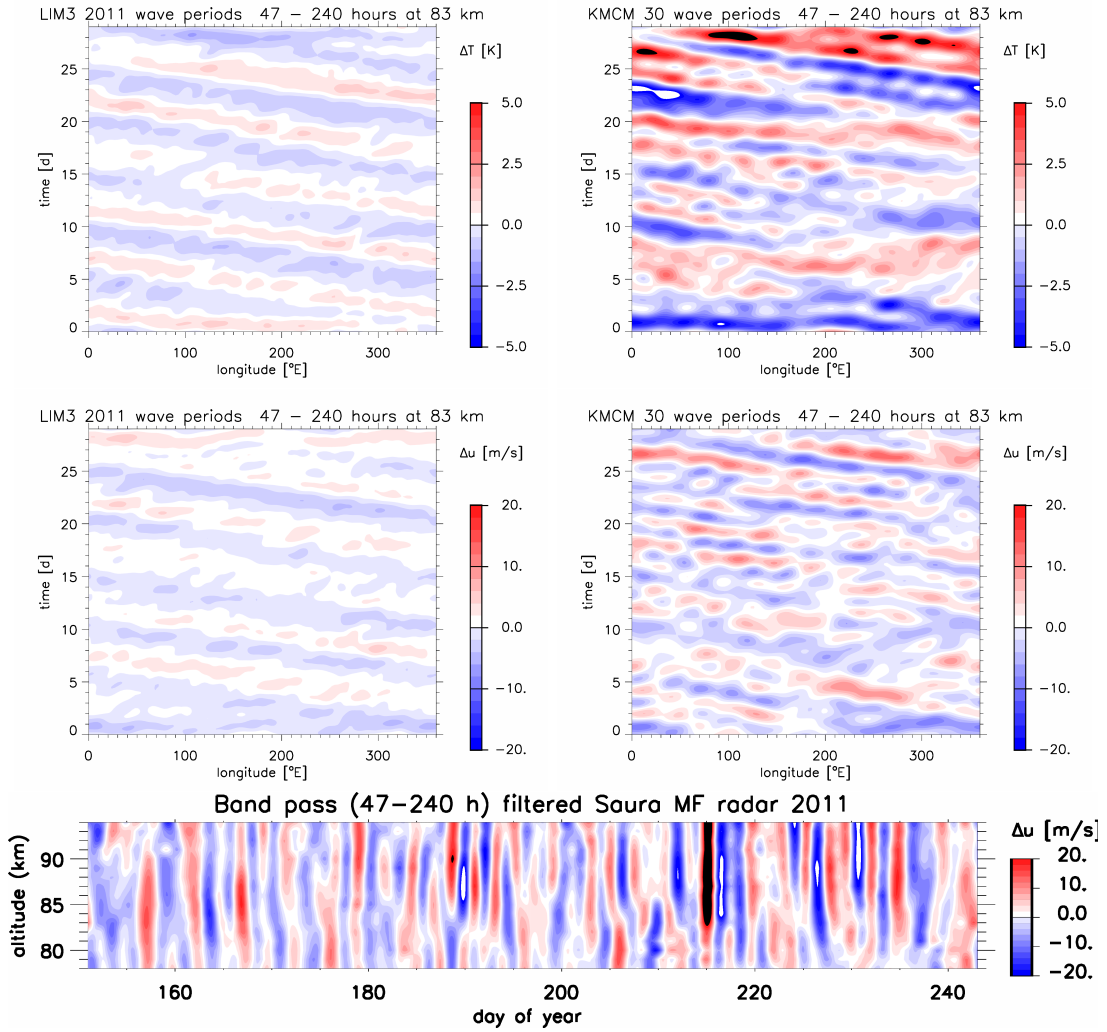


Figure 2.10 Upper and middle panels: Band-pass filter of longitude-time Hovmöller diagrams analogous to Figure 2.9, but over a longer time frame of 29 days, at 85 km altitude. Only waves with a period of at least 47 hours are included. Left side: LIMA, right side: KMCM₃₀. Upper panels: temperature, middle panels: zonal wind. Lower panel: Equivalent band-pass filter of Saura radar zonal wind from June to August 2011, after fitting to remove measurement gaps.

The horizontal propagation of these waves is as fast as atmospheric tides or faster, with zonal wavenumbers 1 or at most 2. A third type of wave is present in KMCM₁₂₀ with westwards propagation and a period of 5 days. While not very strong, this signal is visible in temperature and meridional wind. It can be enhanced by filtering out the higher frequency waves, which is done in Figure 2.10.

2.3.3 5-day wave: Occurrence in LIMA, KMCM and measurements

Up to now, mainly waves with periods shorter than the diurnal tide have been discussed. Satellite measurements indicate the presence of the quasi 5-day wave in both temperatures and noctilucent cloud signatures (*von Savigny et al.*, 2007), which suggests a quantification of the long-period waves in both models and comparison with measurements. The quasi-5 day wave (a normal mode) does not have a sharply defined spectral peak such as tides, but includes waves with periods between 4 and 7 days (*Day and Mitchell*, 2010). However, there has been some controversy about its origin, specifically 2 waves have been identified with periods of 5 days and 6.5 days by *Meyer and Forbes* (1997), supported e.g. by *Liu et al.* (2004). They advocate a 6.5 day period wave in the upper mesosphere and thermosphere, separate from the 5 day period which is the symmetric Rossby (1,1) westward propagating normal mode. However, e.g. *Wu et al.* (1994) see the 6.5 day period as Doppler shifting by the mean background winds of the 5 day wave.

Figure 2.10 shows the longest available time series of both models for the time period in question, 29 days in July 2011 for LIMA and 29 model days at permanent July conditions for KMCM. In order to suppress shorter-period waves, a Fourier band-pass filter was applied with a lower cutoff period of 47 hours. An upper cutoff period of 240 hours was also used, this was to remove seasonal variations. The parameters chosen for this purpose are temperature and zonal wind. Temperature amplitudes can be compared to *von Savigny et al.* (2007) (not included in Figure 2.10). For zonal wind, the Saura radar can be used for comparison. Figure 2.10 only shows those temperature fluctuations that are not zonally symmetric.

For LIMA, 2011 was chosen instead of 2009. Like for radar and satellite measurements, the quasi 5-day wave appears only sporadically in LIMA. It is clearly defined both in temperature and zonal wind within July 2011, but mostly absent in July 2009. Its amplitudes are rather low, typically not exceeding 1 K or 4 m/s at 85 km. In KMCM, the long-period wave signature is well defined in temperature and both horizontal wind components, and present for most of the time period used in this study. Amplitudes can exceed 5 K in temperature and approach 20 m/s in zonal and meridional wind. While the quasi 5-day wave is very clear in Hovmöller diagrams through its westward propagation, the visibility is less for stationary observers since they can only measure the periods of waves but not their propagation.

This can be seen in the lower panel of Figure 2.10 where an analogous band-pass filter was applied to the Saura MF radar zonal wind for summer 2011. The wave structure seen by the radar at 85 km looks similar to that in KMCM at an arbitrary longitude position, e.g. 16°E. In both cases, wave periods of 2-5 days can be distinguished, and the amplitudes are also in good agreement. The lower panel of Figure 2.10 is also consistent with Figure 2 in *Day and Mitchell* (2010). While they show meridional instead of zonal wind, the wave structure is very similar with the dynamics in *Day and Mitchell* (2010) having slightly lower amplitudes. For the horizontal wind components, the Saura measurements support KMCM amplitudes for long-period planetary waves. While LIMA sometimes includes the 5-day wave, its amplitudes are significantly underestimated.

For mesospheric temperatures, a different source of data was used for comparison.

Chapter 2 Dynamics of the mesosphere and lower thermosphere (MLT) region

The Microwave Limb Sounder (MLS) measurements from NASA's EOS Aura satellite was chosen (*von Savigny et al.*, 2007). Their study of summer 2005 finds typical amplitudes of 2-3 K and no persistent presence of the wave: The 5-day wave is found in most of June and parts of August, but not in July, this is shown in Figures 1, 3 and 5 of *von Savigny et al.* (2007). The satellite measurements also show a zonal wave number of 1 which is more similar to the LIMA case, though the sampling ability of the satellite might not reliably detect higher wave numbers as occur in KMCM. As such, the measured amplitudes for the temperature wave are between those of LIMA and KMCM, though closer to KMCM. On the other hand, the MLS measurements support an intermittent nature of the 5-day wave as in LIMA.

The conclusion from the radar and satellite comparisons is that KMCM overestimates frequency and magnitude of the quasi five-day wave somewhat, while LIMA significantly underestimates its amplitudes.

2.4 Conclusions

LIMA and KMCM describe various aspects of middle atmospheric dynamics with different degrees of accuracy. Regarding the mean state of the summer MLT region, LIMA focuses on temperatures especially at NLC altitude, while KMCM features circulation patterns in good agreement with radar observations. In respect to dynamic fluctuations, LIMA includes tidal variations which are similar to those in radar observations, and some synoptic-scale inertia-gravity waves and planetary waves. KMCM on the other hand has a broad wave spectrum, further characterized in Appendix A.2. It includes smaller scale GW, inertia-GW and planetary waves, and in large part compares well to radar and lidar observations. Both models also include long period planetary waves like the quasi 5-day wave, which is more pronounced in KMCM than in LIMA.

3 The Lagrangian Tracer Model MIMAS

In the first section of this chapter, an overview of the Lagrangian ice transport model MIMAS is given. This includes a summary of physical processes, the structure of the input data required by the model, and the format of its output. The following sections will then describe the processes related to mesospheric water vapor and illustrate the mechanisms involved with noctilucent cloud particles, respectively.

3.1 Model structure of MIMAS

3.1.1 Overview

The Mesospheric Ice Microphysics And tranSport model (MIMAS) is a 3-dimensional Lagrangian transport model designed specifically to model noctilucent cloud particles (*Berger and von Zahn, 2002*). MIMAS is independent of LIMA and can be used on multiple dynamic fields (Section 6.2). In earlier publications, it was referred to as LIMA/ICE, since formerly only LIMA dynamics were used. As this name is ambiguous in present circumstances, a replacement was chosen.

Figure 3.1 shows the model structure of MIMAS when used in conjunction with LIMA for NLC simulation, e.g. in (*Lübken et al., 2009; Lübken and Berger, 2011; Lübken et al., 2013b*). LIMA adapts solar cycle data, trace gas concentrations, and reanalysis dynamics from ECMWF up to altitudes of 40 km (see Section 2.1.1). It then uses this data to calculate dynamic fields. These dynamics, plus solar Ly_α data and an initial H_2O distribution are the input for MIMAS. In MIMAS, the mesospheric water vapor is transported by these dynamic fields, spread out by turbulent diffusion, and reduced by photodissociation from solar ultraviolet radiation. It also includes 40 million dust particles which can act as condensation nuclei. These are then coated with ice when in supersaturated regions and eventually grow to NLC particles. The primary model output are trajectories of a collection of dust particles which are sometimes coated with ice. In addition, a three-dimensional image of the NLC is calculated: The light scattering properties (brightness) of the particles are summed up in a spatial grid. For most purposes, only the distributions of the NLC and water vapor are used.

In the following, MIMAS simulations with LIMA dynamic fields are referred to as MIMAS-LIMA, while those with KMCM dynamics are called MIMAS-KMCM. On the other hand, the acronym MIMAS refers to model properties which are independent of the input dynamics.

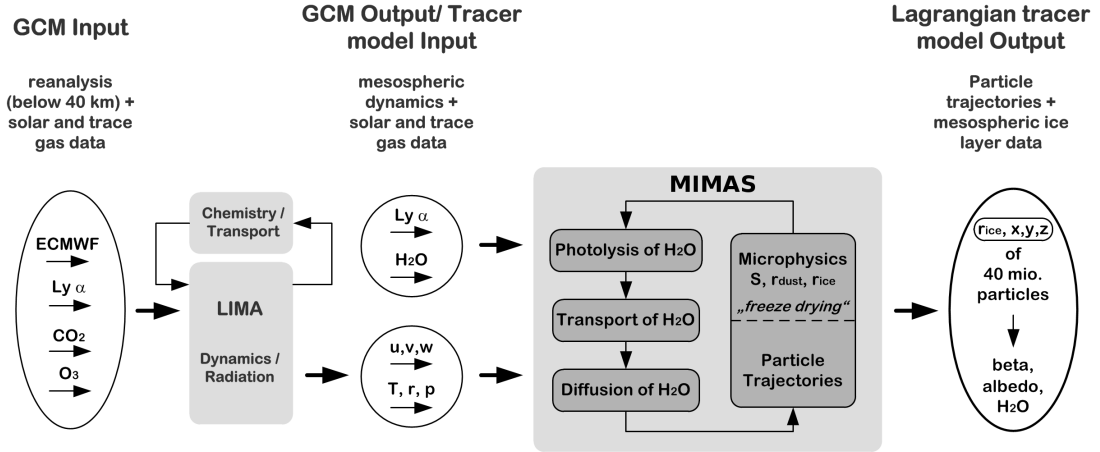


Figure 3.1 Structure of the combined MIMAS-LIMA model, then called LIMA/ICE (adapted from *Lübken et al. (2013b)*).

3.1.2 Model resolution and grid structure

MIMAS is restricted to the environment where noctilucent clouds may occur, namely mid-May to mid-August for the Northern hemisphere. Only the area polewards of 37° and between 77.8 and 94.1 km altitude is included, since conditions in the middle atmosphere do not allow the existence of ice particles outside of this nested domain.

MIMAS uses a horizontal grid with a resolution of 3° in longitude, 1° in latitude. The longitudinal grid size diminishes with latitude as $\Delta s = \frac{3}{360} \cdot \cos \frac{\pi \cdot \Theta}{180} \cdot 40,000$ km. At 70° latitude the cosine term is $\frac{1}{3}$ which makes the longitude and latitude resolution equal, while at the pole there is a coordinate singularity. For the vertical grid, MIMAS uses a geometric altitude grid with a resolution of 100 m. This is in contrast to LIMA, where a triangular horizontal grid and pressure levels with a resolution around 1 km are used.

Since LIMA or KMCM use a different grid (Section 2.1.1), the dynamic output is interpolated to the MIMAS grid at a resolution of one hour. The time step used by MIMAS for most processes including the particle trajectories is 3 minutes, only for water vapor advection it is 90 seconds. The model output consists of several types of files: Once a day at midnight UT, the position and radius of all 40 million model ice particles are saved. Water vapor and the NLC data including brightness, mean particle size and number density are saved hourly on the grid that MIMAS uses for its dynamics. In addition, all particles in the vicinity of Kühlungsborn (54°N), ALOMAR (69°N), and Spitsbergen (78°N) are saved every time step.

3.2 Water vapor in the summer MLT region

In order to model noctilucent clouds, the water vapor which is essential for their formation also must be simulated. In this section, relevant concepts such as transport, diffusion and photodissociation are described along with their implementation in MIMAS, starting with an overview of mesospheric H_2O .

3.2.1 Initialization and relaxation of water vapor

The water vapor present in the polar summer mesosphere region has been studied both experimentally and using modeling. Satellite measurements include the HALogen Occultation Experiment (HALOE) on the Upper Atmosphere Research Satellite (UARS), the Sub-Millimetre Radiometer (SMR) on the Odin spacecraft and the Atmospheric Chemistry Experiment (ACE) on SCISAT-1, among others (*Nedoluha et al.*, 2007; *Vergados and Shepherd*, 2009; *Lossow et al.*, 2008; *Hartogh et al.*, 2010). There are also ground-based instruments such as the MICrowave Spectrometer at IAP (MISI) (F.-J. Lübken, private communication).

In the atmosphere, the amount of a chemical constituent (tracer) at any location and point in time is determined by source, transport and sink (loss) processes. Models must describe or parametrize these processes to achieve accurate tracer concentrations. For water vapor in the middle atmosphere, relevant transport processes are advection and diffusion, described in Section 3.2.2. The major loss process is photolytic dissociation from solar UV radiation (Section 3.2.3). This leaves the source processes, which are more complex: Water vapor is formed by recombination of oxygen with hydrogen, yet the abundance of hydrogen depends itself on the photodissociation of hydrogen-containing molecules like methane.

Simulating the formation of water vapor thus requires a detailed atmospheric chemistry model including all major constituents and processes. As this was considered beyond the scope of MIMAS, H₂O formation is parametrized instead. A heuristic water vapor source term c_0 which depends on latitude and altitude is used. At the beginning of each model simulation, typically May 20, the amount of water vapor is set to this initial profile. Afterward it is constantly nudged towards c_0 (Newtonian relaxation, compare Section 2.1.1):

$$c^{n+1}(\mathbf{x}) = c^n(\mathbf{x}) + \alpha \cdot \Delta t \cdot (c_0(\mathbf{x}) - c^n(\mathbf{x})) \quad (3.1)$$

where $c^n(\mathbf{x})$ is the concentration at time step number n and location \mathbf{x} and Δt is the time interval. The relaxation coefficient α assumes values between $\frac{1}{4 \text{ days}}$ and $\frac{1}{12 \text{ hours}}$. The lower value applies in the interior of the model domain, polewards of 57° and between 80.8 and 91.1 km in altitude. In this region, the slow relaxation ensures that water vapor inhomogeneities may form from interaction with NLC (freeze-drying effect). On the other hand, at the edges of the model domain, much faster relaxation rates stabilize the H₂O concentration in those regions where ice formation is not possible. In combination with transport and photolysis, nudging keeps the water vapor in MIMAS at concentrations consistent with observations (*Hartogh et al.*, 2010).

Figure 3.2 shows water vapor profiles from several measurements and in MIMAS-LIMA at various stages of the simulation. The climatology measured by the MISI instrument is a seasonal average over 4 years. There is a strong seasonal variation at altitudes above 50 km: The typical summer profile from April to September contains about three times more water vapor as the winter profile at 80 km. Within the time period June to August (the NLC season) the variations are only about 10%. This proves that using a constant water vapor source instead of a time-dependent one in MIMAS is a reasonable simplification.

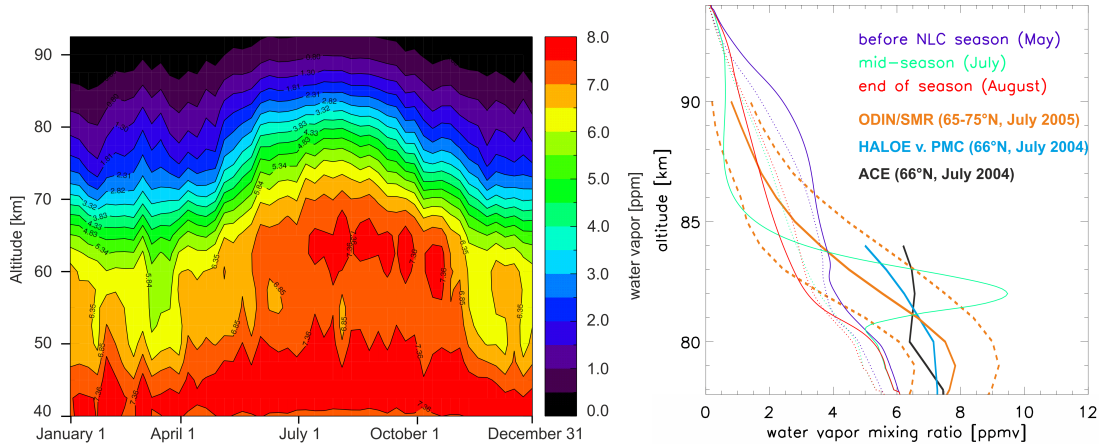


Figure 3.2 Left side: Water vapor climatology at K hlungsborn (54°N) from 2010 to 2013 as measured by MISI. Right side: Water vapor profiles in MIMAS-LIMA (thin lines) and satellites (thick lines). MIMAS source profile c_0 in May (purple), July monthly mean (green) and end of season (red). Solid lines are at 69°N , dotted lines at 54°N . Satellite profiles are taken from Fig. 6 of *Vergados and Shepherd (2009)*.

Shown in the right panel in Figure 3.2, the initialization profile c_0 has higher H_2O concentrations than the steady-state profile in August at all altitudes, especially in the range 83-91 km. This is a result of the water vapor depletion by photolysis (Section 3.2.3). The July profile is even more depleted than the August profile above 84 km. However below this altitude, the July profile is enriched in H_2O , the peak at 82 km reaches nearly 10 ppmv. This reflects how water vapor is redistributed by NLC particle growth around 84 km and by sublimation at lower altitudes.

The right panel in Figure 3.2 also includes satellite H_2O profiles, from Odin/SMR, ACE and HALOE with the v.PMC data retrieval (*McHugh et al., 2005*). All profiles are quite similar, with ACE and HALOE usually within the error bars of Odin. They also include mixing ratio peaks around 78-79 km, presumably from H_2O deposition by mesospheric ice. However, these peaks are lower, less pronounced, and much wider compared to MIMAS-LIMA. This is probably caused by the satellites' lower vertical resolution and the weaker ice formation during the observation years 2004-05. Apart from the strong MIMAS-LIMA deposition peak, the measurements are roughly comparable with the model, the August profile is within the Odin error bars for the most part. The MISI profile is generally lower in water vapor than MIMAS-LIMA at 54°N .

Given the high uncertainty of water vapor measurements above 80 km, the implementation in MIMAS is consistent with measurements. Newtonian relaxation is sufficient as a source term and allows physically consistent modeling of H_2O in the interior part of the model domain.

3.2.2 Water vapor advection and diffusion

To simulate the flow of a chemical constituent such as water vapor on wind fields, the tracer concentration must be transported within the model grid. For a passive chemical tracer moving at velocity u in one dimension, this means solving the continuity equation

3.2 Water vapor in the summer MLT region

$$\frac{\partial c}{\partial t} = -\frac{\partial(u \cdot c)}{\partial x} \quad (3.2)$$

where c is the concentration of the tracer or constituent. MIMAS uses a numerical transport scheme for water vapor which is described in Appendix C.1. In addition to the advection with wind, water vapor in MIMAS is also continually mixed by turbulent eddy diffusion. In one dimension, this is described by Fick's second law

$$\frac{\partial c}{\partial t} = K \cdot \frac{\partial^2 c}{\partial x^2} \quad (3.3)$$

where c is the tracer concentration and K the diffusion coefficient. The general form in multiple dimensions is $\frac{\partial c}{\partial t} = K \cdot \nabla^2 c$. Turbulent diffusion is isotropic, so its horizontal component is very small compared to the vertical because of the very different model scales (≈ 100 km to 100 m). For that reason only vertical diffusion is implemented explicitly.

The values used for K , called K_{zz} for vertical diffusion, are adapted from the sounding rocket climatology at 69°N in *Lübken (1997)*. Shown in Figure 5 of *Berger and von Zahn (2002)*, mesospheric K_{zz} changes strongly with altitude and reaches its maximum of $180 \frac{\text{m}^2}{\text{s}}$ at around 90 km. At NLC altitudes it is much smaller with $\approx 10 \frac{\text{m}^2}{\text{s}}$ at 83 km. MIMAS uses K_{zz} values reduced to 25% of those in *Lübken (1997)* to account for intermittency of turbulence. Even with the small K_{zz} values at the base of the NLC, diffusion is important for counteracting the freeze-drying effect where noctilucent clouds deplete their formation region of water vapor. Latitudinal or time dependencies of K_{zz} are not implemented, since this would require detailed understanding of the gravity wave breaking process causing mesospheric turbulence. The diffusion computation scheme is described in Appendix C.2.

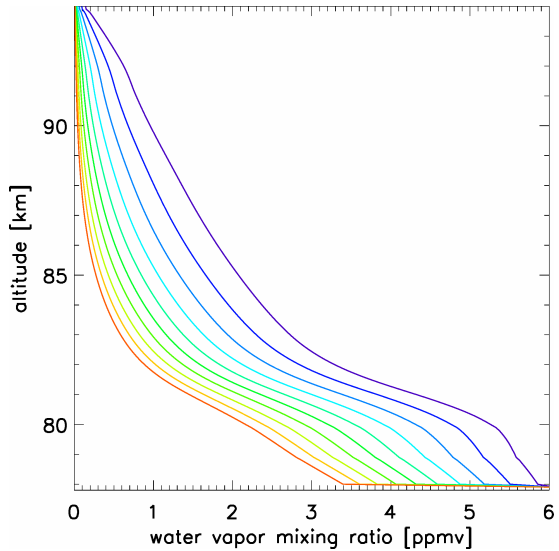


Figure 3.3 Photolytic depletion of a MIMAS-LIMA water vapor distribution at 69°N on June 1 (rightmost profile). Interval between profiles is 24 h.

3.2.3 Photodissociation of H₂O

Water vapor in the environment of NLC is not chemically inert. It is exposed nearly continuously to sunlight which contains much more short-wave UV radiation than in the troposphere. At wavelengths shorter than about 200 nm, ultraviolet light can split off atomic hydrogen from water molecules, in a process called photolytic dissociation. The main wavelength causing this is the Lyman- α hydrogen emission line at 121.56 nm:

Chapter 3 The Lagrangian Tracer Model MIMAS

Most vacuum UV is absorbed by molecular oxygen in the thermosphere (Schumann-Runge continuum). However, the Lyman- α radiation is a strong source of vacuum UV which is less attenuated and thus penetrates into the mesosphere. Details on the attenuation and H₂O absorption are given in Appendix C.3.

In typical polar summer conditions, photodissociation reduces the water vapor at 88 km by half in 2-3 days, at NLC altitudes the process is slower. This can be seen in Figure 3.3: It shows a MIMAS-LIMA sensitivity simulation in which only photolysis affects water vapor over a 9 day period.

However, in regular model simulations H₂O is not depleted indefinitely. Upward transport, diffusion and the nudging process described in Section 3.2.1 counteract photolysis and create an equilibrium at a concentration below the initialization profile. Photolytic dissociation is thus important for the amount of water vapor in the mesopause region, although advection is the major factor for the seasonal variation at NLC altitudes shown in Figure 3.2. Since noctilucent clouds are very sensitive to H₂O, this causes the NLC to vary in brightness when the UV intensity Φ_∞ changes with the solar cycle (*Lübken et al.*, 2009). Solar activity also influences noctilucent clouds in another, indirect way: Increased UV absorption by molecular oxygen heats the mesosphere, which suppresses NLC formation.

3.3 Microphysical processes in MIMAS

This section describes how water vapor nucleates around meteoric smoke particles. The physical processes involved with noctilucent clouds are covered in detail, as well as their implementation in MIMAS (*Berger and von Zahn*, 2002; *von Zahn and Berger*, 2003).

3.3.1 Dust particle size distribution and relocation algorithm

Since MIMAS assumes heterogeneous nucleation for all icy particles in the MLT region, the availability of condensation nuclei (CN) has a large impact on the formation of ice clouds. Tropospheric and stratospheric aerosols are generally not transported up to the mesosphere, so all CN in these altitudes are likely produced in situ. As extraterrestrial meteoroids continuously impact the Earth and a large part evaporates in the altitude region of 80-100 km, *Rosinski and Snow* (1961) first suggested that the trail of ablated material might condense into tiny particles.

Hunten et al. (1980) call these "Meteoric smoke particles" and studied their properties in detail, modeling their formation including the processes of coagulation, sedimentation, turbulent diffusion. They also studied the sensitivity of meteoric smoke formation to several poorly known parameters such as the abundance of micrometeorites. The initial smoke particle size r_0 is particularly important, since the total dust number density at 90 km varies as $n \propto r_0^{-4}$. In the mesosphere, the size distribution is approximately exponential: Fitting the slope of Figure 6a in *Hunten et al.* (1980) for $r_0 = 1$ nm yields $\frac{n(r)}{dr} \propto e^{8.3 \cdot \frac{r}{\text{nm}}}$, i.e. 2 nm particles are 300 times less common than 1 nm.

3.3 Microphysical processes in MIMAS

MIMAS uses this size distribution with $r_0 = 1.2$ nm. The number densities are scaled up to make them compatible with the higher meteoric mass influx of 110 t/d in *Love and Brownlee (1993)* compared to 44 t/d in *Hunten et al. (1980)*. *Hunten et al. (1980)* recommend $r_0 = 0.2$ nm, but their suggestion was not followed here for reasons discussed in Section 3.3.2. The number of particles in a Lagrangian model is limited by computer resources: In the current version of MIMAS with 40 million model particles, each is a proxy for $7.4 \cdot 10^{18}$ real particles, distributed over the grid volume the model particle currently occupies. Number densities in MIMAS are calculated by scaling the number of model particles with this factor and dividing by the grid volume.

At the start of a MIMAS simulation, 40 million model CN are assigned sizes between 1.2 and 3.7 nm, discretized into 5 bins with a width of 0.5 nm each. The number distribution is 86.5% (1.2–1.7 nm), 11.7% (1.7–2.2 nm), 1.7% (2.2–2.7 nm), 0.2% (2.7 – 3.2 nm) and 0.02% (3.2 – 3.7 nm). All particles are randomly distributed polewards of 55° and in a narrow height range (± 1 km) around the mesopause. During the model simulation, all condensation nuclei are advected with the wind field and sediment according to their altitude and size (see Section 3.3.3).

Two additional processes stabilize the dust particle distribution, illustrated in Figure 3.4: Condensation nuclei which are transported equatorward of the 55° latitude circle, below 83 km or more than 1 km above the mesopause are considered outside the possible ice nucleation zone. These particles are randomly relocated to a new position $>55^\circ$ and within ± 1 km of the mesopause (the dust injection region). The same random relocation is applied to every CN within the nucleation region every 6 hours. This simulates the entry of meteoric dust into the mesosphere, preventing its depletion within the nucleation region. Both mechanisms do not apply while CN are coated by ice, so model NLC particles also occur outside of the nucleation zone as defined in Figure 3.4.

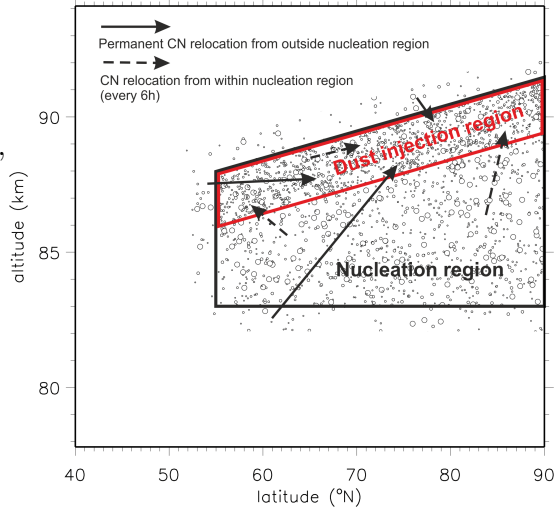


Figure 3.4 Schematic of meteoric dust in MIMAS

3.3.2 Nucleation and particle growth

The saturation ratio of air with water vapor is defined as $S = \frac{p_{\text{H}_2\text{O}}}{p_\infty}$, where $p_{\text{H}_2\text{O}} = c_{\text{H}_2\text{O}} \cdot p$ is the H_2O partial pressure and p_∞ is the saturation vapor pressure over a plane ice surface ($c_{\text{H}_2\text{O}}$ is the water vapor mixing ratio). An environment with a value of $S > 1$ is called supersaturated, which means that ice particles can grow under these conditions, while a saturation ratio below one is subsaturated and leads to ice sublimation.

Ice particles in the mesosphere may form by heterogeneous nucleation around meteoric dust and homogeneous nucleation (*Murray and Jensen, 2010*). However, homo-

Chapter 3 The Lagrangian Tracer Model MIMAS

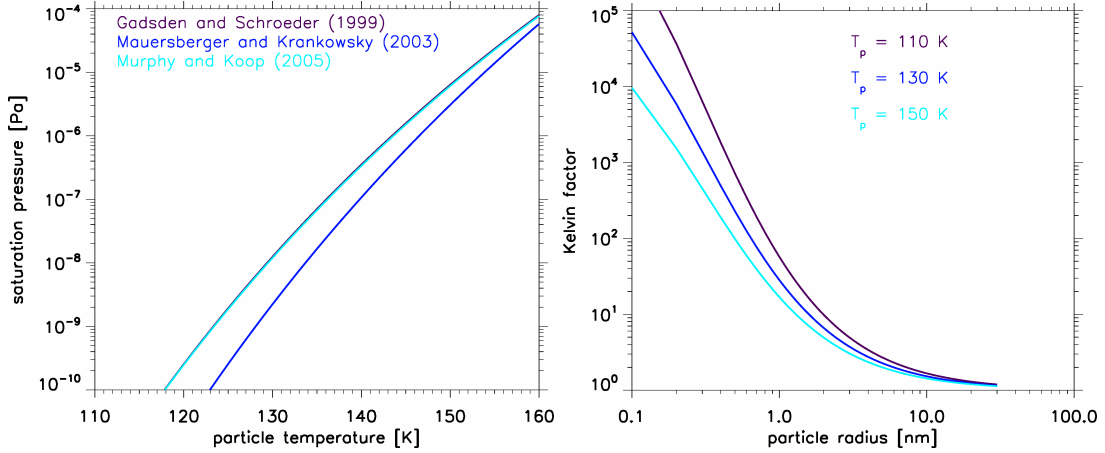


Figure 3.5 Left panel: Water vapor saturation pressure over ice at summer mesosphere temperatures. Right panel: Kelvin factor, i.e. $p_{\text{sat}}(r)$ to p_{∞} ratio.

geneous nucleation requires very high supersaturation ($S > 1000$) only possible with strong GW activity. Ion recombination nucleation has also been suggested (*Sugiyama*, 1994), but *Gumbel et al.* (2003) found that while this may occur under certain conditions, it is likely not a major nucleation process. Heterogeneous nucleation is regarded as the dominant process in NLC (*Gadsden*, 1982; *Turco et al.*, 1982). For that reason, it is the only nucleation process incorporated in MIMAS (*Berger and von Zahn*, 2002).

For calculating saturation ratios, a formula for the saturation vapor pressure is needed. p_{∞} is poorly known at mesospheric temperatures since there are few direct measurements. There are several formulations with different results:

$$p_{\infty} = e^{28.548 - \frac{6077.4}{T_p}} \quad (3.4)$$

$$p_{\infty} = 10^{14.88 - \frac{3059}{T_p}} \quad (3.5)$$

$$p_{\infty} = e^{9.550426 - \frac{5723.265}{T_p} + 3.53068 \cdot \log T_p - 0.00728332 \cdot T_p} \quad (3.6)$$

Equation (3.4) is by *Gadsden and Schröder* (1989), Equation (3.5) by *Mauersberger and Krankowsky* (2003) and Equation (3.6) is from a review article by *Murphy and Koop* (2005). Figure 3.5 compares these formulations for the range of temperatures relevant for NLC. The values of p_{∞} in (3.4) are only 2-3% higher than in (3.6), which makes them difficult to distinguish in Figure 3.5. p_{∞} in (3.5) is lower by a factor of 10 than (3.6) at 120 K and a factor of 2 at 150 K. As *Rapp and Thomas* (2006) point out, (3.5) extrapolates over a larger temperature range than (3.6), so they argue that (3.6) is most appropriate. MIMAS currently uses formula (3.6).

Ice particle temperature T_p is higher than the ambient air temperature because the ice particles are heated from absorbing solar or terrestrial infrared light (*Eidhammer and Havnnes*, 2001):

$$\Delta T = T_p - T \propto \frac{r}{a \cdot n_{\text{air}}} \quad (3.7)$$

where r is the particle radius and n_{air} the number density of air (*Rapp and Thomas*, 2006). The accommodation coefficient a describes the efficiency of thermal energy

3.3 Microphysical processes in MIMAS

transfer from the ice particle to the ambient air. To date, a is very poorly known (*Rapp and Thomas, 2006*). Fig. 6 in *Rapp and Thomas (2006)* shows the dependence of ΔT on altitude and particle size according to *Espy and Jutt (2002)*, assuming $a = 1$. Infrared heating in MIMAS is proportional to Fig. 6 in *Rapp and Thomas (2006)*, but higher by a factor of 2.3 since a value of $a = 0.5$ is used (and a different density profile). ΔT can reach up to ≈ 3 K for large NLC particles (80 nm) at 83 km.

For a meteoric dust particle to gain an ice coating (i.e. heterogeneous nucleation), a saturation ratio of 1 is not sufficient. The surface tension of small particles causes a pressure increase within the particle (Laplace pressure), which accelerates evaporation of the droplet. The saturation pressure dependence on particle radius is called the Kelvin effect:

$$p_{\text{sat}}(r) = p_{\infty} \cdot \exp\left(\frac{2m_{\text{H}_2\text{O}} \cdot \sigma}{k_B \cdot T_p \cdot \rho \cdot r}\right) \quad (3.8)$$

where $m_{\text{H}_2\text{O}} = 2.99 \cdot 10^{-26}$ kg is the molecular mass of water, $k_B = 1.3085 \cdot 10^{-23} \frac{\text{J}}{\text{K}}$ the Boltzmann constant, $\rho = 932 \frac{\text{kg}}{\text{m}^3}$ the density of ice and σ the surface tension of a curved ice-water vapor surface. For very small spherical ice particles σ is (*Tolman, 1949*)

$$\sigma = \frac{\sigma_{\infty}}{1 + \frac{2\delta}{r}} \quad (3.9)$$

with σ_{∞} the surface tension over a plane icy surface. This was linearly fitted by *Hale and Plummer (1974)* as $\sigma_{\infty} = (0.141 - 1.5 \cdot 10^{-4} \frac{T}{\text{K}})$ Pa. $\delta = 1.5 \cdot 10^{-10}$ m is an empirical factor (*Turco et al., 1982*).

$p_{\text{sat}}(r)$ is called the equilibrium vapor pressure, since ice particles stay at constant size when $p_{\text{sat}}(r) = p_{\text{H}_2\text{O}}$. The right panel in Figure 3.5 shows the Kelvin factor, i.e. the ratio $p_{\text{sat}}(r)$ to p_{∞} for three temperatures. It exceeds 30 for particles smaller than 1 nm, at the homogeneous nucleation scale of 0.3 nm it is larger than 1000, with higher values for lower temperatures.

A condensation nucleus with radius r acquires an ice coating when the saturation ratio $S = \frac{p_{\text{H}_2\text{O}}}{p_{\infty}}$ exceeds $\frac{p_{\text{sat}}(r)}{p_{\infty}}$, i.e. the Kelvin factor of the nucleus. Dust particles smaller than 1.2 nm were not included in MIMAS as they would rarely acquire an ice coating and thus would result in unnecessary trajectory calculations.

The growth rate of ice particles in the mesosphere is given by *Hesstvedt (1961)* as

$$\frac{dr}{dt} = \frac{\alpha}{\rho} \sqrt{\frac{m_{\text{H}_2\text{O}}}{2\pi \cdot k_B \cdot T_p}} \cdot p_{\text{sat}}(r) \cdot (S(r) - 1) = \frac{\alpha}{\rho} \sqrt{\frac{m_{\text{H}_2\text{O}}}{2\pi \cdot k_B \cdot T_p}} \cdot (p_{\text{H}_2\text{O}} - p_{\text{sat}}(r)). \quad (3.10)$$

α is called the condensation coefficient, it describes the probability that a water molecule hitting an ice crystal is attached to it. Various sources assume a value between 0.5 (*Reid, 1975*) and 1 (*Turco et al., 1982*), here 0.83 is used (*Gadsden, 1998*). When p_{sat} exceeds $p_{\text{H}_2\text{O}}$, the term becomes negative meaning that the particle sublimates.

The above formulae for particle nucleation and growth assume spherical particles, since standard MIMAS only includes these. For elongated particles, a correction factor to the growth rate is required, which is described in Section 6.1.1.

3.3.3 Particle sedimentation and diffusion

Particle motion in MIMAS is a combination of advection, sedimentation and turbulent diffusion. For horizontal motion only advection applies, this is described in more detail in Appendix C.4. For the vertical motion, sedimentation and eddy diffusion are important and realized in MIMAS as follows: Sedimentation in Earth's gravity affects both meteoric dust and ice particles, its velocity is (e.g. *Reid, 1975*)

$$w_{s,n} = -\frac{g \cdot \rho \cdot r_n}{2n_{\text{atm}}} \sqrt{\frac{\pi}{2m_{\text{atm}} \cdot k_B \cdot T}} \quad (3.11)$$

where $g = 9.55 \frac{\text{m}}{\text{s}^2}$ is the gravitational acceleration at mesosphere altitude and $\rho = 932 \frac{\text{kg}}{\text{m}^3}$ is the density of ice. $m_{\text{atm}} = 4.845 \cdot 10^{-26}$ kg is the molecular mass of air and n_{atm} the number density of air in molecules per m^3 . *Turco et al. (1982)* propose using a correction factor of $\frac{1}{1+\frac{\pi}{8}}$ from inelastic collisions, this would reduce sedimentation rates by 28%. However, this is not included yet in this version of MIMAS. $w_{s,n}$ is linear in radius and reciprocal in air density: Typical sedimentation velocities are $3 \frac{\text{cm}}{\text{s}}$ ($\approx 0.1 \frac{\text{km}}{\text{h}}$) for small 5 nm particles at 88 km and $10 \frac{\text{cm}}{\text{s}}$ ($\approx 0.4 \frac{\text{km}}{\text{h}}$) for 50 nm particles in the NLC layer at 83 km. As for particle growth this applies to spherical particles only, for other shapes there exists a correction factor described in Section 6.1.1.

Ice and dust particles are also affected by eddy diffusion. Like for water vapor (Section 3.2.2), only vertical diffusion is implemented because minor horizontal trajectory deviations have little effect on NLC, while altitude changes of a few hundred meters may have a large impact. The mixing scales in the upper mesosphere are typically around 10 – 100 m. Turbulent velocities reach several $\frac{\text{m}}{\text{s}}$ around 90 km (*Lübken, 1997*). As seen in Figure 2.1, this is far higher than vertical wind amplitudes in LIMA, only KMCM_{120} comes close.

Since the eddy diffusion is chaotic at the model scales, MIMAS treats it as a random motion. *Berger and von Zahn (2002)* describe how they used the broadening of a Delta peak distribution into a Gauss distribution as a benchmark for their implementation. The peak variance increases linearly with $\sigma^2 = 2 \cdot K_{zz} \cdot t$. Performing a random walk $\tilde{w}_t = \zeta \cdot w_t(z_n)$ with $\zeta \in [-1; 1]$ for a large ensemble of particles broadens a Delta distribution in the same way with $w_t^2 = a \cdot K_{zz}$. *Berger and von Zahn (2002)* determined the proportionality factor a by numerical experimentation. a depends on the time step of the random walk. For $\Delta t = 45\text{s}$, i.e. the MIMAS microphysics time step, a is 7.5s. This relates to maximum turbulent velocities of $\approx 5 \frac{\text{m}}{\text{s}}$ at 90 km which is compatible to the $2.6 \frac{\text{m}}{\text{s}}$ in *Lübken (1997)* since the latter is a mean velocity.

4 Morphology of NLC in MIMAS-LIMA

In this chapter, the general structure of noctilucent clouds in MIMAS-LIMA is analyzed. This includes their spatial extent, time scales, and relationship to the ambient conditions involved in their formation. The particle life cycle is also analyzed briefly, preparing for the strong NLC analysis in Chapter 5 and the sensitivity studies in Section 6.1 and Section 6.2.

4.1 General NLC morphology

Berger and von Zahn (2002) describe the mechanisms also used in MIMAS (Chapter 3) in detail. They include a discussion of the cloud morphology, which *von Zahn and Berger* (2003) expand on. While the ice model for this study is very similar, the dynamical fields used at that time were supplied by COMMA/IAP, the predecessor to LIMA. Unlike LIMA, COMMA/IAP did not adapt ECMWF reanalysis data, and had a longitude-latitude grid with a coordinate singularity at the poles (see Section 2.1.1). Thus some of the results in terms of cloud morphology have changed, as first discussed in *Lübken et al.* (2009). In this section, the NLC morphology in MIMAS-LIMA is described in more detail.

4.1.1 Snapshot of NLC in MIMAS-LIMA

In the left panel of Figure 4.1 the horizontal distribution of a noctilucent cloud in MIMAS-LIMA is shown. The date of July 14, 2009, 7 UT was chosen because a strong ice cloud occurs around ALOMAR (69°N, 16°E) at this time. This snapshot shows the horizontal scales of NLC modeled with LIMA background fields. The typical distances between patches of visible ice are on the order of 1000 km. This sample ice cloud is mostly located in regions with a local time between 21 LT and 10 LT (i.e. during night and morning hours) which is typical for the LT variation of NLC in MIMAS-LIMA (see Section 4.1.2). Particles larger than 25 nm are present in roughly the same volume as the domain where the NLC is optically detectable ($\beta_{\max} > 0.1 \cdot 10^{-10} \text{m}^{-1} \text{sr}^{-1}$). The zonal phase propagation of the cloud can be seen in animations of such figures: It ranges from stationary to slowly eastward, in contrast to the westward directed particle transport (see Appendix B.6).

The right panel of Figure 4.1 shows particle size and altitude of the NLC around ALOMAR (within the white framed area in the left panel). This area is ≈ 500 km times 500 km large and also used for localizing NLC events in Chapter 5. A large majority of the ice particles in the sample volume are small (<20 nm) and located

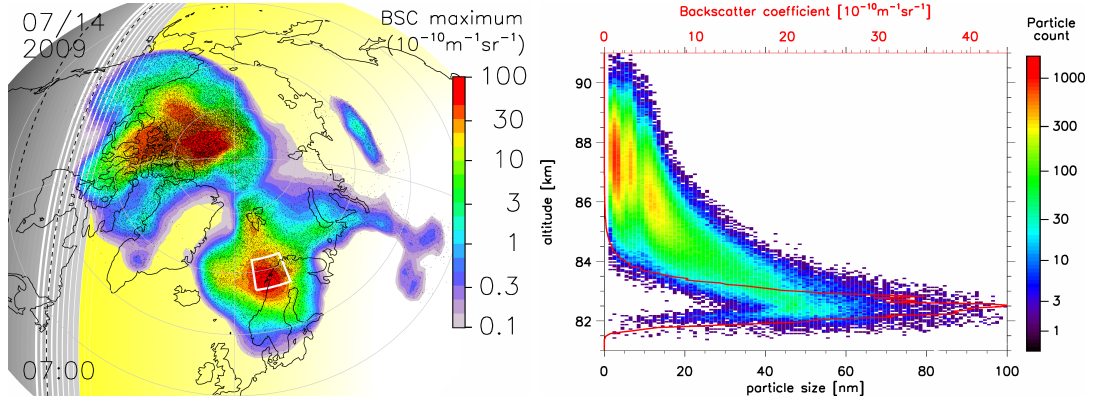


Figure 4.1 Snapshot of a noctilucent cloud in MIMAS-LIMA on July 14, 7 UT. Left panel: Horizontal distribution. Colored contours show NLC maximum backscatter coefficient β_{\max} , while the black dots show model ice particles larger than 25 nm. Yellow and grey shading in the background indicates solar elevation. Grey lines show the area where ice clouds, if present, may be observed as noctilucent clouds. The two dashed lines delimit the approximate area on the ground from where NLC are visible. Right panel: Particle size and altitude around ALOMAR (69°N, white frame in the left panel). Colored boxes show the number of model ice particles in a particular size/height bin, the red profile is the backscatter signal at 532 nm.

above 85 km. However, the backscatter profile is generated almost entirely by the large particles below 85 km, which are fewer in number. Since the increase of backscatter cross section with radius is $\beta \propto r^5$ up to r^6 in the Mie regime, the far higher scatter brightness of the large particles more than compensates their smaller number. The peak of the backscatter signal is located around 82 – 83 km. At this altitude, only large ice particles are found. Other than at high altitudes, small particles only occur within the sublimation zone ≈ 1 km below the backscatter peak.

The changes in particle number density thus give an insight into the NLC life cycle: Most small ice particles nucleate at high altitudes, where nucleation takes place. Some but not all of these particles are transported downwards. These reach their maximum size around the altitude of the scatter signal peak and sublimate rather rapidly afterwards, on account of the steep decrease in both size and number density below the visible layer.

4.1.2 NLC time series

Like for atmospheric dynamics in Section 2.3.1, the temporal evolution at a stationary location is most suitable for comparison with ground-based measurements. Two sample time series of model NLC at ALOMAR are included in Figure 2.7 and Figure 2.8 along with the dynamic fields discussed in Section 2.3.1. Typically, NLC coincide with low temperatures at 83 km, and often but not always with meridional wind turning from southwards to northwards. Figure 4.2 shows a NLC measured by lidar (e.g. *Fiedler et al.*, 2011) over two days. A comparison with the MIMAS-LIMA time series allows pointing out a few principal similarities and differences.

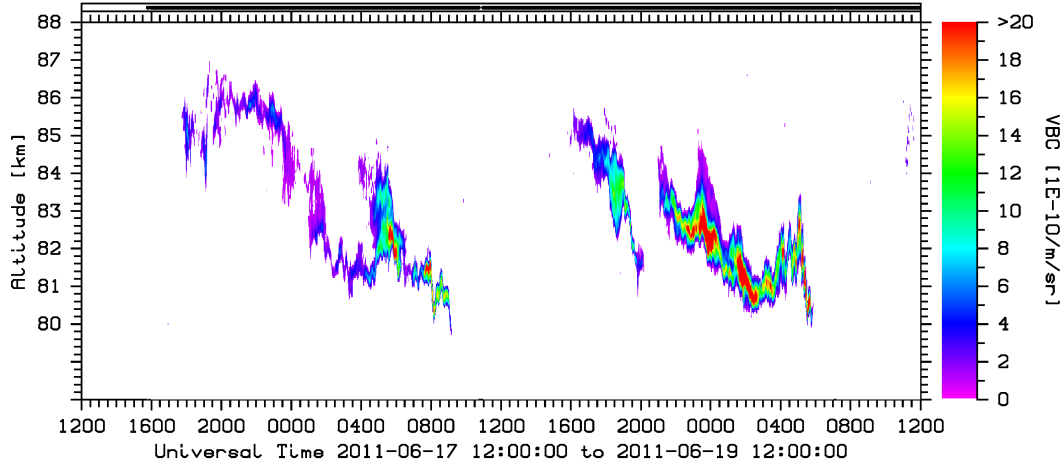


Figure 4.2 RMR-Lidar measurement of noctilucent cloud at ALOMAR, over a two day period in June 2011. The black bar on top indicates the time when the lidar is active. The contours show the volume backscatter coefficient at 532 nm (green) (J. Fiedler, private communication).

The lidar NLC is similar to the modeled ice cloud in many aspects: Both have a mean centroid altitude around ≈ 82.5 km. NLC in MIMAS-LIMA occur once per day most of the time, with durations of several hours. The NLC as observed by lidar tend to last slightly longer compared to the model. However, when only strong ice clouds are considered, the durations are very similar (see Section 4.1.3). There is a strong local time variation of NLC: They typically occur during the night and early morning hours in both MIMAS-LIMA and the lidar (Fiedler *et al.*, 2011; Lübken *et al.*, 2013b). This also applies for the model NLC in Section 2.3.1 and the observation in Figure 4.2. Lastly, the centroid altitude of NLC typically falls during their lifetime both in MIMAS-LIMA and in the observation.

However, the NLC observed by lidar differs from the model ice cloud in a number of aspects: The altitude range of visible ice is 80 to ≈ 86 km, wider than the 81 to 84,5 km in MIMAS-LIMA. At the same time, the ice layer at any specific time is thinner, usually less than 1 km compared to 2 – 2.5 km in the model. The downward progression is much greater in the observed NLC compared to the model: The NLC in Figure 4.2 start occurring as weak clouds at ≈ 85 km, reach their highest brightness around 82 km and disappear soon afterward at 80 – 81 km. In contrast, the downward progression for noctilucent clouds in MIMAS-LIMA is only 1 – 1.5 km.

There are additional differences which can be attributed to different small scale variability: Observed NLC layers change in brightness and especially in altitude much more rapidly than the modeled ice clouds. Centroid altitude fluctuations show waves of a broad spectrum (Kaifler *et al.*, 2013a). However, as found with respect to dynamic variables, the NLC in Section 2.3.1 mainly includes tidal variations, since these constitute most of the variability in LIMA.

4.1.3 Duration of noctilucent clouds

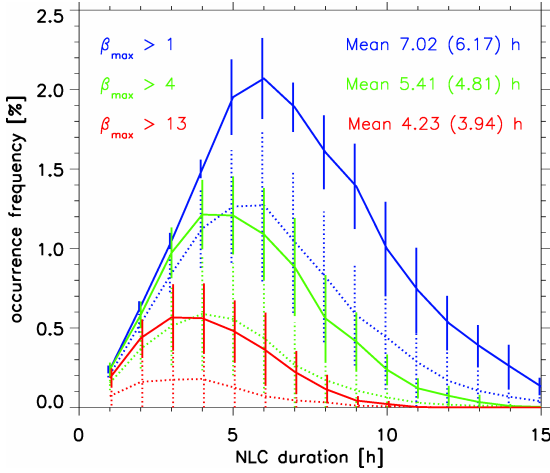


Figure 4.3 Distribution of NLC duration derived from MIMAS-LIMA and mean values at 69°N , calculated at 3 β_{max} -thresholds. Solid lines are from 2008 to 2011, dotted lines and mean in brackets are 2000-2007. Error bars show the variance.

and $13 \cdot 10^{-10} \text{m}^{-1} \text{sr}^{-1}$ are used, based on the NLC classes in *Fiedler et al. (2009)*. Figure 4.3 shows occurrence frequencies, i.e. the probability that an ice cloud with a certain duration is happening at a random point in time.

To match the lidar statistic, Figure 4.3 shows the time period of 2008-2011. For all three thresholds, the modeled duration has a smooth distribution with a distinct peak. The distributions in *Kaifler et al. (2013b)* are more noisy since lidars can only be operated in the absence of thick tropospheric clouds. For the $\beta_{\text{max}} > 4$ threshold, model NLC have a mean duration of 5.41 hours, very close to the lidar statistic for $\beta_{\text{max}} > 2.5$. Lower thresholds correspond to higher durations, by up to ≈ 1.5 h between successive thresholds. Thus, the modeled NLC durations are similar to the measurements, which further validates MIMAS-LIMA.

Since 2008-2011 is a period during solar minimum, the results might be biased compared to a long-term statistic. In years with higher solar activity, NLC are weaker (e.g. *Gadsden and Schröder, 1989*). For this reason the statistic for 2000-2007 (mostly solar maximum) is added in Figure 4.3 for reference. The lower brightness translates into lower occurrence rates especially at high thresholds, but the occurrence rate variance is large especially in the period 2000-2007. The mean cloud duration at all thresholds is slightly lower in 2000-2007 compared to solar minimum. However, for the highest threshold $\beta_{\text{max}} > 13$ this difference is only 0.3 hours, so a relationship between solar cycle and NLC duration is dubious considering the variability. In conclusion, Figure 4.3 shows that NLC duration is a very stable parameter in MIMAS-LIMA. It changes much less with the solar cycle than NLC brightness.

The ice clouds in MIMAS-LIMA have been compared to ALOMAR Lidar observations in a number of parameters, such as brightness, altitude, occurrence rates, diurnal and seasonal variation (*Lübken et al., 2009, 2013b*). Recent refinements to the ALOMAR NLC statistics in *Kaifler et al. (2013a,b)* allow additional comparisons related to the NLC time scales. Fig. 6 in *Kaifler et al. (2013b)* shows lidar NLC durations from 2008 to 2011. At ALOMAR (upper right panel), the average NLC length is 5.4 hours using $\beta_{\text{max}} > 2.5 \cdot 10^{-10} \text{m}^{-1} \text{sr}^{-1}$ as detection threshold. An equivalent analysis with MIMAS-LIMA is presented in Figure 4.3. As in *Kaifler et al. (2013b)*, the duration is calculated as the time period where a NLC is continuously brighter than the threshold. Three thresholds $\beta_{\text{max}} > 1, 4$

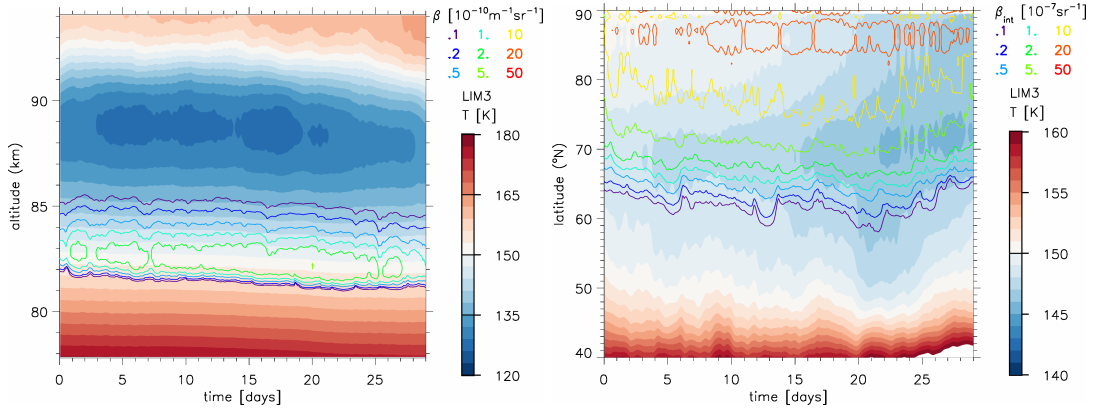


Figure 4.4 July 2009 time series of daily mean temperature and NLC brightness in LIMA. Left panel: Zonally averaged profiles at 69°N. Filled contours show temperature, empty contours backscatter coefficient (β) at 532 nm. Right panel: Latitudinal dependence of zonal daily mean temperature at 83 km and column backscatter (β_{int}).

4.1.4 Morphology of NLC-related parameters

Section 2.3.1 and Section 4.1.2 discuss dynamics and NLC at a singular, fixed position and Section 4.1.1 is concerned with a singular point in time. Figure 4.4 complements this, showing the large-scale structure of temperature and NLC formation with two different projections to account for both meridional and vertical dependencies. The left panel shows that both temperature and the NLC at 69°N have rather stable vertical structures. The mesopause temperature increases by around 5 degrees towards the end of the month. The NLC is brightest at an altitude where the average temperature is 149 K. This applies throughout July 2009, while the NLC altitude gradually drops by about 400 m. The NLC brightness varies little apart from a slight decrease at the end of July.

The right panel focuses on the latitudinal dependence at a typical NLC altitude of 83 km. It highlights the stable temperature at 83 km over a wide latitudinal range, as discussed in Figure 2.1. However, the NLC brightness strongly depends on latitude. The strongest NLC occur at $\approx 86^\circ\text{N}$, even though the temperature at 83 km is minimal around 70°N . At most latitudes, the temperature at 83 km varies only by 2-3 K within the total time period. The furthest southward extent of the ice cloud around July 21 coincides with the minimum temperature. The apparent paradox of a strong latitudinal dependence of NLC without a corresponding temperature change at NLC altitude is explored in Figure 4.5 and later in Section 6.2.2.

Figure 4.5 shows two parameters which are significant to the formation of visible NLC, in the same altitude-latitude projection as in Section 2.1. In the water vapor mixing ratio (left panel), a clear relationship is visible: The vertical gradient of the H_2O mixing ratio is distorted from a steady decrease only at the latitudes where ice clouds form. North of about 65°N , there is a significant depletion of water vapor above 84 km, as well as a layer of highly increased H_2O between 81 and 83 km altitude. The maximum of the deposition layer at the lower edge of the visible ice cloud corresponds well with the cloud brightness. This so-called freeze-drying effect is caused by noctilu-

Chapter 4 Morphology of NLC in MIMAS-LIMA

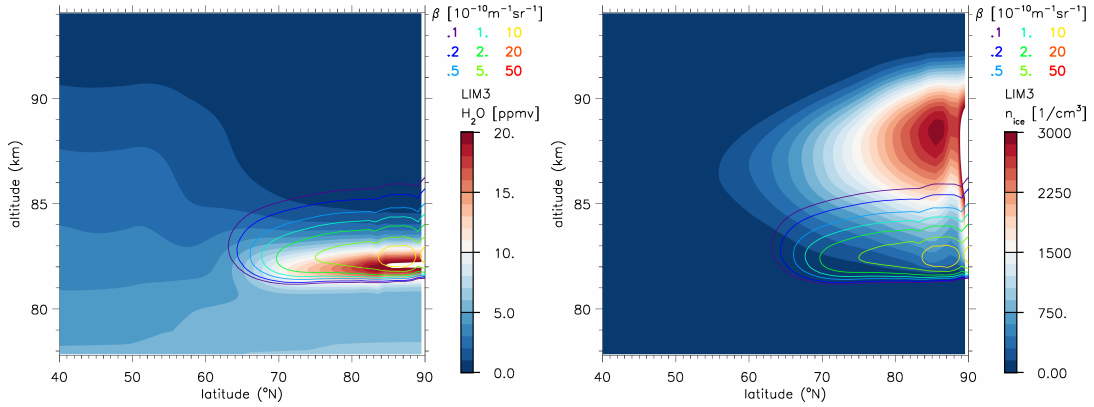


Figure 4.5 July 2009 zonal average of NLC-related parameters in MIMAS-LIMA. Left panel: Water vapor mixing ratio, right panel: ice particle number density. Both panels also show mean NLC backscatter coefficient in contour lines.

cent cloud particles. The NLC redistribute the water vapor in their ambient air by growth and subsequent sublimation (e.g. *Sugiyama, 1994; Berger and von Zahn, 2002; Lübken et al., 2009*).

In the right panel of Figure 4.5, the ice particle number density is plotted. At 69°N , this distribution is similar to the one in Figure 4.1, but it also shows a strong meridional gradient which corresponds to the one in the brightness distribution. At latitudes $> 80^\circ$ and between 88-89 km, particle number densities reach very high values near 3000 cm^{-3} . Figure 2.1 shows that this region combines very low temperatures with low variability, i.e. permanent high supersaturation. Condensation nuclei transported there immediately acquire an ice coating and accumulate there as small icy particles, not able to grow further due to the lack of available water vapor. The high latitude mesopause region is also depleted of condensation nuclei, as seen in Figure B.3.

The large number of small particles serve as a reservoir from which NLC particles are formed after they move to the water vapor rich altitude by sedimentation and diffusion. Thus ice clouds close to the pole are brighter than those at 70°N because of the larger number of small particles above the NLC. These small icy particles are available for growth to larger sizes later. Unlike the NLC brightness, the altitude of noctilucent clouds does not strongly depend on latitude, mainly because of the temperature profile (Section 2.1). The latitude dependence of NLC is explored in more detail in Section 5.4 and Section 6.2.2.

4.2 General trajectory shape

The life cycle of strong NLC will be studied in depth in Chapter 5. In this section, an overview of particle trajectories is presented with no bias towards bright clouds. This also prepares for the sensitivity studies in Chapter 6.

4.2 General trajectory shape

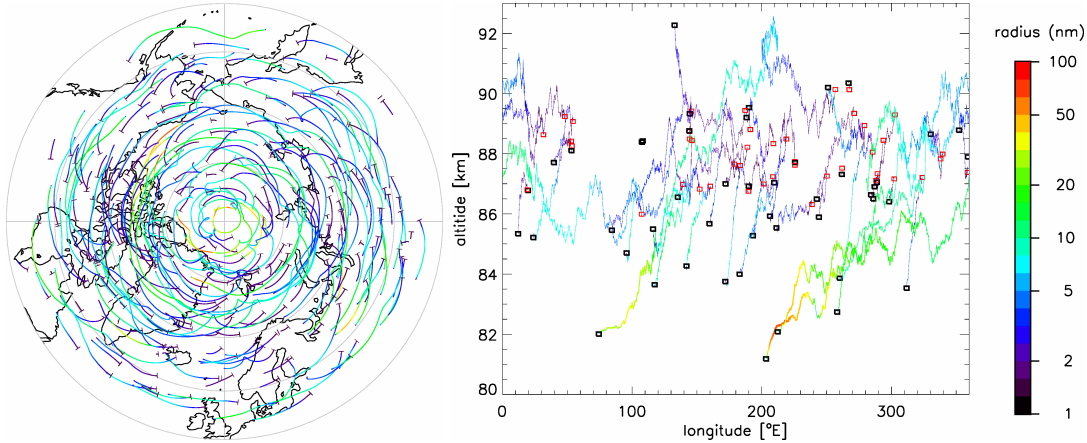


Figure 4.6 Left side: Horizontal ice phase trajectories of 7 condensation nuclei during July 2009 (polar stereographic view), with color showing particle size. The number of trajectories is 316. Trajectory starting points are marked by horizontal lines. Right side: Zonal-vertical ice phase trajectory of a single condensation nucleus during the same time period, which yields 48 separate trajectories. Nucleation locations are marked by red squares, sublimation locations by black squares.

4.2.1 Sample ice trajectories

The left panel of Figure 4.6 shows the ice-phase trajectories of 7 condensation nuclei within July 2009. The apparent number of trajectories is much higher (≈ 300): Dust nuclei periodically gain an ice coating, which typically lasts only for a few hours before it sublimates again. Zonal transport is westward with few exceptions. Eastward transport occurs only rarely at high altitudes. The meridional transport is more complex: It is mostly southward directed but periodically turns northward, as seen by the shifting meridional direction of long particle trajectories around 60°N . The right panel of Figure 4.6 shows the vertical movement of a single dust nucleus over this time frame. Nucleation generally occurs within the altitude range 86 – 90 km, while existing particles are distributed over a wider altitude range of around 82 – 92 km. The vertical trajectories appear less smooth than the horizontal ones because of turbulent motion. At high altitudes, eddy diffusion dominates vertical particle motion at short timescales, as discussed later in Section 5.3. Most particles do not reach a radius of 20 nm during their life cycle, i.e. never grow to visible size. This is visible in both panels of Figure 4.6 by the scarcity of yellow or red trajectory segments. Visible particles are located at the lower edge of the ice domain around 83 km. Unlike nucleation, sublimation may take place in the complete altitude range of 82 – 92 km. While most particles sublimate below their nucleation height (due to sedimentation), occasionally ice particles are also destroyed by transport above the supersaturated region.

4.2.2 Ice trajectory statistics

To better understand the ice particle life cycle, 10,000 condensation nuclei during July 2009 are analyzed, resulting in several hundred thousand continuous ice trajectories.

Chapter 4 Morphology of NLC in MIMAS-LIMA

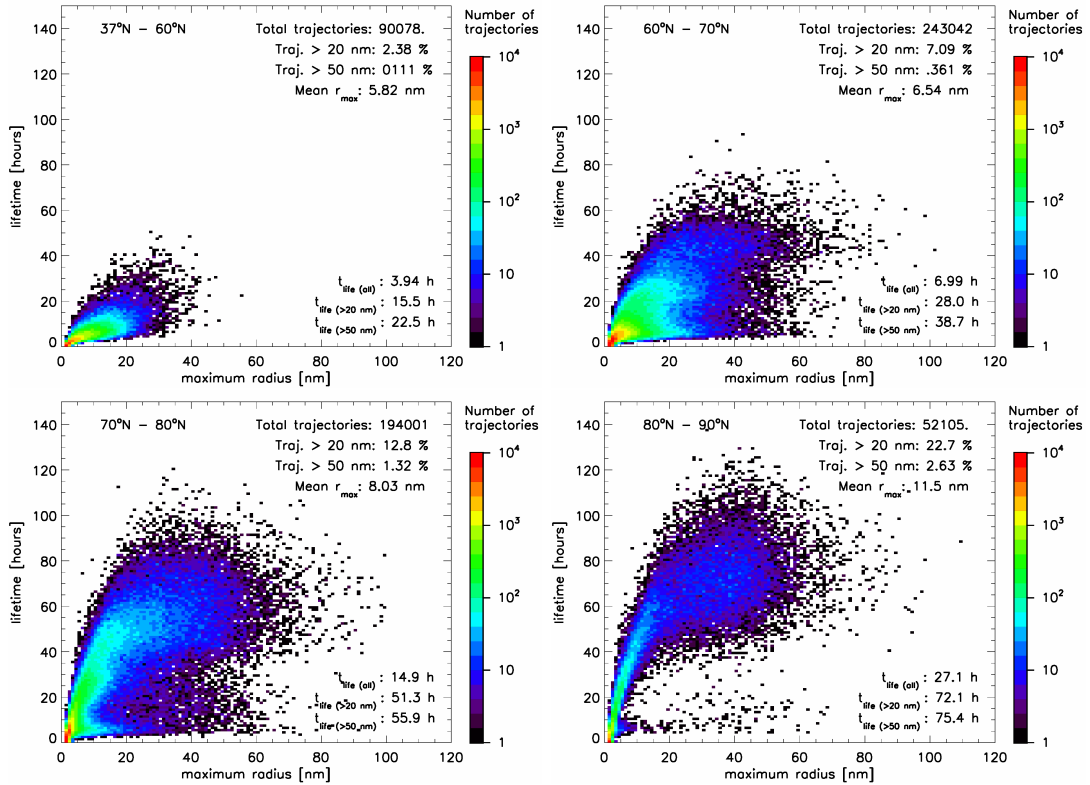


Figure 4.7 Ice particle lifetime and life cycle maximum radius of 10,000 condensation nuclei during July 2009, for 4 different latitude regions. Colors show the number of individual trajectories.

In Figure 4.7, particle lifetime t_{life} and maximum ice radius r_{\max} are extracted from those trajectories. r_{\max} is typically reached near the end of the life cycle. Since there is a strong latitudinal dependence of particle growth conditions, the analysis for these trajectories is split into 4 latitude regions. For each latitude band, the number of trajectories and the mean values of t_{life} and r_{\max} are computed. Since 20 nm is around the lidar detection limit and 50 nm is a typical size for visible NLC particles, frequency and mean lifetime of particles which exceed these thresholds are also calculated.

South of 60°N, not many ice particles form, and those are typically short lived. Only the few particles that reach 20 nm have somewhat longer lifetimes. From 60°N to 70°N, the number of formed ice particles is far larger. It is much more common for the particles forming here to reach 20 nm, and even 50 nm large particles occur frequently. At the two latitude bands closest to the pole, the mean peak radius is slightly higher because fewer particles stay very small in this region. 1 – 2% of all ice particles forming here grow to 50 nm during their lifetime. The size of large particles is about the same at the three higher latitude bands. In contrast to radius, the average lifetime rises rapidly compared to lower latitudes. Over 20% of all particles grow to 20 nm close to the pole, such particles may reach lifetimes of up to 5 days. North of 80°N, the distribution is distinctly lobe shaped: Few particles > 20 nm live for less

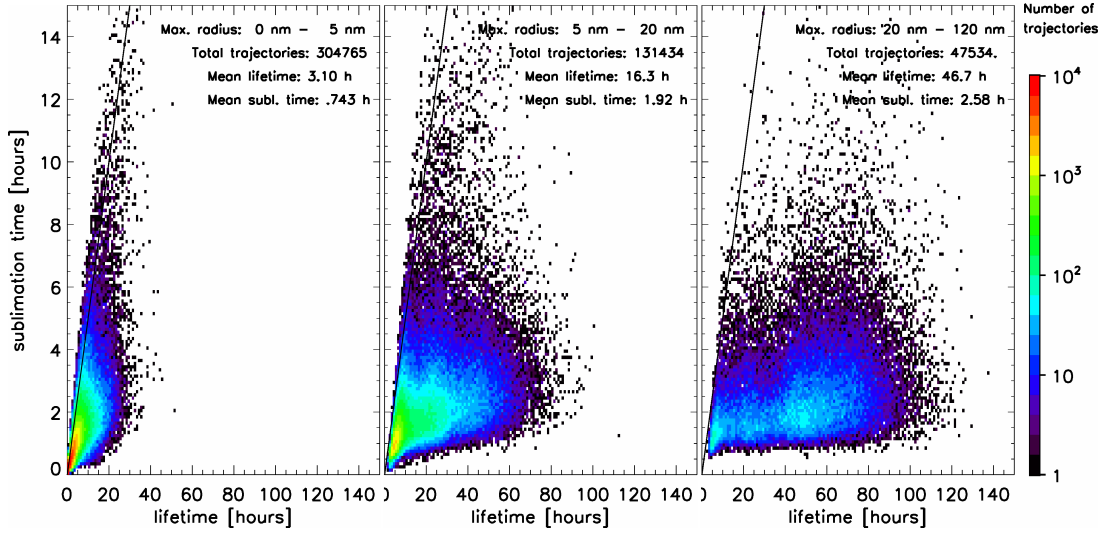


Figure 4.8 Particle total lifetime (t_{life}) versus sublimation time (t_{subl} , time after maximum radius), for 10,000 CN during July 2009 at all latitudes. Colors show the number of individual trajectories. The analysis is divided into 3 size classes based on the maximum lifetime radius. The black line shows $t_{\text{life}} = 2 \cdot t_{\text{subl}}$, i.e. particles for which growth and sublimation phases are equally long.

than 40 hours as discussed later in Section 5.4.1. Another notable feature present in all latitude bands is a lack of correlation between r_{max} and t_{life} when considering only particles > 20 nm. This indicates that the size eventually reached by a noctilucent cloud particle is not determined by its early history.

The same data set is now analyzed with regard to the timing of the radius peak. Sublimation time (t_{subl}) of ice particles is defined as the part of their life cycle after r_{max} is reached. Figure 4.8 shows the relationship of t_{life} to t_{subl} , i.e. the timing of the radius peak. This is not differentiated by latitude region, but rather by the maximum particle size. For particles < 5 nm (left panel), both lifetime and sublimation time are short. In most cases, peak radius occurs after more than half the lifetime. For particles with $5 \text{ nm} < r_{\text{max}} < 20$ nm (middle panel), it is rare that the largest size is reached before mid lifetime. Compared to the small particles, particle age rises much more than sublimation time. For $r_{\text{max}} > 20$ nm (right panel), t_{life} is far larger than t_{subl} . This means that the growth to visible size generally occurs right at the end of the life cycle. Also, there is little correlation between the two parameters. The sublimation time for a particle with $t_{\text{life}} = 20$ h is hardly different from that for a 80 h old particle. This is further discussed in Chapter 5.

While Figure 4.8 revealed that large particles reach their largest size close to the end of their life cycle, this does not specify how long they are detectable. For this purpose a relative threshold is used: Visibility time (t_{vis}) is defined as the time period when the backscatter coefficient at 532 nm is at least 10% of the value at the time when r_{max} is reached. t_{vis} is calculated for all particles, including particles with small r_{max} that might not be detectable by optical methods.

Figure 4.9 shows the dependence of t_{vis} on peak radius r_{max} (which determines

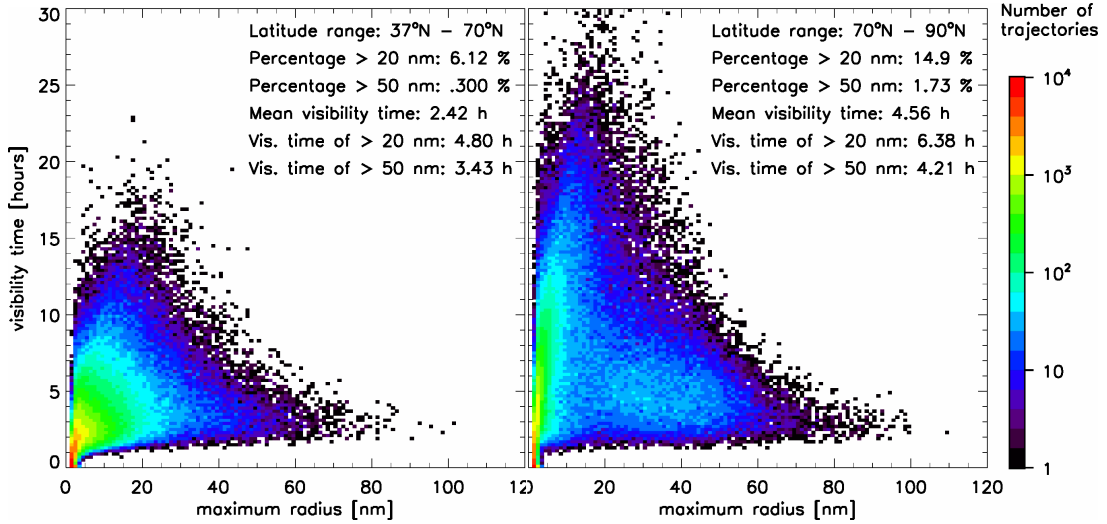


Figure 4.9 Ice particle visibility time, using the 10% of $\beta(r_{\max})$ threshold. t_{vis} (i.e. the width of the radius peak) is shown relative to r_{\max} at two latitude regions, south and north of 70°N.

peak brightness). For $r_{\max} < 20$ nm, t_{vis} has a significant spread and may exceed 20 h. However, this has little practical relevance since those particles do not become physically visible. Both mean t_{vis} and its variance become smaller with increasing particle size. The lower edge of the distribution is at ≈ 2 hours for all radii > 5 nm. At higher latitudes, visibility time is longer, but this difference diminishes for larger particles. Those particles with $r_{\max} > 50$ nm are visible for 2 – 7 h with typical values around 4 h. This growth characteristic is linked to dynamic waves, as discussed in more detail in Section 5.3.

Other statistics can be derived from this data (not shown in figures). The mean nucleation altitude z_{nucl} is higher closer to the pole, the average over all latitudes is 87.9 km. Like t_{life} , z_{nucl} is not correlated with r_{\max} . However, the altitudes of maximum radius and sublimation are closely linked, especially for particles with large r_{\max} : Sublimation typically occurs ≈ 1.0 km below the altitude of the peak radius. Since sublimation happens very quickly after particles reach r_{\max} , visible NLC characteristics are far more closely related to the sublimation process than nucleation processes influence NLC appearance. Larger particles also reach peak size at a lower altitude than smaller ones: The average z_{\max} is 86.4 km for all particles, 83.1 km for $r_{\max} > 20$ nm and 82.4 km for $r_{\max} > 50$ nm. Ice particles around the mesopause stay small because of the lack of water vapor, only those reaching altitudes with more H₂O may grow large.

4.3 Relationship of ambient conditions and ice clouds

There is a close relationship between noctilucent clouds and their ambient conditions, especially temperature (*Fiedler et al., 2011; Hervig and Gordley, 2010*). However, this relationship is not reproduced at small scales (*Lübken et al., 1996*). In this section,

4.3 Relationship of ambient conditions and ice clouds

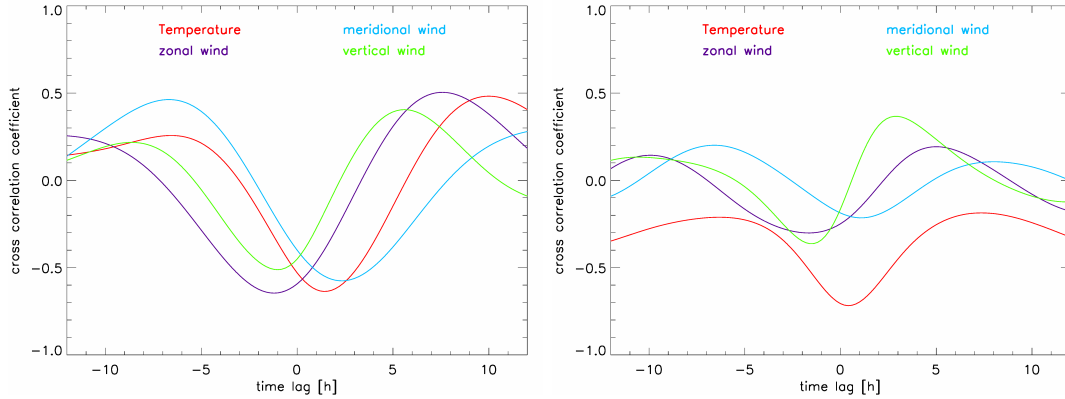


Figure 4.10 69°N zonal mean cross correlation between ambient parameters at 83 km and NLC brightness $\log(\beta_{\max})$. Positive time lag means the ambient parameter precedes the NLC. Left panel: LIM3 in 2009, right panel: KMCM₃₀.

the scale dependence and a possible phase relationship are examined. In addition, the feasibility of parametrizing NLC from their ambient conditions is discussed.

4.3.1 Correlation between ambient conditions and NLC

When analyzing the relationship of ice clouds to their environment, the first question is which parameters are most influential on NLC formation. Judging from the microphysics (Section 3.3), a temperature correlation is highly probable. Correlations with vertical and horizontal wind components are another possibility: Growth conditions have a strong spatial (especially vertical) dependence, so advection may affect particle formation as well. A correlation with water vapor is also likely, but this was left out of this analysis for two reasons: The H₂O depletion and deposition layers vary in altitude with the ice layer, which complicates finding a suitable proxy for the magnitude of local redistribution. Also, H₂O concentration is not a dynamic variable but a tracer like the NLC itself.

Figure 4.10 shows cross correlation functions of the NLC to dynamic variables, on LIMA and (discussed in Section 6.2) KMCM dynamics. The largest correlation of temperature and ice in MIMAS-LIMA (-0.63) occurs at a time shift of one and a half hours, reflecting the time required by temperature to affect NLC. There is also significant β -correlation to wind components: For vertical and meridional wind, it is less than for temperature, but for zonal wind the correlation peaks at -0.64 with maximum brightness around an hour ahead of maximum westward wind. However, large correlations with the wind components reflect the strong tidal components in both temperature and wind variability. This can be seen from the equivalent cross-correlation functions, applied to MIMAS-KMCM. Using KMCM, there is a strong correlation peak for temperature (-0.72), while for the horizontal wind components, correlation does not exceed -0.3 for any time lag. The correlation and parametrization analyses in the rest of this section thus focus on temperature as the ambient parameter most influential on ice formation.

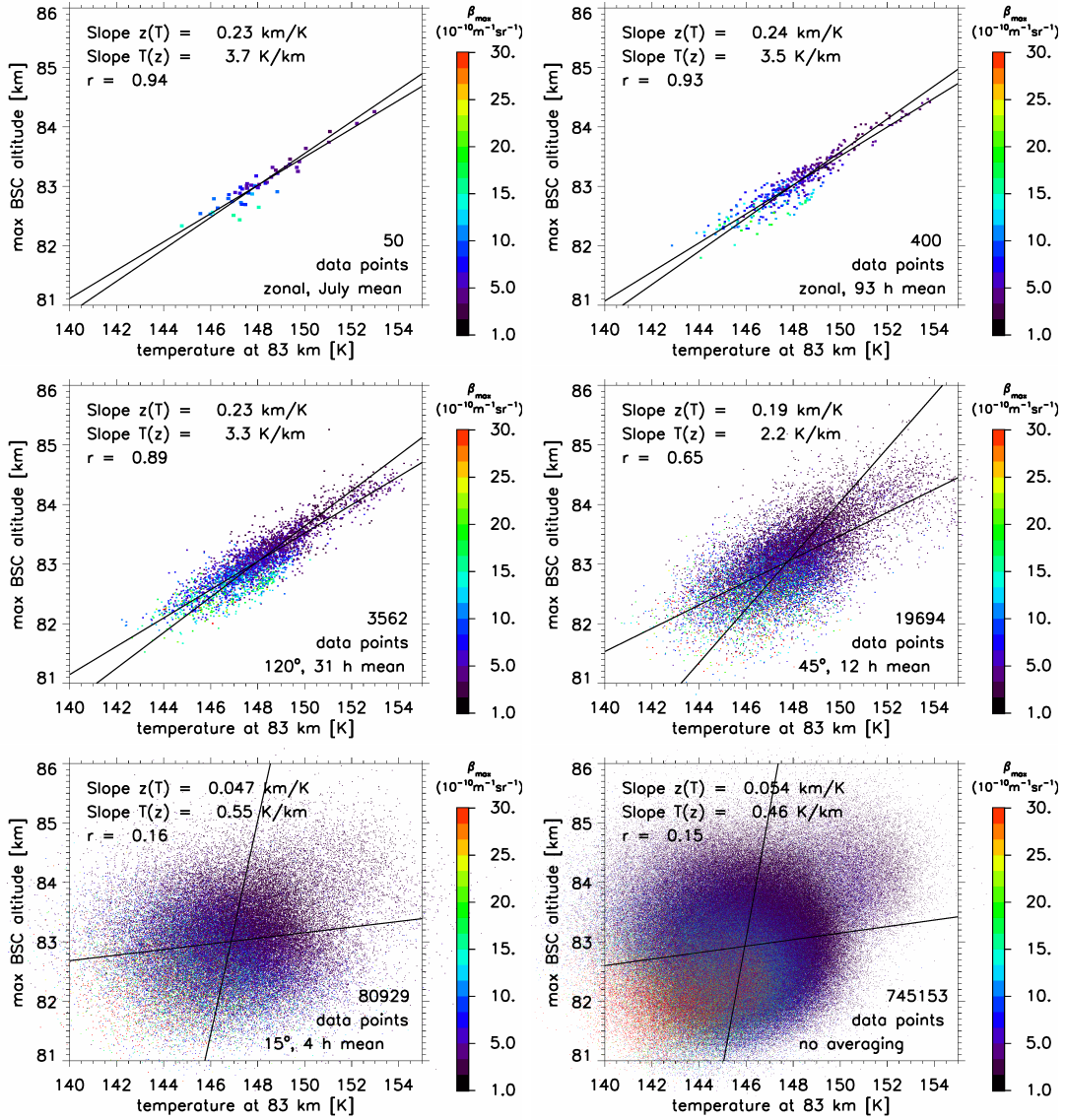


Figure 4.11 Relationship of mean NLC altitude, temperature at 83 km and NLC brightness at different scales, within July of years 1961-2010 at 69°N. At the intervals and length scales shown, an average temperature is calculated, as well as NLC centroid altitude and brightness when $\beta_{\max} > 1$. The averaged values for T_{83} , z_{\max} and β_{\max} are shown in a scatter diagram, with dot color indicating brightness. For T_{83} and z_{\max} , linear regression lines and correlation coefficient r are given. Data points with no NLC brighter than $\beta_{\max} = 1$ are omitted.

4.3.2 Scale dependence of temperature-NLC relationship

The relationship of the ice cloud to temperature has been examined before: Fig. 8 in *Lübken et al. (2009)* shows a close correlation ($r = 0.93$) between the mean centroid NLC altitude and the temperature at 83 km. They use seasonal mean values for

4.3 Relationship of ambient conditions and ice clouds

both NLC statistics and temperature, so it is not clear whether the relationship also applies at smaller scales. Figure 4.11 replicates their analysis, but gradually reduces the averaging scale. The top left panel shows monthly and zonal mean. It differs from the figure in *Lübken et al. (2009)* only because different model versions are used. The following panels have averaging time intervals of 93 hours, 31 h, 12 h, 4 h, and no average i.e. snapshots. The spatial averaging is also reduced, with spatial and temporal scale corresponding as $\Delta \mathbf{x} \approx u \cdot \Delta t$. The proportionality factor u is a typical horizontal wind speed of $40 \frac{\text{m}}{\text{s}}$.

The high correlation of z_{max} to T_{83} in *Lübken et al. (2009)* is reproduced in the top left panel, correlations with β_{max} are also apparent. The same applies for the 93 h averaging, in the top right panel, and for 31 h, r is only slightly reduced. However, at a time scale of 12 h the correlation drops significantly, and for averaging scales of 4 h and less the two parameters are no longer correlated.

Using different thresholds for NLC brightness does not affect this result significantly: When considering only strong NLC with $\beta_{\text{max}} > 13$, the sequence of correlation decreasing along with scale is unchanged, although coefficients are slightly lower at all scales. On the other hand, at 79°N the correlation coefficient without averaging is increased to $r = 0.5$. At 79° , there are less small scale temperature fluctuations (see Section 5.4). Unlike at 69°N , temperature changes between years are larger than those fluctuations, which results in some correlation even without averaging.

Why does temperature at 83 km strongly affect noctilucent clouds, but only when viewed at large scales and long time periods? While the ambient temperature is very important for NLC, its effect is not instantaneous. The transition between no correlation and a very strong one is around the time the particles need to form and become visible, between 4 and 31 hours. At scales smaller than this, there is little correlation because the ice cloud is still in the process of reacting to a temperature change. To find a relationship of NLC to their ambient that is still valid on small scales requires a more complex approach: Other ambient parameters must be used in addition to temperature, or the time lag between T and NLC included. These options will be explored in the rest of this section.

4.3.3 Relationship of temperature, ice mass, and particle radius

A number of attempts have been made to correlate NLC parameters and their ambient conditions. *Merkel et al. (2009)* use the Community Aerosol and Radiation Model of the Atmosphere (CARMA) to find a non-linear relationship between NLC ice water content (IWC), particle effective radius r_{eff} and ambient temperature. IWC is the mass density of ice, typical unit for NLC is $10^{-14} \frac{\text{g}}{\text{cm}^3}$. $r_{\text{eff}} = \frac{\sum r_i^3}{\sum r_i^2}$ is a weighted average of radius which is more sensitive to the larger particles that determine the NLC than to small ice particles.

The Eulerian CARMA model calculates IWC and r_{eff} from a discrete distribution of ice particle radius bins between 2 and 900 nm. *Merkel et al. (2009)* extracted these parameters along with temperature from a total of 75,000 sample volumes containing ice. They averaged over all values of r_{eff} found for combinations of temperature and IWC, shown in the top panels of Figure 4.12. As a parametrization for r_{eff} , they fit an exponential function $r_{\text{eff}} = p_1 \cdot \text{IWC}^{p_2} \cdot e^{p_3 \cdot T}$ to the distribution (a) in Figure 4.12.

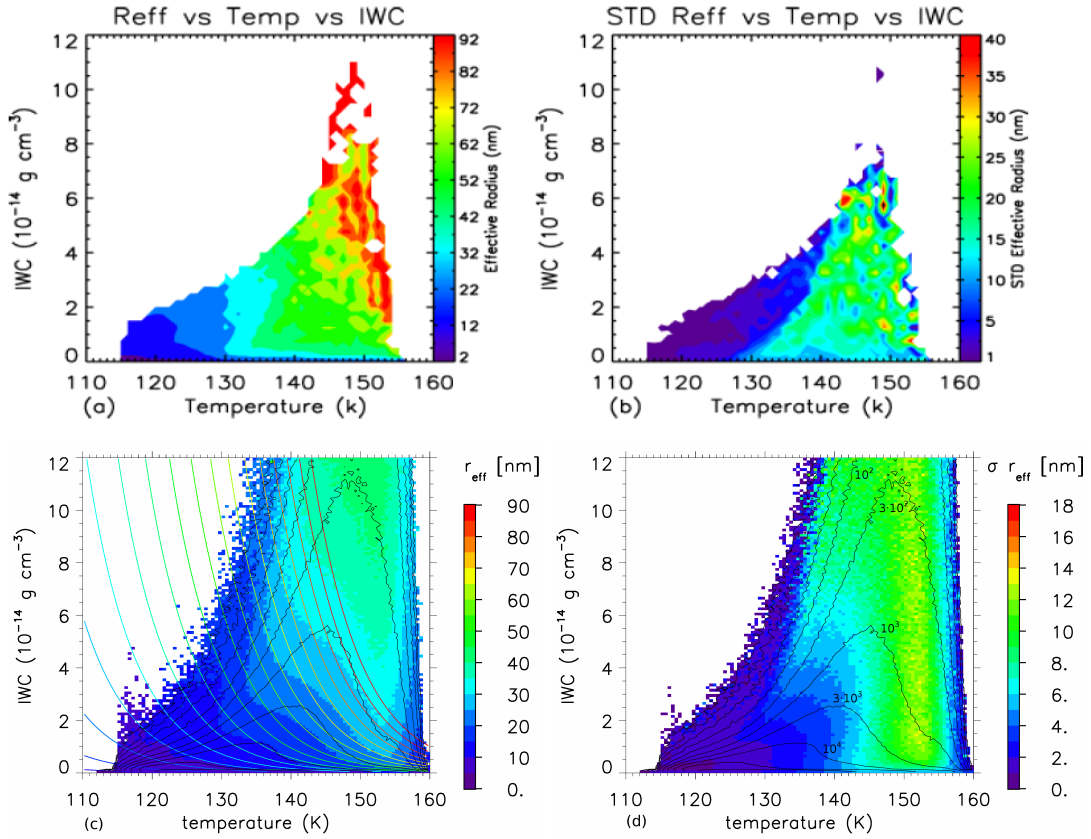


Figure 4.12 Relationship of ice particle effective radius (r_{eff}) to ice water content (IWC) and temperature. Left side panels show the mean, right side the standard deviation of r_{eff} at given combinations of IWC and T . The top panels are from Fig. 3 in *Merkel et al. (2009)* and show CARMA simulations on WACCM dynamic fields. Bottom panels are MIMAS-LIMA simulations over 72 h in July 2009. Colored contours in (c) show the parametrization (Eq. 2 and Fig. 4 in *Merkel et al. (2009)*) fitted to the CARMA simulation in (a). (a) and (c) use the same color scale while (b) and (d) do not. Black contours in the bottom panels (labeled in (d)) show the number of sample volumes per histogram bin.

This parametrization from CARMA is tested here with an analogous analysis using MIMAS-LIMA. IWC and r_{eff} are calculated on the complete model grid for 72 hours in July 2009. This yields a robust statistic of 25 million sample volumes that contain 2.2 billion individual ice particles, shown in the lower panels of Figure 4.12. The overall shape of the MIMAS-LIMA distribution is similar to CARMA, but there are a number of key differences: The temperature range where ice particles may exist is broader in MIMAS-LIMA. Also, much higher IWC values occur compared to CARMA (more than $60 \cdot 10^{-14} \frac{\text{g}}{\text{cm}^3}$, not shown in Figure 4.12 to make the axes compatible). However, this difference in parameter range can be attributed to the higher sampling in MIMAS-LIMA: The distribution (c) contains around 300 times as many sample volumes as its CARMA equivalent (a). The area in (c) where each histogram bin includes at least

4.3 Relationship of ambient conditions and ice clouds

300 sample volumes is very similar to the total area of (a). This implies that the larger parameter area in (c) is caused by more uncommon (T , IWC) combinations at the edges.

Next, the effective radius is compared within the parameter area also covered by CARMA. While the shape of r_{eff} in MIMAS-LIMA is very similar to CARMA, the values are much lower for MIMAS-LIMA. This is best visible by the r_{eff} fit from *Merkel et al. (2009)* which is included in (c). The parametrized effective radius exceeds 90 nm at 150 K and IWC around $6 \cdot 10^{-14} \frac{\text{g}}{\text{cm}^3}$. Such large particle sizes occur only rarely in MIMAS-LIMA, on average particles are much smaller even for high IWC conditions. The particle size in MIMAS-LIMA is validated by lidar measurements from ALOMAR (see Section 6.1.2). SOFIE measurements (Fig. 9 in *Merkel et al. (2009)*) also show lower maximum r_{eff} values than the parametrization. Contrary to the parametrization and not visible in (a), at temperatures above ≈ 153 K the effective radius decreases at constant IWC. This applies to the bottom edge of the NLC, where high equilibrium pressure (Section 3.3.2) ensures that ice particles are sublimating quickly. Under these circumstances, large ice water content only occurs when the particle number is uncommonly high, which corresponds to smaller particles. As with the mean r_{eff} , the radius standard deviation is lower in MIMAS-LIMA (d), especially for temperatures below 140 K. The spread relative to the mean value is largest for temperatures around 150 K and low ice volume, which is comparable to CARMA (b).

The generally low standard deviation supports the parametrization by *Merkel et al. (2009)*, with two caveats: Their fit coefficients produce too high effective radii at large IWC values, but this could be fixed by fitting to a different data set and does not contradict the approach. However, when applied in the lower sublimation region, this fit is not accurate with any coefficients. The reversal of the r_{eff} temperature dependence cannot be reproduced by it, limiting the use for that part of the NLC.

Another drawback of the parametrization in *Merkel et al. (2009)* is that it requires an ice parameter (IWC, i.e. ice mass) in addition to an ambient parameter (temperature) to get a second ice parameter (particle radius). For this reason it is not useable to predict the NLC from ambient conditions alone.

4.3.4 Parametrization of NLC brightness from ambient conditions

In the following, an attempt to parametrize the NLC directly from the ambient temperature is described. Section 4.3.2 showed that this requires averaging to some degree. The approach here is a heuristic parametrization $\beta_{\text{max}}(\check{T}, \Theta)$ that depends on a temperature proxy \check{T} and the latitude Θ . \check{T} is an average over the last 4 hours at 81-86 km altitude, which simulates the response time of the NLC to temperature as shown in Section 4.3.1. The latitude dependence in $\beta_{\text{max}}(\check{T}, \Theta)$ accounts for dependencies in winds, water vapor and wave activity on the distance from the pole. $\beta_{\text{max}}(\check{T}, \Theta)$ is derived by averaging over the NLC brightness at specific latitude and proxy temperature, over a whole season of MIMAS-LIMA simulations (June 1 to August 9). Thus, it is a measure for the typical NLC at a certain latitude and temperature.

$\beta_{\text{max}}(\check{T}, \Theta)$ is shown in the left panel of Figure 4.13. By definition, $\beta_{\text{max}}(\check{T}, \Theta)$ is defined only for the range of \check{T} which occurs in LIMA. Two basic relationships are visible: $\beta_{\text{max}}(\check{T}, \Theta)$ increases with decreasing temperature, and with increasing latitude

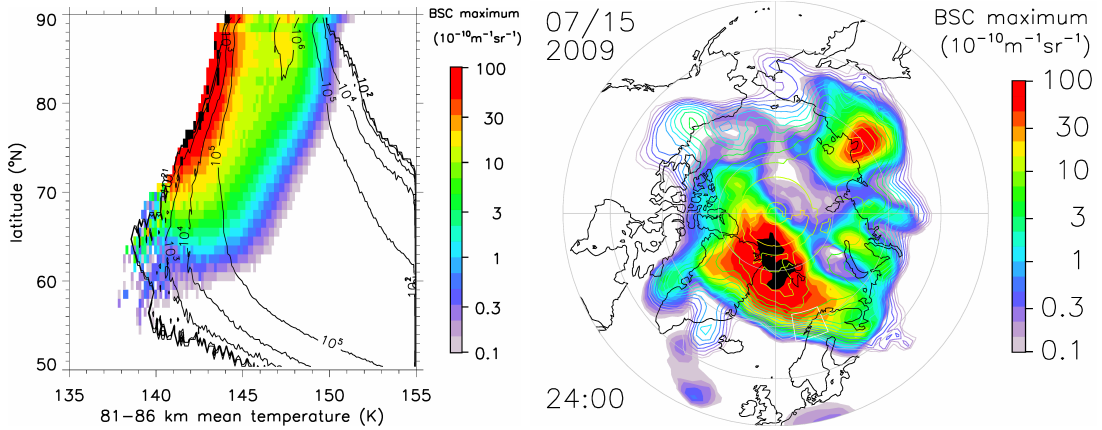


Figure 4.13 Left panel: Heuristic parametrization of NLC brightness (β_{\max}) from temperature proxy \check{T} and latitude. Colors show $\beta_{\max}(\check{T}, \Theta)$, black contour lines the number of model grid volumes with specific values of \check{T} . Right panel: Snapshot of parametrized NLC (contour lines) and modeled NLC (contours).

as discussed in Section 4.1.4. At low temperatures, $\beta_{\max}(\check{T}, \Theta)$ is less useful as those values of \check{T} are increasingly rare.

The accuracy of $\beta_{\max}(\check{T}, \Theta)$ is tested in the right panel of Figure 4.13: At the arbitrary time 24:00 UT on July 15, 2009, the temperature proxy \check{T} is calculated for the entire model domain. From \check{T} , $\beta_{\max}(\check{T}, \Theta)$ is derived in turn and compared to the modeled ice cloud. The parametrized cloud in Figure 4.13 shares only some features with the model ice cloud: At high latitudes $>70^\circ\text{N}$, it lacks both the very bright NLC regions and the void regions, i.e. the parametrized ice cloud looks like a smoothed version of MIMAS-LIMA. At the edge of the NLC region at $60 - 69^\circ\text{N}$, the parametrization roughly parallels the modeled NLC except for a number of protrusions in $\beta_{\max}(\check{T}, \Theta)$ at 180°E , 35°W and 130°W . These do not correlate with the model NLC, similarly the isolated NLC south of 60°N are not matched by the parametrization.

In conclusion, the parametrization does not replicate all features of the modeled ice cloud correctly. The time and altitude averaging windows for \check{T} have also been modified: Both a wider height window of 80-90 km, and a longer time average decrease the correlation between parametrized and modeled NLC. Since $\beta_{\max}(\check{T}, \Theta)$ already includes nonlinear dependencies and latitudinal differences implicitly, an explicit fit function $\beta_{\max}(\check{T})$ like in Section 4.3.3 would also only worsen the correlation. This confirms what Section 4.3.2 suggested: A parametrization of NLC that depends only on temperature cannot accurately describe the ice cloud on scales below ≈ 1500 km and time periods shorter than ≈ 12 h.

This leaves the possibility of including other ambient parameters than temperature. Section 4.3.1 showed that wind components at best have similar correlations to the NLC as temperature, which makes their usefulness for predicting ice clouds questionable. Water vapor or parameters derived from it like saturation ratio or frost point temperature may improve the correlation with NLC, this approach was pursued by *Hervig et al.* (2009b). However, H_2O -related parameters are not available from purely dynamic modeling but require a chemistry model.

5 Ice particle evolution in strong NLC

The central part of this thesis is an analysis of the origin and evolution of strong noctilucent clouds in MIMAS-LIMA. A detailed understanding of NLC growth processes helps linking ice cloud occurrence to background conditions, e.g. temperature and water vapor concentration (see also Section 4.3). Some of the following results are published in *Kiliani et al. (2013)*.

5.1 Description of statistical analysis procedure

5.1.1 NLC event selection

The approach of this chapter is a case study from July 2009, a year with high occurrence of strong NLC. The analysis is conducted at three locations at different latitudes, where measurements are available for validation. At each location, 50 strong ice cloud occurrences are chosen, the statistical analysis then uses superimposed epochs. The focus is on ALOMAR (69°N, 16°E), which has extensive instrumental coverage of NLC and mesospheric dynamics. In addition, Ny-Ålesund on Spitsbergen (79°N, 12°E) was picked for its available lidar measurements (*Höffner and Lübken, 2007*). For noctilucent clouds south of 60°N, the ice cloud selection method is modified: Strong NLC at this latitude are so rare that meaningful statistics cannot be derived at a single location like Kühlungsborn (54°N) during a period of one month only. For that reason, NLC south of 60°N are studied irrespective of their longitude position.

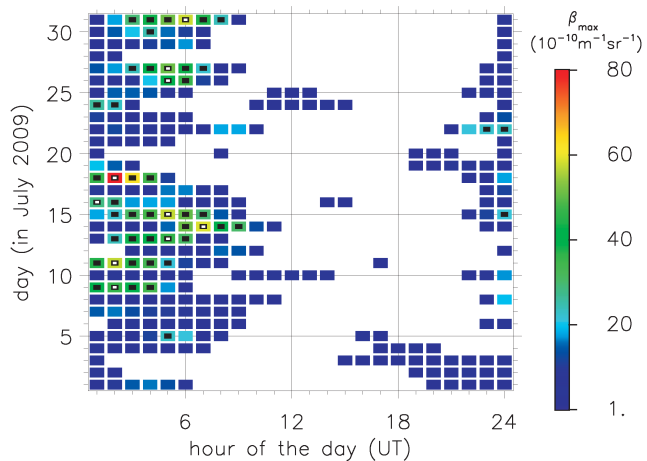


Figure 5.1 Column maximum backscatter coefficient β_{\max} ($\lambda = 532$ nm) at ALOMAR in July 2009. Average β_{\max} above 1 is shown as NLC. 50 time indices with the strongest NLC ($\beta_{\max} > 21.5 \cdot 10^{-10} \text{m}^{-1} \text{sr}^{-1}$) are marked in black. These belong to 14 distinct NLC, for the brightest 10 of these the time of maximum brightness is marked in white (Figure taken from *Kiliani et al. (2013)*).

At each of the three locations, box-shaped sample volumes are defined, limited by longitude and latitude circles. The boxes are centered around ALOMAR and Ny-Ålesund, respectively, with horizontal areas of $\approx 300,000 \text{ km}^2$. An example for the box around ALOMAR is also shown in Figure 4.1. Usually only the brightest part of the ice cloud is found within the box, as in Figure 4.1. The specific boundaries are $67 - 72^\circ\text{N}$, $9 - 24^\circ\text{E}$ (ALOMAR) and $76 - 81^\circ\text{N}$, $0 - 24^\circ\text{E}$ (Spitsbergen). In the case of NLC south of 60°N , the longitude position of the sample volume varies. However, it is always a 15° wide longitudinal segment. The longitude of these segments is the position with the strongest NLC at a particular time.

For this analysis, MIMAS-LIMA NLC are sampled at a time interval of one hour, all within July 2009. To define NLC events, 50 points in time out of a total of $31 \cdot 24 = 744$ are picked at each position where the ice cloud is brightest. This is defined by the peak backscatter coefficient β_{max} at 532 nm, averaged over the three areas (boxes).

Figure 5.1 shows the model NLC around ALOMAR with a sampling interval of one hour. As discussed in Section 4.1.2, bright NLC usually occur in the early morning hours, consistent with *Fiedler et al.* (2011). Over a longer time period, the local time dependence is not as pronounced as in this sample period and agrees better with measurements which were deduced from a longer sampling period (*Lübken et al.*, 2013b). The typical NLC duration is several hours, as discussed in Section 4.1.3.

Selecting NLC events in this way gives the NLC a weight proportional to their duration. This procedure is consistent with the one used for lidar or radar observations (*Fiedler et al.*, 2009). All selected ice clouds are strong for their respective latitudinal position. As mean brightness generally decreases with distance from the pole, there is a large difference in β_{max} between the three latitudinal positions. The lower threshold for ice clouds included in the ensemble is $21.5 \cdot 10^{-10} \text{ m}^{-1} \text{ sr}^{-1}$ for ALOMAR, $47 \cdot 10^{-10} \text{ m}^{-1} \text{ sr}^{-1}$ for Spitsbergen and only $1.2 \cdot 10^{-10} \text{ m}^{-1} \text{ sr}^{-1}$ for latitudes south of 60°N .

5.1.2 Particle ensemble selection

It is not necessary to trace all ice particles in order to represent the visible part of the NLC. For technical reasons, a constant number of 40,000 (out of 40 million) model particles are selected in each ice cloud. Very small particles ($r < 10 \text{ nm}$) contribute

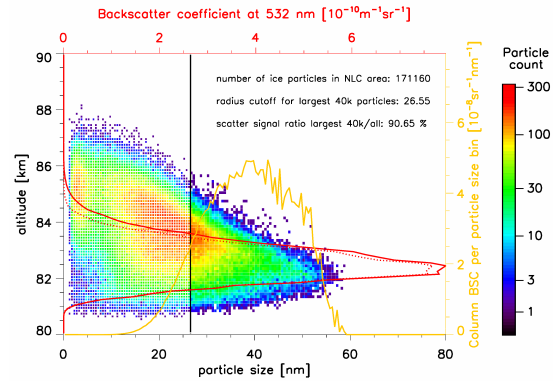


Figure 5.2 Ice particle size and altitude for a noctilucent cloud south of 60°N , on July 22, 7 UT, between 12°E and 27°E . Colored boxes show the number of particles per size/height bin. The largest 40,000 particles are shown as solid boxes, smaller particles are brightened. Red profiles show the volume BSC at 532 nm of all particles (solid line) and the largest 40,000 particles only (dotted line). The yellow profile is the column BSC separated by particle size.

5.1 Description of statistical analysis procedure

only a minuscule amount of scattering at optical wavelengths, since Mie scatter cross section of these is proportional to r^6 . Even when small ice particles far outnumber larger ones, most of the optical signal is generated by large particles. The 40,000 largest particles within the box-shaped NLC areas typically contribute around 99% of the total scatter signal.

The influence of particle size on scatter cross section is shown in Figure 5.2 for a NLC at latitude $<60^\circ\text{N}$. This case was deliberately chosen as a "worst case" because the selected 40,000 particles represent "only" 90% of the optical signal. For other cases the backscatter profiles of the 40,000 particle ensemble and the whole population cannot be distinguished from each other. Here, the selection procedure leads to a cutoff radius of 26.5 nm. Smaller particles still contribute almost 10% of the scatter signal. Those smaller than 10 nm have negligible optical brightness. The scatter profiles are extremely close at the bottom of the NLC and diverge only at the top of the ice layer, since most smaller particles are located above the NLC peak.

In most cases, the 40,000 particle ensemble is much more representative for the NLC compared to the example in Figure 5.2. The ratio $\frac{\beta_{40,000}}{\beta_{\text{total}}}$ is highest for the ice clouds at ALOMAR, with an average of 99.5%, followed by the events at Spitsbergen, with 98.7%. For the NLC at lower latitudes, the mean ratio is still 96.3%.

5.1.3 Trajectory analysis

After selecting which particles to trace, the final step is to compute the trajectories themselves. The timing of the individual NLC events, i.e. appearance at their destination like ALOMAR, is referred to as t_0 when discussing the development of the ice cloud. For instance, $t_0 - 24$ h means the state of ice particles which are going to form a noctilucent cloud within a sample volume 24 h later.

For all ice particles within an event, tracing starts at nucleation and stops when sublimation is complete. As these processes occur in turn many times during an NLC season for individual condensation nuclei, the time of nucleation must be defined more precisely: For the trajectory analysis, only the time period during which the particles are continuously coated with ice is used. For example, consider a dust nucleus which is coated by ice near the beginning of the traced period ($t_0 - 97$ h or earlier, see Appendix C.5). Assume it sublimates within a few hours and then forms a new icy particle before becoming large enough to be observed in the NLC event. In this case, only the time period from the second nucleation is considered.

Within the 40,000 particle ensemble for each of the NLC events, every ice particle has a different nucleation and sublimation time, and thus a different trajectory length. When calculating mean trajectories for NLC development, the number of particles being averaged changes in time, it grows whenever particles nucleate. The full number of 40,000 particles is typically reached a few hours before the NLC event (t_0). From that point on the number of particles diminishes quickly, since sublimation usually happens within only a few hours.

When calculating mean trajectories, each particle is also weighted with its brightness at t_0 , i.e. backscatter signal at $\lambda = 532$ nm. This gives the largest particles (≈ 80 nm at ALOMAR) far greater weight than particles around 20 nm, which makes the results representative for visible NLC particles. This process of signal-weighting

is called Large Particle Analysis (LPA) from now on. All mean values or trajectories are derived this way unless otherwise indicated. Giving equal weight to all of the 40,000 ensemble particles is called Small Particle Analysis (SPA). Unlike LPA, SPA results highly depend on the cutoff radius which is determined by the arbitrary choice of 40,000 particles per NLC event in addition to cloud brightness. At ALOMAR, the mean particle size by LPA is ≈ 60 nm, by SPA ≈ 30 nm (see Table 5.2).

To derive statistics on NLC formation (see Section 5.3), the individual ice particle trajectories from different events at the same location are overlaid. This is called a superimposed epoch analysis, t_0 of each individual event is used as point of reference. Time series with superimposed epochs describe not just single NLC events, but the average ice cloud development relative to t_0 . This allows finding characteristics in cloud formation which are common to all of the events. Superimposed epochs are also used to describe the mean state of NLC particles at particular times like nucleation, sublimation or crossing a predefined radius threshold.

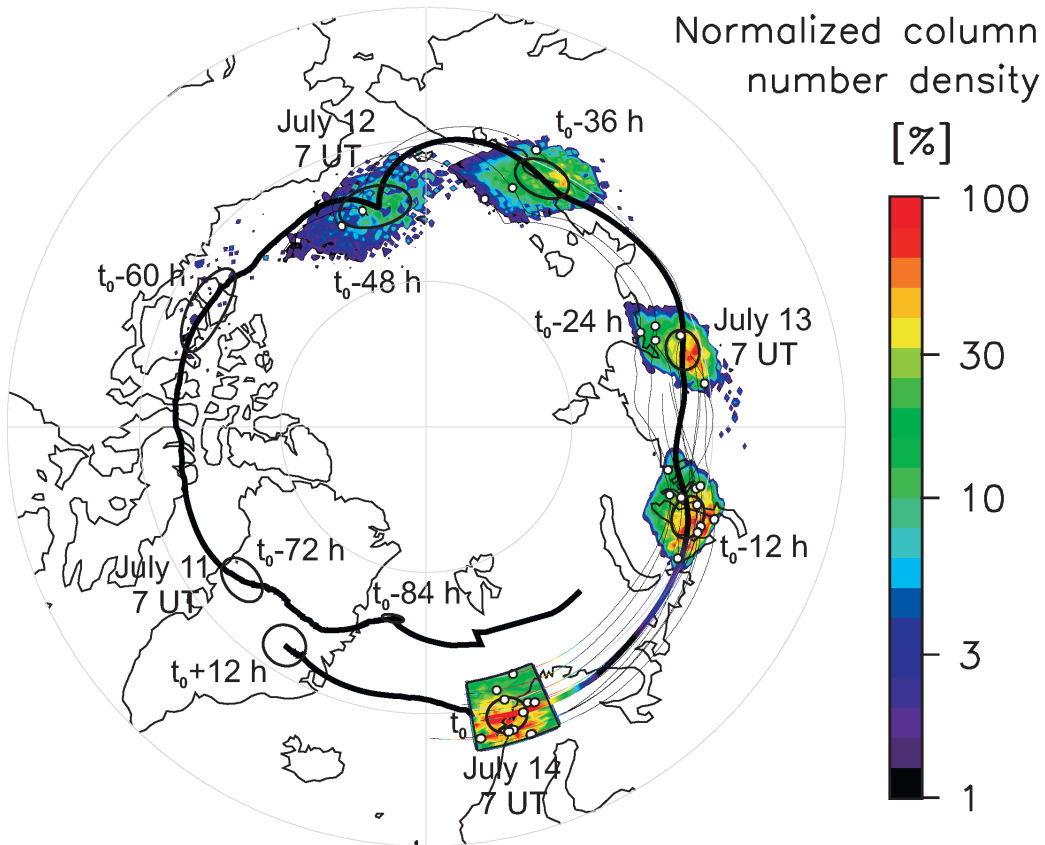


Figure 5.3 Horizontal transport of the particles forming a strong NLC around ALOMAR on July 14, 2009, 7 UT. The thick line is the mean trajectory, with the coloring indicating brightness in % of maximum. The thin lines are trajectories of 10 particles which become large at ALOMAR. Contours show the position of the ice cloud at 12 h intervals, while ellipses indicate mean and distribution width of the NLC position (from *Kiliani et al. (2013)*).

Appendix C.5 contains additional technical information on the trajectory analysis.

5.2 Case study: Evolution of a single NLC event at 69°N

In this section, the mechanisms of noctilucent cloud evolution are discussed for a single NLC event at ALOMAR on July 14, 2009, 7:00 UT. As shown in Figure 5.1, this event occurs at the brightness peak of a model NLC which lasts from 1 until 11 UT and is bright enough for NLC event selection ($\beta_{\max} > 21.5 \cdot 10^{-10} \text{m}^{-1} \text{sr}^{-1}$) from 6 to 9 UT.

5.2.1 Particle transport and growth

Figure 5.3 shows the development and horizontal transport of the sample NLC event. Ice particles are mainly transported westward, with a slight southward component. The meridional transport is not uniform in time, but includes an oscillation caused by atmospheric waves. The backtraced ice cloud is highly coherent for more than a day before t_0 , since spatial dispersion is caused by wind shear only. Vertical wind shear is especially important in this regard: The altitude range of the NLC is several kilometers (see Figure 5.4). Over this height range, wind speeds change significantly, as shown in Figure 2.1. Particles at different altitudes are exposed to different wind vectors, which causes the smearing at the edges of the cloud. On the other hand, horizontal wind shear (the zonal and meridional gradient of the wind vector) changes the shape of the selected part of the ice cloud, which is rectangular at t_0 .

The process of particle nucleation can also be estimated. Among those ice particles that become large ($> 50 \text{ nm}$) at ALOMAR, 10 were selected randomly and their trajectories included in Figure 5.3. These 10 particles are thus representative for the weighted Large Particle Analysis. None of them are older than $\approx 54 \text{ h}$. Also, the number density of the ice cloud at $t_0 - 60 \text{ h}$ is below the plotting threshold of 1% of maximum. This shows that almost all of the ice particles are less than 60 hours old at observation. The mean trajectory before $t_0 - 60 \text{ h}$ holds little physical significance, as very few particles contribute to the average.

Figure 5.4 shows the vertical transport and the nucleation process of the ice particles within the sample NLC. Since this is calculated by large particle analysis (LPA), the altitude distribution at t_0 is identical to the backscatter profile shown in Figure 4.1 of Section 4.1. Before $t_0 - 24 \text{ h}$, the particles are located higher up and cover a much wider altitude range of \approx

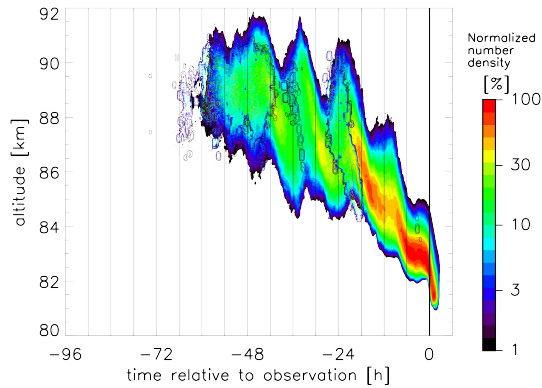


Figure 5.4 Altitude time series of a NLC at ALOMAR on July 14, 2009, 7 UT. Filled contours show the vertical distribution of NLC particles, normalized to the maximum occurring number density per altitude segment. Contour lines show time and altitude of particle nucleation, normalized to the maximum nucleation frequency per altitude bin.

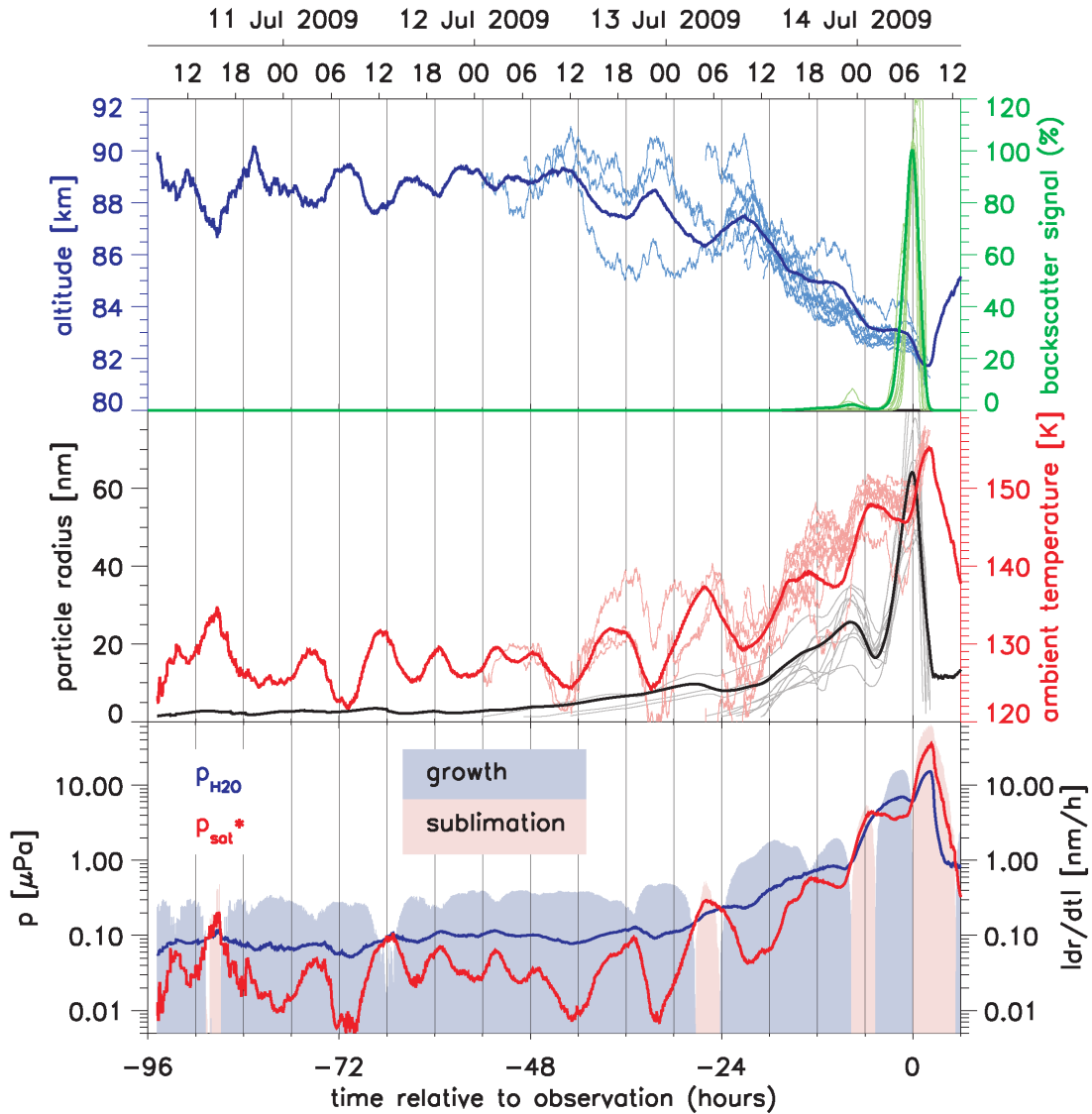


Figure 5.5 Development of ambient and microphysical parameters for the NLC at ALOMAR (July 14, 2009, 7 UT). Thick lines are NLC mean values, while thin lines show the same 10 individual ice particles as in Figure 5.3, starting from the point of nucleation. Upper and middle panel: Altitude, backscatter signal, ambient temperature and radius. Lower panel: Ambient H₂O partial pressure and equilibrium vapor pressure (lines, left scale), and growth/sublimation rate (shading, right scale) (from *Kiliani et al.* (2013)).

85 – 91 km. Figure 5.4 also shows that nucleation does not occur continuously, but in short bursts typically a few hours apart. Comparing newly nucleating particles to those already in existence at the same time, the altitude distributions roughly coincide at least for older particles. More detail on the nucleation process for MIMAS-LIMA NLC particles is given in Section 5.2.2.

5.2 Case study: Evolution of a single NLC event at 69°N

Figure 5.5 shows time series of those particle and ambient parameters most influential on ice particle evolution. For all parameters, the signal-weighted (LPA) mean time series is shown, along with the evolution of the same 10 individual particles as in Figure 5.3. The discussion of the robustness of the mean trajectory in Figure 5.3 equally applies to Figure 5.5.

The mean altitude trajectory in Figure 5.5 is the same as can be seen in Figure 5.4: Particles nucleate near the mesopause in an altitude centered around 88 km, but with significant spread. Both figures show an oscillation in mean altitude, which is caused by transport through atmospheric waves. The single trajectories in Figure 5.5 demonstrate that the vertical movement of individual particles is strongly influenced by diffusion. This turbulent motion is the main cause for the large variance in altitude and background conditions of particles within the NLC (*Berger and von Zahn, 2002*), see also Chapter 4.

Ice particle growth is slow but steady for early nucleating particles (usually $\frac{dr}{dt} \approx 0.3$ nm/h). Before $\approx t_0 - 24$ h, the background conditions influencing growth are quite stable, with ambient temperatures around 130 K. The steady growth is caused by the high saturation ratio at this stage of particle development. Less than a day before t_0 , particle growth accelerates. It also becomes less steady, there are intermittent periods of sublimation between growth phases. The main particle growth (20 to 60 nm) occurs from $\approx t_0 - 4$ h to t_0 , $\frac{dr}{dt}$ peaks around $t_0 - 2$ h at 15 nm/h. As particles grow larger, sedimentation accelerates, while turbulent diffusion diminishes with altitude (see Section 3.2.2). These effects are discussed in more detail in Section 5.3.2.

Around t_0 , ice particles start sublimating. Typically this process is very fast (peak $\frac{dr}{dt} = -60$ nm/h). At $t_0 + 2$ h, most particles have sublimated already, visible from the radius evolution of single particles (and in Figure 5.4). Like radius, scatter signal reaches its maximum around t_0 , however this peak is much narrower: β exceeds 1% of the value at t_0 only from $t_0 - 4$ h to $t_0 + 2$ h. The interval where it exceeds 50% of its maximum (FWHM) is only slightly longer than 2 hours, with 70 and 60 minutes for growth and sublimation, respectively. This implies that ambient conditions, especially temperature, strongly affect the brightness of noctilucent clouds on short time scales of only 2-4 hours, which is consistent to the cross correlation found in Section 4.3.1.

The influence of background variability on particle growth merits closer scrutiny. The time series for temperature and equilibrium vapor pressure p_{sat} in Figure 5.5 include oscillations: Their amplitudes are up to 10 K and a factor of 20, respectively, with periods around 10 hours. These oscillations are caused by particle transport through atmospheric waves, see Section 2.3. They strongly influence particle development: Particle growth is fastest when ambient temperature reaches its minimum. This is best visible in the single trajectories: During supersaturated conditions, new particle nucleation typically occurs when saturation is rising due to falling temperature (see Section 5.2.2). Since the ensemble average is affected by nucleation of new particles, the mean radius does not always increase during supersaturated conditions. This can be seen e.g. at $t_0 - 23$ h, when the mean r stagnates even though all individual particles are growing at the time. The change in ensemble mean from particle nucleation is a limitation of this type of analysis that has to be considered for all NLC average time series.

The influence of changing temperatures on particle growth increases at lower alti-

	Early history	Main growth phase	Sublimation phase
Approx. timing	until $t_0 - 30$ h	$t_0 - 2$ h	$t_0 + 2$ h
$n_{\text{H}_2\text{O}}[\text{cm}^{-3}]$	$5.5 \cdot 10^7$	$3.3 \cdot 10^9$	$7 \cdot 10^9$
$p_{\text{H}_2\text{O}}[\mu\text{Pa}]$	0.08 – 0.12	6.7	15
$p_{\text{sat}}(r)[\mu\text{Pa}]$	0.01 – 0.1	3.6	31
$\Delta p^*[\mu\text{Pa}]$	≈ 0.06	3.1	-16
$\frac{dr}{dt}[\frac{\text{nm}}{\text{h}}]$	≈ 0.3	15	-60
$S^* = \frac{p_{\text{H}_2\text{O}}}{p_{\text{sat}}(r)}$	$\approx 1 - 10$	2	0.5

Table 5.1 Typical values for growth-related parameters in the history of NLC particles, including water molecule number density and partial pressure, equilibrium vapor pressure and growth rate. Values for early particle history are approximated.

tudes, namely around t_0 . Equation (3.10) shows that particle growth rate is determined by the difference of water vapor to equilibrium pressure $\Delta p^* := p_{\text{H}_2\text{O}} - p_{\text{sat}}(r)$, not the particle saturation ratio $S^* := \frac{p_{\text{H}_2\text{O}}}{p_{\text{sat}}(r)}$. Unlike the saturation pressure p_∞ , $p_{\text{sat}}(r)$ is not an intrinsic property of the ambient air since it depends on particle size in addition to ambient parameters (see Section 3.3.2).

Growth-related parameters are shown for different stages of particle evolution in Table 5.1. NLC particles can grow quickly only where the absolute concentration of water molecules is high, which is reflected in its partial pressure. These conditions are found during the main growth phase. Around t_0 , the saturation pressure curve grows too quickly for the increase in water vapor to compensate, and particles start sublimating.

The rapid growth and sublimation at the upper and lower edge of the NLC layer redistributes the mesospheric water vapor. This process ("freeze drying") affects the growth of subsequent ice clouds in turn (e.g. *Sugiyama, 1994; Turco et al., 1982*).

5.2.2 Nucleation process

Figure 5.6 shows the nucleation process for the sample NLC event. These parameters are calculated without signal weighting (SPA) since the focus here is on nucleation mechanisms. Life cycle statistics by LPA are given in Section 5.3.3. Like Figure 5.4, the upper panel of Figure 5.6 shows nucleation occurring in bursts of highly variable intensity. The typical time period separating these bursts is 10 hours, similar to periods seen in ambient temperature fluctuations. Between nucleation periods, very few new particles are forming. The cumulative particle number also shows the scarcity of particles older than 60 h, as discussed regarding Figure 5.5.

In order to specify the nucleation mechanisms, atmospheric properties around the ice particles are analyzed. This requires defining a particle's ambient conditions: Here, the model grid volume the individual particles are located in (see Section 3.1.2) is used. The lower panel of Figure 5.6 includes the ambient saturation ratio S and the average number density of ice particles in the traced volume n_{ice} . Since S does not include the Kelvin effect or infrared heating, it is much higher than the particle saturation ratio

5.2 Case study: Evolution of a single NLC event at 69°N

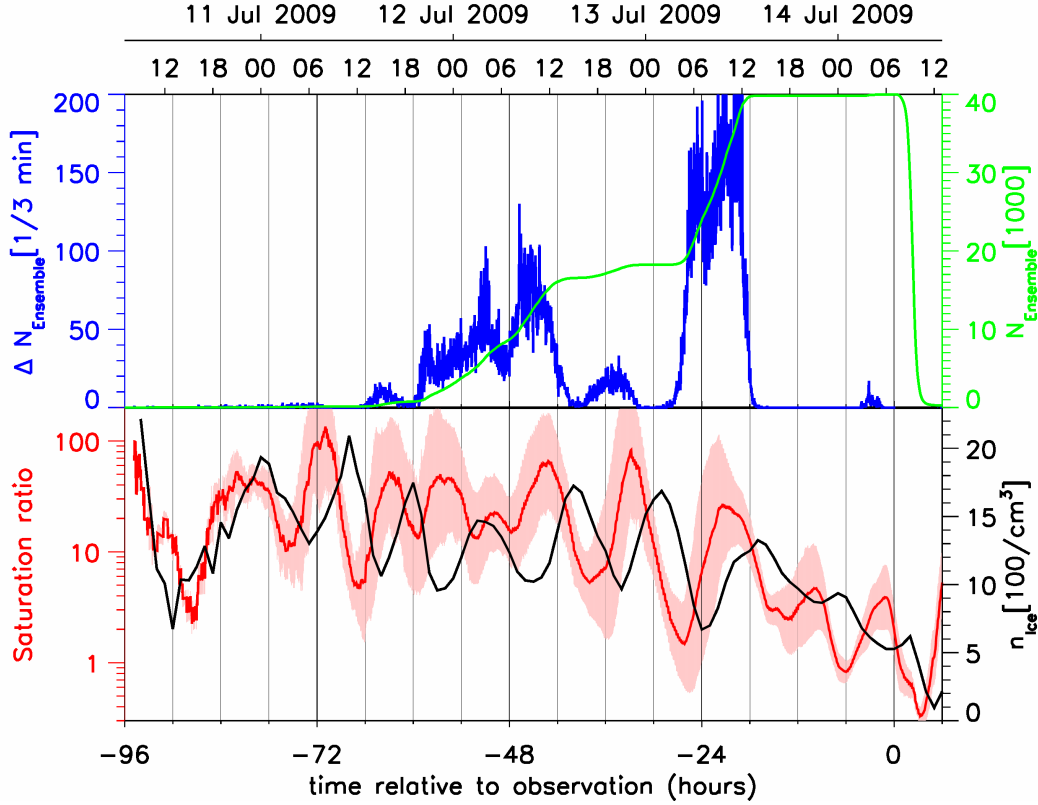


Figure 5.6 Nucleation process and related parameters for the NLC at ALOMAR on July 14, 7 UT. Upper panel: Rate of nucleation (blue) and total number of particles present (green). Lower panel: Ambient saturation ratio (averaged over $\log S$), with shading showing distribution width (red, left scale), and ice particle number density (black, right scale) (from *Kiliani et al.* (2013)).

S^* from Figure 5.5. S is better suited than S^* for Figure 5.6 because it is an intrinsic property of an air parcel. S^* or other particle dependent properties like Δp^* change with particle size, which makes them useful when analyzing particle growth but not suitable for studying nucleation effects.

By comparing upper and lower panels, it can be seen that most icy particles nucleate while supersaturation is rising. Available dust particles acquire an ice coating as soon as S exceeds their individual Kelvin barrier. Some nucleation takes place even while mean S is decreasing: Saturation is not uniform within the cloud, as shown by its large distribution width in the lower panel of Figure 5.6. Also, turbulent diffusion moves some particles into areas with higher saturation fast enough to counteract decreasing mean S . Finally, some dust particles are inserted directly into the supersaturated region by the relocation routine (Section 3.3.1).

There is a distinctive lack of particles older than 96 hours, i.e. $\Delta N \approx 0$ before $t_0 - 96$ h. To interpret this feature, n_{ice} as well as S have to be considered. The ice number density follows the oscillations in saturation ratio with a delay of ≈ 3 hours. That indicates a continuous process of nucleation and sublimation in the respective

Chapter 5 Ice particle evolution in strong NLC

altitude. Small ice particles have a risk of sublimating in each warm phase, which makes their condensation nuclei available for subsequent nucleation. To survive many such low saturation periods is increasingly unlikely, which explains the age limit. In the sample NLC, the oldest of the 40,000 particles is 95 h old at t_0 . Older particles occur for some other ice events at ALOMAR, but are very rare, thus $t_0 - 96$ h is used as the starting point for most time series in this chapter.

The backtracing approach within strong NLC in Chapter 5 does not provide an estimate for the ice particles' chance of growing to visible size: All included trajectories already fulfill this requirement. However, the general life cycle analysis in Section 4.2.2 uses forward trajectories: From Figure 4.7 it can be estimated that around 10% of newly nucleated ice particles at 69°N grow to 20 nm during their lifetime, and less than 1% reach a visible NLC particle size of 50 nm.

An additional characteristic seen in the upper panel in Figure 5.6 is the highly variable intensity of the nucleation bursts, by more than one order of magnitude in ΔN . The burst intensity is better correlated to the saturation ratio minimum of the warm phase preceding the burst than to the maximum S of the cold phase where the particles form. As particle sublimation during warm periods releases their dust nuclei for subsequent ice formation, this indicates that availability of dust particles is the major constraint determining burst intensity, not the supersaturation during the burst (see Section 5.3.3).

5.3 Statistics on NLC development at ALOMAR (69°N)

In this section, the ice particle life cycle including nucleation, growth, and transport is analyzed quantitatively. Statistics like particle age, visibility time, and nucleation conditions are analyzed by superimposed epoch analysis with the 50 event ensemble described in Section 5.1.

5.3.1 General ice particle transport and growth

The analysis is now extended to include all 50 NLC events at ALOMAR in July 2009, at the times indicated in Figure 5.1. Figure 5.7 shows the transport of this 50 event superposition compared to that of individual NLC events. These 10 events are picked at ALOMAR NLC brightness peaks, marked white in Figure 5.1. The individual cloud trajectories are quite similar to each other and the ensemble mean trajectory, as seen from their spread at 12 h intervals and the spatial extent of the superposition. Mesospheric winds in LIMA have low variability time scales ≥ 47 h, as shown in Figure 2.10, which causes parallel transport paths of different NLC. The superposition is mainly elongated in zonal direction, since the long period waves in zonal wind are considerably stronger than in meridional wind (see Appendix A.2).

The mean transport distance of a particle arriving at ALOMAR can be estimated using the NLC particle age at t_0 (see Section 5.3.3). This yields a value of 4500 km ($127^\circ \pm 57^\circ$ zonal, $4^\circ \pm 2^\circ$ meridional). However, the spread only accounts for variations in particle lifetime and not for inaccuracy in the circulation patterns. Section 2.2.1 demonstrated that LIMA overestimates zonal wind by up to 15 m/s and underestimates

5.3 Statistics on NLC development at ALOMAR (69°N)

southward transport by ≈ 6 m/s. Using the MIMAS-LIMA particle lifetime and radar mean winds yields an estimate for transport distance of 3000 km, including a southward transport component of 10° . The larger variability of measured winds also suggests a greater divergence of the transport paths. Another estimate for trajectory length is given in Appendix B.4, using KMCM dynamics.

Figure 5.8 shows the microphysical evolution of the 50 event ensemble at 69°N. To further investigate the main growth and sublimation phases, only the time period from $t_0 - 12$ h to $t_0 + 4$ h is included. A 50 event ensemble time series over the complete life cycle is added in Appendix B.9.

The ensemble evolution is similar to that of the single NLC in Figure 5.5, including the earlier particle history and vertical transport (see Figure B.12). At shorter time scales, there are differences: In the superposition, oscillations in altitude and ambient temperature are smoothed, while the peaks in radius and BSC around t_0 are widened by ≈ 1 h. Temperature fluctuations by ≈ 8 K peak-to-peak as in Figure 5.5 occur for all of the single NLC events in Figure 5.8, but their phase varies between NLC. The superposition only features large temperature variations in the main growth phase, a period of constant temperature around $t_0 - 3$ h and a temperature increase around t_0 : Since the NLC events are selected by brightness, any occurrence which consistently precedes strong NLC is also visible in the superposition. All individual NLC events include a period just before the main growth surge where S temporarily drops slightly below 1 and particles sublimate partially. However, the timing differs between events, from $t_0 - 11$ h to $t_0 - 5$ h. As a result, S does not fall below 2 in the superposition, and the individual sublimation periods appear as merely a phase of stagnating growth.

Figure 5.8 also shows the time when particle radius and NLC brightness reach their maximum for the different NLC events. The ensemble events were selected in Section 5.1.1 to be representative for any strong NLC at ALOMAR, and t_0 is defined as the event's observation time, not the time when individual particles reach their size peak. For an event selected while the NLC is still getting brighter (e.g. July 15, 2 UT, see Figure 5.1), the ice particles are still growing at t_0 . Thus, the time of the radius and β maximum depends on the individual event, it usually occurs between $t_0 - 1$ h and $t_0 + 1$ h. This causes the wider peak in the 50 event superposition. The BSC peak coincides with t_0 only for events selected when the NLC is strongest (like July 14, 7

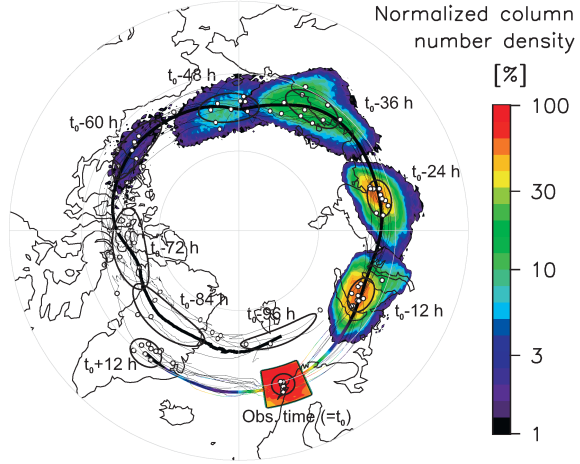


Figure 5.7 Mean transport path of the NLC ensemble towards ALOMAR during July 2009. Contours show particle column number density at 12 h intervals. The thick line is the ensemble mean trajectory, while thin lines are the paths of 10 individual NLC, as the thick line in Figure 5.3. Line coloring represents optical brightness. Ellipses show the ensemble mean position and distribution width at 12 hour intervals, white dots are individual NLC positions (from *Kiliani et al. (2013)*).

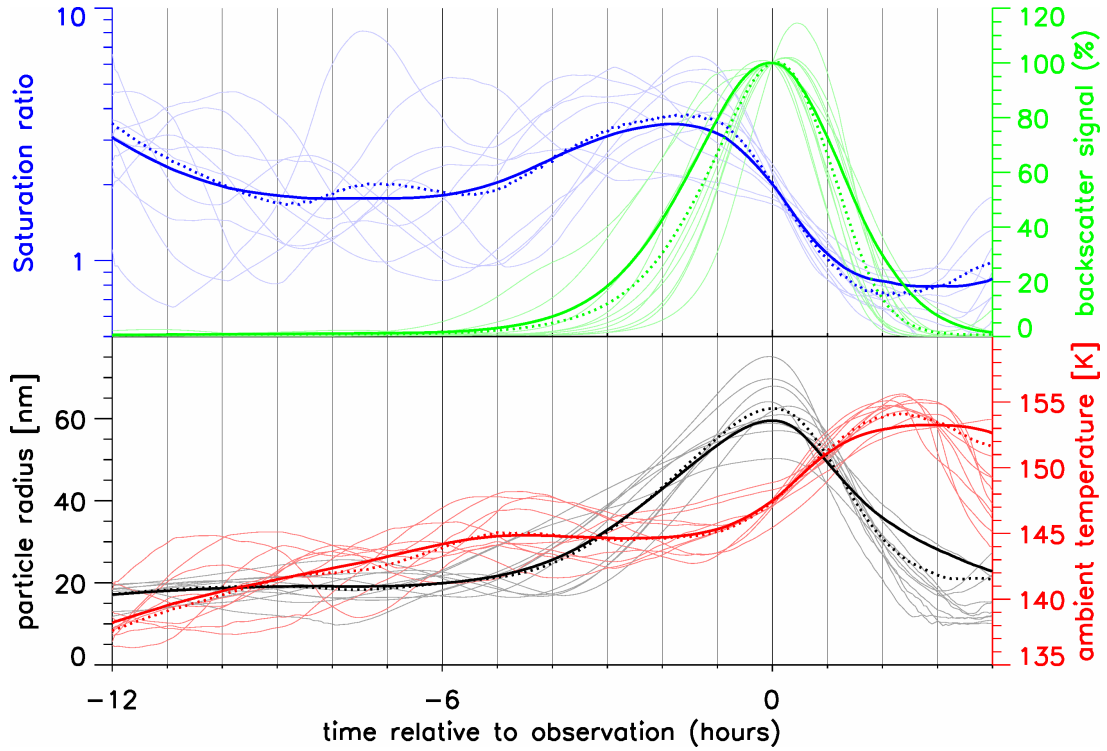


Figure 5.8 Growth-related parameters during the main growth and sublimation phases for the 50 event superposition. Thick lines show 50 event mean, thin lines are 10 individual NLC events as in Figure 5.7. Dotted lines show the ensemble mean of only 14 ice events at the peak brightness of their respective NLC. Upper panel: Ambient saturation ratio (S) and backscatter signal. Lower panel: Mean particle radius and temperature.

UT in Section 5.2). As a result, the superposition of 14 centroid NLC events in Figure 5.8 has more narrow radius and scatter peaks compared to the 50 event superposition.

5.3.2 Vertical motion of NLC

The NLC growth mechanisms are also strongly influenced by the components of vertical motion. These are shown in Figure 5.9, for $t_0 - 12$ h to $t_0 + 4$ h and for the complete life cycle. During the main growth period, particles experience upwelling, reaching 7 cm/s around $t_0 - 3$ h in the superposition and up to 14 cm/s for individual events. These upwellings cause adiabatic cooling of the ambient air. They also counteract sedimentation, keeping the ice particles longer in the H₂O rich altitude around 83 km. Exposure to the ideal growth conditions at this altitude for ≈ 4 hours lets the ice particles grow visible as part of a strong NLC. The particles reach their maximum size just after vertical wind changes to a downwelling, which is consistent with Figure 13 in *Rapp et al.* (2002). This downward wind becomes much stronger after observation and accelerates the sublimation after t_0 considerably. The lower panel of Figure 5.9 also shows some impact of vertical wind before the main growth phase, over time scales of

5.3 Statistics on NLC development at ALOMAR (69°N)

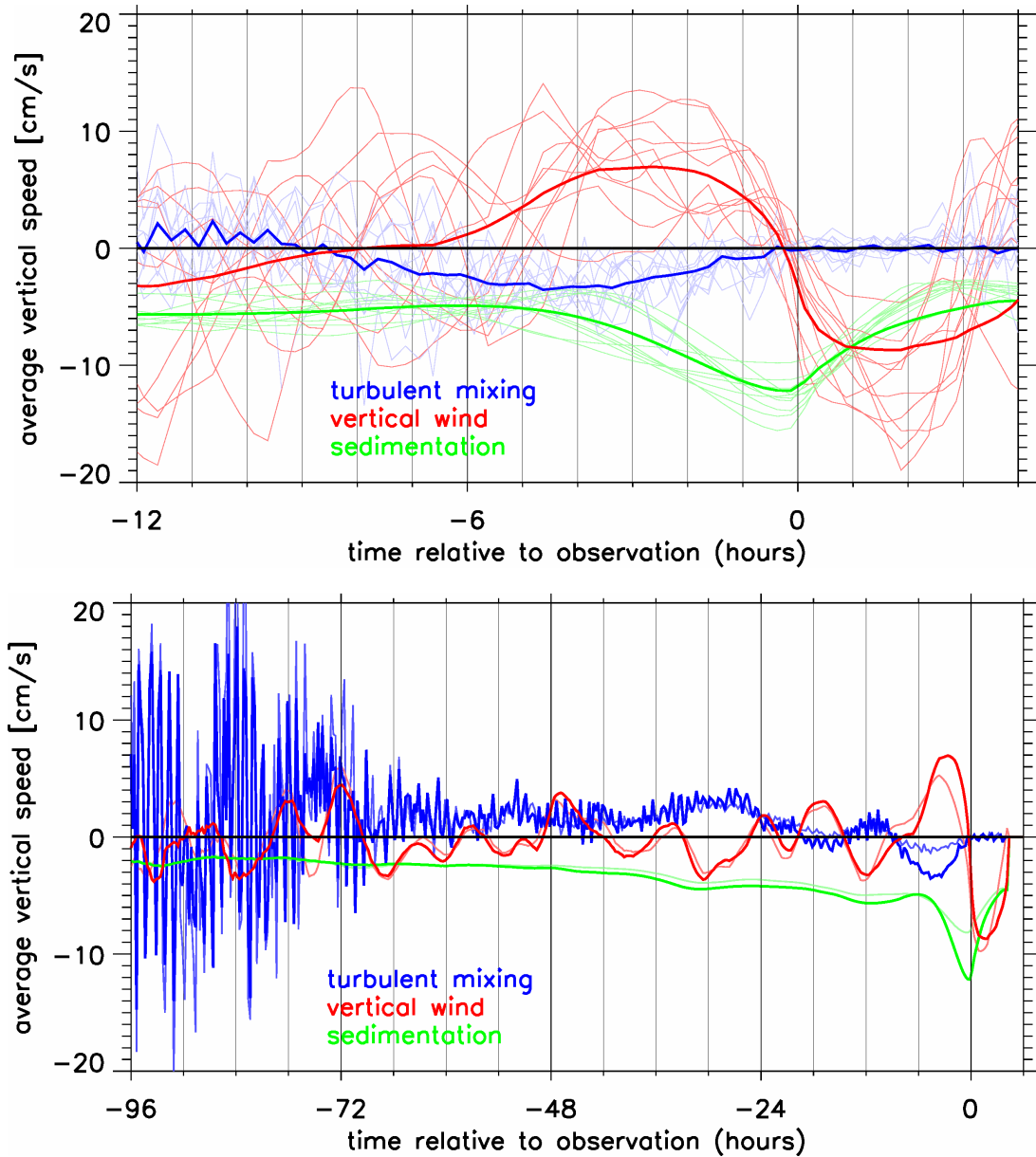


Figure 5.9 Mean vertical motion components from wind, sedimentation, and turbulent diffusion. Upper panel: Main particle growth and sublimation phase $t_0 - 12$ h to $t_0 + 4$ h, including the 50 event superposition and 10 individual events (LPA). Lower panel: Complete life cycle from $t_0 - 96$ h on. Only the 50 event mean is shown, both by LPA (thick lines) and unweighted (SPA, thin lines).

several hours. However, this averages out to nearly zero on longer time scales, since the average vertical wind is very slow compared to the wave amplitudes.

Turbulent diffusion also strongly influences the NLC development: MIMAS uses altitude-dependent vertical diffusion coefficients adapted from the sounding rocket climatology in *Lübken (1997)* (see Section 3.3.3). Turbulent velocities are several m/s

on time scales of a few seconds and still up to 1 m/s at the model resolution of 3 minutes. Turbulent motion is normally isotropic. However, Figure 5.9 shows that the ensemble mean vertical turbulent motion w_t in the NLC has a time-dependent, directed component:

During the main growth phase around $t_0 - 4$ h, the mean turbulent transport speed is up to -3.5 cm/s (downwards), using signal-weighting (LPA). However, the transport speed using SPA is much slower at ≈ -1 cm/s, seen in the lower panel. The reason for this difference is that turbulence can assist particle growth by moving ice particles to areas with better growth conditions. Particles lower in the growth zone are exposed to more water vapor and grow to larger size as a result. Thus, ice particles which are transported downward by turbulence during the main growth phase end up larger than other particles. The importance of turbulent downward transport during the main particle growth phase has also been stated recently by *Megner* (2011).

Before $\approx t_0 - 24$ h there is an upward directed turbulent motion component: Ice particles only survive near the mesopause for an extended period if sedimentation is counteracted to some degree. Since the role of vertical wind over time scales longer than the wave period is minimal, upward turbulent diffusion has to counteract sedimentation for particles to remain stable in altitude.

These directed turbulent motion components are counterintuitive, since mean w_t should converge to zero for a large number of particles because of its isotropy. This does in fact happen for a forward trajectory analysis like in Section 4.2.2. However, the analysis in Chapter 5 uses back trajectories: Growing to large NLC particles is an uncommon ($\approx 1\%$) fate for mesospheric ice particles, so the mean turbulent motion of ice particles that grow to visible size may deviate from the statistical mean.

Figure 5.10 shows how averaging time affects the relative contribution of the vertical transport components. Absolute values of single particle transport velocities are calculated for different time scales t_c . These are then averaged over the particle ensemble (by SPA), and temporally averaged from $t_0 - 72$ h to $t_0 - 24$ h.

Sedimentation rate is independent of the time scale since sedimentation is always directed downward. The vertical wind speed drops off rapidly as the time scale approaches half the typical wave period (10 – 12 h). The turbulent velocity shows the proportionality $w_t \propto \frac{1}{\sqrt{t_c}}$ which is expected for diffusion processes (see Section 3.3.3). At $t_c \geq 8$ h this proportionality is no longer exact because of the upward bias in early particle turbulent motion.

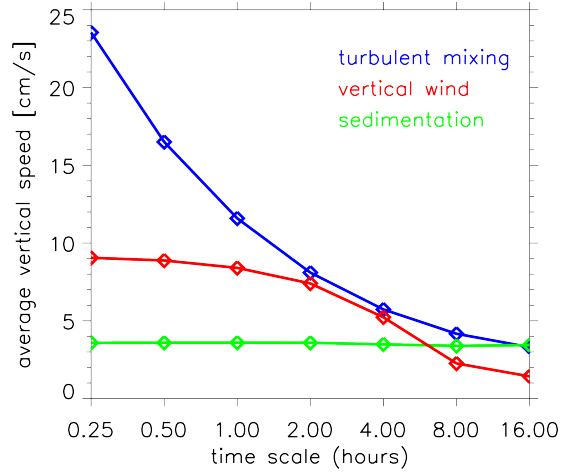


Figure 5.10 Vertical motion components (absolute values) of ice particles, between 3 and 1 days prior to t_0 and on time scales from 15 minutes to 16 hours.

5.3 Statistics on NLC development at ALOMAR (69°N)

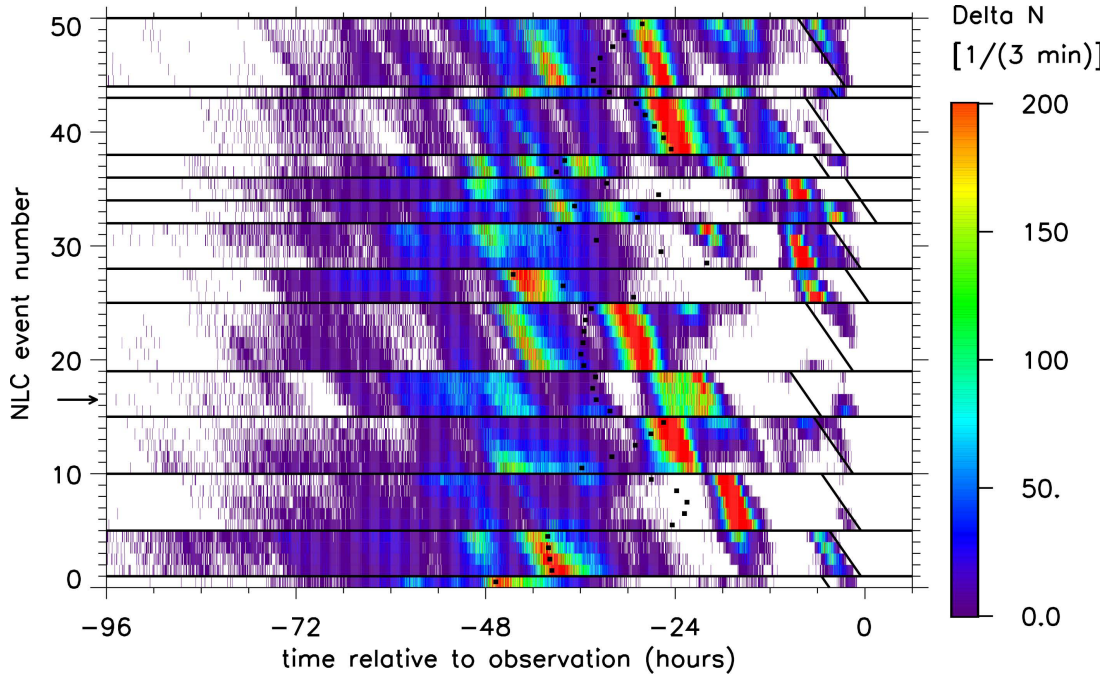


Figure 5.11 Nucleation rate for the 50 strong NLC events at ALOMAR. The events are sorted chronologically: Number 1 is July 5, 5 UT while number 50 is July 31, 8 UT (see Figure 5.1). The sample ice event on July 14, 7 UT is marked by an arrow (no. 17). Horizontal bars separate the 14 distinct NLC in July 2009 (see Figure 5.1). Black dots show mean particle age of the single event (by SPA), while slanted black lines around t_0 show midnight (UT) (from *Kiliani et al.* (2013)).

As seen earlier from the single particles in Figure 5.5, turbulent motion dominates for $t_c \leq 1$ h. Mean vertical wind velocity on these time scales exceeds 8 cm/s, more than twice the typical sedimentation speed. At 2–4 hours, turbulent and vertical wind velocities are similar and still greater than sedimentation rate. At longer time scales, sedimentation gradually becomes the dominant process, although turbulent velocity is still comparable for $t_c = 16$ h.

The vertical motion components in Figure 5.10 are representative mostly for small ice particles around 88 km. Within the NLC layer, the turbulent transport is smaller by a factor of 2–3, due to much lower K_{zz} values. Vertical transport within the NLC is mostly determined by sedimentation and wind. Appendix B.8 contains some more information about vertical transport over the particle lifetime.

5.3.3 Nucleation process of 50 NLC events

In Section 5.3.1, variations in the growth process between different NLC events are pointed out. Since such variations are also expected for the nucleation process, the nucleation rates of the 50 NLC events are analyzed in Figure 5.11. Unlike previous figures which showed only ensemble mean and some single NLC, Figure 5.11 includes all 50 events separately and groups them into the 14 different NLC from which they

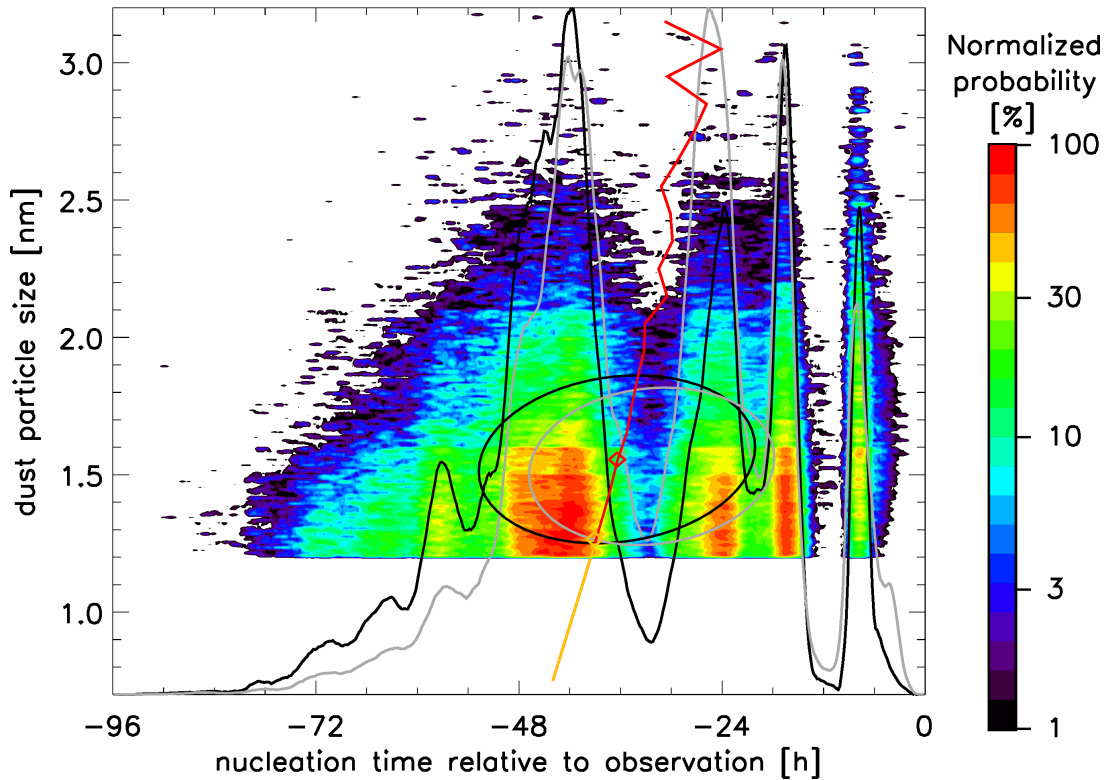


Figure 5.12 Distribution of the ice particles' age and the radius of the dust nucleus it formed around, with Large Particle Analysis (filled contours). Ellipses show the mean and standard deviation of this distribution with LPA (black) and SPA (grey). Solid lines show the particle age distribution, with LPA (black) and SPA (grey). The red line is the average age (LPA) of particles with specific dust nucleus size, while the orange line is its extrapolation for smaller dust nuclei.

were selected (see Section 5.1.1). This illustrates the relationship between the NLC at ALOMAR and the ice events. As in Section 5.2.2, Small Particle Analysis is used.

For the sample ice event (arrow), the nucleation rate is identical to that in Figure 5.6. There are typically multiple nucleation bursts, the strongest occur between $t_0 - 36$ h and $t_0 - 12$ h. Ice events from the same NLC share their nucleation history. The timing of the bursts is shifted by the lag separating the events, this gives them a slanted appearance in Figure 5.11. As for the sample NLC, earlier bursts tend to be less pronounced. The age of the single NLC events is defined as the average time from nucleation to t_0 of 40,000 particles. This ranges from 18 h to 48 h and can vary by as much as 20 h even between events belonging to the same NLC, as the intensity of nucleation bursts can shift rapidly within NLC. In conclusion, NLC particle age is sensitive to even minor changes in ambient conditions.

In Figure 5.12, the nucleation statistics of the 50 events are combined, using both LPA and SPA. The average age of large particles at ALOMAR (LPA) is 36 h with a distribution width of 16 h, and 32 h (SPA). The SPA value is also derived by averaging over the individual NLC age in Figure 5.11. Late nucleating particles have less time

5.3 Statistics on NLC development at ALOMAR (69°N)

to grow to a large size and typically form at the top of the ice layer, as seen for the sample event in Figure 5.4. This causes the 4 h difference in particle age between LPA and SPA. Particle age is not normally distributed and periods of strong nucleation are clearly defined, at $t_0 - 24$ h, $t_0 - 17$ h and $t_0 - 8$ h. These can be traced to strong nucleation bursts in isolated NLC in Figure 5.11.

Figure 5.12 also includes the size of the dust nuclei the NLC particles form around. Condensation nuclei in MIMAS follow the logarithmic distribution from *Hunten et al.* (1980), see Section 3.3.1. Nuclei smaller than $r_{\text{cutoff}} = 1.2$ nm are not included. Since the dust radius strongly affects the nucleation barrier (see Section 3.3.2), the choice of r_{cutoff} potentially affects particle age and other life cycle statistics. Figure 5.12 shows that most ice particles form around smaller dust nuclei (mean radius 1.55 nm, calculated by LPA). However, small CN within NLC particles are still underrepresented within the model dust population. Small dust particles need higher S values for ice nucleation, so they need longer on average to encounter nucleation conditions. As a result, a smaller fraction of small dust sizes are coated with ice at any given time. Since this relationship is nearly linear, it can also be extrapolated linearly: When using a dust population with much lower r_{cutoff} , an adjusted mean nucleus radius in NLC particles of 1.25 nm is predicted.

To also predict the effect of smaller r_{cutoff} on particle age, finding a relationship between dust nucleus size and particle age is required. The timing of the nucleation bursts in Figure 5.12 does not appear to depend on dust size, since the bursts result from ambient conditions. However, late nucleation surges have a higher proportion of large nuclei compared to early ones, since late nucleation occurs at lower saturation conditions (see Section 5.6). Also, the age limit of particles within a dust size class decreases by ≈ 2.5 h per 0.1 nm increase in nucleus size: Ice particles with small nuclei reach a high particle age more often, since the initial growth to 5 nm takes longer and the risk of complete sublimation in warm phases is smaller. These effects result in a clear dependence (red line in Figure 5.12): At small dust size, the mean particle age decreases by ≈ 1 hour for 0.1 nm larger nuclei. This fit is extrapolated to smaller size dust particles (orange line).

This dust size parametrization of particle age is now used on the predicted NLC nucleus distribution. In a simulation with r_{cutoff} reduced to 0.7 nm, a mean particle age of 39.1 h is predicted. Even though a large number of additional ice particles would be coating nuclei below 1.2 nm, the estimated change to particle age is less than 10%. Since the analysis here is during mid season of a year with strong NLC, the effects of the dust population cutoff are usually smaller than in this case study. From this idealized extrapolation, it seems unlikely that a more realistic condensation nucleus distribution would strongly affect particle age.

There are several additional parameters of particle nucleation, discussed in Appendix B.7. To summarize, particle nucleation occurs at an average altitude of 87.8 km and a mean temperature of 130 K. Nucleation at low altitude takes place at higher temperature, and also primarily for the late nucleating particles. The sensitivity of particle life cycle to r_{cutoff} also affects these other nucleation related parameters to some extent (see Appendix B.7). On the other hand, correlation coefficients between parameters relating to visible NLC and the particles' dust nucleus size are typically less than 0.1. This means that r_{cutoff} only affects the early particle history, but not

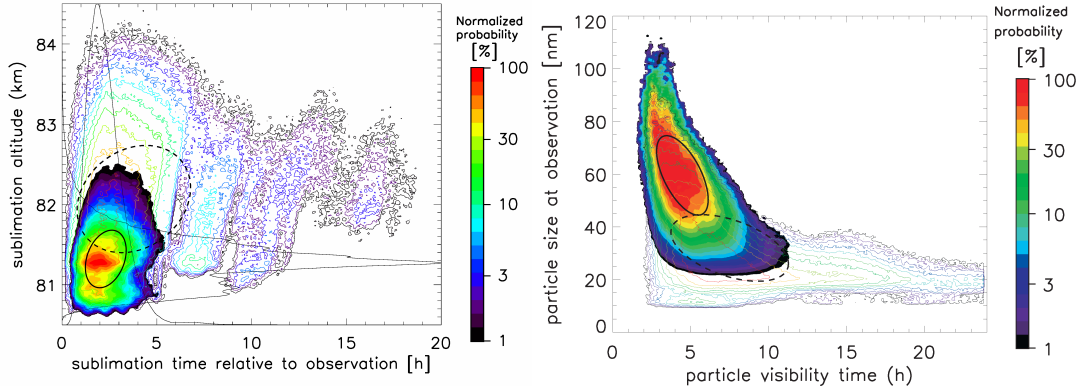


Figure 5.13 Left panel: Time and altitude of ice particle sublimation after t_0 , right panel: Particle visibility time and size at t_0 . Data set is 50 event ensemble at 69°N . Filled contours show signal-weighted distributions (LPA), contour lines the SPA distribution. Mean, distribution width, and covariance of the LPA (SPA) distribution are indicated by the solid (dashed) ellipses.

statistics such as particle size at t_0 , NLC altitude or visibility period.

5.3.4 Sublimation, visibility time and other parameters

Characteristics of later particle evolution are derived by the same approach as those related to nucleation. The left panel of Figure 5.13 shows the time and altitude of ice particle sublimation after t_0 at the lower edge of the NLC. The lifetime after observation (30 min to 5 h) is short compared to the particle lifetime, with an average of 2.3 h and a distribution width of 1.1 h. However, using SPA the range of sublimation times is much larger at 3.8 ± 3.1 h, with some particles lasting for 24 h past observation. Small particles are located higher up in the NLC, which allows many of them to survive the first warm period after t_0 and grow again in the following cold phase. They also sediment more slowly than large particles, so small particles reach the altitude of rapid sublimation later. This hardly affects the sublimation time though, as the delay in sublimation is compensated by the thinner ice coating.

In order to characterize the visible period of NLC particles around t_0 , a threshold based on the scatter brightness at observation is used, similar to Section 4.2.2. Particle visibility time is defined as the time interval around t_0 where an ice particle's BSC exceeds 10% of its value at t_0 . The visibility time is shown in the right panel of Figure 5.13, together with size at t_0 . The mean visibility time using LPA is 4.5 ± 1.7 h, the value for SPA is higher with 7.7 h. Limiting the analysis to very large particles ($r > 80$ nm) reduces visibility time to ≈ 3 h. As in Figure 4.9, particle size and visibility time are anticorrelated. Large particles sediment more rapidly than smaller ones, which removes them from the supersaturated region and limits the time a large size can be maintained. The relative threshold is another factor causing the anticorrelation: When an absolute (fixed) threshold of 20 nm is used instead, mean visibility time is 8 h. It is longest for particles around 55 nm and shorter for both larger and smaller particles. This confirms that the short t_{vis} of very large particles

5.3 Statistics on NLC development at ALOMAR (69°N)

Latitude band	< 60°N	67 – 72°N	76 – 81°N
Observation			
Radius [nm]	37.4 ± 8.6 (1.6)	59.5 ± 15.1 (2.2)	61.3 ± 16.1 (2.7)
Radius [†] [nm]	24.0 ± 8.4	31.9 ± 12.6	39.3 ± 11.9
Altitude [km]	83.1 ± 0.8 (0.11)	82.6 ± 0.6 (0.08)	82.9 ± 0.6 (0.09)
Temperature [K]	143.9 ± 3.8 (0.4)	147.5 ± 3.3 (0.3)	148.6 ± 3.6 (0.4)
$t_0 - 24$ h			
Radius [nm]	6.0 ± 3.5 (0.7)	8.2 ± 3.7 (0.7)	10.6 ± 3.3 (0.4)
Altitude [km]	87.5 ± 1.0 (0.3)	87.1 ± 1.3 (0.3)	86.5 ± 1.3 (0.14)
Temperature	132.0 ± 3.4 (0.9)	132.0 ± 5.1 (1.3)	132.5 ± 5.4 (0.9)
Nucleation			
Time [h]	-19.3 ± 8.3 (2.2)	-36.4 ± 16.4 (2.4)	-63.0 ± 15.0 (1.6)
Altitude [km]	87.0 ± 1.1 (0.2)	87.8 ± 1.6 (0.3)	89.4 ± 1.2 (0.07)
Temperature [K]	132.5 ± 3.0 (0.5)	130.0 ± 4.4 (0.5)	124.1 ± 3.6 (0.3)
Sublimation			
Time [h]	1.8 ± 0.9 (0.12)	2.3 ± 1.1 (0.2)	2.8 ± 1.3 (0.18)
Altitude [km]	81.6 ± 0.5 (0.11)	81.3 ± 0.4 (0.07)	81.6 ± 0.3 (0.07)
Temperature [K]	154.3 ± 1.9 (0.4)	156.3 ± 1.4 (0.15)	157.1 ± 1.4 (0.13)
Visibility time [h]	4.8 ± 1.5 (0.3)	4.5 ± 1.7 (0.4)	4.6 ± 2.0 (0.3)

Table 5.2 Ice particle evolution statistics from 50 NLC events each for three latitudinal bands. Given values are mean and distribution width, plus estimates for the statistical uncertainty of the average in parentheses. Unmarked values are calculated by LPA, while † indicates unweighted statistics (SPA).

is at least partially caused by faster growth and sedimentation. In conclusion, NLC particles are visible for $\approx 3 - 6$ hours, with larger particles visible for a shorter period.

Additional statistics linked to NLC formation at 69°N are summarized in Table 5.2. These include altitude, size, and temperature of NLC particles at observation, and 24 hours earlier, mostly analyzed by LPA. Nucleation and sublimation related data is also listed. Error estimates for these values (in parentheses) are derived from the spread of independent single NLC. For example, NLC observed at ALOMAR usually form at around 130 ± 5 K and sublimate at $\approx 156 \pm 2$ K, while at observation the ambient temperature averages 148 ± 3 K. This table also includes results for the other two latitude regions at 79°N and <60°N, which will be discussed in Section 5.4.

5.3.5 Comparison with COMMA/IAP and measurements

A similar study to this analysis and to *Kiliani et al. (2013)* used COMMA/IAP dynamics (*Berger and von Zahn, 2007*). This study differs from *Berger and von Zahn (2007)* and the NLC morphology in *Berger and von Zahn (2002)* in a number of ways, presumably caused by smoother background conditions and stronger mean upwelling

Chapter 5 Ice particle evolution in strong NLC

in COMMA/IAP. For instance, in COMMA/IAP growth is largely uniform, with no periods of partial sublimation between growth surges. Figures 19 and 25 in *Berger and von Zahn* (2002) also show that particle growth in the last several hours before observation is significantly slower in COMMA/IAP as compared to MIMAS-LIMA: The time period where particles have visible size is at least half a day in COMMA/IAP, whereas in MIMAS-LIMA it is only a few hours. In addition, particles in MIMAS-LIMA typically nucleate around the mesopause at 88 km, while in COMMA/IAP most nucleation takes place between 84 and 86 km. In conclusion, the typical ice particle evolution in MIMAS-LIMA is quite different to that in COMMA/IAP, even though some characteristics like mean particle age are comparable.

Most of the results in Chapter 5 are difficult to verify with observations since they describe properties of ice particle trajectories, not the morphology of the NLC. However, there are a few more observable properties in addition to those discussed in Section 4.1. The lidar statistic over one solar cycle shows a mean NLC altitude for strong NLC ($\beta_{\max} > 13 \cdot 10^{-10} \text{m}^{-1} \text{sr}^{-1}$) of 82.5 ± 0.9 km (*Fiedler et al.*, 2009). This is in good agreement to the (LPA) mean altitude of NLC particles in the ensemble (82.6 ± 0.6 km). Likewise, the altitude of particle sublimation (i.e., the height where the condensation nuclei are released after sublimation is complete) is compared to the lower boundary of NLC measured by lidar: The typical sublimation altitude of 81.3 ± 0.36 km in MIMAS-LIMA agrees well with NLC measurements. *Kaifler et al.* (2011) calculated a lower NLC edge of 82.1 km, however this figure includes both strong and weak NLC. Using just ALOMAR RMR-lidar data of strong NLC in 2009, the mean lower edge is 80.9 ± 0.9 km, which is in good agreement to this analysis (G. Baumgarten, private communication). Another property of the NLC that invites comparison with measurements is the ice particle size. However, this requires a more realistic modeling of particle shape, thus a separate analysis is conducted in Section 6.1.2.

5.4 Results from other latitudes

To investigate the latitudinal dependence of these results, analogous analyses for two additional latitude regions were conducted at Spitsbergen (79°N , 12°E) and south of 60°N . A synopsis of the similarities and differences is presented in this section.

5.4.1 Spitsbergen (79°N)

Figure 5.14 illustrates the nucleation process and the main features of particle growth of NLC at Spitsbergen (79°N , 12°E), additional information like vertical transport is shown in Figure B.13. The evolution of NLC particles at ALOMAR and at Spitsbergen is similar in many regards: Particles nucleate in the mesopause region (see Figure B.13), and initially grow slowly until they reach the upper edge of the NLC region. The main growth occurs ≈ 6 h before t_0 within a single phase of cold ambient conditions. Also shown in Figure B.13: The accelerating particle sedimentation during the main growth phase is counteracted by an upwelling. After the visible period, downward vertical wind is partly responsible for the rapid particle sublimation.

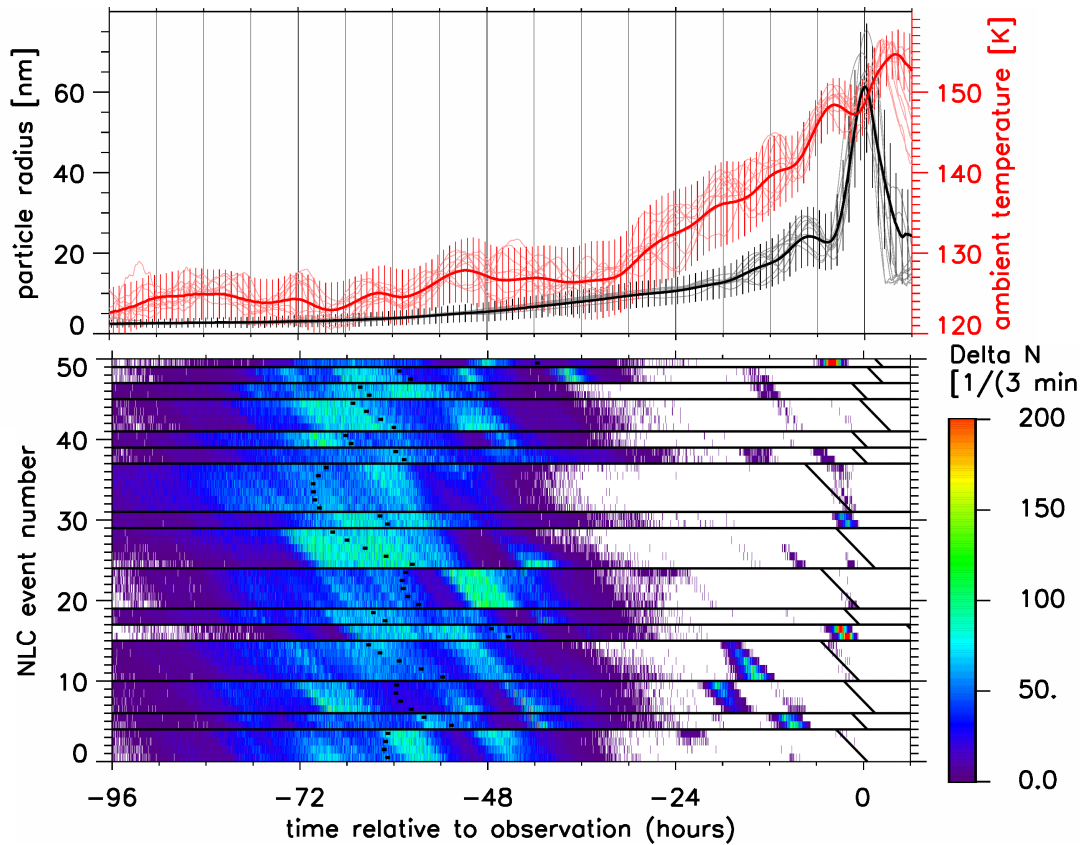


Figure 5.14 Upper panel: Ambient temperature and particle growth at Spitsbergen (79°N), analogous to Figure B.12. Thick lines show the ensemble mean (LPA) of 50 NLC events, thin lines the mean particle development for 10 individual ice events. Lower panel: Particle nucleation for 50 NLC events at Spitsbergen, analogous to Figure 5.11.

However, there are also differences between the two cases: As can be seen from the time of particle nucleation in the lower panel of Figure 5.14, NLC at 79°N are considerably older than those at 69° , with a mean age of 63 ± 15 hours. While nucleation also occurs in bursts, these are less distinguishable at Spitsbergen compared to ALOMAR. Almost all particles are older than 24 h at observation, while at 69°N there is a significant fraction of young NLC particles. The nucleation-related life cycle parameters differ also (see Table 5.2): The mean nucleation height is 89.4 km, 1.6 km higher compared to ALOMAR, while nucleation temperature is 124 K, 6 K less than at ALOMAR. The nucleation temperature is consistent with *Höffner and Lübken (2007)*: They found a temperature of 122.5 ± 1 K at this altitude (DOY 180 to 210), just slightly lower than the model temperature.

There are two main reasons for the differences in ice morphology: The lower temperature of the mesopause at Spitsbergen (see Figure 2.1) causes a higher mean saturation level. In addition, the temperature wave amplitudes are somewhat lower at 79°N . This can be seen both from the single NLC fluctuations in Figure 5.14 compared to Figure

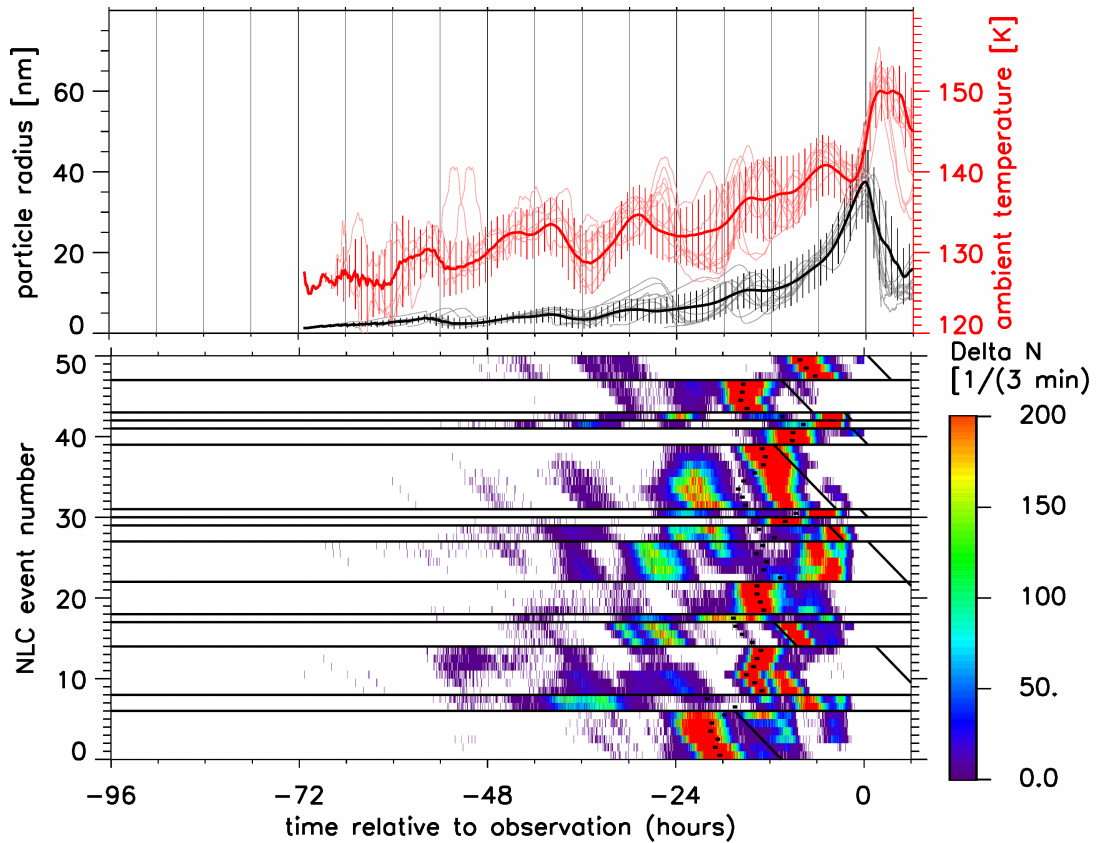


Figure 5.15 Evolution of a superposition of 50 NLC events at latitudes $< 60^\circ\text{N}$, analogous to Figure 5.14.

B.12, and from the variability in Figure 2.1. As a result, ice particles in the mesopause region at 79°N are exposed to both higher and more steady supersaturation conditions than those at 69°N . Even during warm periods, supersaturation usually does not drop low enough for sublimation, which reduces the intensity of nucleation bursts. Comparing $p_{\text{sat}}(r)$ and $p_{\text{H}_2\text{O}}$ at 79°N (not shown) demonstrates that higher saturation and lower variability both contribute to this effect. While the growth conditions for ice particles at 79°N are more stable than at ALOMAR, the initial particle growth is also very slow. This results in the high age of NLC particles at the Spitsbergen location.

The differences in particle life cycle generally affect only the small particles around the mesopause, not the visible cloud: The NLC altitude, ambient temperature, and visibility period are very similar for 69°N and 79°N , see Table 5.2. Apart from somewhat higher NLC brightness at Spitsbergen, the visible part of NLC formation is almost the same at Spitsbergen and ALOMAR.

5.4.2 Latitudes below 60°N

Finally, the formation of NLC south of the 60°N latitude circle is analyzed. Figure 5.15 shows the same nucleation and growth parameters as Figure 5.14 for Spitsbergen, while Figure B.14 adds the vertical trajectories and vertical motion components. NLC

at latitudes south of 60°N are far less bright than those at ALOMAR or Spitsbergen, as seen from Figure 5.2. Shown in the upper panel of Figure 5.15, the particle radius at t_0 is 20 nm smaller compared to strong NLC at 69°N . Again, the ice particle development south of 60°N is similar to that at ALOMAR in some regards. This includes nucleation in bursts, an upwelling accompanied by rapid growth in the hours before t_0 , and sublimation accelerated by a downwelling afterwards.

Compared to NLC closer to the pole, ice particles south of 60°N have considerably reduced lifetimes (19 ± 8 h). Nucleation bursts are even more distinctive than at ALOMAR. At these latitudes, the mean temperature in the NLC nucleation region is higher. This causes lower mean supersaturation, so values of S high enough for ice formation are less common than at ALOMAR. Additionally, temperature variability is higher compared at ALOMAR, as seen from Figure 2.1 and the individual trajectories in Figure 5.15. The strong wave activity makes it unlikely for NLC particles to survive many warm periods. Ice particles either grow to visible size quickly or sublimate before ever reaching large size.

Similar to the Spitsbergen NLC, most of the differences in particle evolution affect ice nucleation and early history. The visibility period is similar to 69°N , even though NLC brightness is much lower. NLC at latitudes below 60°N are highly influenced by background conditions. They are much younger than ice clouds closer to the pole as a result of their sensitivity to waves in the ambient atmosphere. A consequence is that the ice particles nucleate closer to their point of observation.

Since supersaturation conditions at latitudes below 60°N are much less favorable to ice formation than those further north, southward transport of ice particles is a possible source for NLC at low latitudes. The meridional transport around t_0 was calculated for the 50 low latitude NLC events because combined wind and NLC measurements are available at Kühlungsborn (54°N). The model NLC are accompanied by southward directed transport distances of 150 – 500 km in the last 6 hours before t_0 . This compares well with *Gerding et al.* (2007), who found that southward winds are a necessary precondition for NLC formation at 54°N and estimated a southward transport of 400 km.

6 Sensitivity of NLC life cycle

6.1 Influence of aspheric particles on noctilucent clouds

Measurements show that mesospheric ice particles are, in general, not spherically shaped (*Baumgarten, 2001; Eremenko et al., 2005; Baumgarten and Thomas, 2006; Rapp et al., 2007; Hervig et al., 2009a; Hervig and Gordley, 2010*). The standard version of MIMAS uses spherical particles only (see Section 1.2.2 and Section 3.3.2). This simplification is reasonable for most purposes, thus it is also employed for NLC particle simulations with the CARMA aerosol model (*Megner, 2011; Merkel et al., 2009; Bardeen et al., 2010*). The ALOMAR RMR-lidar offers a way to validate particle size by measuring backscattered light at multiple wavelengths, but this requires a more realistic modeling of particle shape. While shape can also be measured through depolarization, this is very challenging in practice because of the rarity of the required conditions. A sensitivity study will be conducted which allows to compare model particle size with the lidar. This study will also quantify the effects on NLC layers from the changed microphysics associated with non-spherical particles, by using the general particle life cycle analysis demonstrated in Section 4.2.

6.1.1 Adaptations to MIMAS for non-spherical particles

Several modifications of MIMAS are necessary to include non-spherical particles, and to compare the resulting ice morphology to that of spherical ice. The time period for this simulation is July 2009, so the dynamic fields driving MIMAS are identical to those in Section 4.2. The microphysical model was enhanced from the standard version: In addition to a spatial coordinate and a radius, each of the 40 million particles now also has a particle shape. This shape is randomly assigned to the condensation nuclei and assumed to stay constant during the particle life cycle. The particles are cylindrical with aspect ratio (AR, diameter divided by height) ranging from 0.1 to 10, i.e. from highly elongated (prolate) to very flat (oblate). This shape distribution is also used by the data retrieval algorithm of the ALOMAR lidar (G. Baumgarten, private communication). The average aspect ratio of this distribution is 3.9 (using $\frac{1}{AR}$ in the average for $AR < 1$, i.e. prolate particles). This is considerably more than AIM satellite measurements indicate (*Hervig and Gordley, 2010; Hervig et al., 2009a*). For that reason two additional simulations were conducted using only slightly aspheric particles, only prolate with $0.32 < AR < 0.87$ in one case and only oblate with $1.1 < AR < 3.2$ in the other. The cases of prolate and oblate particles are treated individually, since the SOFIE instrument does not distinguish between the two. A

Chapter 6 Sensitivity of NLC life cycle

separate analysis allows predictions which shape is likely prevalent. Both additional shape distributions fit the asphericity deduced from SOFIE (2 ± 0.6), because SOFIE sees an $AR = 0.5$ prolate shape simply as an $AR = 2$ particle.

Particle shape modifies the microphysics of the NLC particles in two ways. First, growth and sublimation speed increase with higher asphericity because the surface area S is increasing at constant equivalent volume radius r (the radius of a sphere of same volume):

$$\Phi_{\text{drdt}} = \frac{\left. \frac{dr}{dt} \right|_{\text{cylinder}}}{\left. \frac{dr}{dt} \right|_{\text{sphere}}} = \frac{S_{\text{cylinder}}(r, \epsilon)}{S_{\text{sphere}}(r)} = \left(\epsilon + \frac{1}{2} \right) \left(\frac{2}{3\epsilon} \right)^{\frac{2}{3}} \quad (6.1)$$

where ϵ is the aspect ratio, i.e. the ratio of diameter to length of the axis of symmetry (*Turco et al.*, 1982). Equation (6.1) is an approximation best suited for larger particles. More precise modeling would have to adjust the Kelvin effect, because the local particle curvature changes with its shape.

The other effect is a reduced sedimentation speed (w_s) for prolate or oblate particles. A significant part of the thermal energy of mesospheric ice particles is contained in rotational Brownian motion because of their small size. *Gadsden* (1983) estimates rotational frequencies around 10^6 Hz for spherical NLC particles. Thus, mesospheric ice particles can be assumed to be randomly oriented on the time scales of this model, which allows calculating the average vertical cross section for collisions with air molecules. Since this cross section increases for oblate or prolate shapes at constant volume equivalent radius, needle- and disk-shaped particles fall slower than spheres:

$$\Phi_{\text{sedi}} = \frac{w_{s,\text{cylinder}}}{w_{s,\text{sphere}}} = \frac{\left(\frac{4\epsilon}{9}\right)^{1/6} \cdot \left(1 + \frac{\pi}{8}\right)}{\sqrt{3 + \frac{\pi}{2} + \frac{1}{\epsilon}} \cdot \sqrt{2 + 2\epsilon + \frac{\pi}{2}}}. \quad (6.2)$$

The values for these correction factors are shown in Figure 6.1. Φ_{drdt} and Φ_{sedi} are around 2 and 0.5 for prolate particles with $AR=0.1$, and generally closer to 1 for oblate particles with the inverse aspect ratio. Thus prolate "needles" are expected to have a greater impact on ice morphology than oblate "plates". Φ_{drdt} and Φ_{sedi} also do not equal 1 for cylinders with equal height and diameter: Compared to the reference model (spherical ice), particles grow faster and sediment slower for cylinders with $\epsilon = 1$.

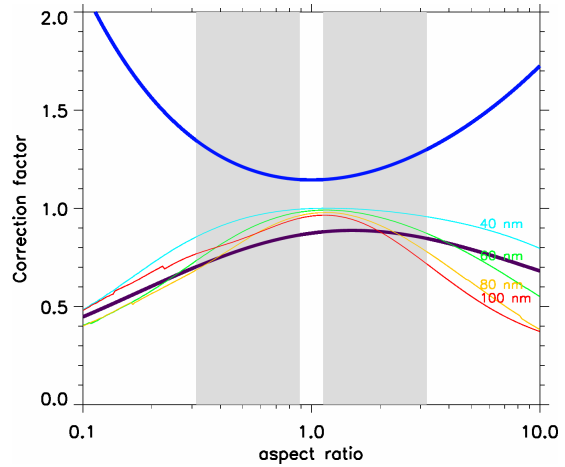


Figure 6.1 Correction factors for particle growth (blue) and sedimentation (purple) of cylinders with aspect ratios $0.1 < AR < 10$, in relation to growth and sedimentation of spheres. Thin lines are the corresponding ratios for backscattering of cylinders to spheres at 532 nm, for several particle sizes. Shading indicates aspect ratios used in the simulations.

6.1 Influence of aspheric particles on noctilucent clouds

Another necessary alteration to the model is the ability to calculate backscatter coefficients for cylindrical particles with variable aspect ratios and for multiple wavelengths. The standard version of MIMAS calculates NLC brightness for 532 nm (green) only. All particles are assumed as spherical, and the scatter coefficients of all particles within each grid volume are added up. The aspheric particle simulations use the same grid but with scatter coefficients for randomly oriented cylinders of variable aspect ratio, derived by the T-matrix method (*Mishchenko and Travis, 1998*). Also, volume backscatter coefficients for 355 nm (UV) and 1064 nm (IR) are calculated in addition to 532 nm. Figure 6.1 also shows the effect on the scatter coefficients (at 532 nm) of changing from spheres to cylinders of equivalent radius. Generally, the scatter signal is smaller for elongated or flattened particles. However, this does not mean that NLC with highly aspherical ice are dimmer, since the two effects mentioned above change the particle growth. For studying the change in morphology (Section 6.1.3), a smaller selection of dust nuclei (40,000 out of 40 million) is analyzed in high time resolution comparable to Section 4.2, in order to conduct an analogous analysis.

6.1.2 Validation of particle size with 3-color lidar measurements

Lidar measurements at three wavelengths generate two independent color ratios (CR, see also Appendix B.1). Interpreting the lidar data requires finding combinations of particle size and shape which fit the measured color ratio distribution. In Figure 6.2, the existing ALOMAR lidar statistic on NLC color ratios is compared to color ratios derived by modeling. The color ratio combinations resulting from several discrete particle shapes and monodisperse size up to ≈ 120 nm are plotted as colored lines in several panels of this figure: In panel (b), the CR combination for AR=1 cylinders is shown along with those for highly prolate or oblate particles, while (c) and (d) show the color ratios for moderately prolate and oblate particles. When neglecting the wavelength dependence of the refractive index, small particles approach the limit of Rayleigh scattering: For $r \ll \lambda$, $\beta_\lambda(r) \propto r^2 (\frac{r}{\lambda})^4$ applies, so $\frac{\beta_{355\text{nm}}(r)}{\beta_{532\text{nm}}(r)} \rightarrow (\frac{532\text{nm}}{355\text{nm}})^4 \approx 5$. Similarly, $\frac{\beta_{1064\text{nm}}(r)}{\beta_{532\text{nm}}(r)} \rightarrow \approx 0.06$. The Rayleigh limit can be seen by the convergence of the monodisperse distribution curves for small radii. Since small particles are already hard to detect, the low contrast in color ratio makes it even more difficult to determine their size, at least by optical methods.

Several of the CR lines for different shapes in Figure 6.2 intersect each other: For variable particle shape, there are often many combinations of particle size and shape that fit a given (measured) pair of IR/Vis and UV/Vis color ratios. This is further complicated since lidar measurements do not detect a single ice particle, but a distribution of a large number of particles of different size and shape (*Baumgarten, 2001*). Measured color ratios are thus weighted averages of single particle values and depend on the combined distribution of particle size and shape. A mix of two or more different particles can result in any color ratio pair that lies somewhere between the CR combinations of the constituent particles. The effect of this ensemble averaging on color ratios is shown in the top left panel of Figure 6.2, where the CR combinations for log-normal size distributions lie far inside the volume spanned by the monodisperse curve. However, measurements with lower IR/Vis ratios than spheres cannot be explained in this way, which makes the area to the left of the black lines a "forbidden area" implying

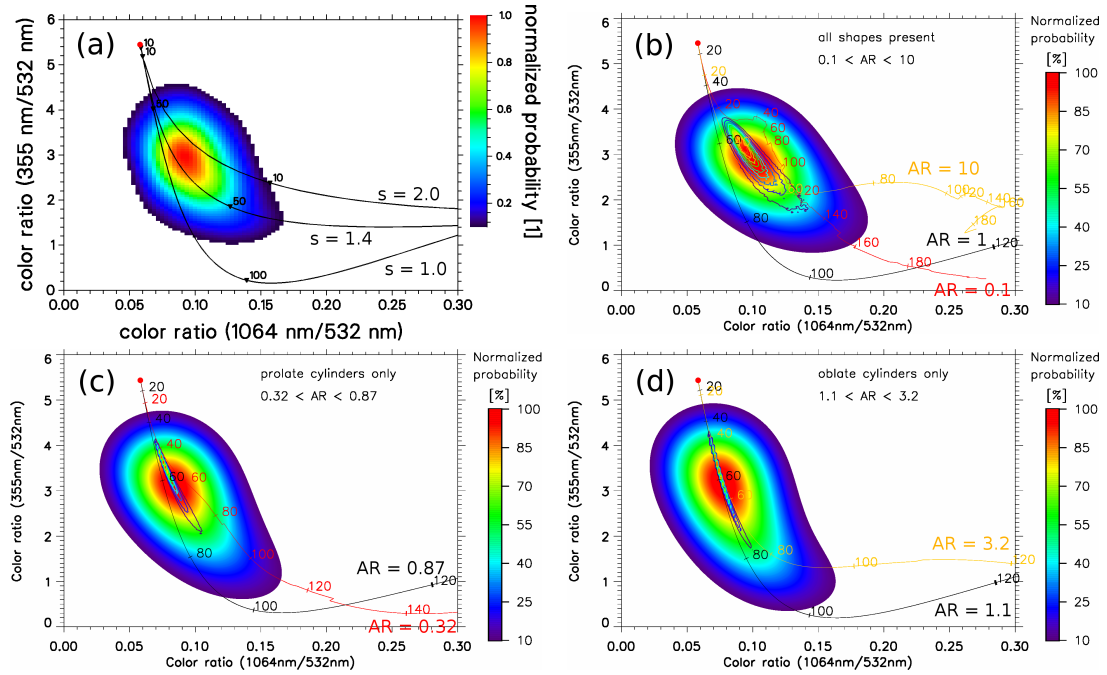


Figure 6.2 Top left panel: Measured multi-year statistic of color ratios of strong NLC from the ALOMAR lidar (1998-2009). Other panels show model color ratios using cylindrical particles, with different particle shape distributions. Contour lines show distributions resulting from microphysical modeling directly. Filled contours apply a measurement error calculated from the spread of the lidar color ratios. The outermost line is the 10% of maximum level. In (b), (c), and (d), color ratios for some specific shapes and arbitrary size are plotted as lines, with radius shown at 20 nm intervals. The lines in (a) show spherical particles, with monodisperse (lowest line) and two lognormal distributions. Red dots show the color ratio limit for Rayleigh scattering.

measurement errors or particle shapes inconsistent with the optical modeling.

After this introduction to color ratios, the measured distribution is now compared to the modeled ones. The data set used for the ALOMAR lidar statistic in Figure 6.2(a) includes only strong NLC ($\beta_{532\text{nm}} < 13 \cdot 10^{-10} \text{m}^{-1}\text{sr}^{-1}$) within the time period of 1998 to 2009, weaker NLC are discounted. The three model data sets used for the comparison as described in Section 6.1.1 include all NLC in the latitude range 67°N to 72°N within July 2009. As for the lidar, only volumes with backscatter coefficients of more than 13 (at 532 nm) are used. This approach differs from the one used in *Kiliani et al.* (2013), where the model simulation itself did not incorporate asphericity, but synthesized optical signals for the color ratio comparison by randomly assigning a non-spherical shape to each particle. In contrast, the particles in the current simulations are assumed to be cylindrical and experience growth and sedimentation as non-spherical particles. This is more realistic and also improves the comparison to lidar observations.

The modeled color ratios of the three shape distributions are shown in empty contour lines, normalized to maximum value. For the $0.1 < AR < 10$ cylinder simulation,

6.1 Influence of aspheric particles on noctilucent clouds

Data set	lidar	all shapes	prolates	oblates
Color ratio UV/Vis ($\frac{\beta_{355\text{nm}}}{\beta_{532\text{nm}}}$)				
Mode (most common CR)	2.95	2.89	3.12	3.17
10% isoline: minimum CR	1.01	0.83	0.62	0.35
10% isoline: maximum CR	4.58	4.46	4.76	4.92
Color ratio IR/Vis ($\frac{\beta_{1064\text{nm}}}{\beta_{532\text{nm}}}$)				
Mode (most common CR)	0.093	0.101	0.084	0.078
10% isoline: minimum CR	0.045	0.041	0.027	0.022
10% isoline: maximum CR	0.168	0.188	0.166	0.163

Table 6.1 Characteristic values of the color ratio distributions from the ALOMAR RMR-Lidar and MIMAS-LIMA, with different non-spherical particle distributions.

the size of the area showing CR combinations occurring in the model (contour lines in Figure 6.2 (b)) is quite large. This is due to the wide range of shapes present, especially the high aspect ratio needles. The simulations with more moderate non-spherical particles (c) and (d) have much narrower distributions of color ratios. This applies especially for the disc-shaped particles in (d), because slightly oblate particles have color ratio combinations close to the AR=1 line up to ≈ 60 nm, the size range of most visible particles. The model run with needle-shapes has a slightly wider CR distribution with higher IR/Vis ratio (i.e., further away from the black line).

To make the model results comparable to lidar data, measurement uncertainty also has to be considered. The filled distributions in the top right and bottom panels of Figure 6.2 are derived by smoothing the simulated color ratios with a Gaussian filter whose width is calculated from the lidar measurement error. For those smoothed distributions, the modes (i.e., the most common CR combinations) are compared to the measured data set. Additionally, the general distribution shape is analyzed, by comparing the area of CR combinations at least 10% as common as the mode (i.e., the outer edge of the plot area). These values are tabulated in Table 6.1.

In general, the comparison looks best for the wide shape range cylinders: The modes of the UV/Vis distribution match closely, while the simulated IR/Vis ratio is larger than measurements by ≈ 0.008 . In contrast, the IR/Vis mode of the simulation with only needles is about 0.009 lower than the measurements, while for the simulation with only oblate particles this difference increases to 0.015. Also, the UV/Vis modes for both simulations with only moderately aspheric particles are ≈ 0.2 higher compared to the observations. Comparing only the distributions' modes would lead to the conclusion that the $0.1 < AR < 10$ particle distribution fits the measurements best, since it would require only a minor reduction of the largest aspect ratios to reduce the IR/Vis mode to the measured value.

Comparing the 10% maximum isolines differentiates the comparison: In general, the area enveloped by this isoline is larger for the model simulations than for the measurements, which suggests that the error values used for the smoothing filter are slightly too high. Reducing the error would not remove all differences in the shape

Chapter 6 Sensitivity of NLC life cycle

of the 10% isolines however, since the underlying distributions before adding errors would still differ from the (unknown) error-free lidar distribution. Minimum IR/Vis and both minimum and maximum UV/Vis of the all shapes simulation compare best to the measured color ratios, while its maximum IR/Vis ratio is too large by 0.02. For the smaller aspect ratio simulations, minimum IR/Vis and minimum UV/Vis are too small compared to the measurement while maximum UV/Vis values are too large, in all cases the comparison is worse for the oblate particle distribution than for the prolates. Only the maximum IR/Vis value is better for the moderate prolate simulation than for the one with highly aspheric particles.

To summarize, the measured color ratios best fit the modeled distribution which includes cylinders of aspect ratios between 0.1 and 10, but some aspects of it are better explainable with the moderately prolate (i.e, needle) shape distribution. The simulation using only oblate particles yields the poorest comparison among the three simulations. The true shape distribution is likely a mixture of the three modeled distributions: The mode in the lidar data suggests that highly prolate particles are less common, since these are the primary cause for high IR/Vis modes. From the position of the distribution "tail" it is also unlikely that strongly oblate large particles are common. The most likely shape distribution is one consisting mainly of needle-shaped particles with (inverse) aspect ratios up to about 6 and also including many particles close to AR=1. The color ratios from an exclusively spherical distribution (i.e., the standard particle shape in the model) mostly resembles that for the slightly oblate distribution, and thus matches the measured ratios very poorly. In conclusion, the size of ice particles in MIMAS-LIMA when including non-spherical particles is in good agreement to lidar observations.

6.1.3 Influence of non-spherical particles on general NLC morphology

Since non-spherical particles were shown to fit measurements better than spherical ones, their impact on NLC formation and life cycle is estimated. The left panel of Figure 6.3 shows the averaged optical brightness profile at the latitude region of ALOMAR, for a time period of one month. Cylindrical particles with various shapes instead of spherical ice make the NLC brighter and also shift it slightly upward. The three aspheric simulations differ slightly in the extent of the change: The simulation with only disc shaped particles shows the least increase in cloud brightness, while the β increase for the needles is higher and closely approaches that of the simulation with strongly aspheric cylinders. Considering only the $\beta_{532\text{nm}}$ dependence on shape shown in Figure 6.1, this increase in brightness is counterintuitive since at constant radii the scattering intensity of non-spheres decreases compared to spheres. However, the changed microphysics cause an increase in NLC particle size, which more than compensates for this decrease. The higher brightness for prolate compared to oblate particles is mainly due to the slower sedimentation speed, though the slightly faster growth also has an effect.

While the left panel of Figure 6.3 compared the model simulations with different shape distributions, it did not examine how particle evolution within individual simulations depends on the particles' aspect ratio. In the right panel of Figure 6.3, the trajectories of 40,000 particles in the model run with $0.1 < \text{AR} < 10$ are separated by individual aspect ratio. While the simulation was initiated with particle shape equally

6.1 Influence of aspheric particles on noctilucent clouds

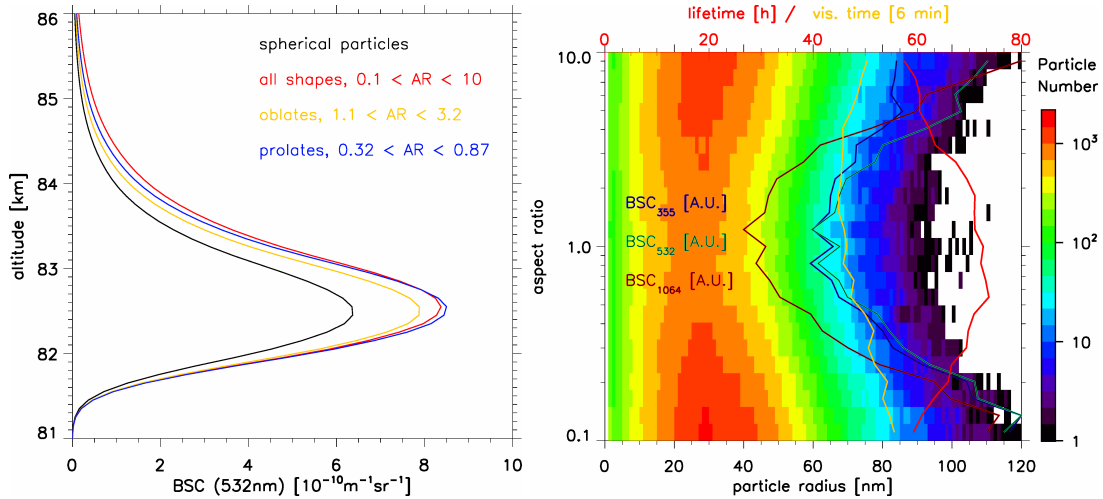


Figure 6.3 Left panel: Comparison of backscatter profiles for the reference simulation with spherical ice particles and three simulations of aspheric particle ensembles. $\beta_{532\text{nm}}$ is averaged for latitudes $> 60^\circ\text{N}$ during July 2009. Right panel: Effects of non-spherical particles on NLC morphology, north of 60°N in July 2009. Contours show combined size and shape distribution in the altitude range 81.8 to 83.4 km, in units of particle number present for one hour. The three colored profiles with thin black lines show the relative intensity of scattered light at the ALOMAR lidar wavelengths by the various particle shapes. Particle lifetime (red profile) and visibility duration (orange), defined as in Section 4.2.2, are weighted by the particles' maximum brightness at 532 nm.

distributed between these extremes, they evolve differently. Within the main NLC layer, highly elongated or flattened particles are about twice as numerous as particles with $\text{AR}=1$. Their radii are also significantly larger, by over 15 nm. This leads to the observed large difference in brightness, where the high aspect ratio particles are responsible for 2.5 to 3 times the backscattered light compared to the near spherical ones. The relative difference is largest in the infrared channel. At UV and visible wavelengths, oblate particles scatter less than prolate ones. The NLC particle shape distribution in the right panel of Figure 6.3 also explains why the agreement of color ratios between measurements and model in Figure 6.2 is better than in *Kiliani et al.* (2013). In that comparison, the particles were assigned random shapes without modeling their evolution, which precluded preferential formation of highly aspheric large particles. This change alone shifted the mode of the distribution in the IR/Vis from 0.005 smaller than measured to 0.008 larger here, allowing a deduction of a likely true distribution.

The right panel of Figure 6.3 also shows the influences of particle shape on lifetime and the width of the scatter peak, i.e. visibility time. Highly oblate or prolate particles have a lower age. This is explained by increased growth and sublimation rates for aspheric particles, with a similar effect as increased temperature fluctuations. Most of the time, the environment in the mesopause region favors slow growth. As a result, non-spherical particles take less time to grow to visible size. The difference is smaller

Chapter 6 Sensitivity of NLC life cycle

than Φ_{drdt} , since a reduced sedimentation rate counteracts the faster growth: The time particles require to reach the H₂O-rich NLC layer is increased. There is also a slight dependence of visibility time on shape. Surprisingly, t_{vis} increases for non-spheres, when from Φ_{drdt} the opposite would be expected. The increase is distinctly tilted and occurs primarily for needles. This indicates that the slower sedimentation affects the visibility time more than the faster growth and sublimation.

There are a few effects of non-spherical particles not considered in these simulations which might also have some impact on the morphology. For stringent non-spherical modeling, particle shape could not be assumed to stay constant from dust nucleus to large ice particle, it would change along with growth. The nucleation barrier (Kelvin effect) also depends on particle shape once local curvature is factored in. Another effect that mainly concerns the larger, visible particles is the heating from solar infrared absorption which is proportional to volume. Since the heat transfer to the surrounding air is proportional to the particles' surface, a non-spherical particle will get heated by sunlight less than a spherical one, further increasing the growth rate difference between spheres and non-spheres.

In conclusion, changing the microphysics of MIMAS to include non-spherical particles is necessary to bring the simulated scatter signal in agreement with observations. The likely shape distribution includes more prolate than oblate particles, with somewhat higher mean asphericity compared to the value predicted by SOFIE (2.0). The main changes to morphology are larger particle size for the highly elongated particles, resulting in an increased scatter signal. Particle lifetimes are slightly reduced for aspheric particles (up to 15%), while the visibility period is slightly extended (up to 15% for prolate particles).

6.2 Sensitivity to dynamic wave spectrum: Ice morphology with KMCM

Apart from the influence of non-spherical particles, there is another sensitivity study which is relevant to the ice layer morphology. The dynamic fields of LIMA show little variability on scales smaller than several hundred kilometers as a consequence of the model wave spectrum which does not include short-period gravity waves. There are several variations of KMCM output with different wave spectra, as discussed in Section 2.1.2. These are used to compare the morphology of the resultant ice layers, focusing on the wave spectrum dependency of NLC.

6.2.1 Introduction and analysis methods

The KMCM run used for this analysis simulates permanent July conditions. It includes gravity waves up to a spectral resolution of 120 but no tides. The short time step of 11.25 minutes resolves even short period gravity waves well enough that even time interpolation does not cause noticeable aliasing effects. The model uses hybrid vertical levels, which is almost equivalent to pressure levels in the mesosphere region, and it extends well into the lower thermosphere. The length of the KMCM dynamic data set, 29 consecutive days, is a time period comparable to the one used in Section 4.2

6.2 Sensitivity to dynamic wave spectrum: Ice morphology with KMCM

and Section 6.1.

As a result of the spectral structure, KMCM calculates atmospheric parameters in spherical harmonics instead of a spatial grid. To make its results compatible with MIMAS requires several steps of data processing. First, a processing routine transforms the atmospheric parameters from the harmonic functions onto a global 1° by 1° longitude-latitude grid. This subroutine also supports wave filtering, i.e. evaluating the spherical harmonics only up to certain zonal and meridional wave numbers.

The fields generated by the previous step are not yet usable by MIMAS. A second postprocessing routine is needed to calculate density and vertical wind speed from temperature, pressure and pressure velocity $\omega = \frac{dp}{dt}$. Then the pressure level grid is converted to geometric altitudes and the horizontal grid to the MIMAS resolution. A slight adjustment was also made to the altitude of the fields, which were shifted upwards by 2 km. At 80 km, this is approximately the value required by implementing the altitude dependence of Earth's gravitational field, which was not done in KMCM.

In addition to these grid conversions, KMCM dynamic fields require time interpolation for compatibility with MIMAS. MIMAS-LIMA uses dynamics at a resolution of 60 minutes, but this would not suffice for the shorter period waves in KMCM. To resolve this, the time interval of the files supplied to MIMAS was reduced to 12 minutes. This is a multiple of the MIMAS internal time step of 3 minutes, which simplified the implementation. However, only the time resolution of the dynamic fields was changed while the zonal grid resolution was left at 3° . At low latitudes this is insufficient for resolving small scale KMCM gravity waves, but at higher latitudes it is acceptable: The longitudinal grid size Δs at 70°N is still 110 km, partly resolving waves down to horizontal wavelengths of 400 km.

6.2.2 Morphology of ice clouds in MIMAS-KMCM

As discussed in detail in Chapter 2, there are a number of profound differences between the dynamic fields generated by LIMA and KMCM. As a result, the ice layers simulated on KMCM dynamics also differ from typical MIMAS-LIMA simulations. In the following, these differences are investigated and, where possible, explained. Mostly, KMCM₃₀ dynamics are used for this comparison, because the scale of the wave structures is similar to LIMA and to radar measurements (see Appendix A.2). This allows estimating which of the changes in morphology are caused by the differences in mean dynamics, as compared to differences in waves.

A good starting point for discussing the general shape of the NLC in MIMAS-KMCM are the sample ice clouds in Section 2.3.1. Figure 2.7 and Figure 2.8 each include NLC time series for KMCM₃₀ and KMCM₁₂₀. The KMCM₃₀ panels of these figure show NLC with similar brightness but higher occurrence rate compared to MIMAS-LIMA. The typical duration in MIMAS-KMCM is slightly shorter, corresponding to the prevailing wave period in KMCM₃₀, the 15-hour inertia gravity wave. NLC occurrence is much better correlated with low temperatures at 83 km than with wind components, see also Figure 4.10. In comparison, the NLC in MIMAS-KMCM₁₂₀ is much weaker, has a shorter average duration and greater vertical variability due to short period waves in temperature and vertical wind. The inertia-GW is still visible, but overlaid with smaller scale structure from gravity waves. Both MIMAS-KMCM₃₀ and MIMAS-

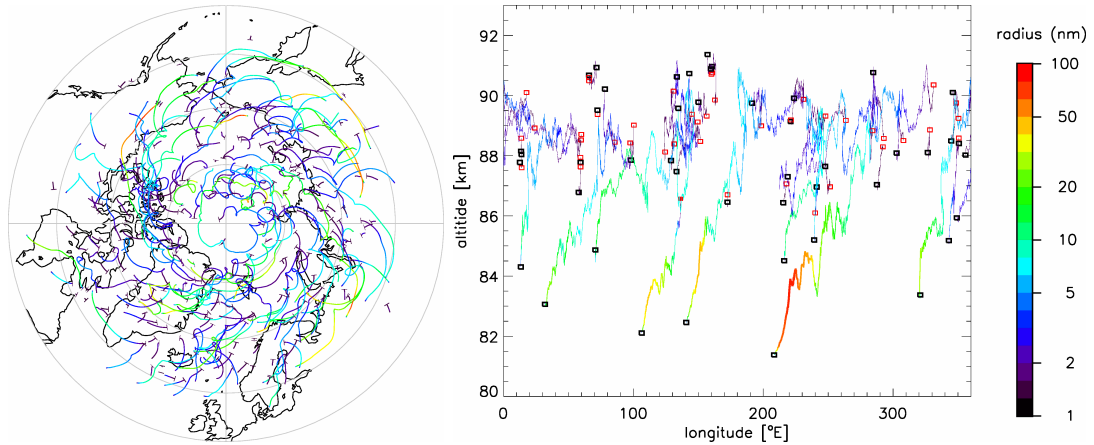


Figure 6.4 Sample trajectories analogous to Figure 4.6. Left panel: Horizontal projection of ice phase trajectories of 7 condensation nuclei over 25 days of KMCM₃₀, consisting of 313 separate trajectories. Color shows particle radius on the scale used by the right-side figure. Right panel: Zonal and vertical transport of one CN over the same time period, in 47 continuous segments. Red dots mark nucleation position, black dots sublimation position.

KMCM₁₂₀ also feature a multi-day modulation in the NLC brightness, best correlated to temperature. The zonal structure (shown in Figure B.9) reinforces this impression. Consequently the long-period modulation propagates westwards along with the 5-day wave in temperature.

In order to compare the basic shape of ice particle trajectories in MIMAS-KMCM to that in MIMAS-LIMA, Figure 6.4 shows the trajectories and radius evolution of a small selection of condensation nuclei for MIMAS-KMCM₃₀ in the same way as Figure 4.6. The horizontal trajectories are predominantly westward directed, but slower than for MIMAS-LIMA. MIMAS-KMCM trajectories have a considerably larger southward transport component, and as a consequence of the larger wind variability they look much more chaotic compared to MIMAS-LIMA trajectories. Very often, individual particle paths form counterclockwise loops, and even those trajectories which are too short for loops have a strong tendency to curve towards the right. The loops are caused by the gravity waves in KMCM, and likely show the polarization relation of the wind components. While a preferential curving can also be found in MIMAS-LIMA trajectories, the strong zonal winds and smaller wave amplitudes make such loops much rarer.

Figure 6.4 also includes zonal-vertical trajectories for MIMAS-KMCM₃₀. Within NLC altitudes, these look very similar to those in MIMAS-LIMA, apart from the smaller westward transport component. At higher altitudes, there are a few differences: In MIMAS-KMCM, it is much more common to see particles sublimating at an altitude above their nucleation height. This is most likely a result of the greater mean upwelling within the nucleation region at 69°N, in combination with the steeper temperature gradient above the mesopause (see Figure 2.2). At high altitudes, particles in MIMAS-KMCM are also primarily transported eastward due to the lower altitude of zonal wind

6.2 Sensitivity to dynamic wave spectrum: Ice morphology with KMCM

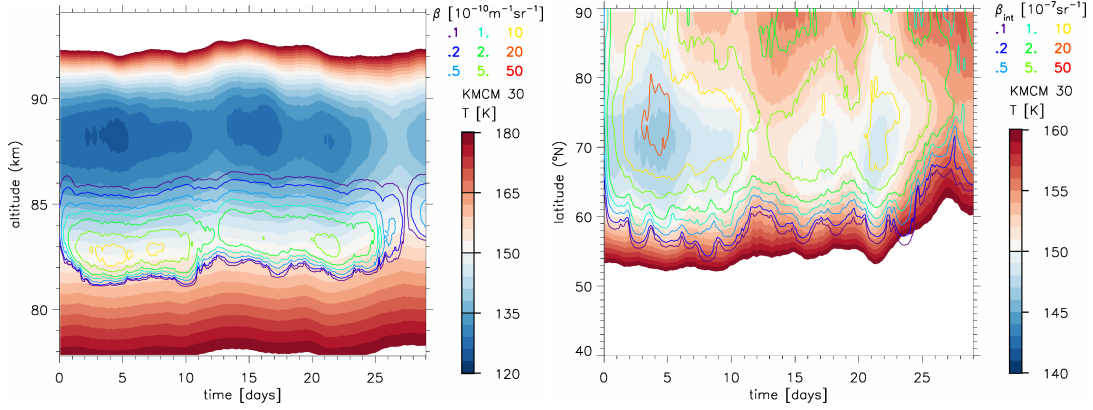


Figure 6.5 Time series of KMCM₃₀ zonal mean temperature (filled contours) and NLC brightness (contour lines), analogous to Figure 4.4. Left panel: Vertical structure of temperature and backscatter coefficient at 69°N. Right panel: Latitude time series of temperature at 83 km and column integrated scatter coefficient. All time series are processed with a 24 hour smoothing filter.

reversal.

Figure 6.5 characterizes the large-scale evolution of the NLC in MIMAS-KMCM over the time period of 29 model days, including temperature because of its effect on ice formation. In the left panel, the average vertical structure is shown. The first obvious difference to Figure 4.4 is a far greater variability in the zonal mean, both in temperature and in the ice formation. The mesopause temperature fluctuates by up to 15 K, and at 83 km the variations still amount to more than 8 K. This strongly affects the mean NLC formation: The centroid altitude roughly follows the 150 K isoline, while cloud brightness reacts to mean temperature in a relationship close to linear with an average column backscatter of $2.7 \cdot 10^{-7} \text{sr}^{-1}$ for every Kelvin below 154 at 83 km, 69°N. Since the MIMAS-KMCM is initialized with no NLC particles present, it takes some time until enough small ice particles grow to visible size that particle growth and sublimation reach an equilibrium state. This time frame is 2-3 days, as can be seen in Figure 6.5 by the time it takes until the NLC no longer strongly increases in brightness.

The right panel of Figure 6.5 also shows the latitudinal dependence of ice clouds. Comparing this to Figure 4.4 reveals a fundamental difference between the MIMAS NLC generated with the two dynamic models. While MIMAS-LIMA features a latitudinal gradient with NLC becoming stronger all the way towards the pole, in MIMAS-KMCM ice formation peaks around 70-75°N and declines near the pole. The most likely causes for this will be discussed in the next figure. Another striking difference is the latitudinal extent of the ice clouds: Within MIMAS-KMCM, NLC form around 5 degrees further south, even though mean temperatures at 83 km are considerably higher south of 60°N, also visible in Figure 2.1 and Figure 2.2. In general, ice formation is much better correlated to temperature at 83 km in KMCM₃₀ compared to LIMA: When the 154 K isoline moves north by about 10° during the last few days of the month, the NLC shrinks by almost the same amount.

Chapter 6 Sensitivity of NLC life cycle

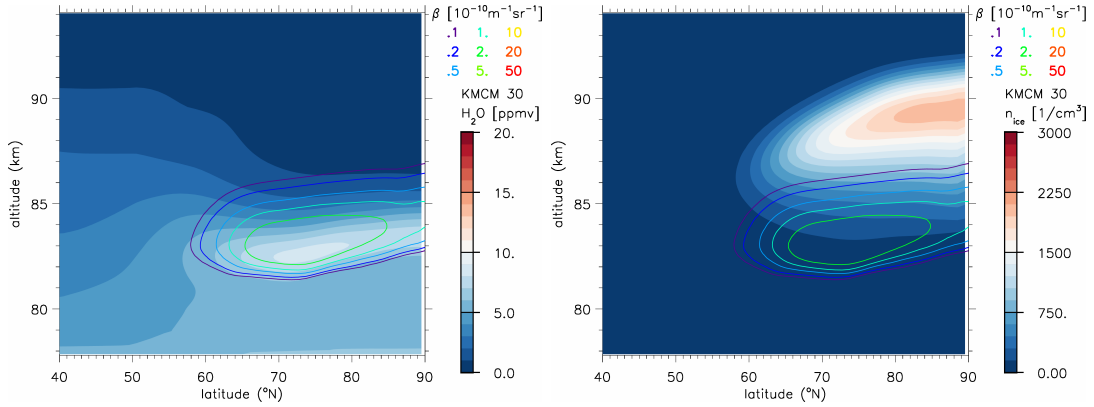


Figure 6.6 29 day average of MIMAS-KMCM₃₀ model parameters related to ice formation. Left panel: Water vapor mixing ratio, right panel: ice number density. Both panels also show mean NLC formation (backscatter coefficient at 532 nm) in contour lines.

Observations and most models find a clear increase of noctilucent cloud brightness toward the pole (e.g. *Höffner et al.*, 2003; *Karlsson and Rapp*, 2006; *Deland et al.*, 2007, 2010). The meridional structure of MIMAS-KMCM ice clouds (also shown in Figure B.5) is thus anomalous, while that for MIMAS-LIMA is supported by observations. Possible reasons for this feature are examined with the mean dynamics shown in Figure 2.1 and Figure 2.2: The mean mesopause temperature and altitude of both models are very close north of 65°N. The decrease of mesopause temperature toward the pole is larger in KMCM than in LIMA. This suggests that MIMAS-KMCM ice clouds should even feature a brightness increase toward the pole that is at least as strong as in MIMAS-LIMA. Since the model simulation produces the opposite result, mean temperature cannot be the major cause for the anomalous brightness decrease toward the pole.

The remaining possibilities are the mean meridional and vertical winds, also shown in Figure 2.1 and Figure 2.2. The mean meridional transport in KMCM is considerably stronger, causing a larger southward transport component for ice particles and atmospheric water vapor. The area close to the pole also experiences a stronger mean upwelling in KMCM, which might influence the water vapor concentration and also the number of small ice particles that enter the water vapor-rich NLC layer.

Analogous to Figure 4.5 for MIMAS-LIMA, Figure 6.6 shows the latitude-dependent mean profiles of H₂O mixing ratios, the number density of icy particles, and the visible NLC (backscatter coefficient) in MIMAS-KMCM. In addition to the brightness decrease towards the pole (also visible in Figure 6.5), the NLC at the pole is located 1.5 km higher than at 70°N. The H₂O mixing ratios have the same basic structure as in MIMAS-LIMA, with the deposition layer extending further south and not as highly pronounced, with a peak around 75°N. The water vapor depletion in polar latitudes at altitudes above 84 km is less pronounced than in LIMA, which refutes one possible explanation for the brightness decrease near the pole: The stronger southward transport in KMCM could potentially deplete the polar mesopause region of H₂O, but appar-

6.2 Sensitivity to dynamic wave spectrum: Ice morphology with KMCM

ently vertical transport and increased wave mixing replenish the water vapor close to the pole sufficiently to compensate.

Other possible explanations for the latitude-dependance of NLC in MIMAS-KMCM are linked to the spatial distributions of dust condensation nuclei and small icy particles. In MIMAS-KMCM, there are more CN at lower latitudes and less close to the pole, compared to MIMAS-LIMA (Appendix B.2). The MIMAS-KMCM ice particle number density (right panel in Figure 6.6) still increases steadily towards the pole when integrated vertically, but within the altitude region below 87 km it stagnates north of 70°N . This is a consequence of the dust particle distribution and is in contrast to MIMAS-LIMA, where the amount of ice particles increases strongly towards the pole. The bright NLC at polar latitudes in MIMAS-LIMA is thus largely a consequence of a high particle number density, which is not shared by MIMAS-KMCM. In the absence of higher particle numbers, the slightly higher temperature at the pole causes the decrease in MIMAS-KMCM NLC brightness.

So far, only the average dynamic fields have been considered as causes for unusual NLC structure in MIMAS-KMCM, but not the considerable differences in wave structure as discussed in Section 2.3.1 and Section 2.3.2. However, there have been earlier test simulations of MIMAS driven by KMCM gravity waves superimposed onto LIMA dynamics (see Appendix B.5). These dynamic fields combined the LIMA mean temperature and circulation with a wave spectrum similar to KMCM. In these simulations, the latitude-dependence of ice formation was almost the same as in MIMAS-LIMA, suggesting that the NLC maximum at 75°N is caused by the KMCM mean dynamics, not by the characteristics of its gravity waves.

In summary, the latitudinal ice distribution of MIMAS-KMCM is not supported by observations (satellites, lidars). The temperature structure was ruled out as a possible cause since it would have the opposite effect. It is just as unlikely that the KMCM meridional winds are significantly too strong, since they fit the Saura radar measurements at 69°N much better than LIMA. Finally, the KMCM vertical winds are determined by the meridional circulation (Downward Control Principle). Thus, the anomalous ice distribution in MIMAS-KMCM is most likely not the result of any particular deficiency in the KMCM dynamic fields. The probable cause is the MIMAS condensation nucleus redistribution (Section 3.3.1), which is optimized for LIMA circulation patterns: While its limitations as discussed in Section 5.3.3 have limited impact when used with LIMA dynamic fields, the lack of dust particles close to the pole has a larger effect on KMCM with its stronger meridional circulation and upwelling.

6.2.3 Dependence of NLC life cycle on resolved gravity waves

While Section 6.2.2 discussed the main features of MIMAS-KMCM and the limitations of combining MIMAS with KMCM, the aim of this study is to investigate the sensitivity of the ice cloud morphology to changes in the wave spectrum. These aspects will be considered now, by comparing the average NLC brightness and altitude in MIMAS-LIMA and MIMAS-KMCM with zonal wave numbers of 15, 30, 60 and 120 (see Section 6.2.1). Additionally, the simplified trajectory analysis introduced in

Section 4.2 is used to compare results from Chapter 5 with trajectory statistics of MIMAS-KMCM.

Figure 6.7 shows the mean NLC brightness and altitude at the latitude of ALOMAR. NLC brightness decreases with increasing zonal wave numbers. Ice clouds in MIMAS-KMCM₁₅ have the highest average brightness among all data sets, with $\beta_{\max} \approx 8$. For zonal wave numbers 30, 60, and 120, β_{\max} is reduced by 16%, 47%, and 89%, respectively (see Table 6.2). Since the wave spectra of the KMCM data sets differ mostly for short periods (see Appendix A.2), this reduction in NLC brightness is consistent with *Rapp et al.* (2002). NLC brightness in MIMAS-LIMA is comparable to MIMAS-KMCM₆₀. The decrease in brightness at higher wave numbers is less pronounced in β_{int} compared to β_{\max} : MIMAS-KMCM₆₀ and MIMAS-KMCM₁₂₀ feature large variations in NLC altitude resulting from gravity waves, these height variations flatten the β peak in Figure 6.7.

Ice clouds in MIMAS-KMCM are located higher up on average compared to MIMAS-LIMA. This is most likely a consequence of the larger temperature gradient below the mesopause in KMCM, which results in a 150 K isoline about 500 m higher (at 70°N) compared to LIMA. The stronger upwelling in KMCM at 83 km is another factor contributing to an increase of NLC height. There is also a dependency of cloud height on the KMCM wave spectrum: The NLC altitude is shifted upward when including more gravity waves, only slightly for MIMAS-KMCM₃₀ but by 1 km in MIMAS-KMCM₁₂₀ compared to MIMAS-KMCM₁₅. This is linked to the shortened life cycle of NLC particles in an environment with strong waves.

The four MIMAS-KMCM simulations were configured to generate high temporal resolution trajectories for 40,000 model particles as described in Section 4.2, in addition to the standard MIMAS output. These trajectories are evaluated now in all five data sets (including MIMAS-LIMA for July 2009) to compare the particle history of the two models and estimate the impact of including short-period gravity waves.

Figure 6.8 shows histograms of trajectory statistics for the ALOMAR latitude band 67 – 72°N. Only those particles are analyzed which reach their maximum size within this region, and all statistics are weighted with the individual particle peak brightness. In that way, the results are representative for visible NLC and comparable to those from Chapter 5. The individual histograms are then normalized proportional to the maximum brightness-weighted occurrence in any of the 5 model data sets, so their integrated area reflects the data set’s averaged NLC brightness in the 67-72°N band.

The first such statistic is the maximum radius reached within the ice particles’ life cycle, shown in the upper left panel of Figure 6.8. This peak size is very similar

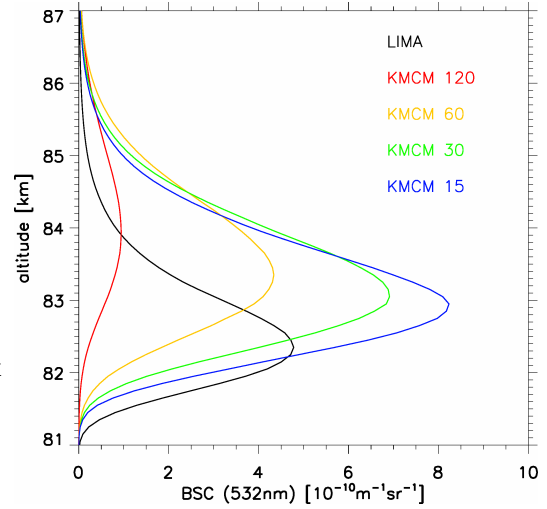


Figure 6.7 Dependence of average NLC brightness on dynamic fields. Profiles show $\beta_{532 \text{ nm}}$ for MIMAS-LIMA and MIMAS-KMCM_{15–120}, averaged zonally and over 25 days at 67-72°N.

6.2 Sensitivity to dynamic wave spectrum: Ice morphology with KMCM

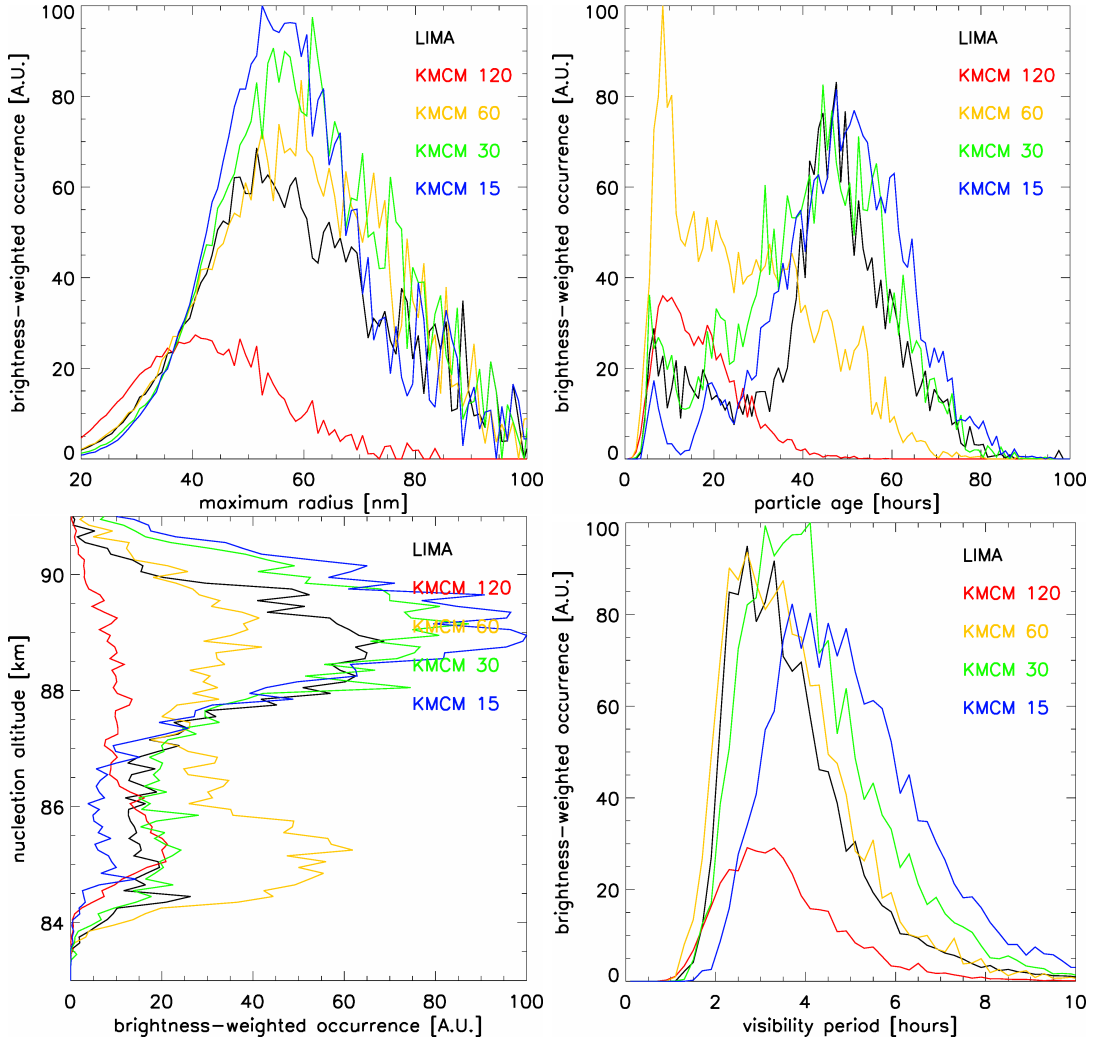


Figure 6.8 Ice life cycle parameters of 40,000 trajectories in MIMAS-LIMA and MIMAS-KMCM_{15–120} at 67 – 72°N. All profiles show normalized occurrence frequency, weighted by the brightness at maximum size. Upper row: Maximum particle radius and particle lifetime. Lower row: Altitude of nucleation and visibility time.

between ice simulations using LIMA and those run on KMCM with total wave numbers 15 to 60. There is some difference in number of particles present, which is largest for MIMAS-KMCM₁₅, which accounts for the different backscatter profiles in Figure 6.7. In all cases but MIMAS-KMCM₁₂₀, the visible particles are ≈ 60 nm large on average, usually in the range 40 – 80 nm. With KMCM₁₂₀ dynamics, the average radius of visible ice particles is only ≈ 40 nm, but this is resulting from the short-period GW activity which reduces NLC brightness considerably below observed levels. The similar particle sizes developing in highly different background conditions indicate that NLC particle radius is among the most robust of parameters in MIMAS.

The MIMAS particle lifetime (upper right panel) with LIMA, KMCM₁₅ and KMCM₃₀ is similar: Few large particles reach the NLC layer and sublimate in less than 24 hours

Chapter 6 Sensitivity of NLC life cycle

from nucleation, most have a lifetime between one and three days. However, for MIMAS-KMCM₆₀ and MIMAS-KMCM₁₂₀ the situation is different: Most particles have a much shorter lifetime, the peak of the distribution is around 10 hours in both cases. In MIMAS-KMCM₁₂₀, the lifetime only exceeds 40 hours in rare cases, while for MIMAS-KMCM₆₀ this limit is at around 60 h. The stronger temperature fluctuations in high wave number KMCM data sets reduce the age of ice particles, also shown in the summary table Table 6.2. This supports the analysis in Section 5.4, where the stronger dynamic fluctuations at lower latitudes were given as one reason for the reduced particle age there. Unlike for the different latitude bands in Chapter 5, mean background conditions are identical for KMCM_{15–120}, so the change in NLC particle age is clearly linked to wave activity here.

The altitude of nucleation (lower left panel) depends on the temperature profile around the mesopause, which is very similar between LIMA and KMCM (Figure 2.5). It shows a similar pattern as particle age: The average nucleation height in MIMAS-KMCM₁₂₀ is 2 km lower than in MIMAS-KMCM₁₅, with MIMAS-KMCM₆₀, MIMAS-LIMA, and MIMAS-KMCM₃₀ in between. On KMCM with stronger dynamics, NLC particles nucleate both lower and with a smaller time period before becoming visible. The stronger wave activity causes favorable conditions for particle nucleation more frequently at lower altitudes around 85 km. Also, stronger waves reduce the probability that ice particles survive for a long time, as discussed in Section 5.4.2. While nucleation at high altitudes still occurs, those particles usually sublimate without growing to visible size, so they are not included in this statistic.

Finally, particle visibility time (lower right panel of Figure 6.8) is defined as the width of the brightness peak using a 10% of maximum threshold. In Chapter 5, visibility time varied very little between the latitude bands, even while the NLC brightness was very different. The variations here are somewhat larger: In MIMAS-KMCM₆₀, visibility times are comparable to MIMAS-LIMA, in MIMAS-KMCM₁₂₀ they are slightly shorter and in MIMAS-KMCM₃₀ and MIMAS-KMCM₁₅ longer than in MIMAS-LIMA. The most likely explanation are the disparate vertical wind amplitudes of the KMCM data sets, shown in Figure 2.3 and Figure A.3. The difference in vertical wind variability between KMCM₁₅ and KMCM₁₂₀ is much more pronounced than the latitudinal difference of LIMA wave amplitudes (see Figure 2.1). Since Section 5.3.2 also demonstrated the influence of vertical wind on the main NLC growth, this along with the changed period of temperature waves are the most plausible reasons.

The shorter overall wave period and stronger up- and downwelling in high resolution KMCM also explain the upward shift in MIMAS NLC altitude. Because ice clouds have less time to grow large, they also sediment less during their visible period and reach their maximum size at slightly higher altitudes.

Several additional particle life cycle parameters are analyzed in the same way in Figure B.6. In summary, the altitude of the sublimation layer in MIMAS-KMCM is higher than in MIMAS-LIMA but largely independent of the wave spectrum. Transport distances over the particle life cycle are also estimated: Zonal transport distances in MIMAS-KMCM are far smaller than in MIMAS-LIMA as a result of the weaker zonal circulation in KMCM. The meridional transport distances on the other hand are considerably larger in MIMAS-KMCM compared to MIMAS-LIMA. MIMAS-KMCM₃₀ yields similar transport distances as the estimate in Section 5.3.1.

6.2 Sensitivity to dynamic wave spectrum: Ice morphology with KMCM

Model data set	KMCM ₁₂₀	KMCM ₆₀	KMCM ₃₀	KMCM ₁₅	LIM3
$\beta_{\max}[10^{-10}\text{m}^{-1}\text{sr}^{-1}]$	0.94	4.34	6.91	8.23	4.78
$\beta_{\text{int}}[10^{-7}\text{sr}^{-1}]$	2.60	10.1	14.3	16.0	8.07
z_{\max} [km]	84.0	83.4	83.1	83.0	82.4
Maximum radius [nm]	43.2	60.6	61.5	58.9	59.7
Peak size altitude [km]	83.6	83.3	83.2	83.0	82.4
Particle lifetime [h]	16.9	26.9	41.8	48.3	43.6
Visibility period [h]	3.5	3.7	4.2	5.1	3.8
Nucleation altitude [km]	86.8	87.0	88.3	88.8	87.9
Sublimation altitude [km]	82.2	82.0	82.0	82.0	81.4
Lifetime transport [$^{\circ}$ W]	32	52	80	91	151
Lifetime transport [$^{\circ}$ S]	3.6	5.1	7.9	9.2	3.8

Table 6.2 Mean values for MIMAS NLC NLC morphology and particle life cycle statistics, on KMCM₁₂₀, KMCM₆₀, KMCM₃₀, KMCM₁₅, and LIM3 dynamics.

In conclusion, most of the properties of NLC particles are sensitive to atmospheric waves. Strong short-period waves reduce particle age, the duration of the main particle growth and sublimation (i.e., the visibility time), and the altitudes of both the visible NLC and the nucleation layer. The mean NLC brightness also decreases with increasing short period wave amplitudes, consistent with *Rapp et al. (2002)*. This occurs most strongly on KMCM₁₂₀ dynamics. However, the particle size is far less affected than the brightness. The particle size decreases significantly only in KMCM₁₂₀ and is the most robust result of these simulations. The particle characteristics in MIMAS-LIMA are most similar to MIMAS-KMCM₃₀ overall, which also supports the analysis in Chapter 5 since its main results do not change strongly when using the dynamics of a completely different atmospheric model.

7 Summary and outlook

In this thesis, the morphology and life cycle of noctilucent clouds (NLC) is examined with the Lagrangian 3-D particle model MIMAS. MIMAS simulations are performed on different background conditions, i.e. LIMA and also KMCM. The mechanisms behind NLC are investigated by tracing the particles of bright ice clouds from formation to their sublimation at the lower edge of the NLC. Additionally, the sensitivity of NLC to atmospheric wave activity and particle shape is analyzed.

7.1 Summary

The dynamics of the middle atmosphere is analyzed, comparing LIMA and KMCM results to available radar and lidar measurements. Local Time variations of mean temperatures and winds in LIMA are supported by measurements, while circulation patterns and gravity waves are better realized in KMCM.

Noctilucent clouds in MIMAS-LIMA have durations, altitudes, and local time variations similar to lidar measurements, although model NLC have less small scale structure. The typical life cycle of NLC particles is analyzed by tracing a small selection of particles at high resolution. Only $\approx 10\%$ of ice particles grow to 20 nm or larger, and just around 1% grow to typical NLC particle size of 50 nm. Those large particles are visible for around 5 hours. Their lifetime is typically 1 – 4 days, increasing towards higher latitudes.

The NLC is strongly influenced by its ambient conditions: Cloud brightness reacts quickly to temperature changes, with a delay of only ≈ 1.5 hours. This implies that lidar measurements of NLC yield information about the local atmospheric background. The NLC altitude is closely linked to ambient temperature if averaged over a sufficient scale and time period (≈ 1500 km and 12 h).

Strong noctilucent clouds at 3 locations are selected in July, 2009 simulations of MIMAS-LIMA. Large particles within the ice clouds are traced backwards to their origin, for a detailed study of strong NLC life cycle. NLC particles are transported mainly westward, with a slight southward component. They nucleate at high altitudes (≈ 88 km), and grow slowly (0.3 nm/h) at the beginning of their life cycle. Turbulent diffusion dominates vertical motion at this stage. The main particle growth occurs in the H₂O-rich layer at 83 km within only a few hours, with growth rates up to 15 nm/h. The particle nucleation commonly occurs in bursts, when supersaturation is rising.

The transport and growth characteristics are very similar for different NLC events. A bright NLC at t_0 is usually preceded by a saturation maximum around $t_0 - 2$ h and an upwelling which counteracts sedimentation (≈ 10 cm/s at $t_0 - 3$ h). Turbulence

Chapter 7 Summary and outlook

also plays a role during that period: Those ice particles that are randomly moved downward often grow largest since growth conditions are optimal at the lower edge of the NLC. After t_0 , particles usually sublime within ≈ 2 hours, assisted by downward vertical winds.

The age of NLC particles at 69°N varies widely between ≈ 18 and 48 h, with an average of 36 h. At 79°N , ice particles are older (63 h) and clouds are brighter by more than a factor of 2. This is caused by the higher supersaturation and lower variability near the mesopause. For ice clouds south of 60°N , the reverse applies: Lower supersaturation and large temperature variability cause short-lived (19 h) NLC particles and ice clouds which are much less bright (below 10% of ALOMAR brightness).

NLC are significantly influenced by ice particle shape, due to altered growth, sedimentation, and optical properties. By extending MIMAS to simulate cylindrical particles with different shapes, optical NLC signatures are generated that are consistent with ALOMAR lidar observations. Cylindrical particles become larger, which increases the NLC brightness. They also have slightly shorter lifetimes and a prolonged visibility time.

Lastly, the sensitivity of NLC to gravity wave activity and scales is examined by using MIMAS with KMCM dynamics. At 69°N , model NLC using KMCM dynamic fields with zonal wave numbers ≤ 30 are similar to those from using LIMA. Additional short period gravity waves reduce the brightness and increase the altitude of NLC. NLC particles form at lower altitudes and have shorter lifetimes and visibility periods than those in environments with lower wave activity.

7.2 Outlook

There is ample scope for further analysis of the NLC morphology with MIMAS. Specifically, the sensitivity studies in Chapter 6 pose additional questions: Detailed investigation of the growth of cylindrical particles would yield a better understanding of the mechanisms involved, especially regarding vertical transport. The inclusion of non-spherical ice particles also allows a comparison of cloud brightness with satellite observations.

Related to this, further study of those components of MIMAS with poorly known parameters is warranted: The lack of dust particles smaller than 1.2 nm, the diffusion coefficients and the infrared particle heating all affect ice formation strongly. Extending the sensitivity studies and analyses as in Chapter 6 could validate and possibly optimize the microphysics used in MIMAS, especially with regard to dust cutoff radius and infrared particle heating.

The NLC simulations on KMCM dynamics are another field with potential for expansion: Improved KMCM dynamics include smaller scale dynamics than the simulation used for this study, and add tides in addition to gravity waves. This allows NLC simulations on more realistic background conditions, including a significantly smaller gravity wave scale limit. Other possibilities are a more in-depth analysis of the main phase of particle growth in bright ice clouds as in Chapter 5, the vertical motion including wave-dependent KMCM turbulent mixing coefficients, and further investigation of the anomalous decrease of NLC brightness at high latitudes.

Appendices

A Additional information on dynamics

In this chapter, additional data is provided on the dynamics of the middle atmosphere. This includes the temperature tide including lidar measurements, and analysis of the dynamic spectra in LIMA, KMCM and radar measurements.

A.1 Temperature local time dependence

In Figure A.1, the temperature local time variation in LIMA is shown, analogous to the horizontal wind components in Figure 2.6. Like for horizontal wind, there is a strong tidal signature. Another similarity is the predominance of a diurnal signal at lower altitudes around noctilucent clouds, while above 87 km there is a mix of diurnal and semidiurnal tide. At NLC altitude, the cold phase of the diurnal tide is ≈ 23 to 6 UT. This is closely linked with the local time variation of the NLC. We find a time lag of 1 h to 90 minutes between temperature and cloud brightness. The temperature and ice cloud LT variations in Figure A.1 mostly replicate those seen from Figure 2.8 and Figure 5.1.

At some locations, the LIMA thermal tide is in general agreement with resonance lidar measurements, while at others, the comparisons yield poorer results. In Figure A.2, a data set is from the IAP mobile Fe-Lidar while based at ALOMAR (J. Höffner, private communication). In the Fe-Lidar, the tide includes diurnal and semidiurnal components at all altitudes. Since the lower edge of the measurement is 84 km, a comparison is only possible above the NLC altitude. The phase of the tidal components in the Fe-Lidar measurement is very different from LIMA, cold and warm phases at 85 km are shifted to ≈ 8 h later in the measurement. As in the model, the measured tides includes a vertical phase progression, at a rate similar to LIMA but covering the

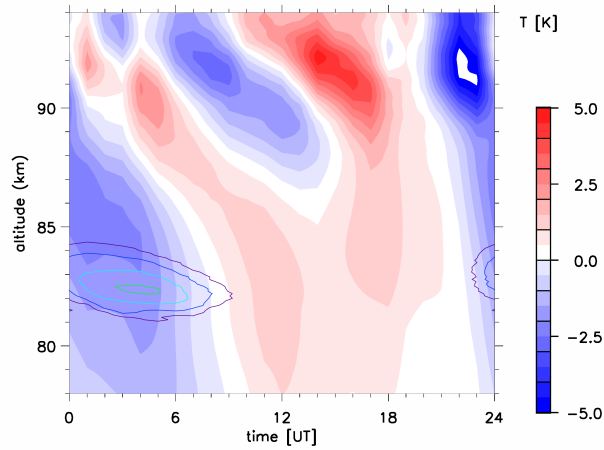


Figure A.1 Local time variation of temperature and NLC in LIMA at ALOMAR (69°N). Analogous to Figure 2.6, a July average from 2009-2012 is computed. Contour lines show the NLC local time distribution.

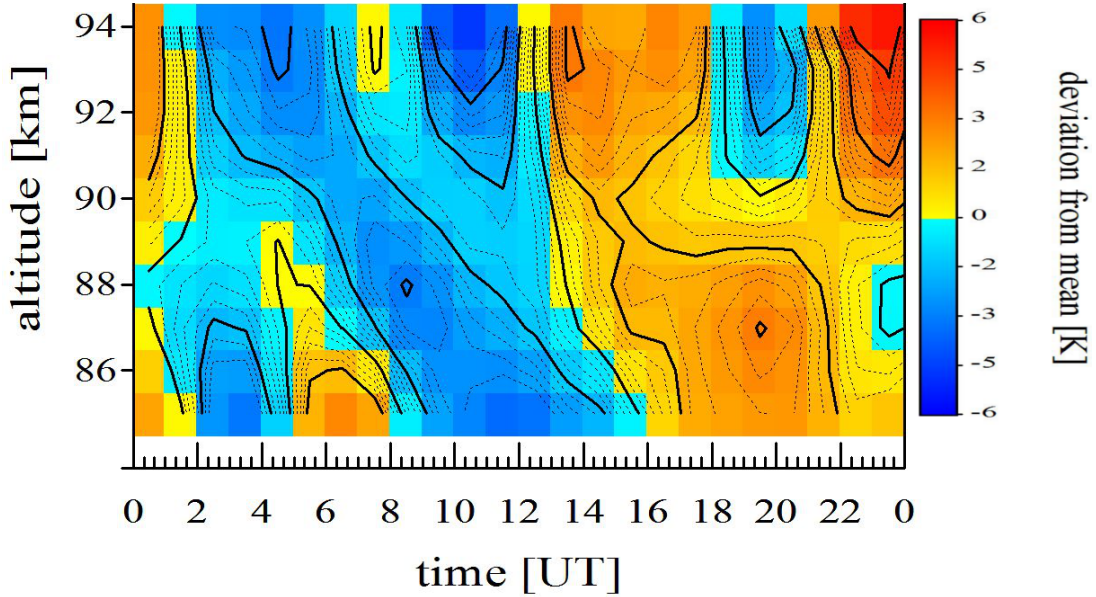


Figure A.2 Lidar measurements of temperature local time variation: Superposition of Fe-Lidar temperature measurements in July 2008-2009 at ALOMAR (J. Höffner, private communication).

whole altitude range. At the upper end of the measurement around 94 km, it is most similar to LIMA.

A second set of measured data was available from the ALOMAR Na-Lidar (T. Dunker, private communication). However, the coverage of this measurement set is very poor, thus it does not show a clearly recognizable tide because of insufficient coverage.

At the Antarctic Davis station, the statistical base is more robust than for Figure A.2. The diurnal temperature tide at Davis is in general agreement with LIMA (J. Höffner, private communication). However, this does not apply for other locations like Kühlungsborn: The IAP K-Lidar (data shown in *Gerding et al. (2013)*) produces results that significantly differ from LIMA: Here, the NLC occurs preferentially during the warm phase, indicating that meridional transport has a larger role than (small) thermal tides (private communication, M. Gerding). In summary, the various temperature tide measurements do not consistently support the LIMA local time variations. However, most of them have very poor sampling, especially compared to the Saura radar which was used to validate local time variations in winds.

For interpreting local time variations seen in the wind components and temperature as modes of atmospheric solar tides, it also helps to compare the estimated phases of the diurnal tide to those resulting from the linear tidal theory. *Chapman and Lindzen (1970)* calculated a latitude-dependent phase relationship, which for high latitudes and at 85 km altitude approaches 0 LST for maximum northward wind, 6 LST for maximum temperature, 12 LST for maximum upwelling and 18 LST for maximum westward wind. For zonal and meridional wind, this phase relationship is recognizable in both radar measurements and LIMA. For temperature, the phase of the LIMA

A.2 Fourier spectrum of waves in the MLT, in models and measurements

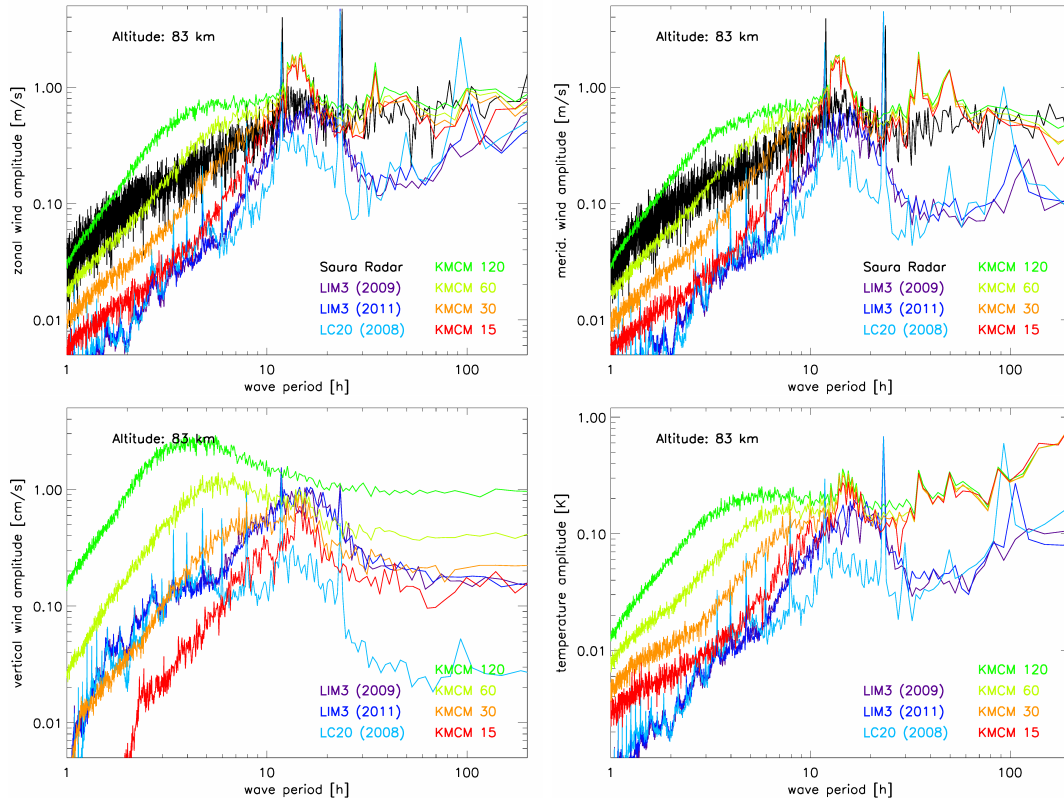


Figure A.3 Fourier spectra at 83 km altitude of zonal (upper left), meridional (upper right) and vertical (lower left) wind and temperature (lower right). All spectra include LIM3 during July of both 2009 and 2011, LC20 (July 2008), and KMCM in four versions with wavenumber limits of 120, 60, 30, and 15. All model spectra are computed individually at 120 longitude positions at 69°N and zonally averaged afterwards. The horizontal wind components additionally show 4 year average Saura MF radar measured spectra, from June to August each.

tide is at least not far off. However, only the relationships between the tidal phases are in agreement with *Chapman and Lindzen (1970)*, while the individual phases are contradicted by current measurements. This comparison includes only the diurnal tide, so it does not apply for higher altitudes where the semidiurnal tide is dominant. The linear tidal theory cannot easily be used in the mesopause region especially because of mode-coupling and dissipative effects occurring in this altitude region.

A.2 Fourier spectrum of waves in the MLT, in models and measurements

The dynamic fields of LIMA and KMCM were compared with available measurements in Section 2.3.1. Figure A.3 goes into more detail on this with an analysis of the Fourier temporal spectra at NLC altitudes (83 km). For all wind components and temperature,

Appendix A Additional information on dynamics

the spectra shown include all 4 versions of KMCM, the ECMWF-based LIM3 version and the NCEP-based LC20 version of LIMA. The radar spectra in the horizontal wind components were calculated after closing measurement gaps by interpolation, and an extension of the time period from July only to June-August in order to reduce the noise of the spectrum.

The spectra for zonal and meridional wind look quite similar with only a few differences. In both wind components, the four versions of KMCM dynamics feature slopes usually in the range $\frac{3}{2}$ to $\frac{5}{2}$ for periods shorter than 12 hours. Furthermore, the KMCM spectra are parallel to each other with successive wavenumber versions having amplitudes 2 to 2.5 times larger in this frequency range. The KMCM₁₂₀ spectra flatten out at around 4 hours, KMCM₆₀ at 6 hours, and all four spectra converge at around 12 hours. Since the KMCM data set does not include tides, there are no peaks at 12 or 24 hours in the spectra. The maximum wave amplitudes are at 15 hours, this corresponds to the inertia GW found in Section 2.3.1 and Section 2.3.2. At periods longer than 12 h, the four KMCM spectra are very close together in both zonal and meridional wind. There is one minor peak at 35 hours which cannot be linked to any of the waves described in Section 2.3.2, and another peak at ≈ 50 h that is only present in the meridional wind. Except for these features, the spectral amplitudes stay relatively constant for both u and v at long periods.

In LIMA, the horizontal wind spectral amplitudes are usually lower than KMCM₁₅ for periods below 12 h, with little variation between the two years in LIM3. The NCEP driven Twentieth Century (LC20) run has spectral amplitudes close to LIM3 for periods < 6 h, while for 6 to 12 h periods LC20 amplitudes are lower than LIM3. LC20 also prominently features multiple tidal harmonics (8 h, 6 h etc.) which are hardly noticeable in LIM3. The 12 and 24 hour main tidal peaks are strong in all LIMA versions and exceed the amplitudes at any particular wave period in KMCM. At wave periods between 12 and 24 h, LIMA spectral amplitudes are close to those in KMCM, while at longer periods they drop off considerably. For periods longer than 2 days, zonal wind amplitudes increase again to a level close to KMCM, while meridional wind amplitudes stay small. A five-day wave peak is visible in zonal and meridional wind of LIM3 in 2011, but not in 2009. In LC20, the only discernible long-period wave is a distinctive four-day wave.

The Saura radar spectrum features a considerably shallower slope for short-period waves. This is probably caused in part by measurement errors, and at time periods shorter than 2 h it is not physically significant because the sampling interval is 30 minutes. The spectral amplitudes agree best with KMCM₆₀ at 3 hours and with KMCM₃₀ around 7 h. Higher order harmonics, i.e. with period ≤ 8 h, are not prominent in the radar spectrum. This supports the tides in LIM3 compared to the LC20 version of LIMA. The tidal peaks at 12 and 24 h are very similar to LIMA as shown in Section 2.2.3. Between 12 and 24 hours, the wave amplitudes are between those of LIMA and KMCM, while for long periods above 24 h, the radar amplitudes are slightly below KMCM but considerably above LIMA. There are no distinctive peaks in the radar spectrum beyond 24 hours. In summary, the Saura spectra match KMCM₃₀ and KMCM₆₀ best at periods shorter than 12 hours and KMCM in general for wave periods longer than 24 h, while the radar agrees well with LIMA in the spectral range from 12-24 h including the tidal peaks.

A.2 Fourier spectrum of waves in the MLT, in models and measurements

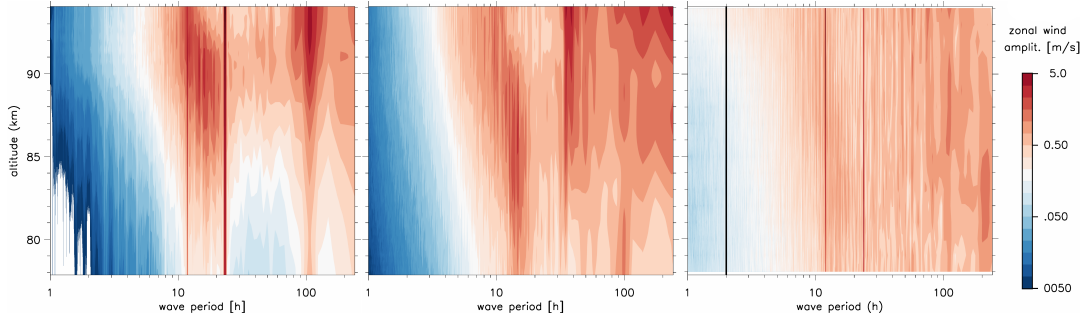


Figure A.4 Vertically resolved zonal wind spectra of LIMA (LIM3 in July 2011, left), KMCM₃₀ (middle) and the Saura radar (69°N, 16°E, right). Model spectra are taken at 69°N and averaged over 120 longitudinal positions, the radar spectrum is a 4 year average from June to August each.

Figure A.3 also shows vertical wind and temperature spectra because of their high importance for ice formation, even though no measurements are available for direct comparison here. Temperature measurements by lidar are not suitable for calculating spectra because of their short duration, and there are very few vertical wind measurements at all since its low amplitudes compared to horizontal wind make it very difficult to measure. The temperature spectra are very similar to those in the zonal wind for both LIMA and KMCM. In LIMA, the tidal peak for temperature at 12 hours is smaller than the ones for horizontal wind, while the peak at 5 days in LIM3 is more distinct in temperature than in zonal wind. As for KMCM, the 15 h peak is less clear in temperature than in wind (see Section 2.3.2), but unlike for horizontal wind, wave amplitudes go up at long wave periods.

The vertical wind spectra, shown in the lower left of Figure A.3, look significantly different from other parameters in both models. The KMCM spectra at different total wavenumbers show much greater variations in vertical wind amplitude than for the other parameters, and also do not converge for all long wave periods, but only to a lesser degree and over a short window near 15 hours. For periods below 4 hours, the amplitude ratios of successive spectrally filtered KMCM versions are close to 5, at longer periods these ratios decrease gradually towards the inertia GW peak at 15 h. The spectrum of KMCM₁₂₀ flattens out at around 3 h and at 5 h for KMCM₆₀. The LIMA vertical wind has much higher amplitudes in relation to KMCM than horizontal wind or temperature, with LIM3 amplitudes comparable to KMCM₃₀ at most wave periods. Tidal peaks in LIM3 are still visible but much smaller than for other parameters, this is consistent with Section 2.3.2 where there is no obvious westwards propagating wave in LIMA vertical wind. The LC20 version of LIMA generally has small vertical wind amplitudes but includes mainly a semidiurnal tide and multiple tidal harmonics.

Since spectra in Figure A.3 are only at one specific altitude level (83 km), Figure A.4 exemplarily shows the vertical dependence of the zonal wind spectra. Only LIM3 in July 2011, KMCM₃₀ and the Saura MF radar are included in the figure. At 83 km these spectra are identical to those shown in Figure A.3, because of this only the dependence on altitude will be discussed here.

Appendix A Additional information on dynamics

Both LIMA and KMCM show a significant vertical gradient in the wave amplitudes. It is roughly equal at all periods in LIMA, while in KMCM the gradient is stronger for shorter period waves. In comparison, the Saura radar spectrum features this vertical gradient for short-period waves only. For periods longer than the semidiurnal tide it is hardly noticeable. As a side-effect, this difference in vertical gradients causes the LIMA spectrum to agree better with the radar at higher altitudes (≈ 90 km), while the LIMA amplitudes are consistently below measured amplitudes at 83 km. Apart from generally increasing wave amplitudes at higher altitudes, the LIMA spectrum changes relatively little with altitude. In KMCM, the peak amplitude of the inertia-GW shifts towards slightly shorter periods. The most notable difference of models and measurements is the vertical rise in wave amplitudes that both LIMA and KMCM show at all periods, but this is observed by the radar data only to a much smaller extent and only for waves with periods shorter than ≈ 12 hours.

B Additional information on NLC

This appendix complements Chapter 4, Chapter 5 and Chapter 6 by adding a number of topics about the ice cloud morphology and evolution which were left out of the main part of this thesis to limit its scope. They cover a wide range of subjects, from light scattering over dust particle population to additional details of the NLC morphology in MIMAS-LIMA and MIMAS-KMCM, as well as MIMAS simulations on hybrid fields formed from LIMA and KMCM.

B.1 Light scattering on cylindrical ice particles, color ratios

The RMR lidar located at ALOMAR uses three distinct frequency channels for the Mie scatter measurements of NLC particles, 355 nm, 532 nm and 1064 nm (*Baumgarten et al.*, 2010). While the intensity of the scattered light in any of these channels is determined by size and number of particles present, intensity ratios between two channels (color ratios, CR) only depend on the distribution of particle size and shape. The latter is the reason why non-spherical particles have to be taken into account for interpreting optical measurements (*Baumgarten and Thomas*, 2006; *Rapp et al.*, 2007). In this study, the measured color ratios are compared directly to those computed from model particle distributions, so no assumptions are required for the shape distribution.

Figure B.1 shows the backscatter color ratios 355 nm/532 nm (UV/Vis) and 1064 nm/532 nm (IR/Vis) of randomly oriented cylinders for radii up to 200 nm and for aspect ratios between 0.1 and 10 (*Baumgarten et al.*, 2007). The UV/Vis ratio is high for small particles and decreases towards ≈ 100 nm (the first UV resonance) at AR=1. At radii higher than that the ratio increases again up to a peak at 153 nm (first green resonance). Shape has a large effect too: For particles between 50 and 80 nm the ratio generally decreases from needles to plates. The UV/Vis ratio for needles is lower than for AR=1 until 55 nm, for larger particles it is higher. Oblate particles (discs) have a reduced UV/Vis ratio for particles smaller than ≈ 75 nm, for larger particles it is increased.

The IR/Vis ratio rises continuously towards larger particle sizes up to the first 532 nm resonance at 153 nm, this rise is also accelerating steeply around 100 nm. The peak is around 3 for near-spherical particles at 153 nm. this was not used for the figure scaling to preserve contrast at the sizes and shapes where particles are observed. Spherical particles have the smallest attainable IR/Vis ratio among all particle shapes over a wide size range up to ≈ 100 nm. Prolate particles have larger IR/Vis ratios than

Appendix B Additional information on NLC

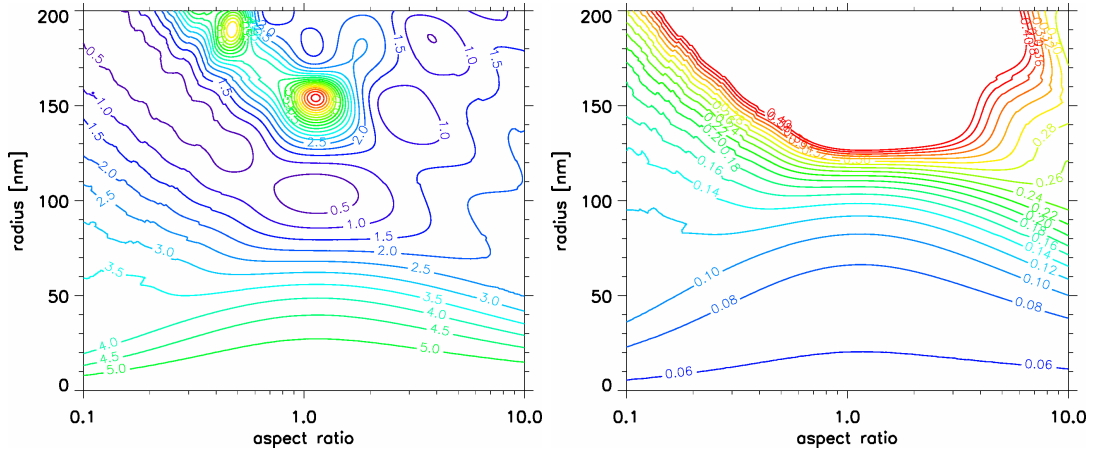


Figure B.1 Backscatter color ratios UV/Vis (355 nm/532 nm, left panel) and IR/Vis (1064 nm/532 nm, right panel) for different particle equivalent radii and aspect ratios.

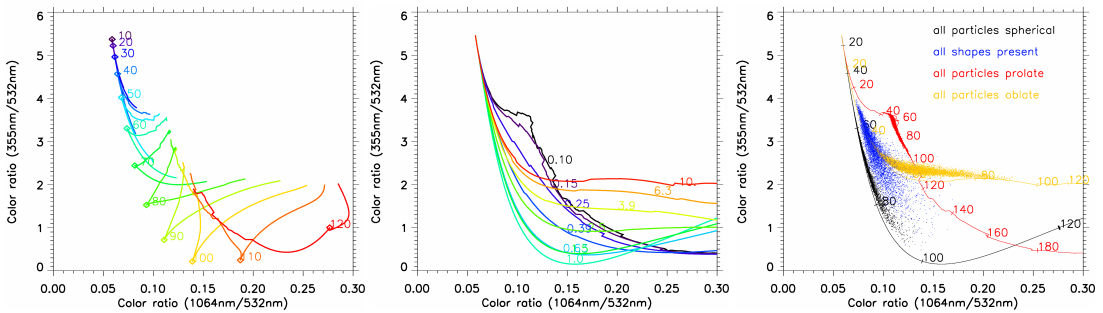


Figure B.2 Left panel: Color ratio combinations for fixed volume equivalent radius and variable shape. Middle panel: CR combinations for fixed particle aspect ratio and variable equivalent radius. Right panel: CR combinations for MIMAS-LIMA particle distributions (only spherical shape) which are assigned idealized cylindrical shapes.

AR=1 cylinders, the difference is largest around 55 nm and diminishes again for larger particles. IR/Vis is also increased for oblate (flat) particles up to about 120 nm radius, but less than for needle-shaped ones at radii smaller than 55 nm. The jagged lines occurring at high aspect ratios, esp. prolate, are due to artifacts in the calculation of the scatter coefficients. However, these are not large enough to materially alter the results.

Figure B.2 shows combinations of color ratios for single particles with variable size and aspect ratio, and CR combinations that develop from idealized particle distributions. While the dependencies for single color ratios were discussed in Figure B.1, Figure B.2 is better suited to illustrate which combinations of color ratios indicate certain particle sizes and shapes. Spherical particles and those with an AR close to 1 are recognizable by their low combined UV/Vis and IR/Vis ratios, i.e. CR combinations close to black line in the right panel. The best indicator for highly prolate

B.2 Dust particle distribution

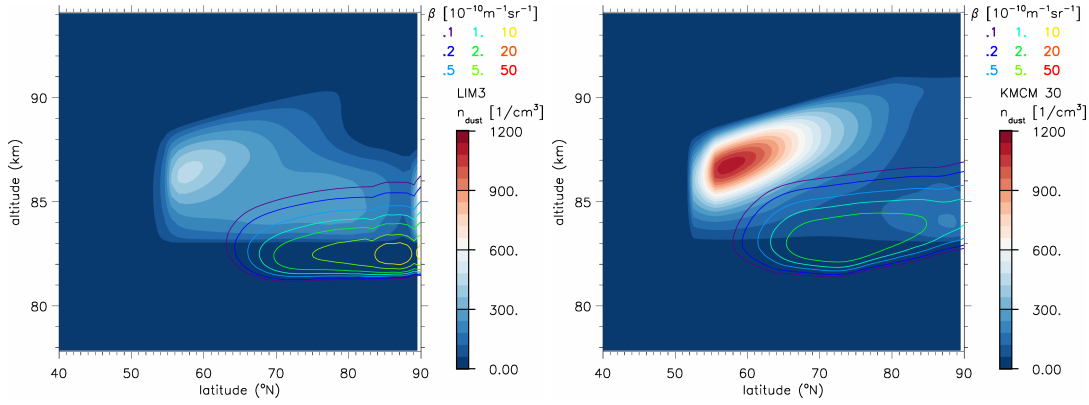


Figure B.3 July mean condensation nucleus number density (filled contours) and NLC signal (open contour lines), in MIMAS-LIMA (left panel) and MIMAS-KMCM₃₀ (right panel).

(needle-shaped) particles are high UV/Vis ratios (> 3) combined with relatively high IR/Vis ratios (> 0.1), since this combination is significantly away from the AR= 1 envelope and cannot originate from a superposition of spherical particles (of particles < 100 nm). Highly oblate (disc-shaped) particles are only clearly recognizable above ≈ 60 nm, the most reliable indicator are moderately high UV/Vis ratios (> 2) combined with high IR/Vis ratios (> 0.15). The right panel of Figure B.2 illustrates how particle distributions with highly non-spherical particles may be recognized from combinations of color ratios. In practice, the interpretation is more complex, as the well-recognizable high-AR particles are usually a minority, and non-spherical particles with smaller aspect ratios are harder to distinguish.

B.2 Dust particle distribution

The left panel of Figure B.3 shows the number density of condensation nuclei (CN). MIMAS constrains these to only those latitudes and altitudes where nucleation can occur during normal conditions (see Section 3.3.1). As a result, their spatial distribution has well defined lower, upper, and Southern boundaries. Dust particles are also distributed inhomogeneously within the MIMAS nucleation zone: The largest concentration of CN is at 86.5 km and 58°N. While technically part of the NLC domain, nucleation is rare in this area, so dust particles tend to accumulate until they are moved to a region with higher saturation. There is also a bite out above 87 km at latitudes close to the pole, since dust particles moved to this region are immediately coated by ice due to the permanent supersaturation.

The latitude gradient of the dust distribution in MIMAS-KMCM (right panel) is considerably stronger than in MIMAS-LIMA: The condensation nuclei in MIMAS-KMCM are depleted throughout the polar region, with less remaining dust at lower altitudes. In contrast, the region of high dust concentrations at lower latitudes is more pronounced compared to MIMAS-LIMA. This may result from the stronger meridional temperature gradient in KMCM in addition to the southward transport and partly

Appendix B Additional information on NLC

explains the comparatively strong NLC formation around 60°N. The strong upwelling close to the pole in KMCM combined with the southward meridional wind deplete the polar cap NLC altitudes of condensation nuclei much more than LIMA dynamics, where the dust particles are more stable in location and spatially homogenous.

B.3 Spectrum of NLC

Figure B.4 extends the spectral analysis of the dynamic fields in Section A.2 to the NLC itself. The NLC spectra resemble those in Figure A.3 to some degree: There is an increase in wave amplitudes up to a period of 12-24 h, at longer periods the amplitudes remain constant.

For LIMA, four different years of ice simulations with LIM3 dynamics were chosen. 2009 and 2010 have stronger NLC formation compared to 2011 and 2012 due to mesospheric temperature and solar cycle, this relates into higher spectral amplitudes at all frequencies. The tidal peaks in temperature and horizontal wind of LIMA dynamics are also present in Figure B.4, but less prominent compared to those in dynamic components.

The NLC spectra with KMCM show a significant transition in the variability time scale between high spectral resolution and spectrally filtered dynamics. For zonal wave numbers limit up to 60, the difference is mostly an increase in short timescale variability, very similar to horizontal wind and temperature in Figure B.4. For KMCM₁₂₀ the spectral amplitudes are much lower, corresponding to the overall lower NLC brightness (see Section 6.2.3)

The MIMAS-LIMA spectra all include a decreased slope just below 2 h and a sharp increase around 1.3 h. This is not observed for the KMCM spectra. The difference is that the MIMAS simulations with KMCM are conducted with an output resolution of 12 minutes, identical to the KMCM dynamical data Section 6.2.1. On the other hand, the LIMA simulations have an output interval of 1 h. While they were interpolated to 12 min for the purpose of computing spectra, this is not equivalent to increased time resolution, and causes artifacts as a result.

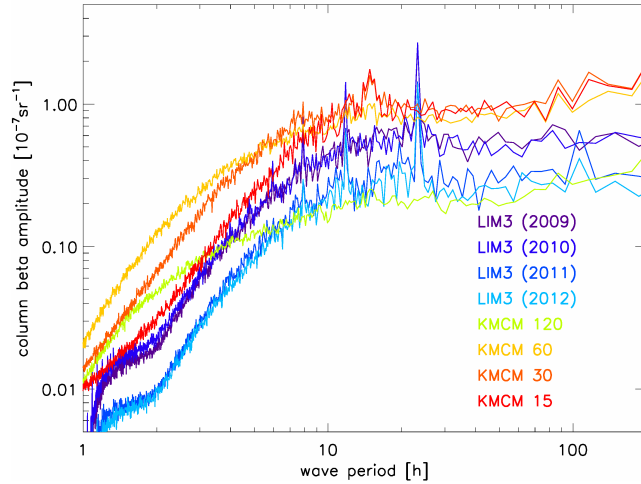


Figure B.4 Fourier spectrum of NLC backscatter signal at 69°N. Data sets use MIMAS with KMCM₁₅, KMCM₃₀, KMCM₆₀, and KMCM₁₂₀ dynamics, and MIMAS-LIM3 during July of 2009 to 2012. Spectra are computed individually for 120 longitudinal positions and then zonally averaged.

B.4 Additional ice cloud morphology of MIMAS-KMCM

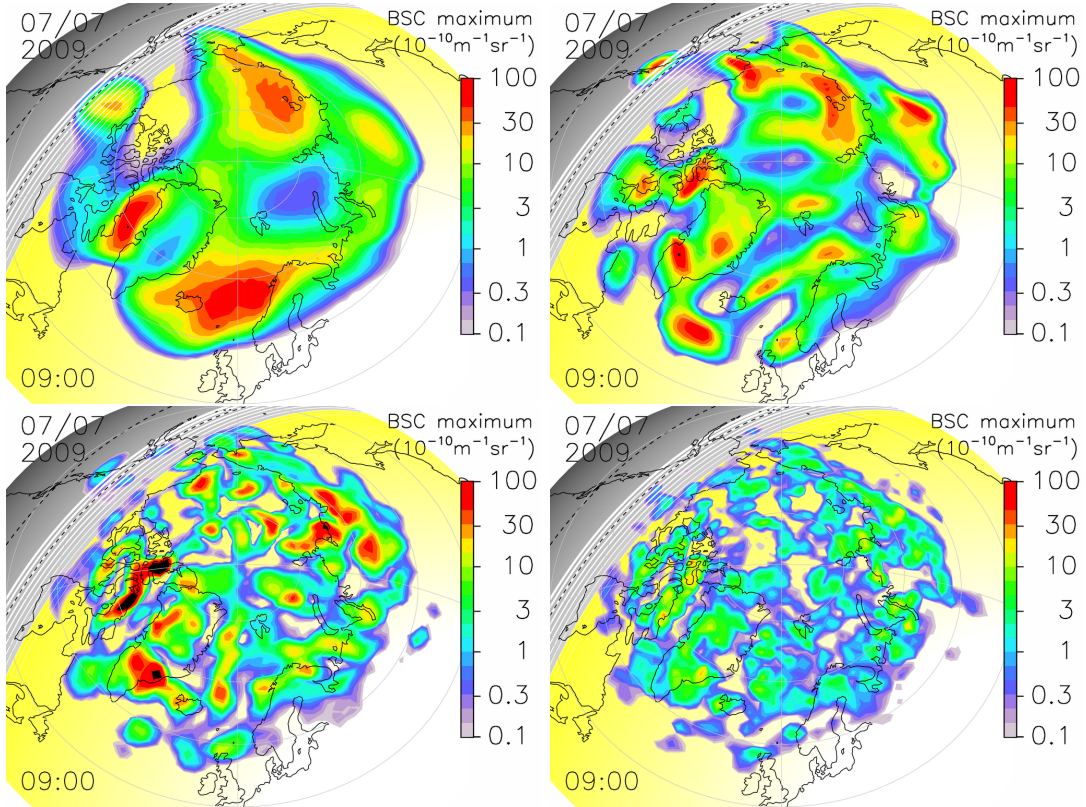


Figure B.5 Snapshot of MIMAS noctilucent cloud analogous to the left panel of Figure 4.1. The ice cloud is at the same point in time, but simulated on 4 different sets of spectrally filtered KMCM output. Upper left: KMCM_{15} , Upper right: KMCM_{30} , Lower left: KMCM_{60} , Lower right: KMCM_{120} .

B.4 Additional ice cloud morphology of MIMAS-KMCM

Figure B.5 shows snapshots of the NLC in MIMAS-KMCM, comparable to Figure 4.1 for MIMAS-LIMA. The differences in the resolved scales between the spectrally filtered KMCM data sets and LIMA are clearly visible in the ice cloud morphology. NLC in MIMAS-KMCM have a much higher spatial resolution, resulting from the smaller scale of dynamic waves. The only KMCM data set with similar spatial resolution as LIMA is KMCM_{15} . NLC using KMCM_{30} or KMCM_{60} dynamics are much more structured on scales around 1000 km than ice clouds in MIMAS-LIMA, while the cloud brightness is not strongly reduced compared to MIMAS- KMCM_{15} . Only in MIMAS- KMCM_{120} are dynamic fluctuations too strong for bright NLC to form in this snapshot. Cloud brightness in all MIMAS- KMCM_{120} data sets reaches its maximum at While ice cloud

The different latitudinal structure of ice clouds on KMCM dynamics is another feature that is easily visible in Figure B.5: With all KMCM data sets, the MIMAS ice clouds are brightest around 70-75 dg N, as discussed in Section 6.2.2. At latitudes around 60°, ice clouds in MIMAS-KMCM are considerably stronger than in MIMAS-LIMA, while at the pole NLC in MIMAS-LIMA are brighter. As a consequence of the

Appendix B Additional information on NLC

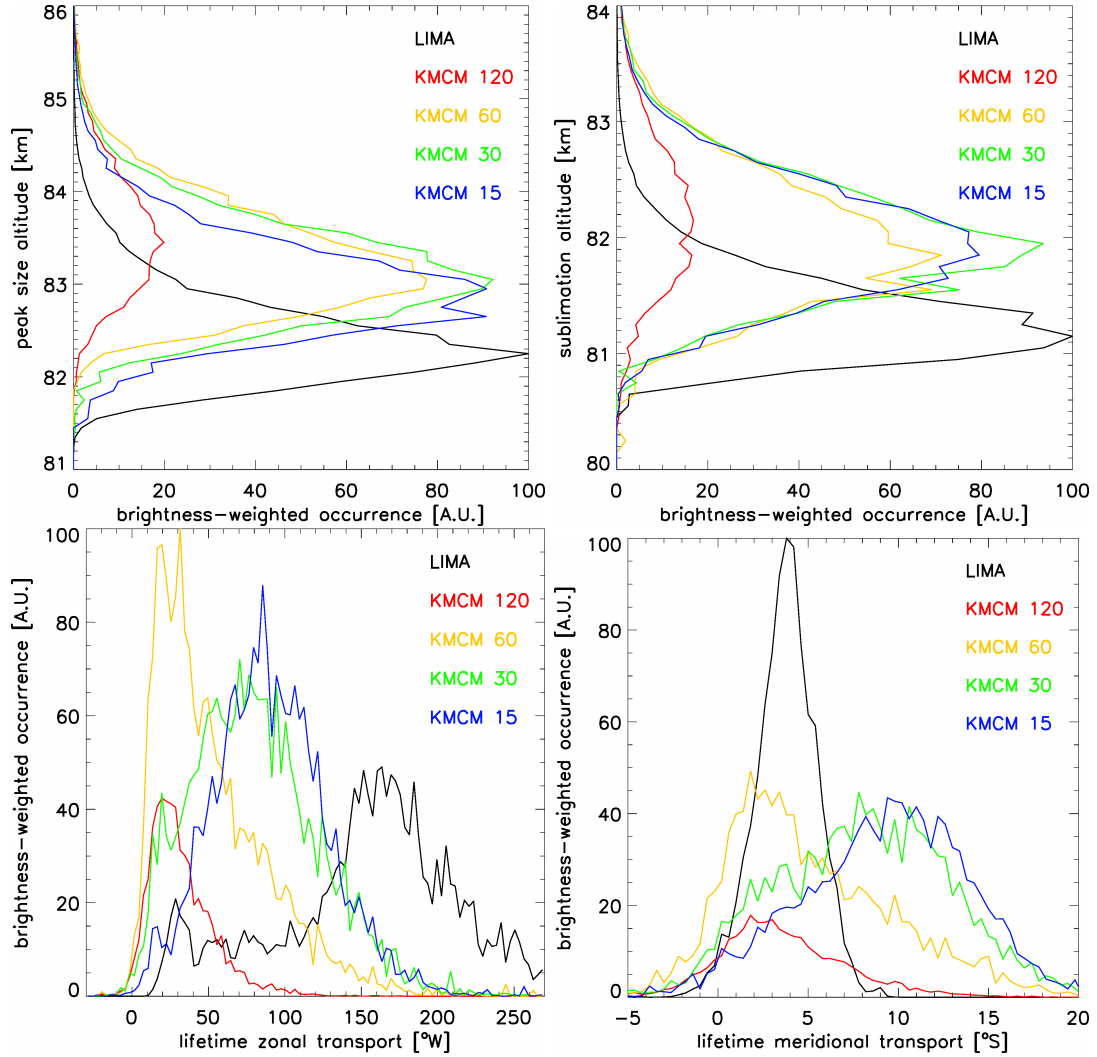


Figure B.6 Additional life cycle parameters of 40,000 trajectories in MIMAS-LIMA and MIMAS-KMCM_{15–120} at 67–72 °N, analogous to Figure 6.8. Upper row: Altitude of maximum particle radius and of sublimation. Lower row: Lifetime transport in zonal and meridional directions.

different latitude dependence, "voids", i.e. areas without NLC that are enclosed by NLC, are much more common in MIMAS-KMCM (at all spectral resolutions).

Figure B.6 shows the dependence on wave spectrum of several NLC parameters not included in Figure 6.8. The altitude of peak particle size (upper left panel) is very similar to the β -peak in Figure 6.7 for the different data sets and shows the same dependence on the wave spectrum. On the other hand, the sublimation altitude (upper right panel) is very stable at 82 km between the MIMAS-KMCM data sets: The only slight deviation is an increase by 0.2 km in MIMAS-KMCM₁₂₀, indicating that the lower edge of the NLC is less sensitive to the wave spectrum. Sublimation altitude in MIMAS-LIMA is lower by 0.6 km, resulting from the differences in the temperature

B.5 NLC simulation with hybrid LIMA+KMCM dynamics

profile and upwelling.

The lower two panels of Figure B.6 show the zonal and meridional transport of the NLC particles during their life cycle. These are determined by particle lifetime and the typical mesospheric winds in LIMA and KMCM. Between the KMCM data sets, both transport components decrease with increasing wave activity because of the lower particle age in MIMAS-KMCM₆₀ and MIMAS-KMCM₁₂₀. Zonal transport distance in MIMAS-LIMA is far larger than with any KMCM data set, while only MIMAS-KMCM₁₂₀ has less meridional transport than MIMAS-LIMA. Since the mean circulation of KMCM was shown in Figure 2.4 to agree better with radar measurements than LIMA, the KMCM derived values can be used as an alternative estimate for the NLC particle transport distance. The mean transport distances with MIMAS-KMCM₃₀ is similar to the estimate in Section 5.3.1.

B.5 NLC simulation with hybrid LIMA+KMCM dynamics

While the KMCM horizontal winds are in good agreement with measurements, the ice cloud morphology of MIMAS using these dynamic fields deviates from observations, most notably in the latitude dependence of cloud brightness (see Section 6.2.2).

For this reason, it was attempted to combine the mean atmospheric state and tides from LIMA with dynamic wave structure from KMCM. To this end, KMCM₁₂₀ and KMCM₃₀ dynamic fields were subtracted from each other to extract KMCM dynamics containing only gravity waves with zonal wave numbers 31-120. These gravity waves were then superimposed on LIMA dynamics. The resulting synthetic dynamic fields contain the mean atmospheric state (temperature and circulation) from LIMA, tides from LIMA, and short-period gravity waves from KMCM. MIMAS ice simulations on these fields are called MIMAS-Hybrid. The comparison with radar winds in Section A.2 showed that the amplitudes of short-period GW in KMCM₁₂₀ are somewhat too strong, likely a result of the zonal wave number cutoff at 120. The synthetic fields allow a reduction of this problem, by multiplying wave amplitudes in all dynamic parameters with a factor which makes them compatible with measurements. In addition to using the full amplitudes from KMCM wave numbers 31-120 (MIMAS-Hybrid_{full}), synthetic fields with $\frac{1}{2}$ (MIMAS-Hybrid_{half}) and $\frac{1}{4}$ (MIMAS-Hybrid_{quarter}) wave amplitudes are constructed.

These results were not discussed in the main part of this thesis since the physical stringency of dynamic fields constructed in such a way is dubious. However, they are included here as they are helpful in interpreting the NLC morphology of MIMAS-KMCM. Once KMCM dynamics are available that include thermal tides and have temperature profiles more consistent with observations, there will no longer be any requirement for measures such as the LIMA-KMCM hybrid dynamics.

Figure B.7 shows MIMAS-Hybrid temperature and NLC time series at ALOMAR, analogous to Section 2.3.1. The KMCM GW in the temperature fields are clearly visible even at one quarter wave amplitude. At half and full wave amplitudes, the temperature time series resembles the lidar measurement in Figure 2.8 to a large degree because of the mix of tides and gravity waves. The changes in the NLC morphology

Appendix B Additional information on NLC

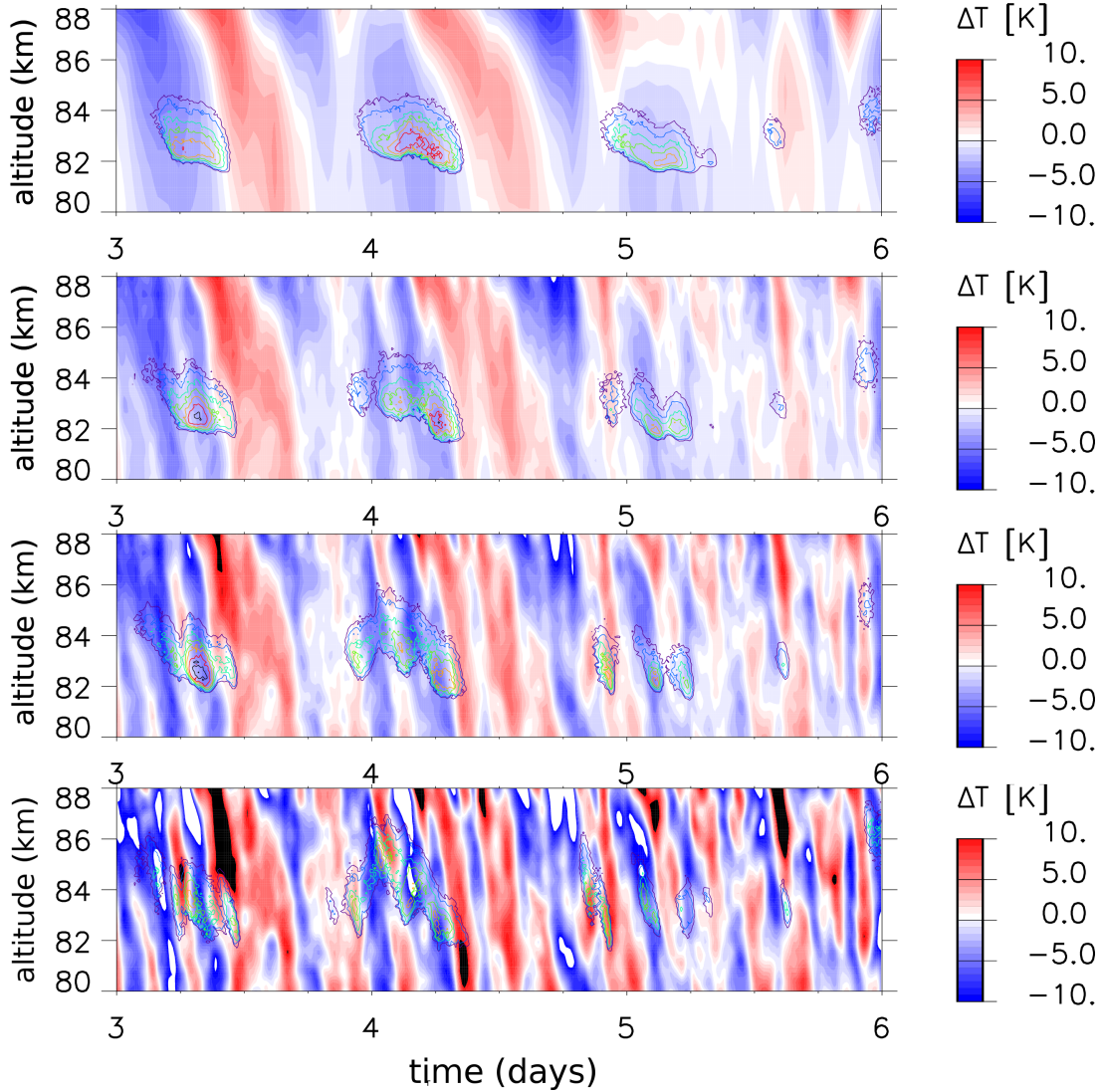


Figure B.7 4 day time series of MIMAS NLC, simulated with LIMA+KMCM hybrid dynamic fields. Top panel: LIMA, Upper middle: Hybrid of 25% of KMCM wave amplitude. Lower middle: Hybrid (50% wave amplitude), Bottom panel: Hybrid (full KMCM wave amplitude). KMCM waves include zonal wave numbers 31-120.

from increasing wave amplitudes in MIMAS-Hybrid are similar to those in MIMAS-KMCM: The short-period waves greatly increase the temporal variability of ice clouds, both in brightness and in altitude. MIMAS with Hybrid_{half} and Hybrid_{full} dynamics features NLC that change brightness and altitude on time scales of ≈ 4 hours, and cover a wide altitude range from ≈ 81.5 -86.5 km. This resembles the measured NLC in Figure 4.2 more than NLC in MIMAS-LIMA do. The local time dependence that stems from the LIMA tidal signal is retained, but smoothed compared to LIMA, also similar to Figure 4.2.

In Figure B.8, snapshots of MIMAS-Hybrid with different wave amplitudes are

B.6 Zonal propagation of ice clouds

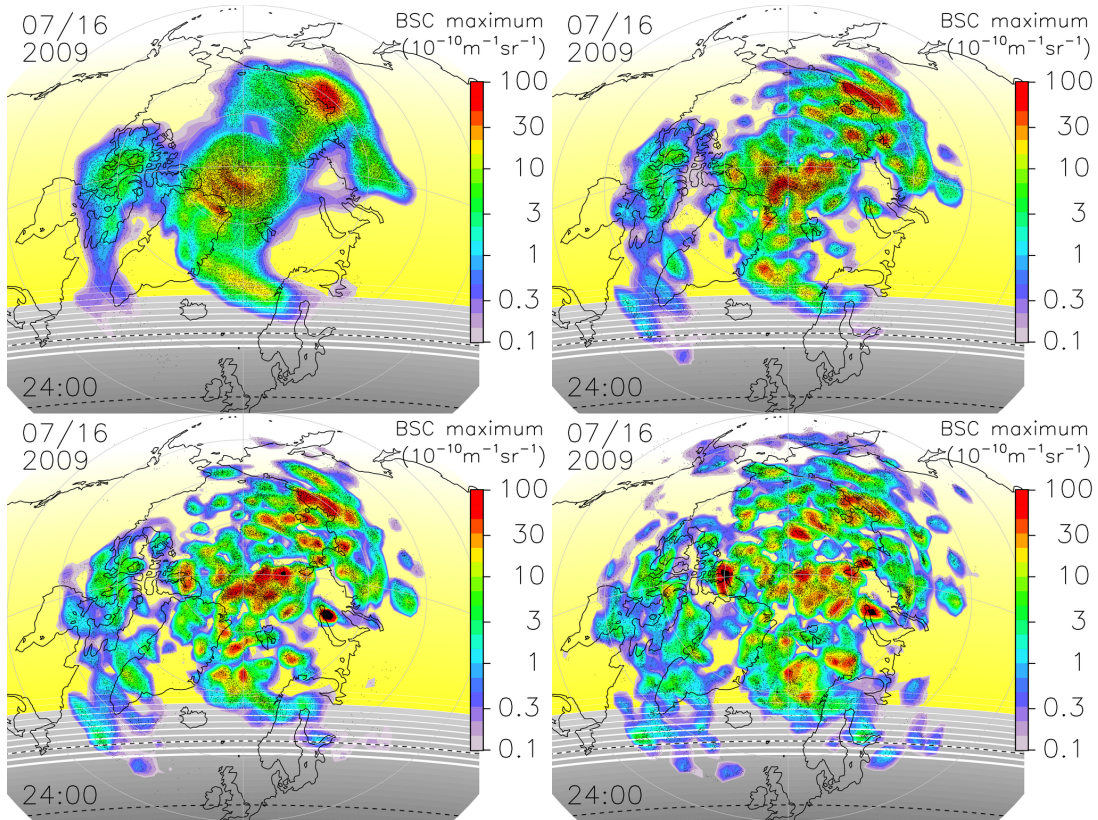


Figure B.8 Snapshot of MIMAS NLC, simulated with LIMA+KMCM hybrid dynamic fields. Upper left: LIMA, Upper right: Hybrid of 25% of KMCM wave amplitude. Lower left: Hybrid (50% wave amplitude), Lower right: Hybrid (full KMCM wave amplitude). KMCM waves include zonal wavenumber 31-120.

shown, analogous to Figure B.5. Compared to the LIMA snapshot, NLC in MIMAS-Hybrid have much higher spatial variability, hybrid fields with half wave amplitudes are sufficient for most of the variability increase. However, the large-scale structure of the NLC still resembles LIMA to a large extent: Unlike for MIMAS-KMCM, the latitude dependence of MIMAS-Hybrid NLC brightness is very close to that of MIMAS-LIMA, with the brightest NLC close to the pole. The outer edge of the NLC region is slightly further south in MIMAS-Hybrid: The strong GW allow occasional development of NLC in areas where the average temperatures in LIMA no longer allow the growth of large particles.

In summary, MIMAS-Hybrid generates a NLC morphology that is clearly improved compared to MIMAS-KMCM and MIMAS-LIMA.

B.6 Zonal propagation of ice clouds

Figure B.9 demonstrates how horizontal wave propagation in the background dynamics (especially temperature) influences the zonal propagation in the NLC. Analogous to

Appendix B Additional information on NLC

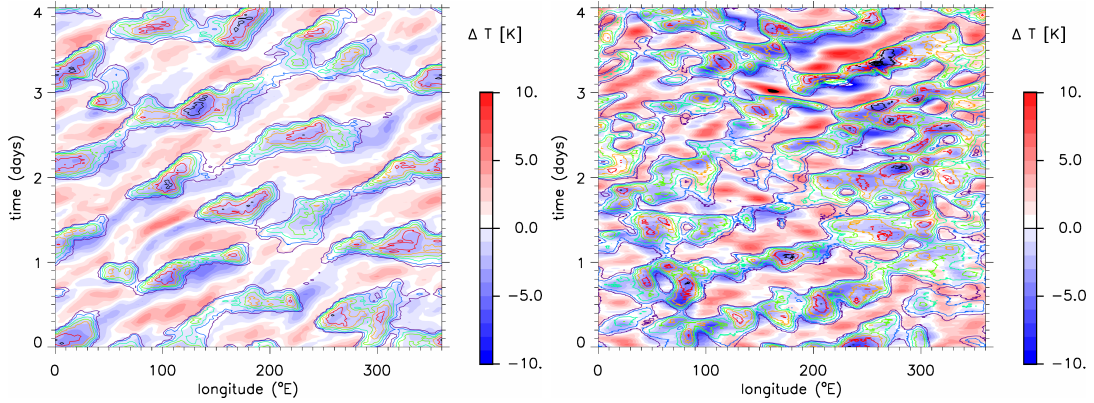


Figure B.9 Similar to Figure 2.9, but showing the zonal propagation of temperature and NLC at 83 km, 69°N on different dynamic fields. Left panel: MIMAS-LIMA (LIM3), Right panel: MIMAS-KMCM₃₀.

Section 2.3.2, zonally resolved temperature at the ALOMAR latitude of LIMA and KMCM₃₀ is shown over a period of 4 days. Unlike in Figure 2.9 the NLC albedo (column backscatter signal) is included. For MIMAS-LIMA, the eastward propagating inertia-GW (Section 2.3.2) are present in the ice cloud, along with the tidal signal. The slower phase speed of the inertia-GW makes these often more visible than the tide. This leads to model NLC apparently moving eastward in some places for a few hours. NLC appear preferentially during the cold phase, although the correlation is not very high as seen also in Section 4.3.

As KMCM₃₀ lacks the small scale eastward propagating gravity waves of KMCM₁₂₀, only the inertia-GW with periods around 15 h are visible in the temperature. These waves are also present in the MIMAS-KMCM NLC. However, due to their intermittent nature there is no clearly recognizable horizontal phase propagation of ice clouds in MIMAS-KMCM₃₀. Section 4.3.1 showed a slightly better correlation of local temperature with MIMAS NLC for KMCM than for LIMA, this is also visible in this figure.

B.7 Additional nucleation-related statistics of strong NLC

In Figure B.10, altitude and ambient temperature at nucleation are shown. Most particles nucleate around between 87 and 90 km with an average nucleation altitude of 87.8 km. There is also a weaker secondary maximum around 85.5 km. This low nucleation is mostly due to the late nucleating ice, i.e. young particles.

The temperature where nucleation takes place is usually within the range of 120 to 140 K, in a monomodal distribution with an average of 130 K. The slight peaks in the temperature distribution which occur in regular 1 K intervals are a model artifact. In MIMAS-LIMA, the temperature used for determining the individual particles' individual saturation is rounded to the next lower integer for computational speed, so nucleation typically occurs when ambient temperatures fall just below an integer

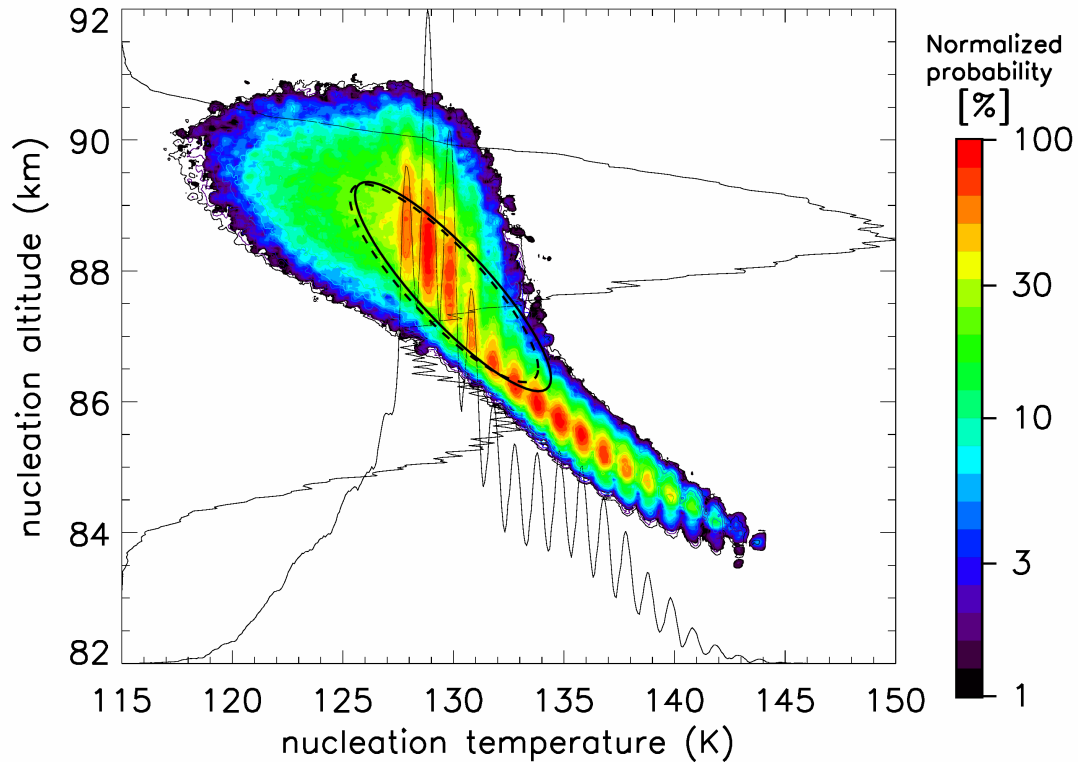


Figure B.10 Altitude and ambient temperature at ice nucleation for 50 NLC events at 69°N. Contours show the distribution using LPA (filled) and SPA (empty lines). The horizontal and vertical curves show the one-dimensional distributions of nucleation temperature and altitude, respectively, using LPA (signal-weighting). The ellipses show mean, distribution width, and covariance for LPA (solid line) and SPA (dashed).

value.

Altitude and temperature of nucleation are strongly correlated, as expected from the vertical gradient of both temperature and H₂O partial pressure. The low nucleating ice particles form at somewhat lower saturation ratios compared to those created higher up. This requires larger condensation nuclei, which is consistent to the nucleus size distribution in the late bursts of Figure 5.12.

The dependence of nucleation altitude and temperature on the size of the coated dust nucleus are also estimated, as for ice particle age in Figure 5.12. For the altitude of nucleation an adjusted value of 88.2 km is calculated, while for nucleation temperature the adjusted estimate is 128 K, slightly below 2 K colder than the value in MIMAS-LIMA.

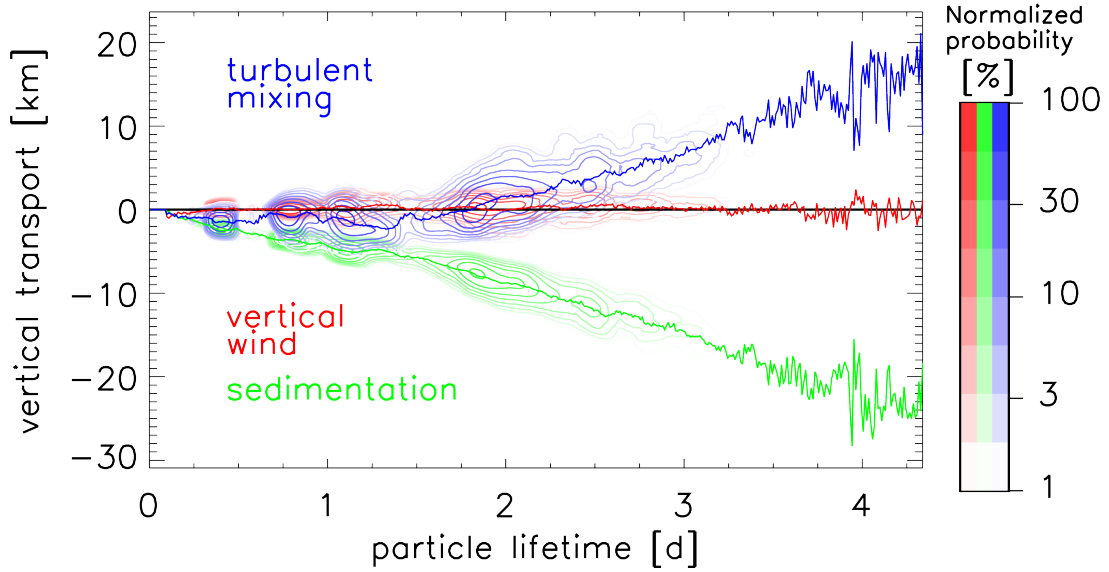


Figure B.11 Vertical transport components of strong ice particles over their whole life cycle (LPA). Contours show the frequency distribution of the lifetime transport components, normalized to the maximum value. The horizontal profiles show the mean lifetime transport components separated by particle age.

B.8 Vertical transport over particle lifetime

Figure B.11 shows the contributions to vertical transport over particle lifetime (LPA). The lifetime sedimentation increases close to linear with the particle age. Ice particles which are 48 hours old sediment a distance of ≈ 9 km during their lifetime on average. Vertical wind has only a very small contribution to particle motion, when integrated over the particle lifetime. While some particles experience an up- or downwelling of more than 1 km over their lifetime, the wind contribution to vertical transport is negligible on average, at least compared to the other components. Diffusion is the most variable component, with life cycle turbulent transport of particles of the same age differing by as much as 10 km. Particles less than ≈ 40 hours old are primarily transported downward before their main particle growth. For older particles, this downward component is compensated by their early upward motion.

B.9 Additional analysis of particle life cycle at different latitudes

Figure B.12 shows the mean NLC parameters over the complete particle life cycle at ALOMAR, similar to Figure 5.5 for the sample NLC. While its features can be discussed with Figure 5.5 and Figure 5.8, it is included here to show the ALOMAR equivalent for the upper panels of Figure 5.14 and Figure 5.15.

The lower panel of Figure B.13 shows the components of vertical particle movement, which looks very similar compared to that in Figure 5.9. The upwelling during the

B.9 Additional analysis of particle life cycle at different latitudes

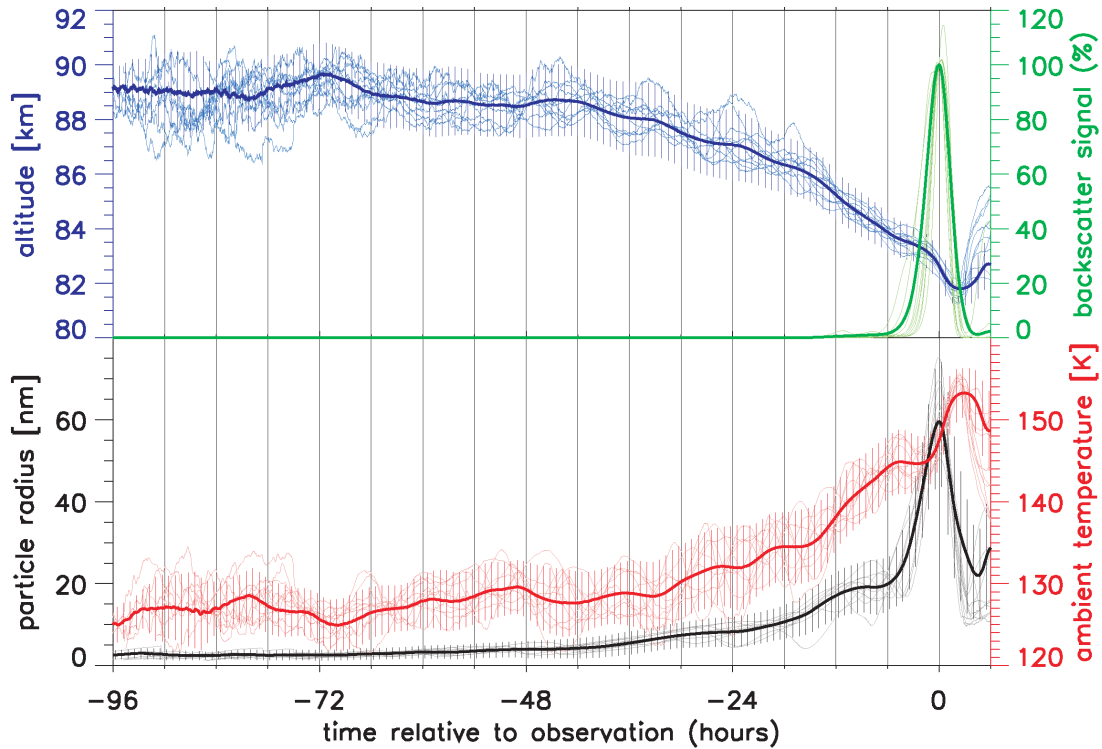


Figure B.12 50 event superposition of NLC parameters similar to Figure 5.5. Thick lines show the ensemble mean, while thin lines are trajectories of 10 single NLC, the same as in Figure 5.7. Vertical bars show the standard deviation of the superimposed distribution. (from *Kiliani et al.* (2013))

main growth phase is just as recognizable as the downward turbulent transport during this period. In this context, the main growth phase is even slightly shorter at 79°N , since both of these peaks start 1-2 hours closer to t_0 compared to 69°N . The upward diffusion for old particles from $\approx t_0 - 72$ h to $t_0 - 24$ h is more clearly visible than at ALOMAR, since the mean particle age is higher, making the average less noisy.

At latitudes south of 60°N , features of the early particle history such as the upward turbulent motion are not well recognizable. However, the vertical transport in the main growth phase shows the same pattern as at 69°N and 79°N . The timing of zero vertical wind in the NLC occurs around $t_0 - 1$ h, whereas at ALOMAR it occurs at $t_0 - 0.3$ h and at Spitsbergen almost exactly at t_0 .

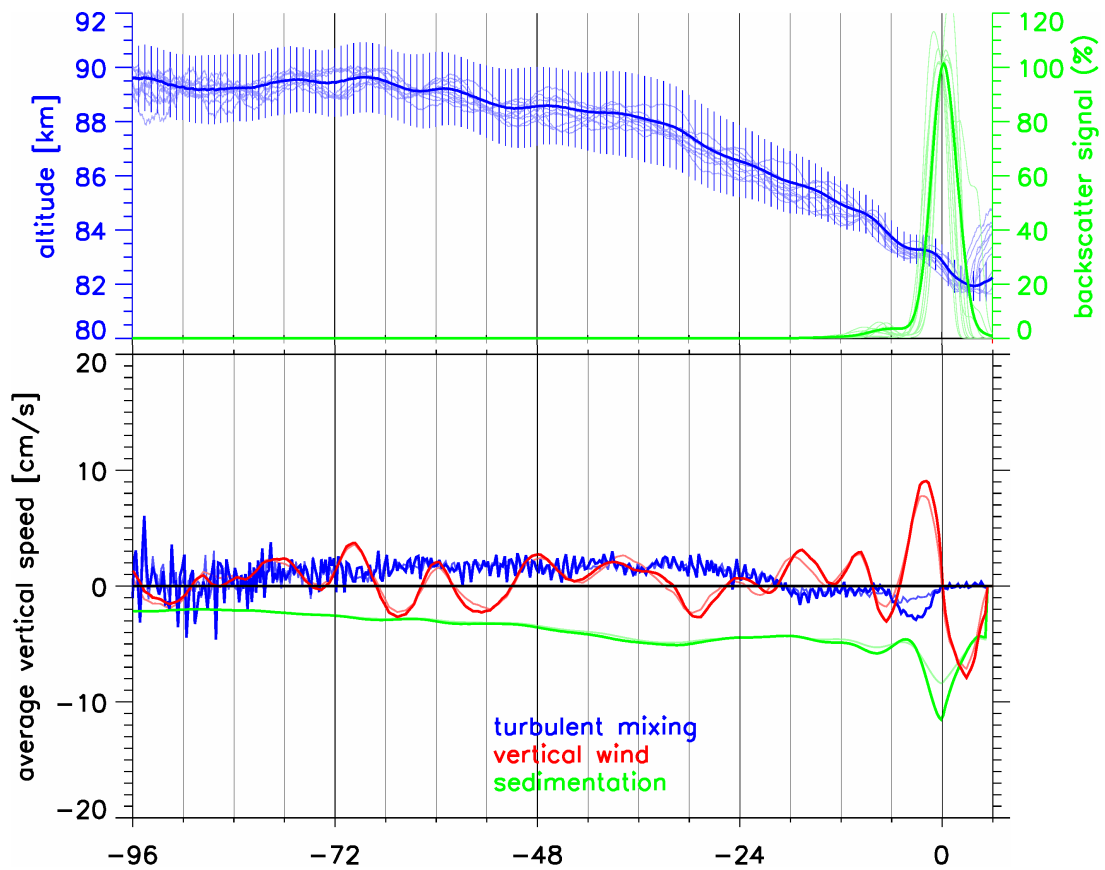


Figure B.13 Superposition of 50 strong NLC events observed at Spitsbergen (79°N, 11°E). Upper panel: Time series of vertical particle motion and backscatter signal, see Figure B.12. Lower panel: Components of vertical motion, see Figure 5.9.

B.9 Additional analysis of particle life cycle at different latitudes

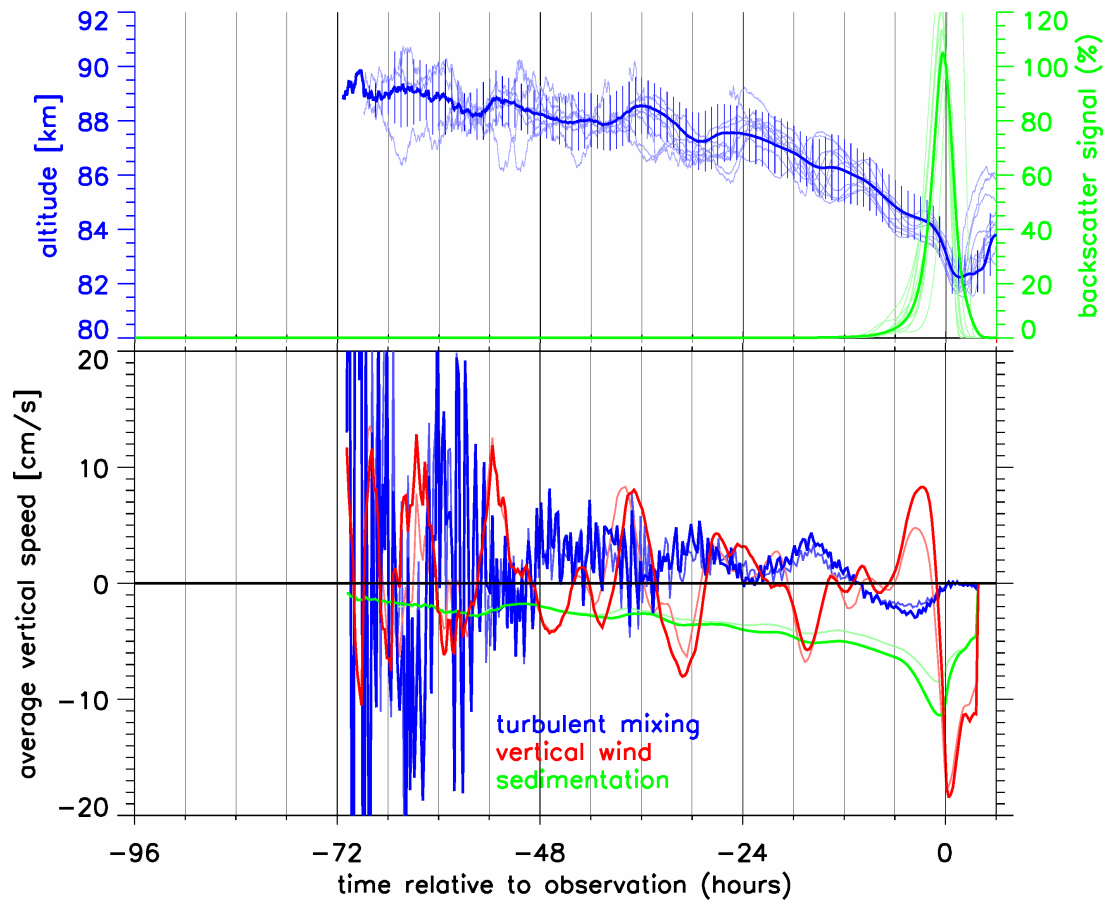


Figure B.14 Evolution of a superposition of 50 NLC events observed south of the 60°N latitude circle, analogous to Figure B.13. For detailed information, see also the captions of Figure B.12, Figure 5.9, and Figure 5.11.

C Technical details of MIMAS

In this appendix, more details are given concerning the physical mechanisms of NLC and their implementation in MIMAS. Additionally, some technical improvements to MIMAS are introduced which concern the random number generation, the dust nucleus relocation algorithm, and the interpolation of dynamic fields.

C.1 Water vapor transport scheme

The continuity equation (3.2) is a partial differential equation for which exact solutions are usually not available in geophysical applications. A model which advects atmospheric constituents with winds thus requires a transport scheme that solves (3.2) numerically with various degrees of accuracy.

Such an algorithm should fulfill a number of requirements, apart from computational simplicity: It should be conservative, i.e. the mass of the tracer in the model domain should stay constant. It also should be sign preserving, which means it avoids negative tracer concentrations. Monotonicity means that existing peaks and minima are preserved and no new ones created, non-diffusivity that peaks and minima are not broadened.

It is not possible to combine all of these requirements perfectly: Monotonicity and sign preservation are linked and best realized in simple schemes like the first-order upstream method. However, these tend to have large false (numerical) diffusion which is highly undesirable for an advection scheme. Higher order algorithms can reduce the diffusion greatly, but the calculations are more complex and they produce spurious peaks and negative concentrations. These can be suppressed to a certain degree with sophisticated filters (*Dabdub and Seinfeld, 1994*).

Current transport schemes adjust and limit the mass flux around local extrema to limit diffusion without creating false peaks (*Bott, 1992*). The one used in MIMAS is described in *Walcek and Aleksic (1998)*; *Walcek (2000)*. It is monotonous and mass conserving with very low numerical diffusion of structures at least two grid cells wide.

In numerical solutions for partial differential equations such as (3.2), grid size and time step have to be chosen carefully to ensure numerical stability. This is equivalent to fulfilling the Courant-Friedrichs-Lewy condition

$$C = \frac{u \cdot \Delta t}{\Delta x} \leq C_{\max} \tag{C.1}$$

where Δt is the time step and Δx the length interval (i.e. grid size). C is called the Courant number, the maximum stable value C_{\max} is typically 1. In MIMAS, the

Appendix C Technical details of MIMAS

time step for H₂O advection was set to 90 seconds for that reason, so (C.1) is always fulfilled even for maximum vertical wind amplitudes and zonal transport close to the pole, where Δx is minimal because of the coordinate singularity.

C.2 Diffusion scheme: Crank-Nicholson

The computation scheme used in MIMAS for water vapor diffusion is the Crank-Nicolson discretisation (*Press et al.*, 2002), a second-order implicit numerical solution of (3.3). It is

$$\frac{c_i^{n+1} - c_i^n}{\Delta t} = \frac{D}{2(\Delta x)^2} \cdot ((c_{i+1}^{n+1} - 2c_i^{n+1} + c_{i-1}^{n+1}) + (c_{i+1}^n - 2c_i^n + c_{i-1}^n)) \quad (\text{C.2})$$

where c_i^n is the concentration of the bin number i at time step n . With $r = \frac{D\Delta t}{2(\Delta x)^2}$ it transforms to the set of linear equations

$$-r \cdot c_{i+1}^{n+1} + (1 + 2r) \cdot c_i^{n+1} - r \cdot c_{i-1}^{n+1} = r \cdot c_{i+1}^n + (1 - 2r) \cdot c_i^n + r \cdot c_{i-1}^n. \quad (\text{C.3})$$

As a tridiagonal matrix, this can be solved with the efficient Thomas algorithm. Since the Crank-Nicolson scheme is implicit, numerical stability is less problematic than with the advection scheme (Section C.1). Even at altitudes with high K_{zz} values, a time step of 3 minutes is sufficient for modeling H₂O diffusion.

C.3 UV flux parametrization, photolysis equation

The rate of photolysis is determined by the reaction cross-section, the H₂O concentration and the solar UV flux $\phi(z, \chi, \lambda)$ at altitude z , solar zenith angle χ and wavelength λ . *Chabrillat and Kockarts* (1997, 1998) describe the attenuation by O₂ with a reduction factor

$$R_M(z, \chi) = \frac{1}{\Phi_\infty} \cdot \int_{121.4\text{nm}}^{121.9\text{nm}} \phi(z, \chi, \lambda) d\lambda \quad (\text{C.4})$$

where Φ_∞ is the solar flux at the top of the atmosphere. $R_M(z, \chi)$ is the proportion of the Lyman- α flux that penetrates to a particular altitude at a given solar elevation. *Chabrillat and Kockarts* (1997) give the parametrization

$$R_M(z, \chi) = \sum_{i=1}^3 b_i \cdot e^{-c_i \cdot N_{\text{O}_2}(z, \chi)} \quad (\text{C.5})$$

where N_{O_2} is the oxygen slanted column number density in the direction of the sun. b_i and c_i are fit coefficients derived by photochemical modeling and measurements. Finally, N_{O_2} is calculated as

$$N_{\text{O}_2}(z, \chi) = \frac{p_{\text{O}_2}(z) \cdot H}{k_B \cdot T} \cdot \sec \chi = \frac{p_{\text{O}_2}(z) \cdot N_A}{m_{\text{Air}} \cdot g} \cdot \sec \chi \quad (\text{C.6})$$

with $p_{\text{O}_2}(z)$ the oxygen partial pressure at altitude z (21% of total pressure), H the scale height and k_B the Boltzmann constant. The right side of the equation is derived by the relationship $H = \frac{N_A \cdot k_B \cdot T}{m_{\text{Air}} \cdot g}$ for the scale height, here N_A is Avogadro's constant, m_{Air} the molar mass of air and g the gravitational acceleration. The $\sec \chi$ term describes how the optical path of incident radiation increases when the sun is not in zenith. This is an approximation because of Earth's curvature, it becomes increasingly inaccurate as the sun approaches the horizon.

With this parametrization, the photodissociation rate at a given altitude is

$$J_{\text{H}_2\text{O}}(z, \chi) = \Phi_\infty \cdot R_M(z, \chi) \cdot \sigma_{\text{H}_2\text{O}} \cdot c_{\text{H}_2\text{O}}(z) \cdot \rho(z). \quad (\text{C.7})$$

In (C.7), $c_{\text{H}_2\text{O}}(z)$ is the water vapor mixing ratio and $\rho(z)$ the air density. The H_2O photodissociation cross-section $\sigma_{\text{H}_2\text{O}}$ was taken from *Lewis et al.* (1983), here a constant value of $1.53 \cdot 10^{-17} \text{cm}^2$ is used since the wavelength dependence of $\sigma_{\text{H}_2\text{O}}$ within the Ly- α line width is small.

C.4 Particle advection

In order to model the movement of particles, the equation of motion $\frac{d}{dt} \mathbf{x}_n = \mathbf{u}(\mathbf{x}_n)$ has to be solved. \mathbf{x}_n is the three-dimensional coordinate of the particle n and $\mathbf{u}(\mathbf{x}_n)$ the wind vector at its position. This is idealized since it only describes advection. The full components of the equation of motion are

$$\frac{dx_n}{dt} = u(\mathbf{x}_n) \quad \frac{dy_n}{dt} = v(\mathbf{x}_n) \quad \frac{dz_n}{dt} = w(\mathbf{x}_n) + w_{s,n} + w_{t,n} \quad (\text{C.8})$$

where $u(\mathbf{x}_n)$, $v(\mathbf{x}_n)$, and $w(\mathbf{x}_n)$ are the zonal, meridional, and vertical wind components at the position of particle n while x_n , y_n are the particle's zonal and meridional distance from a reference point and z_n its altitude. $w_{s,n}$ and $w_{t,n}$ are sedimentation rate and turbulent diffusion for particle n , described further down. MIMAS solves (C.8) with the first-order forward Euler method for a displacement per time step of

$$x_n^{i+1} = x_n^i + u(\mathbf{x}_n^i) \cdot \Delta t \quad (\text{C.9a})$$

$$y_n^{i+1} = y_n^i + v(\mathbf{x}_n^i) \cdot \Delta t \quad (\text{C.9b})$$

$$z_n^{i+1} = z_n^i + (w(\mathbf{x}_n^i) + w_{s,n}^i + w_{t,n}^i) \cdot \Delta t \quad (\text{C.9c})$$

The time step $\Delta t = 3$ minutes is very short compared to the time scale of waves in the model, which is several hours (see Section 2). The potential improvement in accuracy from using a higher order method such as Runge-Kutta is small because of the short time step, and the first-order solution (C.9) is computationally efficient. For $u(\mathbf{x}_n)$, $v(\mathbf{x}_n)$, and $w(\mathbf{x}_n)$, older versions of MIMAS use discrete values at the grid point closest to the particle. More recently, the dynamic fields are linearly interpolated to the particle's position (see Section C.7).

C.5 Details of NLC tracing method

For each of the 50 NLC events per latitudinal location, MIMAS was run for a period of 6 complete days. The starting point of the simulations is always 0:00 four days

Appendix C Technical details of MIMAS

before the date of the ice event, so the traced time period always includes at least 97 hours before the timing of the event and at least 24 hours afterwards. This time frame around the noctilucent cloud events was chosen so only very few particle trajectories are truncated, although this occurs for a number of particles at 79°N especially.

The MIMAS output routine was rewritten for the tracing study in Chapter 5: For each of the NLC events, only the 40,000 particle ensemble is traced, but at the time resolution used internally by the model (3 minutes). Normally, MIMAS processes the ice particles' position and size into reduced statistics like backscatter coefficient, which are saved once per hour. However, for this analysis, high resolution time series are generated of particle position, radius, and ambient parameters like temperature, water vapor, and vertical wind.

The program code of MIMAS includes several stochastic processes which are implemented using a (pseudo) random number generator. These include dust particle relocation (Section 3.3.1), both for preserving dust nuclei in the NLC domain and the 6 h periodic redistribution, as well as vertical diffusion of dust and icy particles (Section 3.3.3). Like all generators of pseudo random numbers, the one in Fortran 90 requires initialization with a seed number. It produces a deterministic sequence of random numbers after that. As a consequence, a MIMAS simulation with the same identical starting point is repeatable, i.e. a repeat of the simulation yields the exact same microphysical state for all model particles. However, there is a caveat: MIMAS allows interruption and re-initialization of the simulations, from arbitrary restart points at midnight of each model day. When a simulation is re-initialized, the random number sequence diverges from that in an uninterrupted model, changing the particle trajectories.

As has been tested by comparing continuous to interrupted MIMAS simulations, the large-scale structure of NLC evolves almost independently of random forks in single particles' trajectories. Instead, it depends only on the background dynamics. Thus, deterministic particle trajectories are not essential for most uses of MIMAS. On the other hand, a tracing study using backtrajectories requires a deterministic program code, otherwise the particles in the repeat run end up at different locations from the original simulation. To that end, the MIMAS programming was modified by reinitializing the random number sequence once per day. The random number seed is derived from the date, which makes the model code deterministic i.e. repeatable. The same deterministic version of MIMAS was used for the NLC event selection (Section 5.1.1) and for the trajectory calculation. Thus, backtrajectories of those particles within NLC could be calculated with a version of MIMAS only slightly modified compared to the standard version.

C.6 Improvements to dust relocation algorithm

The dust particle redistribution as described in Section 3.3.1 is an improved version of an earlier implementation. The original algorithm is optimized for computational efficiency, but has some deficiencies in the distribution produced. Figure C.1 shows the vertically integrated destinations of the relocation algorithm in both versions. With the original algorithm (left panel), two types of artifacts occur. There is a distinctive

C.6 Improvements to dust relocation algorithm

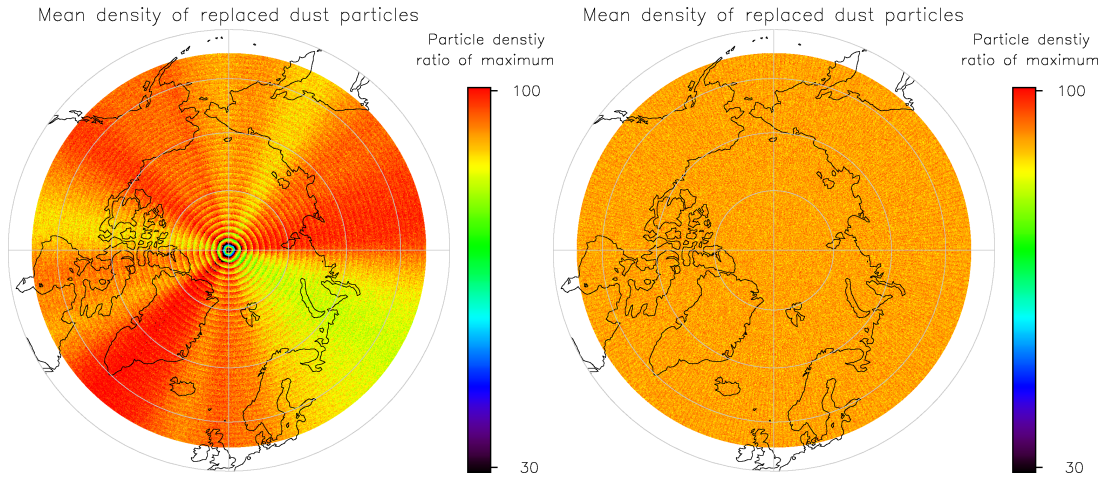


Figure C.1 Horizontal distribution of relocated condensation nuclei. Left panel: Original MIMAS dust particle redistribution, right panel: Redesigned redistribution algorithm.

radial asymmetry which is independent of latitude. The number of relocated dust particles varies between sectors by as much as 20%. This stems from those dust nuclei which are randomly relocated every 6 hours. In the original code, this relocation conserves the particles' longitude. Since model NLC have large scales, a forming ice cloud causes a lack of dust particles which persists even in the meridional and vertical integration. Conversely, sublimating NLC leave behind an excess of condensation nuclei. These zonal anisotropies are preserved in the original relocation algorithm, causing the imbalance between sectors as seen from the pole.

A second type of artifact visible in the left panel of Figure C.1 are concentric rings at 1° latitude intervals. These are most pronounced close to the pole and scarcely visible south of 70°N . They are caused by the procedure of how a latitude position is assigned to relocated dust particles. In the original code, the length of latitude circles ($\sin(\theta) \cdot 40,000$ km) is tabulated at 1° intervals. An integer latitude is assigned by weighting a uniform random number with the median length of the latitude circles, to account for a smaller probability per latitude close to the pole. However, a fractional latitude is assigned with a uniform random number. This causes discontinuities in probability density at the integer latitude circles, especially close to the pole where the length of one latitude circle to the next varies most.

The first type of artifact (radial asymmetry) can be easily fixed: Including a random zonal transport component in the periodic dust relocation algorithm ensures that longitudinal imbalances in nucleus density are removed. For the concentric ring artifacts, a continuous approach removes the discontinuities. By transforming a uniform random number with the arcsin function, a latitude distribution is generated which is uniform on a sphere. The distribution of relocated dust nuclei with both modifications is shown in the right panel of Figure C.1, only random variance is discernible here. Current versions of MIMAS use these modifications. The distribution of dust nuclei at the start of a MIMAS simulation also featured the concentric ring artifacts, but this

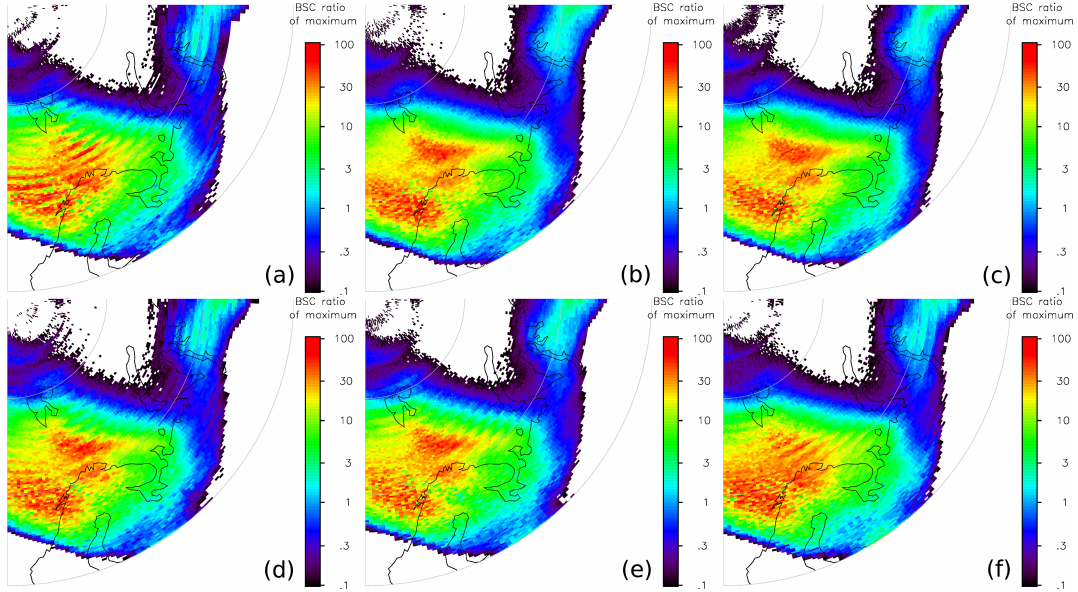


Figure C.2 Brightness of sample NLC with various degrees of microphysics grid interpolation. No interpolation (a) and 3-d interpolation of all parameters including temperature, wind components, density and water vapor (b). In the remaining panels, interpolation is omitted for single parameters: Zonal wind (c), meridional wind (d), temperature (e) water vapor (f).

was fixed with the same method.

C.7 Interpolation of background fields

Another area where the programming of MIMAS was optimized is the interaction between background dynamics and ice particle trajectories. In the original code, all microphysical and transport processes are applied using the dynamic fields at the nearest model grid vertex Section 3.1.2. Within each model grid volume, particles are exposed to constant dynamics, while at borders of two grid volumes there are discontinuities. These affect the particle history and the structure of NLC, especially at scales smaller than the model grid. Avoiding discontinuities improves the physical consistency of the model, so the previously discrete dynamic fields are now interpolated. Since this affects the microphysics of the 40 million particle ensemble, linear interpolation is chosen to limit the computational expense.

Figure C.2 shows the effects of the interpolation on the brightness of a sample ice cloud. Only part of the polar region is included as these changes are limited to smaller scales. In the original implementation (a), there are pronounced artifacts at each integer latitude circle, concentric rings of brightness variations. Linear interpolation of all microphysics parameters (b) removes the artifacts, as expected. In each of the remaining panels of Figure C.2, all parameters except one are interpolated. Both horizontal wind components, temperature, and water vapor are exempted to isolate the reason(s) for the artifacts. As there are no visible artifacts in (c), u is ruled out

C.7 Interpolation of background fields

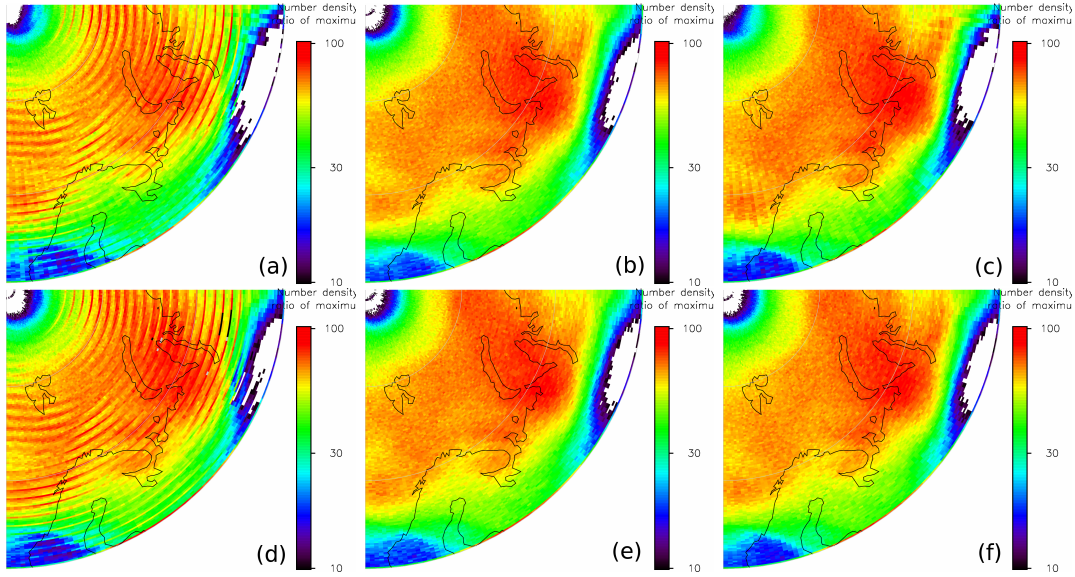


Figure C.3 Analogous to Figure C.2, but showing ice particle number density in percentage of maximum.

as a major factor for the inhomogeneity in NLC brightness. However, omitting the interpolation of either v , T , or $p_{\text{H}_2\text{O}}$ causes concentric ring artifacts, although less compared to (a). In (d) and (f), the artifacts are present in NLC of any brightness, while for temperature (e) they appear mostly in bright ice clouds.

To interpret the cause of the ring-shaped artifacts, Figure C.3 shows particle number density of the same 6 NLC simulations as Figure C.2. In contrast to brightness, number density is independent of particle size. Combining number density and scatter signal allows to discriminate between inhomogeneities in the spatial particle distribution and those in their size. As in Figure C.2, there are highly visible concentric rings present in Figure C.3 (a). These are overlaid with a much weaker, second set of radial artifacts along some meridians. No artifacts are present in (b), and neither in (e) or (f). This confirms that temperature and water vapor only cause artifacts in ice particle size, but not in their number. Panel (c) of Figure C.3 includes only the weak radial artifacts. However, (d) is almost identical to (a), leading to the conclusion that the inhomogeneities in particle number density almost exclusively stem not interpolating the meridional wind.

Considering both number density and brightness distribution leads to the conclusion that the concentric ring artifacts in cloud brightness originate from two sources: Inhomogeneities in particle distribution from (mostly meridional) wind, and those in particle size from temperature and water vapor. The number density artifacts can be explained by the slow mean v : At any latitude circle where the meridional wind reverses direction, ice particles are either depleted or trapped on a latitude circle, leading to high local concentrations. Strong meridional gradients in v may cause such inhomogeneities by themselves, although the effect is strongest at a wind reversal, and the lack of horizontal diffusion ensure they persist for some time. Similarly, lack of zonal wind interpolation causes the radial artifacts. These are much weaker compared to the

Appendix C Technical details of MIMAS

ring type artifacts because of the strong zonal wind in LIMA, with wind reversal very uncommon at NLC altitudes.

Discontinuities in temperature and water vapor cause artifacts by a different mechanism: In those areas with rapid particle growth or sublimation, the cloud brightness changes much faster than the time period required for meridional transport through 1° latitude bands. The latitudinal discontinuities in T and $p_{\text{H}_2\text{O}}$ cause large differences in growth conditions of adjacent particles (see Section 5.2). This can lead to large differences in the stage of growth or sublimation across latitude circle, i.e. artifacts.

There are some additional artifacts in the MIMAS model output which do not result from lack of interpolation: In direct vicinity to the pole, a numerical effect in vertical wind amplitudes also affects NLC modeling north of $\approx 85^\circ\text{N}$. As there is not simple fix for this, NLC results within this region should be used with caution.

In summary, interpolating the background dynamics in the microphysical modeling is required when analyzing NLC at a scale below that of the dynamic grid. Artifacts from omitting interpolation are caused by discontinuities in meridional transport, in combination with those in growth conditions.

Bibliography

- Backhouse, T. W., The luminous cirrus clouds of June and July, *Meteorol. Mag.*, *20*, 133, 1885.
- Bardeen, C. G., O. B. Toon, E. J. Jensen, M. E. Hervig, C. E. Randall, S. Benze, D. R. Marsh, and A. Merkel, Numerical simulations of the three-dimensional distribution of polar mesospheric clouds and comparisons with Cloud Imaging and Particle Size (CIPS) experiment and the Solar Occultation For Ice Experiment (SOFIE) observations, *J. Geophys. Res.*, *115*(D14), D10204, doi:10.1029/2009JD012451, 2010.
- Baumgarten, G., Leuchtende Nachtwolken an der polaren Sommermesopause: Untersuchungen mit dem ALOMAR Rayleigh/Mie/Raman Lidar, Ph.D. thesis, Universität Bonn, BONN-IR-2001-10, Bonn, Germany, 2001.
- Baumgarten, G., and G. E. Thomas, The importance of ice particle shape on UV measurements of polar mesospheric clouds: SBUV/2 observations, *J. Atmos. Sol.-Terr. Phys.*, *68*, 78–84, doi:10.1016/j.jastp.2005.08.007, 2006.
- Baumgarten, G., J. Fiedler, and G. von Cossart, The size of noctilucent cloud particles above ALOMAR (69N,16E): Optical modeling and method description, *Adv. Space Res.*, *40*, 772–784, doi:10.1016/j.asr.2007.01.018, 2007.
- Baumgarten, G., J. Fiedler, and M. Rapp, On microphysical processes of noctilucent clouds (NLC): observations and modeling of mean and width of the particle size-distribution, *Atmos. Chem. Phys.*, *10*, 6661–6668, 2010.
- Baumgarten, G., et al., On the horizontal and temporal structure of noctilucent clouds as observed by satellite and lidar at ALOMAR (69N), *Geophys. Res. Lett.*, *39*, L01803, doi:10.1029/2011GL049935, 2012.
- Becker, E., Frictional Heating in Global Climate Models, *Monthly Weather Review*, *131*, 508, doi:10.1175/1520-0493(2003)131<0508:FHIGCM>2.0.CO;2, 2003.
- Becker, E., Sensitivity of the Upper Mesosphere to the Lorenz Energy Cycle of the Troposphere, *Journal of Atmospheric Sciences*, *66*, 647, doi:10.1175/2008JAS2735.1, 2009.
- Becker, E., Dynamical Control of the Middle Atmosphere, *Space Sci. Rev.*, *168*, 283–314, doi:10.1007/s11214-011-9841-5, 2012.

Bibliography

- Becker, E., and U. Burkhardt, Nonlinear Horizontal Diffusion for GCMs, *Monthly Weather Review*, *135*, 1439, doi:10.1175/MWR3348.1, 2007.
- Berger, U., Modeling of middle atmosphere dynamics with LIMA, *J. Atmos. Sol.-Terr. Phys.*, *70*, 1170–1200, doi:10.1016/j.jastp.2008.02.004, 2008.
- Berger, U., and U. von Zahn, Icy particles in the summer mesopause region: Three-dimensional modeling of their environment and two-dimensional modeling of their transport, *J. Geophys. Res.*, *107*, 1366, doi:10.1029/2001JA000316, 2002.
- Berger, U., and U. von Zahn, Three-dimensional modeling of the trajectories of visible noctilucent cloud particles: An indication of particle nucleation well below the mesopause, *J. Geophys. Res.*, *112*(D11), D16204, doi:10.1029/2006JD008106, 2007.
- Bott, A., Monotone Flux Limitation in the Area-preserving Flux-form Advection Algorithm, *Mon. Weather Rev.*, *120*, 2592, doi:10.1175/1520-0493(1992)120<2592:MFLITA>2.0.CO;2, 1992.
- Chabrillat, S., and G. Kockarts, Simple parameterization of the absorption of the solar Lyman-alpha line, *Geophys. Res. Lett.*, *24*, 2659–2662, doi:10.1029/97GL52690, 1997.
- Chabrillat, S., and G. Kockarts, Correction to "simple parameterization of the absorption of the solar lyman-alpha line", *Geophys. Res. Lett.*, *25*, 79–79, doi:10.1029/97GL03569, 1998.
- Chang, L. C., et al., Comparison of diurnal tide in models and ground-based observations during the 2005 equinox CAWSES tidal campaign, *J. Atmos. Sol.-Terr. Phys.*, *78*, 19–30, doi:10.1016/j.jastp.2010.12.010, 2012.
- Chapman, S., and R. Lindzen, *Atmospheric tides. Thermal and gravitational*, Springer, Dordrecht, 1970.
- Dabdub, D., and J. H. Seinfeld, Numerical advective schemes used in air quality models - sequential and parallel implementation, *Atmos. Environ.*, *28*, 3369–3385, doi:10.1016/1352-2310(94)00124-4, 1994.
- Day, K. A., and N. J. Mitchell, The 5-day wave in the Arctic and Antarctic mesosphere and lower thermosphere, *J. Geophys. Res.*, *115*, D01109, doi:10.1029/2009JD012545, 2010.
- Deland, M. T., E. P. Shettle, G. E. Thomas, and J. J. Olivero, Latitude-dependent long-term variations in polar mesospheric clouds from SBUV version 3 PMC data, *J. Geophys. Res.*, *112*, D10315, doi:10.1029/2006JD007857, 2007.
- Deland, M. T., E. P. Shettle, P. F. Levelt, and M. G. Kowalewski, Polar mesospheric clouds (PMCs) observed by the Ozone Monitoring Instrument (OMI) on Aura, *Journal of Geophysical Research (Atmospheres)*, *115*, D21301, doi:10.1029/2009JD013685, 2010.

- Drob, D. P., et al., An empirical model of the Earth's horizontal wind fields: HWM07, *Journal of Geophysical Research (Space Physics)*, *113*, A12304, doi:10.1029/2008JA013668, 2008.
- Dunkerton, T. J., Nonlinear Propagation of Zonal Winds in an Atmosphere with Newtonian Cooling and Equatorial Wavedriving., *J. Atmos. Sci.*, *48*, 236–263, doi:10.1175/1520-0469(1991)048<0236:NPOZWI>2.0.CO;2, 1991.
- Eidhammer, T., and O. Havnes, Size dependence of the mesospheric dust temperature and its influence on the noctilucent clouds and polar mesosphere summer echo phenomena, *J. Geophys. Res.*, *106*, 24,831–24,842, doi:10.1029/2001JA900036, 2001.
- Eremenko, M. N., S. V. P. A. Y. Zsetsky, B. Karlsson, C. P. Rinsland, E. J. Llewellyn, and J. J. Sloan, Shape and composition of PMC particles derived from satellite remote sensing measurements, *Geophys. Res. Lett.*, *32*(16), L16S06, doi:10.1029/2005GL023013, 2005.
- Espy, P. J., and H. Jutt, Equilibrium temperature of water-ice aerosols in the high-latitude summer mesosphere, *J. Atmos. Sol.-Terr. Phys.*, *64*, 1823–1832, doi:10.1016/S1364-6826(02)00191-8, 2002.
- Fiedler, J., G. Baumgarten, and F.-J. Lübken, NLC observations during one solar cycle above ALOMAR, *J. Atmos. Sol.-Terr. Phys.*, *71*, 424–433, doi:10.1016/j.jastp.2008.11.010, 2009.
- Fiedler, J., G. Baumgarten, U. Berger, P. Hoffmann, N. Kaifler, and F.-J. Lübken, NLC and the background atmosphere above ALOMAR, *Atmos. Chem. Phys.*, *11*, 5701–5717, doi:10.5194/acp-11-5701-2011, 2011.
- Fomichev, V. I., and G. M. Shved, Net radiative heating in the middle atmosphere, *Journal of Atmospheric and Terrestrial Physics*, *50*, 671–688, 1988.
- Fomichev, V. I., J.-P. Blanchet, and D. S. Turner, Matrix parameterization of the 15 micrometer CO₂ band cooling in the middle and upper atmosphere for variable CO₂ concentration, *J. Geophys. Res.*, *103*, 11,505, doi:10.1029/98JD00799, 1998.
- Fritts, D. C., and M. J. Alexander, Gravity wave dynamics and effects in the middle atmosphere, *Reviews of Geophysics*, *41*, 1003, doi:10.1029/2001RG000106, 2003.
- Gadsden, M., Noctilucent clouds, *Space Sci. Rev.*, *33*, 279–334, doi:10.1007/BF00196999, 1982.
- Gadsden, M., A note on the orientation and size of noctilucent cloud particles, *Tellus Series B Chemical and Physical Meteorology B*, *35*, 73–75, doi:10.1111/j.1600-0889.1983.tb00009.x, 1983.
- Gadsden, M., Noctilucent clouds seen at 60°N: origin and development, *J. Atmos. Sol.-Terr. Phys.*, *60*, 1763–1772, doi:10.1016/S1364-6826(98)00154-0, 1998.
- Gadsden, M., and W. Schröder, *Noctilucent clouds*, Springer-Verlag, New York, 1989.

Bibliography

- Gerding, M., J. Höffner, M. Rauthe, W. Singer, M. Zecha, and F.-J. Lübken, Simultaneous observation of noctilucent clouds, mesospheric summer echoes, and temperature at a midlatitude station (54°N), *J. Geophys. Res.*, *112*(D11), D12,111, doi:10.1029/2006JD008135, 2007.
- Gerding, M., M. Kopp, P. Hoffmann, J. Höffner, and F.-J. Lübken, Diurnal variations of midlatitude NLC parameters observed by daylight-capable lidar and their relation to ambient parameters, *Geophys. Res. Lett.*, *40*, 63906394, doi:10.1002/2013GL057955, 2013.
- Gumbel, J., and G. Witt, Rocket-borne photometry of NLC particle populations, *Adv. Space Res.*, *28*, 1053–1058, doi:10.1016/S0273-1177(01)80036-3, 2001.
- Gumbel, J., D. E. Siskind, G. Witt, K. M. Torkar, and M. Friedrich, Influences of ice particles on the ion chemistry of the polar summer mesosphere, *J. Geophys. Res.*, *108*, 8436, doi:10.1029/2002JD002413, 2003.
- Hale, B. N., and P. L. M. Plummer, Molecular model for ice clusters in a supersaturated vapor, *J. Chem. Phys.*, *61*, 4012–4019, doi:10.1063/1.1681694, 1974.
- Hartogh, P., G. R. Sonnemann, M. Grygalashvyly, L. Song, U. Berger, and F.-J. Lübken, Water vapor measurements at ALOMAR over a solar cycle compared with model calculations by LIMA, *J. Geophys. Res.*, *115*, D00I17, doi:10.1029/2009JD012364, 2010.
- Hervig, M. E., and L. L. Gordley, Temperature, shape, and phase of mesospheric ice from Solar Occultation for Ice Experiment observations, *J. Geophys. Res.*, *115*(D14), D15208, doi:10.1029/2010JD013918, 2010.
- Hervig, M. E., L. L. Gordley, M. H. Stevens, J. M. Russell, III, S. M. Bailey, and G. Baumgarten, Interpretation of SOFIE PMC measurements: Cloud identification and derivation of mass density, particle shape, and particle size, *J. Atmos. Sol.-Terr. Phys.*, *71*, 316–330, doi:10.1016/j.jastp.2008.07.009, 2009a.
- Hervig, M. E., M. H. Stevens, L. L. Gordley, L. E. Deaver, J. M. Russell, and S. M. Bailey, Relationships between polar mesospheric clouds, temperature, and water vapor from Solar Occultation for Ice Experiment (SOFIE) observations, *J. Geophys. Res.*, *114*, D20203, doi:10.1029/2009JD012302, 2009b.
- Hesstvedt, E., Note on the Nature of Noctilucent Clouds, *J. Geophys. Res.*, *66*, 1985–1987, doi:10.1029/JZ066i006p01985, 1961.
- Hoffmann, P., E. Becker, W. Singer, and M. Placke, Seasonal variation of mesospheric waves at northern middle and high latitudes, *J. Atmos. Sol.-Terr. Phys.*, *72*, 1068–1079, doi:10.1016/j.jastp.2010.07.002, 2010.
- Höffner, J., and F.-J. Lübken, Potassium lidar temperatures and densities in the mesopause region at Spitsbergen (78°N), *J. Geophys. Res.*, *112*(D11), D20114, doi:10.1029/2007JD008612, 2007.

- Höffner, J., C. Fricke-Begemann, and F.-J. Lübken, First observations of noctilucent clouds by lidar at Svalbard, 78°N, *Atmos. Chem. Phys.*, *3*, 1101–1111, 2003.
- Holton, J. R., The Influence of Gravity Wave Breaking on the General Circulation of the Middle Atmosphere., *Journal of Atmospheric Sciences*, *40*, 2497–2507, doi:10.1175/1520-0469(1983)040<2497:TIOGWB>2.0.CO;2, 1983.
- Hunten, D. M., R. P. Turco, and O. B. Toon, Smoke and dust particles of meteoric origin in the mesosphere and stratosphere, *J. Atmos. Sci.*, *37*, 1342–1357, doi:10.1175/1520-0469(1980)037(1342:SADPOM)2.0.CO;2, 1980.
- Jesse, O., Auffallende Abenderscheinungen am Himmel, *Meteorol. Zeitung*, *2*, 311–312, 1885.
- Kaifler, N., G. Baumgarten, J. Fiedler, R. Latteck, F.-J. Lübken, and M. Rapp, Coincident measurements of PMSE and NLC above ALOMAR (69° N, 16° E) by radar and lidar from 1999-2008, *Atmos. Chem. Phys.*, *11*, 1355–1366, doi:10.5194/acp-11-1355-2011, 2011.
- Kaifler, N., G. Baumgarten, J. Fiedler, and F.-J. Lübken, Quantification of waves in lidar observations of noctilucent clouds at scales from seconds to minutes, *Atmos. Chem. Phys.*, *13*, 11,757–11,768, doi:10.5194/acp-13-11757-2013, 2013a.
- Kaifler, N., G. Baumgarten, A. R. Klekociuk, S. P. Alexander, J. Fiedler, and F.-J. Lübken, Small scale structures of NLC observed by lidar at 69°N/69°S and their possible relation to gravity waves, *J. Atmos. Sol.-Terr. Phys.*, *104*, 244–252, doi:10.1016/j.jastp.2013.01.004, 2013b.
- Karlsson, B., and M. Rapp, Latitudinal dependence of noctilucent cloud growth, *Geophys. Res. Lett.*, *33*(11), L11812, doi:10.1029/2006GL025805, 2006.
- Kilian, J., G. Baumgarten, F.-J. Lübken, U. Berger, and P. Hoffmann, Temporal and spatial characteristics of the formation of strong noctilucent clouds, *Journal of Atmospheric and Solar-Terrestrial Physics*, *104*(0), 151 – 166, doi:10.1016/j.jastp.2013.01.005, 2013.
- Kockarts, G., Nitric oxide cooling in the terrestrial thermosphere, *Geophys. Res. Lett.*, *7*, 137–140, doi:10.1029/GL007i002p00137, 1980.
- Kutepov, A. A., A. G. Feofilov, A. S. Medvedev, A. W. A. Pauldrach, and P. Hartogh, Small-scale temperature fluctuations associated with gravity waves cause additional radiative cooling of mesopause the region, *Geophys. Res. Lett.*, *34*, L24807, doi:10.1029/2007GL032392, 2007.
- Leslie, R. C., Sky Glows, *Nature*, *32*, 245, doi:10.1038/032245a0, 1885.
- Lewis, B. R., I. M. Vardavas, and J. H. Carver, The aeronomic dissociation of water vapor by solar H Lyman-alpha radiation, *J. Geophys. Res.*, *88*, 4935–4940, doi:10.1029/JA088iA06p04935, 1983.

Bibliography

- Li, Q., et al., Microphysical parameters of mesospheric ice clouds derived from calibrated observations of polar mesosphere summer echoes at Bragg wavelengths of 2.8 m and 30 cm, *J. Geophys. Res.*, *115*(D14), D00I13, doi:10.1029/2009JD012271, 2010.
- Liu, H.-L., E. R. Talaat, R. G. Roble, R. S. Lieberman, D. M. Riggan, and J.-H. Yee, The 6.5-day wave and its seasonal variability in the middle and upper atmosphere, *J. Geophys. Res.*, *109*, D21112, doi:10.1029/2004JD004795, 2004.
- Lossow, S., J. Urban, J. Gumbel, P. Eriksson, and D. Murtagh, Observations of the mesospheric semi-annual oscillation (MSAO) in water vapour by Odin/SMR, *Atmospheric Chemistry & Physics*, *8*, 6527–6540, 2008.
- Love, S. G., and D. E. Brownlee, A Direct Measurement of the Terrestrial Mass Accretion Rate of Cosmic Dust, *Science*, *262*, 550, 1993.
- Lübken, F., U. Berger, and G. Baumgarten, Stratospheric and solar cycle effects on long-term variability of mesospheric ice clouds, *J. Geophys. Res.*, *114*(A13), 0–+, doi:10.1029/2009JD012377, 2009.
- Lübken, F.-J., Seasonal variation of turbulent energy dissipation rates at high altitudes as determined by in situ measurements of neutral density fluctuations, *J. Geophys. Res.*, *102*(D12), 13,441–13,456, 1997.
- Lübken, F.-J., Thermal structure of the arctic summer mesosphere, *J. Geophys. Res.*, *104*(D8), 9135–9149, doi:10.1029/1999JD900076, 1999.
- Lübken, F.-J., and U. Berger, Latitudinal and interhemispheric variation of stratospheric effects on mesospheric ice layer trends, *J. Geophys. Res.*, *116*(D15), D00P03, doi:10.1029/2010JD015258, 2011.
- Lübken, F.-J., K.-H. Fricke, and M. Langer, Noctilucent clouds and the thermal structure near the Arctic mesopause in summer, *J. Geophys. Res.*, *101*, 9489–9508, doi:10.1029/96JD00444, 1996.
- Lübken, F.-J., U. Berger, and G. Baumgarten, Temperature trends in the midlatitude summer mesosphere, *J. Geophys. Res.*, *118*, doi:10.1002/2013JD020576, 2013a.
- Lübken, F.-J., U. Berger, J. Kiliani, G. Baumgarten, and J. Fiedler, Solar Variability and Trend Effects in Mesospheric Ice Layers, in *Climate and Weather of the Sun-Earth System (CAWSES)*, edited by F.-J. Lübken, pp. 317–338, Springer, Dordrecht, doi:10.1007/978-94-007-4348-9_18, 2013b.
- Mauersberger, K., and D. Krankowsky, Vapor pressure above ice at temperatures below 170 K, *Geophys. Res. Lett.*, *30*, 1121, doi:10.1029/2002GL016183, 2003.
- McClintock, W. E., D. W. Rusch, G. E. Thomas, A. W. Merkel, M. R. Lankton, V. A. Drake, S. M. Bailey, and J. M. Russell, III, The cloud imaging and particle size experiment on the Aeronomy of Ice in the mesosphere mission: Instrument concept, design, calibration, and on-orbit performance, *J. Atmos. Sol.-Terr. Phys.*, *71*, 340–355, doi:10.1016/j.jastp.2008.10.011, 2009.

- McHugh, M., B. Magill, K. A. Walker, C. D. Boone, P. F. Bernath, and J. M. Russell, Comparison of atmospheric retrievals from ACE and HALOE, *Geophys. Res. Lett.*, *32*, L15S10, doi:10.1029/2005GL022403, 2005.
- Megner, L., Minimal impact of condensation nuclei characteristics on observable Mesospheric ice properties, *J. Atmos. Sol.-Terr. Phys.*, *73*, 2184–2191, doi:10.1016/j.jastp.2010.08.006, 2011.
- Merkel, A. W., D. R. Marsh, A. Gettelman, and E. J. Jensen, On the relationship of polar mesospheric cloud ice water content, particle radius and mesospheric temperature and its use in multi-dimensional models, *Atmos. Chem. Phys.*, *9*, 8889–8901, 2009.
- Meyer, C. K., and J. M. Forbes, A 6.5-day westward propagating planetary wave: Origin and characteristics, *J. Geophys. Res.*, *102*, 26,173, doi:10.1029/97JD01464, 1997.
- Mishchenko, M. I., and L. D. Travis, Capabilities and limitations of a current FORTRAN implementation of the t-matrix method for randomly oriented, rotationally symmetric scatterers, *J. Quant. Spectrosc. Radiat. Transfer*, *60*, 309–324, doi:10.1016/S0022-4073(98)00008-9, 1998.
- Mlynczak, M. G., and S. Solomon, A detailed evaluation of the heating efficiency in the middle atmosphere, *J. Geophys. Res.*, *98*, 10,517, doi:10.1029/93JD00315, 1993.
- Murphy, D. M., and T. Koop, Review of the vapour pressures of ice and supercooled water for atmospheric applications, *Quart. J. R. Met. Soc.*, *131*, 15391565, doi:10.1256/qj.04.94, 2005.
- Murray, B. J., and E. J. Jensen, Homogeneous nucleation of amorphous solid water particles in the upper mesosphere, *J. Atmos. Sol.-Terr. Phys.*, *72*, 51–61, doi:10.1016/j.jastp.2009.10.007, 2010.
- Nedoluha, G. E., R. M. Gomez, B. C. Hicks, R. M. Bevilacqua, J. M. Russell, B. J. Connor, and A. Lambert, A comparison of middle atmospheric water vapor as measured by WVMS, EOS-MLS, and HALOE, *Journal of Geophysical Research (Atmospheres)*, *112*, D24S39, doi:10.1029/2007JD008757, 2007.
- Nussbaumer, V., K. H. Fricke, M. Langer, W. Singer, and U. von Zahn, First simultaneous and common volume observations of noctilucent clouds and polar mesosphere summer echoes by lidar and radar, *J. Geophys. Res.*, *101*, 19,161–19,168, doi:10.1029/96JD01213, 1996.
- Ogibalov, V. P., and V. I. Fomichev, Parameterization of solar heating by the near IR CO₂ bands in the mesosphere, *Advances in Space Research*, *32*, 759–764, doi:10.1016/S0273-1177(03)80069-8, 2003.
- Press, W. H., S. A. Teukolsky, W. T. Vetterling, and B. P. Flannery, *Numerical recipes in C++ : the art of scientific computing*, Cambridge University Press, New York, 2002.

Bibliography

- Rapp, M., and F.-J. Lübken, Polar mesosphere summer echoes (PMSE): Review of observations and current understanding, *Atmos. Chem. and Phys.*, *4*, 2601–2633, 2004.
- Rapp, M., and G. E. Thomas, Modeling the microphysics of mesospheric ice particles: Assessment of current capabilities and basic sensitivities, *J. Atmos. Sol.-Terr. Phys.*, *68*(7), 715–744, doi:10.1016/j.jastp.2005.10.015, 2006.
- Rapp, M., F.-J. Lübken, A. Müllemann, G. E. Thomas, and E. J. Jensen, Small-scale temperature variations in the vicinity of NLC: Experimental and model results, *J. Geophys. Res.*, *107*, 4392, doi:10.1029/2001JD001241, 2002.
- Rapp, M., G. E. Thomas, and G. Baumgarten, Spectral properties of mesospheric ice clouds: evidence for non-spherical particles, *Geophys. Res. Lett.*, *112*(D3), D03,211, doi:10.1029/2006JD007322, 2007.
- Rauthe, M., M. Gerding, J. Höffner, and F.-J. Lübken, Lidar temperature measurements of gravity waves over kühlungsborn (54°n) from 1 to 105 km: A winter-summer comparison, *J. Geophys. Res.*, *111*, D24,108, doi:10.1029/2006JD007354, 2006.
- Reid, G. C., Ice clouds at the summer polar mesopause, *J. Atmos. Sci.*, *32*, 523–535, doi:10.1175/1520-0469(1975)032<0523:ICATSP>2.0.CO;2, 1975.
- Rosinski, J., and R. H. Snow, Secondary Particulate Matter from Meteor Vapors., *Journal of Atmospheric Sciences*, *18*, 736–745, doi:10.1175/1520-0469(1961)018<0736:SPMFMV>2.0.CO;2, 1961.
- Russell, J. M., III, et al., The Aeronomy of Ice in the Mesosphere (AIM) mission: Overview and early science results, *Journal of Atmospheric and Solar-Terrestrial Physics*, *71*, 289–299, doi:10.1016/j.jastp.2008.08.011, 2009.
- Singer, W., J. Bremer, W. K. Hocking, J. Weiss, R. Latteck, and M. Zecha, Temperature and wind tides around the summer mesopause at middle and Arctic latitudes, *Adv. Space Res.*, *31*(9), 2055–2060, doi:10.1016/S0273-1177(03)00228-X, 2003.
- Singer, W., R. Latteck, and D. A. Holdsworth, A new narrow beam Doppler radar at 3 MHz for studies of the high-latitude middle atmosphere, *Adv. Space Res.*, *41*, 1487–1493, doi:10.1016/j.asr.2007.10.006, 2007.
- Stevens, M. H., et al., Validation of upper mesospheric and lower thermospheric temperatures measured by the Solar Occultation for Ice Experiment, *J. Geophys. Res.*, *117*, D16304, doi:10.1029/2012JD017689, 2012.
- Strobel, D. F., Parameterization of the atmospheric heating rate from 15 to 120 km due to O₂ and O₃ absorption of solar radiation, *J. Geophys. Res.*, *83*, 6225–6230, doi:10.1029/JC083iC12p06225, 1978.
- Sugiyama, T., Ion-recombination nucleation and growth of ice particles in noctilucent clouds, *J. Geophys. Res.*, *99*, 3915–3929, doi:10.1029/93JA02822, 1994.

- Tolman, R. C., The Effect of Droplet Size on Surface Tension, *J. Chem. Phys.*, *17*, 333–337, doi:10.1063/1.1747247, 1949.
- Turco, R. P., O. B. Toon, R. C. Whitten, R. G. Keesee, and D. Hollenbach, Noctilucent clouds - Simulation studies of their genesis, properties and global influences, *Planet. Space Sci.*, *30*, 1147–1181, doi:10.1016/0032-0633(82)90126-X, 1982.
- Vergados, P., and M. G. Shepherd, Retrieving mesospheric water vapour from observations of volume scattering radiances, *Ann. Geophys.*, *27*, 487–501, doi:10.5194/angeo-27-487-2009, 2009.
- von Savigny, C., C. Robert, H. Bovensmann, J. P. Burrows, and M. Schwartz, Satellite observations of the quasi 5-day wave in noctilucent clouds and mesopause temperatures, *Geophys. Res. Lett.*, *34*, L24808, doi:10.1029/2007GL030987, 2007.
- von Zahn, U., and U. Berger, Persistent ice cloud in the midsummer upper mesosphere at high latitudes: Three-dimensional modeling and cloud interactions with ambient water vapor, *J. Geophys. Res.*, *108*, 8451, doi:10.1029/2002JD002409, 2003.
- Walcek, C. J., Minor flux adjustment near mixing ratio extremes for simplified yet highly accurate monotonic calculation of tracer advection, *J. Geophys. Res.*, *105*, 9335–9348, doi:10.1029/1999JD901142, 2000.
- Walcek, C. J., and N. M. Aleksic, A simple but accurate mass conservative, peak-preserving, mixing ratio bounded advection algorithm with FORTRAN code, *Atmospheric Environment*, *32*, 3863–3880, doi:10.1016/S1352-2310(98)00099-5, 1998.
- Wu, D. L., P. B. Hays, and W. R. Skinner, Observations of the 5-day wave in the mesosphere and lower thermosphere, *Geophys. Res. Lett.*, *21*, 2733–2736, doi:10.1029/94GL02660, 1994.
- Xu, J., C. Y. She, W. Yuan, C. Mertens, M. Mlynczak, and J. Russell, Comparison between the temperature measurements by TIMED/SABER and lidar in the midlatitude, *Journal of Geophysical Research (Space Physics)*, *111*, A10S09, doi:10.1029/2005JA011439, 2006.
- Xu, J., H.-L. Liu, W. Yuan, A. K. Smith, R. G. Roble, C. J. Mertens, J. M. Russell III, and M. G. Mlynczak, Mesopause structure from Thermosphere, Ionosphere, Mesosphere, Energetics, and Dynamics (TIMED)/Sounding of the Atmosphere using Broadband Emission Radiometry (SABER) observations, *J. Geophys. Res.*, *112*(D9), D09102, doi:10.1029/2006JD007711, 2007.
- Zhu, X., An Accurate and Efficient Radiation Algorithm for Middle Atmosphere Models., *Journal of Atmospheric Sciences*, *51*, 3593–3614, doi:10.1175/1520-0469(1994)051<3593:AAAERA>2.0.CO;2, 1994.

List of Figures

1.1	Schematic polar region temperature profile	1
1.2	Sample NLC photograph	3
1.3	NLC mechanisms schematic	4
2.1	LIMA summer climatology	10
2.2	KMCM summer climatology	12
2.3	Wind variability in KMCM	13
2.4	Wind at 69°N: Models and measurements	14
2.5	Temperature at 69°N: Models and measurements	14
2.6	LIMA horizontal wind LT variations (69°N)	16
2.7	Meridional wind time series at ALOMAR	18
2.8	Temperature sample time series at ALOMAR	19
2.9	Zonal wave propagation in LIMA and KMCM	21
2.10	Long-period waves in LIMA and KMCM	22
3.1	MIMAS model structure	26
3.2	Mesospheric water vapor: Measurements and MIMAS profiles	28
3.3	H ₂ O photolysis in MIMAS	29
3.4	Schematic of meteoric dust in MIMAS	31
3.5	Water vapor saturation pressure	32
4.1	Horizontal and vertical/radius snapshot of NLC in MIMAS-LIMA	36
4.2	Lidar measurement of noctilucent cloud	37
4.3	Noctilucent cloud duration	38
4.4	Vertical and latitude time series of temperature and NLC in LIMA	39
4.5	Climatology of NLC-related parameters in MIMAS-LIMA	40
4.6	Sample horizontal and vertical ice particle trajectories	41
4.7	Ice particle lifetime and maximum radius	42
4.8	Timing of peak size for mesospheric ice particles	43
4.9	General particle visibility time	44
4.10	Cross correlation between ambient parameters and NLC	45
4.11	Scale dependence of correlation temperature-NLC height	46
4.12	NLC parametrization from temperature and ice water content	48
4.13	Heuristic NLC parametrization from temperature	50
5.1	Model NLC time series at ALOMAR in July 2009	51

List of Figures

5.2	Particle size distribution and cutoff radius	52
5.3	Single NLC trajectory (69°N)	54
5.4	Single NLC altitude trajectory and particle age (69°N)	55
5.5	Single NLC growth and microphysics (69°N)	56
5.6	Single NLC nucleation process	59
5.7	Transport of NLC ensemble at 69°N	61
5.8	Microphysics during NLC main growth phase	62
5.9	Time series of NLC particle vertical motion	63
5.10	Time scale dependence of vertical motion components	64
5.11	Nucleation process of 50 NLC ensemble	65
5.12	Dependence of particle age on dust nucleus size	66
5.13	NLC particle sublimation process and visibility time	68
5.14	NLC particle history at Spitsbergen	71
5.15	NLC particle history at latitudes < 60°N	72
6.1	Microphysics correction factors for aspheric particles	76
6.2	Color ratios at ALOMAR and in MIMAS-LIMA	78
6.3	Morphology of NLC with cylindrical particles	81
6.4	Sample ice particle trajectories in MIMAS-KMCM ₃₀	84
6.5	Latitudinal and vertical time series of NLC in MIMAS-KMCM ₃₀	85
6.6	Climatology of NLC-related parameters in MIMAS-KMCM ₃₀	86
6.7	NLC brightness dependence on wave spectrum	88
6.8	Wave spectrum dependence of MIMAS NLC life cycle parameters	89
A.1	ALOMAR temperature tide in LIMA	97
A.2	Lidar measurements of temperature tide at ALOMAR	98
A.3	Fourier spectra of model and radar dynamic fields	99
A.4	Vertically resolved Fourier spectra of zonal wind	101
B.1	Color ratio dependence on particle size and shape	104
B.2	Color ratio combinations for idealized distributions	104
B.3	Vertical and latitudinal distribution of condensation nuclei	105
B.4	Fourier spectrum of ice in MIMAS-LIMA and MIMAS-KMCM	106
B.5	Snapshots of MIMAS-KMCM	107
B.6	Additional GW dependence of NLC life cycle parameters	108
B.7	Time series of MIMAS-LIMA+KMCM hybrid simulation	110
B.8	Snapshot of MIMAS-LIMA+KMCM hybrid simulation	111
B.9	Zonal propagation of NLC in MIMAS-LIMA and MIMAS-KMCM ₃₀	112
B.10	Altitude and temperature of NLC particle nucleation	113
B.11	Lifetime vertical particle transport	114
B.12	Growth and microphysics of NLC ensemble (69°N)	115
B.13	Vertical development of NLC at Spitsbergen	116
B.14	Vertical development of NLC at latitudes < 60°N	117
C.1	Dust particle redistribution algorithm	123
C.2	Interpolation of dynamic fields in MIMAS: Brightness	124
C.3	Interpolation of dynamic fields in MIMAS: Number density	125

List of Tables

5.1	Growth parameters during ice life cycle	58
5.2	Life cycle statistics of strong NLC particles	69
6.1	Color ratio distribution values	79
6.2	Wave spectrum dependence of NLC particle life cycle	91

List of Symbols and Acronyms

Symbols

β	backscatter coefficient
β_{\max}	column maximum backscatter coefficient
β_{int}	column integrated backscatter coefficient
ϵ	aspect ratio (diameter divided by height)
K_{zz}	vertical diffusion coefficient
λ	(light's) wavelength
$p_{\text{H}_2\text{O}}$	water vapor partial pressure
$p_{\text{sat}}(r)$	equilibrium vapor pressure
p_{∞}	saturation vapor pressure
r	(particle) radius
r_{cutoff}	dust distribution size limit
S	saturation ratio
t_0	NLC event observation time
T	temperature
T_p	particle temperature
t_{life}	(particle) lifetime
t_{subl}	sublimation time
t_{vis}	visibility period
v	meridional wind
w_s	sedimentation rate
w_t	turbulent velocity
z	altitude

Abbreviations and Acronyms

ALOMAR	Arctic Lidar Observatory for Middle Atmosphere Research
AR	Aspect Ratio
BSC	BackScatter Coefficient
CARMA	Community Aerosol and Radiation Model of the Atmosphere
CN	Condensation Nucleus
COMMA/IAP	COlogne Model of the Middle Atmosphere - Version IAP
CR	Color Ratio
ECMWF	European Center for Medium-Range Weather Forecasts
FWHM	Full Width at Half Maximum
GW	Gravity Wave
IAP	Institute of Atmospheric Physics
IWC	Ice Water Content
LIMA	Leibniz Institute Middle Atmosphere model
LPA	Large Particle Analysis
KMCM	Kühlungsborn Mechanistic Circulation Model
MIMAS	Mesospheric Ice Microphysics And tranSport model
MLT	Mesosphere and Lower Thermosphere
NLC	NoctiLucent Cloud
PMC	Polar Mesospheric Cloud
RMSD	Root-Mean-Square Deviation
SOFIE	Solar Occultation For Ice Experiment
SPA	Small Particle Analysis
UT	Universal Time

Acknowledgments

I would like to take this opportunity to thank all of my colleagues at the Institute of Atmospheric Physics. Your friendliness and kindness in helping out those who needed assistance has made the time here at IAP a great and memorable experience.

I would especially like to thank my supervisor, Professor Franz-Josef Lübken, for his invaluable guidance during my time at IAP. He has given me many inspiring ideas to pursue in my research, valuable feedback to my results, advice on how to structure and write this thesis, and patience when I did not always articulate as clearly as he hoped. As director, he has always been willing to listen to my concerns and those of others at the institute.

My most heartfelt thanks go to Gerd Baumgarten, who spent many hours helping me correct drafts of my article and this thesis. In many cases, he has been very patient in reading through the frustrating unrefined first drafts along with giving helpful comments to help improve this thesis. He has also given me several data sets to work with and offered opinions and suggestions for improvement on numerous of my preliminary results. He advised me on Unix shell scripting, remote computing and several other topics. Finally, he has given me the opportunity to visit the ALOMAR observatory twice, where I was able to do practical atmospheric research.

I gratefully acknowledge the European Centre for Medium-Range Weather Forecasts (ECMWF) for providing their reanalysis data.

I would like to thank the Climate And Weather of the Sun-Earth System (CAWSES) project within the DFG for supporting this PhD position.

I would also like to offer many thanks to the following people:

Uwe Berger, for his advice on Fortran programming, and for answering numerous questions about the structure and program code of MIMAS (former LIMA/ICE) and the data linked to it. He has helped and guided me in several topics along with improving my understanding of atmospheric physics in the process.

Erich Becker, for giving me access to KMCM dynamic data and detailed instructions on how to use it. He gave me a new viewpoint and helped me get a better understanding of my topic in the process.

Markus Rapp, for giving easy to follow and highly educational lectures on atmospheric physics. He has helped me considerably to understand the subjects, with my mathematics background and no prior knowledge of atmospheric physics.

Peter Hoffmann, Irina Strelnikova, Josef Höffner, Tim Dunker, and Jens Fiedler for providing me with measurements to use in this thesis, and helping me understand and interpret the data sets.

Jens Hildebrand, for knowing everything there is to know about LaTeX and helping

Acknowledgments

me out with TeX typesetting problems on many occasions including a format template for this thesis, along with his very meticulous proofreading.

Maren Kopp, for answering many scientific and organizational questions, and helping me solve occasional problems. Thank you for being there when I needed someone to talk to, and for being a great friend in general.

Dirk Rachholz, for teaching me a lot about using IDL, creating animations and computing in general. Also, for being around to talk to and share many laughs with.

Manja Placke and Vivien Matthias, for sharing their experiences about completing a PhD thesis, and advice about important points that should not be forgotten.

Michael Gerding, for teaching me a lot about lidar measurements especially at Kühlungsborn, and on atmospheric physics.

Natalie Kaifler, for helping me with her extensive knowledge of Unix shell commands.

My mother, Susanne Kiliani, and my brother David Kiliani, for their valuable assistance in proofreading my thesis.

Last but certainly not least my fiancée, Vichaya Sdoodee. She has helped me greatly to improve the style and readability of parts of this thesis, in spite of the intense effort, not being a physicist herself, but a physician. She has also helped me rehearse for several presentations, and has given me a lot of general and motivational advice, helping me push through stressful times and stay focused in spite of difficulties.

Erklärung

Hiermit versichere ich an Eides statt, die vorliegende Arbeit selbständig und ohne fremde Hilfe verfasst, keine außer den von mir angegebenen Quellen und Hilfsmitteln verwandt und die den genutzten Werken inhaltlich oder wörtlich entnommenen Stellen als solche kenntlich gemacht zu haben.

Die Arbeit wurde bisher weder im Inland noch im Ausland in gleicher oder ähnlicher Form einer anderen Prüfungsbehörde vorgelegt. Weiterhin erkläre ich, dass ich ein Verfahren zur Erlangung des Doktorgrades an keiner anderen wissenschaftlichen Einrichtung beantragt habe.

Kühlungsborn, den 27. Juni 2014

(Johannes Kiliani)